University
of Southampton

Fabrication of high temperature superconducting Ag/Bi-2223 tapes and current leads for superconducting particle accelerator magnets

Stavros Avgeros

Applied Superconductivity Group
Faculty of Applied Science and Engineering

Southampton, England
December 2004

Dedicated to:

Georgios A. Chrysanthis

"Liberty"

UNIVERSITY OF SOUTHAMTON

ABSTRACT

Faculty of Engineering and Applied Science
School of Engineering Sciences

Doctor of Philosophy

Fabrication of HTS Ag/Bi-2223 Tapes and Current Leads for superconducting particle accelerator magnets

By **Stavros Avgeros**

The processing of composite Ag/(Pb,Bi)-2223 tapes has been extensively investigated since the year 1989, where the first tapes were made by the oxide-powder-in-tube (OPIT) technique. The formation of the Bi-2223 phase is via a Pb-induced liquid phase which is known to assist the Bi-2223 formation. However there are many unsolved microstructural inhomogeneities and defects in current OPIT tape; consequently research has begun to focus on the role of the liquid phase. In this study, differential thermal analysis studies on green Ag/(Bi,Pb)2223 tape showed two phase transitions with onset temperatures 800°C and 820°C. From microstructural examination of the long-term phase formation in the tapes the higher temperature endotherm was associated with a partial melt. In this study it is demonstrated how control of the heating rate can promote the partial melt (characterised by DTA) and thereby improve the transport current, Ic, in the fully processed tape. XRD, SEM and transport measurements in field show microstructure features typical of an increased volume of liquid phase: a reduction in secondary phase volume and pores with corresponding increase in c-plane texture.

Two prototype binary HTS current leads for superconducting magnets rated for current 7.5 kA are designed and constructed. The HTS part consists of Ag/Bi-2223 tapes. The construction of the current lead is reviewed. Several design considerations are validated with experimental measurements in specially designed and constructed apparatus.

A low heat leak cryogenic station is designed, constructed and set-up in order to accommodate thermo-electric tests of resistive conduction cooled current leads for superconducting particle accelerator magnets rated for currents 60 A and 120 A. Furthermore, the cryogenic station is tested and its suitability for the tests is verified.

A cryogenic station is designed, built and set-up in order to measure the quench propagation in HTS composite current leads. The conditions of quench propagation in composite HTS elements for current leads are successfully reproduced in adiabatic conditions. The transient response of the HTS element (Ag/Bi-2223 tape-stainless steel shunt) subjected to quench is recorded in terms of temperature and voltage time characteristics and analysed.

Table of Contents

Chapter 1

Introduction

1.1. Introduction and justification

Almost a century has passed since the discovery of low temperature superconductivity (LTS) at 4.2 K in 1911 by H. Kamerlingh Onnes [1] in his laboratory in Holland. Since then, continuous research into the field of superconductivity has lead into the discovery of many superconducting materials (pure elements and compounds) and in depth investigation of their properties. Superconductivity is a state of matter where the material has zero electrical resistance and the magnetic flux is expelled from the interior of the superconducting sample when it is placed in an external magnetic field.

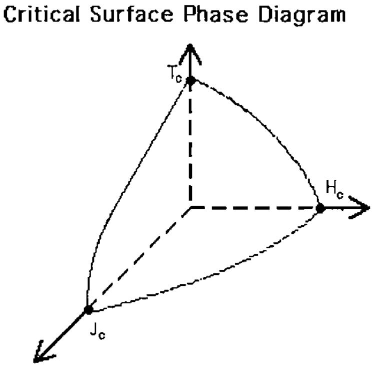

Figure 1.1. *The critical surface phase diagram of type I superconductor*

One characteristic feature of superconductivity is the critical temperature Tc. It is defined as the temperature at which the electrical resistance of the superconducting specimen drops to zero and the magnetic flux lines start to expel from the interior as the specimen is being cooled in an external magnetic field (field cooled). Each type of superconductor has different value of critical temperature, but no one has higher than 138 K at the present time [2], [3], while the extremely low Tc of 0.0154 K has been found in tungsten. Superconductivity breaks down reversibly if a sufficient high external magnetic field (higher than the unique critical field Hc in type I superconductors or the upper field Hc_2 in type II) is applied or if a high enough electrical current (higher than the critical current Ic) passes through the material. The dependence of these three critical quantities to each other constructs the critical surface diagram as shown above, that separates the normal from the superconducting region in the H-T-J geometrical space.

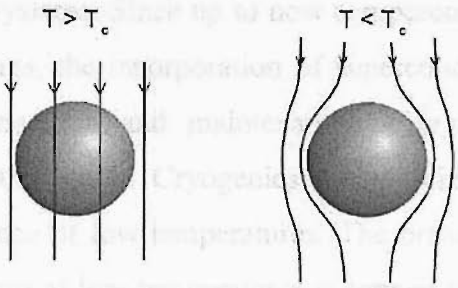

Figure 1.2. *A schematic of the expulsion of the magnetic flux lines below Tc in an applied magnetic field (field cooled specimen)*

The field of Applied Superconductivity is expanding

Since the discovery of the phenomenon, there has been extensive research activity associated with all aspects of superconductivity. The various physical and superconducting properties and the material science of superconducting materials have been and still continue to be the subject of extensive experimental and theoretical investigations. Still today, there are many unanswered questions, thus making impossible to predict the future evolution of the physics and chemistry of superconductors. Very soon it was realised that superconductivity could be used in applications in order to take advantage of some of its unique properties. In large scale applications in the field of electrical power engineering, the potential of use of superconductors can be found mainly in the following sectors: In Electrical Grids; for the generation, transmission and storage of power, fault current limitation and improving power supply quality i.e. in generators, cables, transformers, fault current limiters. In motors; dc and ac electric motors - propulsion systems. In Bearings; for friction-less motion, i.e. fly-wheels, magnetic levitation. ***Magnet Systems***, current leads, open system MRI (magnetic resonance imaging), magnetic separators, particle beam focusing magnets, very high field research magnets.

At the present time, we have reached the stage at which superconductivity is entering more and more real life applications. Just before employing superconductor as a major element and establishing its use as a novel engineering strategy in applications, more investigations are required; most often, superconductors currently are met in demonstrating devices. Numerous projects worldwide test the potential, applicability, compatibility and performance of superconducting materials as components of electrical and electronic systems. Since up to now a superconductor can exist only at extremely low temperatures, the incorporation of superconductive technologies into devices requires the generation and maintenance of cryogenic environments to support the superconducting parts. Cryogenics is the science associated with the production and maintenance of low temperatures. The branch of engineering that is associated with applications at low temperatures is termed as cryogenic engineering. For obvious reasons, the field of Applied Superconductivity is closely related to the field of cryogenic engineering; a relation, that necessitates the simultaneous study of these two areas of applied engineering for the continuous research and development of useful and novel technological applications, at least until one of the most ambitious assumptions will be ever realised: the occurrence of superconductivity at room temperature that sounds impossible at the present time.

Two main areas of potentially increasing interest of application of superconductor will be subject of investigation in this work:

A. Aspects on HTS wire manufacturing technology for low loss transport of electrical energy

The most obvious benefit that arises from the application of superconductivity is the transport of electrical current with negligible resistive losses. The property of zero electrical resistance of a superconductor below its critical temperature can be used in superconducting wires in order to eliminate the Joule heat dissipation $Q = I^2 \times R$ that causes considerably large energy losses in electrical systems. In the setting up of a superconducting system for transport of electrical energy, a necessary accompanying supportive framework is the cryogenic system that will provide the necessary low temperature for the maintenance of the superconducting property. Liquefied gases with boiling points at sufficient low temperatures can be used for that purpose. They are termed as liquid cryogens and among them are liquid helium (4.2 K), liquid argon (87.1 K), liquid oxygen (90 K), liquid hydrogen (20 K) and liquid nitrogen (77 K).

Moreover, the current progress in the field of cryogenic engineering made possible the cryogen-free cooling technology with the use of mechanical refrigerators capable of reaching temperatures as low as 4.2 K. One way or another, the production and maintenance of cryogenic temperatures is not generally cheap and therefore one should choose superconductors with Tcs above the temperature of 77 K (the boiling point of nitrogen at atmospheric pressure) for production of superconducting wires. Liquid nitrogen is cheap to produce and maintain and therefore is suitable for cryogenically supporting large scale applications of superconductivity. High temperature superconductivity (HTS) is a term associated with superconductors that have high critical temperatures; in many of the HTS materials it exceeds the value of 77 K. The nature of mechanism of superconductivity in these materials is different than the low temperature superconductors (LTS). The very first high temperature superconductor was discovered in 1986 [4] and now, after years of investigations, is about to initiate a technological “revolution”. LTS material has been used up to now in all the largest machines worldwide; superconducting magnet technology widely employs NbTi superconductor that guarantees superior mechanical and electrical properties but needs expensive liquid helium cooling at 4.2 K and even superfluid helium at 1.9 K to enhance its superconducting properties. HTS material could play important role in magnet technology in the future, but not until its superconducting and mechanical properties are improved, because the current status does not completely satisfy the requirements. Nevertheless, HTS material could be used in cables and wires. One of the most important parameters that characterizes a superconducting wire and judges to a high degree its suitability for applications is its critical current density Jc ($A\cdot cm^{-2}$). In the terminology of applied superconductivity, it represents a measure standard of the ability of the wire to carry high electrical current density without loosing its superconducting properties. The critical current density, J_c, is the critical current of a superconductor divided by the cross sectional area of the superconductor. As a quantity, it is useful when characterizing the quality of a superconducting material. The critical current density, J_c should not be confused with the engineering critical current density, J_e. The engineering critical current density, J_e, is the critical current of the wire divided by the cross sectional area of the entire wire, including both superconductor and normal metal materials. For applications it is favourable to have high values of Jc in order to use conductors of smaller cross sections and hence reducing the cost of the system. Moreover, the design and fabrication of superconducting wires must take into account the electromagnetic properties of the superconducting material (Tc, Hc_2, Jc), the fabrication technique used and the stabilisation criterion required. Superconducting wires experience stresses due to thermal cycling, coil winding and electromagnetic forces [11] during operation. Therefore, the design of such conductors must also take into account the mechanical characteristics of the superconducting core. The obvious advantages when using HTS instead of conventional copper conductors and LTS are associated with the property of zero electrical resistance in combination with the cheap cooling requirements (liquid nitrogen) and are underlined below:

- Energy savings; the energy losses of HTS devices are significantly lower thus leading to higher efficiencies and lower operating costs.

- Size; HTS devices are much smaller and lighter than the copper solutions at the same power rating.

- Electrical current capacity; HTS materials have current capacities many times that of copper.

- Environmental; in addition to lower energy losses helping the environment there are other benefits such as the elimination of oil in transformers and stray magnetic fields in cables.

The most general requirements of HTS wire in applications can be found among the following:

- Long lengths, with homogenous electrical transport properties
- High transport properties: high and uniform critical current density
- Uniform dimensional characteristics (width, thickness and straightness)
- Room temperature mechanical strength to withstand the manufacturing and installation operations

- Low temperature mechanical strength to withstand the cooling-down and cable life operations

- Stability under thermal cycles

- Low a.c. losses

- Relatively cheap HTS material, manageable, and economical procedure of processing to obtain the format of wire.

Benefits

In the United States, Europe and Japan, the race is on to commercialise this next-generation wire that can carry over one hundred times more current than conventional copper and aluminium conductors of the same dimension. The superior power density of HTS wire will enable a new generation of power industry technologies. It offers major size, weight and efficiency benefits. HTS technologies will drive down costs and increase the capacity and reliability of electric power systems in a variety of ways:

- High capacity wire capable of transmitting two to five times more power. This new wire will offer a powerful tool to improve the performance of power grids while reducing their environmental footprint.

- Compact, efficient and powerful motors with output ratings of 1000 hp and above. The use of HTS technology enables the design of high-efficiency motors that are dramatically smaller and lighter than the conventional motors they replace.

- Inherently safe, environmentally friendly and "smart" transformers. Superconductivity enables these devices to automatically limit the spread of dangerous fault currents, offering important system reliability and performance benefits.

Power generators

HTS technology also enables other applications such as compact and efficient generators that provide fast, reactive power support. These HTS 100MW generators can help keep the grid running smoothly in the face of new patterns of power flows brought on by deregulation of power generation throughout the world. (Stand-alone fault current limiters represent a new class of devices that will protect power grids from troublesome current surges that can cause costly outages and damage utility system components).

Power storage

Utility and industrial customer demand for grid stabilization and power quality technology are being addressed through compact power storage systems. These compact power storage systems incorporate conventional low-temperature and revolutionary HTS materials, to smooth voltage disturbances on power grids and in industrial plants.

Long term research effort is targeting now to develop HTS conductors to meet the above requirements and benefit from the various advantages that the new HTS technology has to offer in the manipulation of electrical energy.

The case of high temperature superconducting composite Ag/Bi2223 tapes

The superconductor $(Bi,Pb)_2Sr_2Ca_2Cu_3O_{10+\delta}$ (BiPb-2223) belongs to the oxide HTS family and has critical temperature about 110 K. Composite superconductors can be made by embedding strands of superconducting material, i.e. precursor ceramic powder of the (Bi,Pb)2223 phase in a normal metal matrix [5]-[10]. The choice of silver as the matrix material is driven by the requirements of a metal that is not easily oxidised, is chemically non-active with the ceramic oxide and has oxygen permeability. After thermo-mechanical processing a silver sheathed/ceramic composite is obtained with a solid compact superconducting core that is able to carry high current densities in liquid nitrogen (OPIT-oxide powder in tube- technique). The metal sheath serves as mechanical reinforcement to the brittle ceramic core and also provides thermal stability against accidental transitions into the normal state (quenching) during operation.

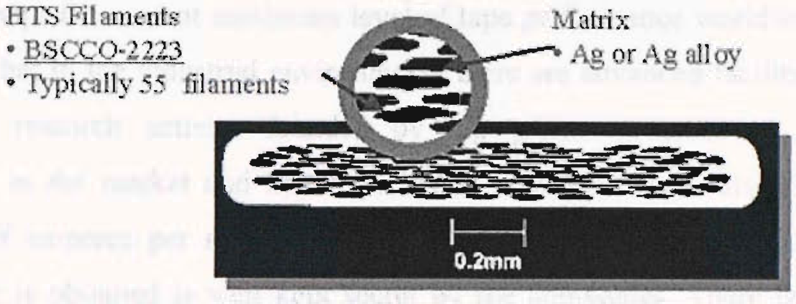

Figure 1.3. *Cross section of a typical multifilamentary Ag/Bi-2223 tape*

By the OPIT technique, companies like American Superconductor Corporation (AMSC), Sumitomo Electric Industries and Norbic Superconductor Technologies (NST) manufacture kilometres of tape capable of carrying current densities above 20 kA·cm^{-2} at LN$_2$ temperature without any resistive losses. Yet, no perfection in the performance of the Ag/Bi-2223 tape has been achieved but a high level of maturity has been reached in the industrial production - a high level of knowledge in the research laboratories. An indicative resume of the progress in the tape manufacturing worldwide can be seen in the industrial performance of the American Superconductor Corporation wires. The AMSC is considered as the world's leader manufacturer and supplier of Ag/Bi-2223 tape. At the present, the record values of some characterization parameters in the production of Ag/Bi2223 tape at AMSC can be seen in the table below [12].

Record AMSC Bi-2223 wire performance at 77 K

	Production wire	Experimental wire
Ic (A, self field)	155	175
Ic (A, 0.1 T, //c)	68.3	74.3
Je (A/cm^2, self field)	18,000	20,200
Jc (A/cm^2, self field)	46,200	51,800
Jc (A/cm^2, 0.1 T)	20,300	22,100

There are numerous artefacts that arise during the tape processing that limit the critical current which are not always easy to get rid of. The level of understanding of these limitation factors has been raised satisfactorily after years of research; yet there is substantial room for improvements in the future. The results in the above table indicate perhaps the current maximum level of tape performance worldwide. We can understand that in the industrial environments there are advanced facilities and large coordinated research activity founded by big grants in order to demonstrate competence in the market and hence the value of Jc has been raised to tenths of thousands of amperes per square centimetre. How this impressive superconductor performance is obtained is well kept secret by the companies. There is the general agreement that the target is to reduce the amount of non-superconducting phases in the HTS core that produce complications in the flow of the supercurrent and to use very accurate temperature control during the heat treatments at the manufacturing stages. The critical temperature and the upper critical field are characteristics of the superconducting material which are determined by its chemical composition (phase) and crystal structure. Hence, the wire fabrication technique has no significant influence on Tc and Hc_2, but the current carrying capability of HTS materials is determined by the microstructure of the composite and can be greatly influenced by the fabrication method. In American Superconductor Corporation it is believed that higher levels of performance are expected with elimination of the residual Bi-2212 in the tape superconducting core [12]. Whether this is the main obstacle or one of the other numerous barriers, many of them being unsolved microstructural inhomogeneities and other unknown defects in the current OPIT tape, still there is plenty of capacity for investigations and hence improvements. The difficult nature of the material science of the tapes can be partially assigned to the complexity of the Bi-2223 phase field. Perhaps, as a result, there is a lack of any well-defined peritectic and no consensus exists on how to process the tape; instead, Ag/Bi-2223 tape production has become proprietary. As a result, the tape microstructure is full of secondary phases – bulbous Ca-Sr-Cu-O phases and Bi-2212 intergrowths – which not only reduce the phase volume of the Bi-2223 formed but also create obstacles for Bi-2223 texture and transport current path. New reaction paths for the Bi-2223 phase formation should be found that result in superior superconductor microstructure and hence improved transport properties. One of the purposes of the thesis is to identify possible reaction paths of Bi-2223 that will enhance the structure of the Bi-2223 core and raise the value of critical current density.

B. Use of superconductors in large scale particle accelerator magnets

Superconducting magnets provide high magnetic fields with low consumption of electric power at high electrical current densities, thus a given magnetic field can be achieved with a certain number of ampere/turns in a small volume of magnet winding. In the large particle accelerators like CERN or FERMI-LAB, very high magnetic fields are required to accelerate, focus, manipulate and analyse the beams of charged particles in order to investigate the fundamental properties of matter. The use of superconducting magnets saves large amounts of energy when producing the required high magnetic fields.

The case of HTS binary current leads

The correct design of the supportive cryogenic system to the accelerator magnets must take into account the various sources of heat leaks into the cryogenic environment. These losses reduce the efficiency of the refrigeration system, whether it is liquid cryogen or mechanical refrigeration. In the case of liquid helium-superfluid helium cryogenic system they cause significant evaporation and loss of expensive cryogen that needs to be recycled and re-liquefied. Radiation and conduction losses are common sources of helium loss but a main heat load comes from the power supply. The current leads connect the warm cables from the power supplies at room temperature to the superconducting magnets. Thousands of amperes of electrical current are required for production of high magnetic fields. Large amounts of heat are conducted through the conductor current leads to the magnet support cryogenic environment by physical heat conduction in addition to the resistive heat, in the case of conventional current lead conductors. The total amount of heat (conduction and resistive) is introduced into the NbTi or Nb_3Sn and Nb_3Al magnets and large amounts of expensive liquid helium coolant could be lost due to evaporation. Therefore the system would be impractical to run under these conditions. The design of the current leads has to be such as to minimize the total thermal loss (Joule heat generation and heat conduction). This procedure is termed as optimisation of the current leads and is crucial for the economical operation of the system. In the optimisation of the current lead, key role plays the use of superconducting material HTS and LTS that actually acts as “thermal break” and can reduce the heat leaks by a factor of greater than 10.

Also the total cooling power can be reduced by 30% in comparison to the conventional current leads [13].

The incorporation of superconducting materials in these technological areas assists the efficient energy management and macroscopically the effects are undoubtedly beneficial. This thesis deals with aspects related to the application of HTS material in current leads used in superconducting particle accelerator magnets.

The content of the thesis

In order to add new information in the already rich but not saturated knowledge in the field of HTS wire/tape manufacturing technology, silver sheathed composite Ag/(Pb,Bi)2223 tapes were fabricated through the OPIT technique, and investigations were carried out in order to improve their transport properties. In order to study the application of HTS material in current leads, various aspects in cryogenic engineering, superconductivity and heat transfer have also been studied. Principles of cryogenic design have been applied in order to build two cryogenic stations for various types of measurements at cryogenic temperatures. In these cryostats, the ability to use cryogen-free cooling technologies with the use of Gifford McMahon (GM) mechanical cryo-refrigeration was demonstrated. The cooling in these cryostats has been achieved by a two-stage G-M cryocooler that has been capable of reaching the temperature of liquid helium (4.2 K) with a non-negligible cooling power capability. Cryogenic engineering techniques have been also applied in order to design and built prototype binary HTS current leads (of electrical current rating 7.5 kA) for the Inner Triplet superconducting accelerator magnets at CERN, the European Organization for Nuclear Research, which is a representative example where advanced large scale superconductor technologies and cryogenics are applied. The work for the thesis can be divided into the following sections:

1. Studies on composite Ag/Bi-2223 superconducting tapes

2. Design and manufacturing of HTS current leads for superconducting particle accelerator magnets

3. Design, construction and set-up of a cryogenic station for studying quench propagation in composite superconducting current leads

4. Design, construction and set-up of a cryogenic test facility for assessing the thermoelectric performance of resistive conduction cooled current leads for superconducting particle accelerator magnets

1.2. Historical review of Superconductivity

The historical review in a branch of science provides the ability to understand deeper the associated phenomena. In the field of applied superconductivity, it is not out of purpose to refer to the history of superconductivity, since any reference to the past minimizes the possibility of misunderstanding of the reality. Below, the discoveries of superconductivity over the past century are briefly introduced.

At the beginning of the 20th century, Heike Kamerlingh Onnes did the first important step at 10th of July 1908. For the first time the helium gas has been liquefied, and therefore the study of the material properties at very low temperatures has become possible. The boiling points of the two helium isotopes ^{4}He and ^{3}He are 4.21 K and 3.19 K respectively. The second significant step comes only three years later. In 1911, Onnes was measuring the electrical resistance of the element mercury and found that in a very small region 4.2 K to 4.19 K, the resistance drops suddenly to zero; superconductivity has just been discovered [1]. Onnes continued measurements in gold, but no such phenomenon was observed. Superconductivity is a property of only certain materials at low temperatures and not of all the pure metals. Today we know that only 26 out of 90 elements that exist in nature are superconductors at very low temperatures. Gold, silver and copper are not superconductors. Niobium has among the elements the highest critical temperature Tc=9.5 K. Tin has Tc=0.9 K, aluminium has Tc=1.1 K, Sn has Tc=37.7 K and lead Tc=7.2 K; they are all low temperature superconductors. Seventy six years after the discovery of superconductivity, at October the 14th 1987, another Nobel Prize sets the beginning of the high temperature superconductivity. The Prize goes to Bednorz and Muler, who presented in 1986 their work *"Possible high Tc superconductivity in the system Ba-La-Cu-O"*. Until that moment, the record was at 23 K (Nb_3Ge) since 1973. The efforts for the discovery of high Tc superconductors has been a race that still continues until today. The interest is huge mainly because the high Tc superconductivity is promising for practical applications. Bednorz and Muller have broken the unbreakable record for 13 years of Nb_3Ge by only 7 K. But the discovery that the Ba-La-Cu oxide was a superconductor was a huge success. The metal oxides are usually insulators and until the discovery of Bednorz and Muller they were not even candidates for superconductivity. Their work oriented the interest of the research towards metal oxides with the copper as a base. Only in an interval of one year, in 1987, the groups of Chu and Wu have broken all the records and reached the unbelievable value of Tc=93 K. Chu and Wu discovered that a compound of Y-Ba-Cu-O was superconducting below 93 K. A new technological area was born, since the superconductors could exist above the boiling point of N_2 (77 K). The efforts for the discovery of new superconductors of even higher critical temperatures still continues, hundreds of publications and conferences have subject the HTS and their properties. But the history is not only written through the experimental effort. Theoretical research for the understanding of the phenomenon is intense and has already passed through determined steps, but the subject still remains open without being possible to predict the future surprises. Onnes had believed initially in the prospect of generation of high magnetic fields using super-currents of high intensity. But soon he realised that this was not achievable, since the electrical resistance was returning to its normal value when high currents pass through the material.

Until 1933, when Meissner and Ochsenfeld [14] made the first experimental investigation of the magnetic properties of superconductors, there was the impression that the characteristic properties of the superconducting state are simple consequences of the infinite conductivity. Therefore the experiments of Meissner and Ochsenfeld were an important stage for the future shaping of the theories of superconductivity. For the first time it was made clear that the absence of magnetic flux (Meissner effect) is a fundamental feature of the superconductors which is not induced to other properties. Immediately after the discovery of the phenomenon P. Langevin made the first allusion that the phenomenon could be treated as a phase transition. Landau has valorised this several years later. In fact, the first thermodynamic study of the transition to the superconducting state was made in 1934 by Gorter and Casimir. In this study a serious theoretical process of the two fluid model was presented. From one side the usual fluid of the conduction electrons with density n_n (normal) and current density J_n and from the other side the superfluid that its carriers (later named as Cooper pairs) have the property to pass through the positive ion lattice without being decelerated. The superfluid density is symbolized n_s (superfluid) and the supercurrent density J_s. The coexistence of the normal and *"super"* electrons has become the base of a fertile phenomenology. In 1935 the London brothers constructed an electrodynamic theory in which the total current has two components: $J_{total}=J_n+J_s$. The normal electrons obey the Ohm's law ($Jn\sim E$), the super-electrons obey the London equations. The theory of the London brothers was the first satisfactory explanation of the phenomenon; the Meissner effect was dealed and explained as a fundamental phenomenon which is not originated from the property of the infinite conductivity. Until that moment, a twenty-year interval of intense but unfruitful efforts of microscopic-based explanation was intervened. Therefore, the success of the London brothers was huge in spite of the fact that their theory was pure phenomenological. The quantum based interpretation of this theory as it was initially proposed by Fritz London was a daring idea that is equivalent to the use of the ideas of the quantum mechanics of the microcosm into the dealing of the problems of the macrocosm. According to F. London, superconductivity is interpreted as a macroscopic quantum effect, but without this to be originated from a composition of the quantum microscopic mechanisms. This will originate from the BCS theory that comes later. There is a difference between phenomenological and microscopic theories. The basic advantage of a phenomenological theory is its simplicity which gives the ability of a short description of the phenomenon but also the fact that many times is the only possible choice. It is also true that many times the microscopic models are based on some assumptions (of a phenomenological nature), without being possible to check their accuracy. In the Heisenberg model of ferromagnetism, the extraction of the Hamiltonian through the quantum mechanics of the interaction of the N particles is in reality not possible. At this point it can be claimed that the macroscopic description does not require accuracy at the microscopic level. This is one of the big mysteries of the statistical physics. The phenomenological theory of Ginzburg and Landau (1950) for superconductivity can be valued in the same frames as above. This theory builds up on the initial theory of Landau (1936) about the critical behaviour. Landau got his Nobel Prize for his contribution in the theory of condensed matter and phenomena of superfluidity and superconductivity. The theory of Ginzburg-Landau for the critical behaviour of superconductivity survives until today, giving important conclusions and leading to significant improvements despite of the appearance of a strong microscopic theory, the BCS theory [15]. The microscopic theory of Bardeen, Cooper and Scrieffer, known as BCS theory, is considered to be one of the greatest successes in the many body techniques. This theory appeared in 1957 after a long period of intense theoretical research towards the understanding of the responsible for the superconductivity interaction at microscopic level. The studies of Frohlich (1950-1954) play a determined role at the end of this period and the constant reference point of all the efforts is the Bloch theory (1928) for the conduction of metals. In 1959, Gorkov have managed to extract the Ginzburg-Landau equations from the microscopic BCS theory. Therefore until 1986, the phenomenon of superconductivity appears to have a satisfactory explanation. The superelectrons have the tension to form pairs (Cooper pairs) with the intermediation of an attraction to the lattice of the positive ions. This coupling allows the pairs to coordinate and finally to produce a macroscopic quantum effect. These mechanisms are the base of the foundation of the microscopic BCS theory and the success of Gorkov has allowed the connection of the microscopic theory to the phenomenological theories of Landau and London. The experimental data of the new high Tc superconductors bring this satisfactory idea. The high Tc superconductors show low concentrations of carriers and Fermi velocities and at the same time they show high critical temperatures. The pairing mechanism of the BCS theory cannot explain the high critical temperatures, so therefore other alternative pairing mechanisms have already been proposed and being investigated today. There is not a clear answer about the high Tc superconductors, but the full analysis of the BCS theory under the conditions of high Tc superconductivity appears to be impossible. This problem is one of the greatest in Physics and remains open today. Behind any theoretical explanation, there is the fact that it became possible to obtain superconductivity above the boiling point of liquid nitrogen. This implies that someone can take advantage of the properties of superconductivity and use them in engineering applications in an economical manner, as it will be the subject of this thesis.

1.3. Fundamental properties of the superconducting state

The superconducting state of matter is characterized by several unique properties. Below, the phenomenon of superconductivity is defined by introducing its most fundamental properties briefly.

1.3.1. Zero electrical resistance

The electrical resistivity of superconductors drops to zero at temperatures below the critical temperature Tc, which has a characteristic value for each superconducting material. The value of resistivity does not just approach zero, but it has precisely the value of zero. The persistent current in a superconducting ring was observed to flow without any detectable reduction for a period of one year. The prediction for this resistanceless flow is a period of 10^5 years characteristic decay time that was found using nuclear magnetic resonance to measure any decrease in the produced magnetic field by the circulating current.

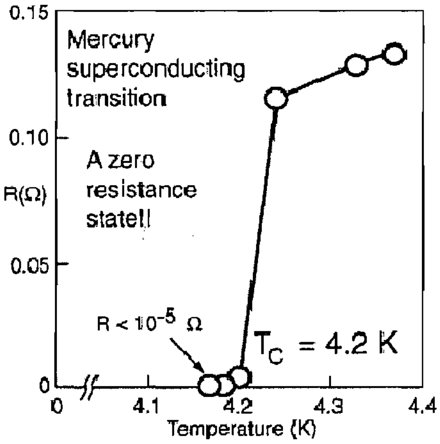

Figure 1.4. *The drop to zero of the electrical resistance of the superconducting mercury at 4.2 K*

1.3.2. Perfect diamagnetism

The infinite conductivity is the most obvious property of superconductivity. Perhaps, the most substantive property is the destruction of the phenomenon by the application of a “strong” magnetic field. When a sample is at the normal state in a homogenous magnetic field and is cooled to the superconducting state, the magnetic flux is expelled from the interior of the sample (Meissner effect)

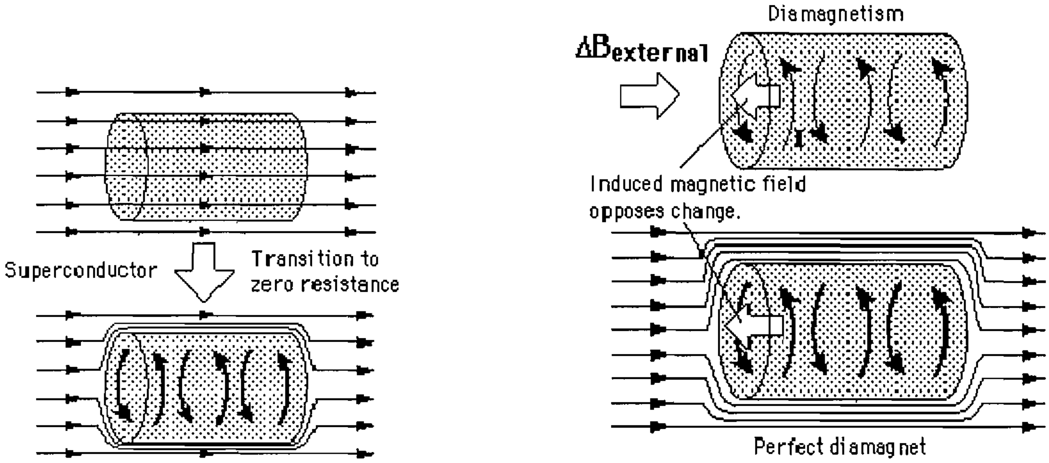

Figure 1.5. *The Meissner effect*

1.3.3. The critical field

The Meissner effect appears only in weak magnetic fields. If the sample is in the superconducting state at temperature $T<Tc$, then there is a unique magnetic field Hc(T) that at fields higher than this the sample passes to the normal state. This phase transition is reversible. In the type II superconductors two characteristic critical fields exist, H_{c1} and H_{c2}. For $H>H_{c2}$ the sample is in the normal state and for $H<H_{c1}$ is superconducting. In the region $H_{c1}<Hc<H_{c2}$ the sample is in the mixed state.

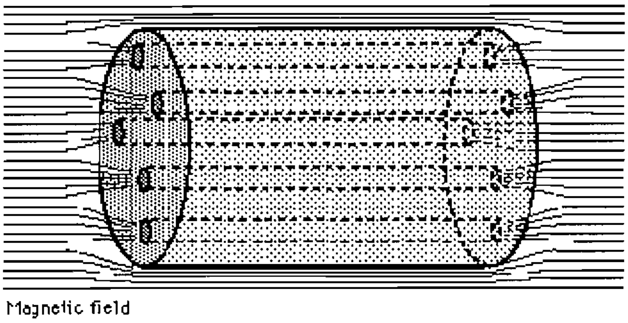

Figure 1.6. *Meissner effect in the mixed state*

Here the phenomenon occurs into regions inside the sample; the flux lines pass through the material but some regions remain superconducting. For type I superconductors, the experiments show that the relationship Hc(T)-T can be described by the empirical relation below:

$$H_C(T) = H_C(0) \cdot \left[1 - \left(\frac{T}{T_C} \right)^2 \right]$$

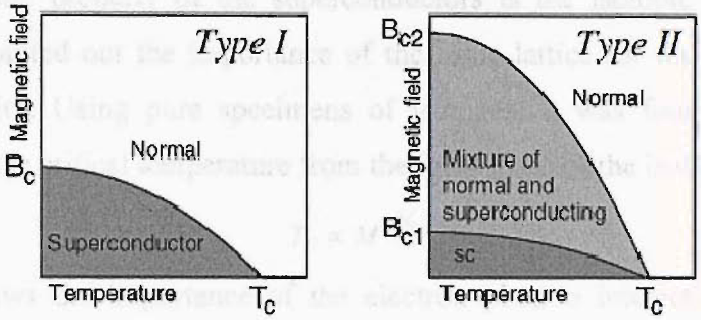

Figure 1.7. *The H-T diagram for type I and II superconductor*

1.3.4. Quantisation of magnetic flux

If a metal ring is placed inside a magnetic field perpendicular to the ring plane and then transformed by cooling to the superconducting state and the field is removed, then the magnetic flux of the ring cannot pass through the superconducting material and is trapped. The trapped flux is kept by the existence of circular supercurrents of practical infinite duration. The trapped flux is quantitized in units of the quantity fluxoid, φ_0 :

$$\varphi_0 = \frac{hc}{2e} = 2.07 \cdot 10^{-7}\, gauss \cdot cm^2$$

1.3.5. The specific heat and the gap

The transition from the normal to the superconducting state in zero applied field is a second order phase transition and the phenomenon near the Tc is a critical phenomenon. The specific heat will show discontinuity without the phenomenon being accompanied by latent heat. The specific heat of the electrons depends linearly to the temperature when the sample is in the normal state. The passing to the superconducting state will be accompanied by a rapid discontinuity at Tc while for low temperatures the specific heat decreases to zero exponentially. This dependence is characteristic of an energy gap between a ground and elementary excitation of the system. The gap is

$$\Delta_0 \propto 2 \cdot k \cdot T_C$$

1.3.6. The isotopic effect

The characteristic property of the superconductors is the isotopic effect. Detailed studies have pointed out the importance of the ionic lattice for the phenomenon of superconductivity. Using pure specimens of isotopes, it was found the following dependence of the critical temperature from the ionic mass of the isotope:

$$T_C \propto M^{-1/2}$$

This result shows the importance of the electron phonon interaction as a pairing mechanism between the electrons for the formation of the Cooper pairs.

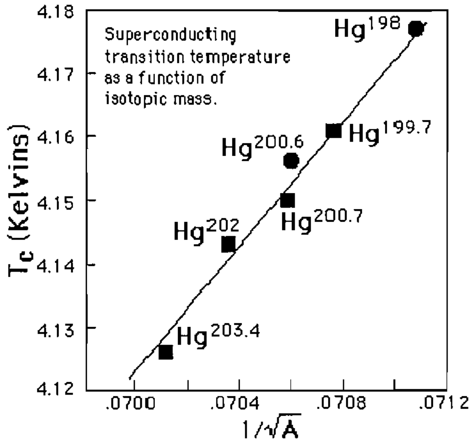

Figure 1.8. *The dependence of the Tc of mercury on the mass atomic number of its isotopes*

1.3.7. London Equations [15]

In 1935 the London brothers have derived equations that relate the electric and magnetic fields E and B inside a superconductor to the current density

$$\vec{E} = \mu_0 \lambda_L^2 \frac{d}{dt} \vec{J}$$

$$\vec{B} = -\mu_0 \lambda_L^2 \cdot \vec{\nabla} \times \vec{J}$$

The constant of proportionality in these expressions is the London penetration depth λ_L,

$$\lambda_L = \left(m / \mu_0 n_S e^2 \right)^{1/2}$$

where n_S is the density of superconducting electrons.

1.3.8. Ginzburg-Landau Theory [16]

The phenomenological Ginzburg-Landau theory provides a good description of many of the properties of both classical and high-temperature superconductors. This theory assumes that in the superconducting state the current is carried by super electrons of mass m^*, charge e^* and density n^* where these quantities are equal to $2m$, $2e$, $n_S^* = \frac{1}{2} n_S$ in terms of the free electron values m, e, n_S respectively. The order parameter $\phi(\vec{r})$ is complex,

$$\phi(\vec{r}) = |\phi(\vec{r})| \cdot e^{i\Theta}$$

and its square $|\phi|^2$ is identified with the super electron density

$$n_S^* = |\phi|^2$$

The parameter ϕ is zero above T_C and increases continuously as the temperature is decreased below T_C as shown in the top part of figure 1.11. The bottom part of figure 1.11 shows the dependence $\phi(x)$ on the distance x inside the surface of a superconductor. Below, but close to, T_C, the Gibbs free energy per unit volume G_S is expanded in terms of the order parameter and then minimized with respect to ϕ to provide the first GL equation in the London-Landau gauge $(\vec{\nabla} \cdot \vec{A} = 0)$:

$$\left(1/2m^* \right) \left[\hbar^2 \cdot \nabla^2 \phi - 2i\hbar e^* \vec{A} \cdot \vec{\nabla} \phi - e^{*2} \cdot A^2 \phi \right] - a\phi - b|\phi|^2 \phi = 0$$

Minimisation of G_S with respect to the vector potential $\vec{A}$ provides the second GL equation:

$$\vec{\nabla} \times \left(\vec{\nabla} \times \vec{A} \right) + \frac{i\hbar e^*}{2m^*} \left(\phi^* \vec{\nabla} \phi - \phi \vec{\nabla} \phi^* \right) + \frac{e^{*2}}{m^*} \vec{A} |\phi|^2 = 0$$

These two coupled equations determine the properties of the superconducting state. It is assumed that below but near T_C the parameter a depends linearly on the temperature,

$$a(T) \approx a_0 \left[(T/T_C) - 1 \right]$$

and b is independent of the temperature, where a_0 and $b = b_0$ are both positive so $a(T)$ is negative below T_C. Deep inside a superconductor in the absence of a magnetic field, we have the following expression near T_C

$$|\phi|^2 = n_S^* = -a/b = \left(a_0/b_0\right)\left[1-\left(T/T_C\right)\right]$$

and the temperature dependence is plotted in figure 1.11 (top). The coherence length ξ, the characteristic length over which ϕ varies in the manner illustrated in fig. 1.11 (bottom), is the first of the two fundamental length scales from the GL theory:

$$\xi^2 = \hbar^2/2m^*|a|$$

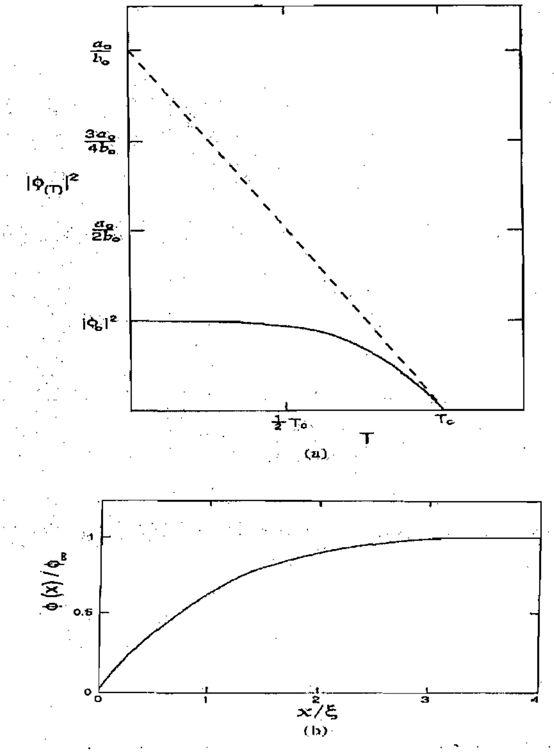

Figure 1.9. *Top: Temperature dependence of the GL order parameter* $|\phi|^2$ *showing its value* $|\phi_0|^2$ *at* $T = 0$, *and the linear behaviour near* T_C *that extrapolates to the value* a_0/b_0, *bottom: Dependence of the GL order parameter* $\phi(x)$ *on the distance* x *inside a superconductor*

The condensation energy of the super electrons, the energy released per unit volume by transforming normal electrons to the superconducting state, is given by

$$E_{cond} = \frac{1}{2}\left(a^2/b\right) = B_C^2/2\mu_0$$

In the presence of an applied magnetic field the line integral of $\bar{J}/|\phi|^2$ around a closed path inside the superconductor and the flux Φ enclosed by this path obey the relation

$$\left(m^*\mu_0/e^{*2}\right)\cdot\oint\left(\bar{J}/|\Phi|^2\right)\cdot dl+\Phi=n\Phi_0$$

where n is an integer and the quantum of flux Φ_0 has the value

$$\Phi_0=h/e^*$$

The above equation is the quantum condition whereby the sum of the enclosed flux Φ and the line integral of the current density J is quantized.

A parallel magnetic field $B(x)$ and a current density $J(x)$ decay exponentially with the distance x inside the surface of a superconductor in accordance with the expressions

$$B(x)=B_0\cdot e^{-x/\lambda}$$

$$J(x)=J_C\cdot e^{-x/\lambda}$$

where the London penetration depth λ_L, the second fundamental length scale, is given by

$$\lambda_L^2=\frac{m^*}{\mu_0 e^{*2}|\phi_\infty|^2}$$

The ratio $k=\lambda/\xi=1/\sqrt{2}$ divides superconductors into the two types

$$k\le 1/\sqrt{2}\ \text{(Type I)}$$

$$k\ge 1/\sqrt{2}\ \text{(Type II)}$$

Type II superconductors have lower, thermodynamic, and upper critical fields given by

$$B_{C1}=\frac{\Phi_0\cdot\ln k}{4\pi\lambda^2},\quad B_C=\frac{\Phi_0}{2\sqrt{2}\pi\xi\lambda},\quad B_{C2}=\frac{\Phi_0}{2\pi\xi^2}$$

respectively, where $B_{C1}\cdot B_{C2}=B_C^2\cdot\ln k$. The Meissner effect is complete for $B_{app}<B_{C1}$ and as B_{app} is increased above the low critical field B_{C1}, flux penetrates the material in the form of vortices. The magnetization continues to increase until the

upper critical field B_{C2} is reached where the vortex cores almost overlap and bulk superconductivity is destroyed.

1.3.9. The Bardeen, Cooper, Schrieffer (BCS) theory [15]

The basic idea of the microscopic BCS model is the existence of a weak attractive interaction between the electrons with the intermediation of the positive ions of the metallic lattice. This idea has been proposed by Cooper in 1956, but historically this mechanism was proposed in 1950 by Frohlich and immediately after it was strengthened by the discovery of the isotopic effect. This phenomenon made clear that the metal ions play a basic role in the formation of the superconducting state. Without the intermediation of the ions of the metal lattice, the coupling of the electrons in pairs (Cooper pairs) would not be possible since the electrons repel each other (Coulomb repulsion), even if this repulsion must be finally considered electrically shielded due to the existence of the rest of the electrons.

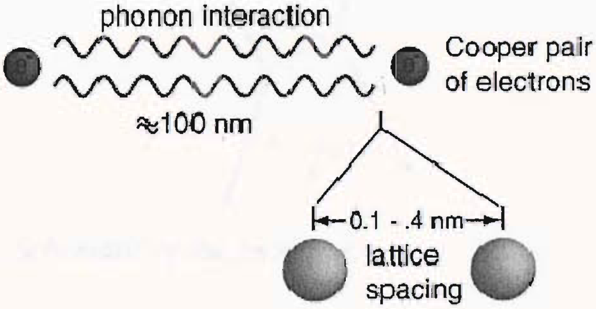

Figure 1.10. *The Cooper pair*

The coupling mechanism is described nicely by the expression *"The two electrons gain by sitting close together in the same depression of the mattress"* or even by *"attraction in a soft bed"*. The electron in its passing affects the lattice (bed) and this affection attracts another near by electron. It is about an indirect attraction with the intermediation of the lattice.

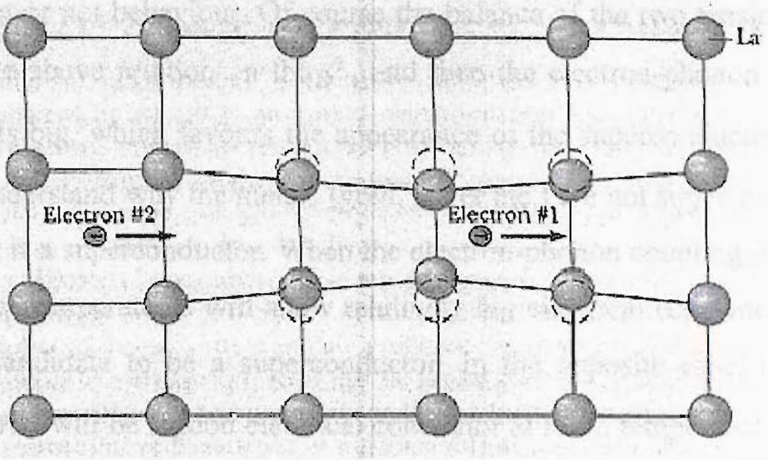

Figure 1.11. *Schematic of the attraction of two electrons by the intermediation of the lattice*

Such an attractive interaction could result if when calculating the energy of a pair we take into account a strong (virtual) intermediate state that the electrons exchange a phonon ($\hbar\omega_{\vec{q}}$) as it is shown in the figure.

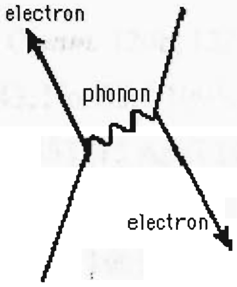

Figure 1.12. *Schematic of the phonon exchange between two electrons*

The mathematical expression of the scattering in the figure is

$$V\left(\vec{k},\vec{k}',\vec{q}\right)=\frac{g^{2}\cdot\hbar\cdot\omega_{\vec{q}}}{\left(E_{\vec{k}+\vec{q}}-E_{\vec{k}}\right)^{2}-\left(\hbar\cdot\omega_{\vec{q}}\right)^{2}}$$

where $\hbar\cdot\vec{k}$, $\hbar\cdot\vec{k}'$ are the momenta of the incoming electrons, $\hbar\cdot\vec{q}$ is the momentum of the phonon that is exchanged and g is a coupling constant between the electrons and phonons. The interaction becomes negative, and therefore attractive for $\left|E_{\vec{k}+\vec{q}}-E_{\vec{k}}\right|<\hbar\cdot\omega_{\vec{q}}$. Of course the final result will be shaped from the relative values of this interaction and the shielded repulsive (positive) Coulomb interaction between the electrons. The correlation of the two anti-parallel tensions is responsible for the fact that there is not a simple rule to decide when the total interaction is attractive or repulsive and consequently the material will show according to the case superconducting or not behaviour. Of course the balance of the two tensions depends according to the above relation on the g^2, and then the electron-phonon coupling is strong when g is big, which favours the appearance of the superconductivity. At this point we can understand why the metals (gold, silver etc.) are not superconductors but instead the lead is a superconductor. When the electron-phonon coupling is strong, the material at room temperatures will show relatively big electrical resistance but at the same time is candidate to be a superconductor. In the opposite case, if g is very small, the material will be a good electrical conductor at room temperature but then it is almost certain that the repulsive Coulomb interaction will overcome, even at the lowest temperatures, the attractive electron-phonon interaction and the material will not be a superconductor no mater how low the temperature goes (e.g. copper).

References

[1] H. Kamerlingh Onnes, ***Leiden Comm.*** 120b, 122b, 124c, 1911

[2] P. Dai et al, ***Physica C,*** Vol. 243, No. 3&4 1995, pp. 201-206.

[3] A. Schilling, et al., ***Nature,*** Vol. 363 (15 April 1993): 56-58.

[4] J. G. Bednorz and K. A. Muller, ***Z. Phys. B*** 64, 189-193 (1986)

[5] Sato K et al, ***IEEE Trans. on magn.*** 1991, vol. 27, no.2, pp. 1231-1238

[6] Minot M.J et al, ***IEEE Trans. Appl. Supercond.,*** 1995, vol. 5, no.2, pp. 1246-1250

[7] Carter W.L. et al, ***IEEE Trans. Appl. Supercond.,*** 1995, vol. 5, no.2, pp. 1145-1149

[8] Martini L. et al, ***Cryogenics*** 1993, vol. 33, no. 1, pp.77-80

[9] Motowildo L.R., ***Applied Superconductivity***, 1993, vol. 1, no. 10-12, pp. 1503-1514

[10] Christopherson C.J. and Rilley G.N, ***Appl. Phys. Letters***, 1995, vol. 66, no.16, pp.2277-2279

[11] Ogiwara H. et al, ***IEEE Trans. on magn.*** 1994, vol. 30, no. 4, pp. 2399-2401

[12] Y. B. Huang et al, ***IEEE Trans. Appl. Supercond.,*** 13 (2): 3038-3041 Part 3 JUN 2003

[13] Amalia Ballarino, CERN, Geneva, Switzerland, Proceedings of EPAC 2000, Vienna, Austria

[14] Meissner and R. Ochsenfeld, ***Naturewissenschaften*** 21 787 (1933)

[15] F. London and H. London, Proc. Roy. Soc. (London) A141, 71 (1935)

[16] V.L Ginzburg and L. Landau, Zh. Eksp. Teor. Fiz. 20, 1964 (1950)

[17] J. Bardeen, L. N. Cooper and J. R. Schriefer, ***Phys. Rev.*** 108, 1175 (1957)

Chapter 2

The Ag/(Bi,Pb)-2223 tapes

2.1. Introduction

Since the discovery of the high-Tc superconductors, a great deal of effort has been focused on conductor processing with the aim of realizing high-field and high temperature superconducting magnets and electric power applications at 77 K (LN_2). Important and crucial requirements for the conductors in order to be used in technological applications are: a) high critical current density $\mathbf{J_C}$, b) workability for fabricating long lengths of wire and c) mechanical and thermal stability achieved by a metal sheath. Ag/(Bi,Pb)2223 tapes are currently the most widely used high temperature superconductor, HTS, in both demonstrator projects and commercial applications [1], [2]. The most commonly applied and successful technique for its fabrication is the **oxide-powder-in-tube, "OPIT",** method [1]. With higher critical current densities the market potential of tapes can be improved, as not only may more HTS applications become feasible, but also the price of the HTS part of applications may be lowered. Although today's Ag/(Bi,Pb)2223 tapes have large transport current densities, there remains plenty of room for improvement. A better understanding of the tape processing will allow industry to quickly become competitive rather than being slowed down by numerous complex processing problems.

The processing of composite Ag/(Pb,Bi)-2223 tapes has been extensively investigated since the year 1989, where the first tapes were made by the oxide-powder-in-tube (OPIT) technique. The formation of the Bi-2223 phase is via a Pb-induced liquid phase which is known to assist the Bi-2223 formation. However there are many unsolved microstructural inhomogeneities and defects in current OPIT tape; consequently research has begun to focus on the role of the liquid phase. In this study, Ag/(Pb,Bi)-2223 composite tapes are fabricated through the OPIT technique by a two heat treatment process in atmosphere 7.5% partial pressure O_2 with one intermediate rolling. A reaction path for the Bi-2223 formation from the precursors is found that is thought to enhance the liquid assisted formation mechanism of the superconducting core. The heating rate in the 1st heat treatment is used as a tool in order to promote this reaction path. The temperature range 700 °C to 832 °C (832 °C is the heat treatment temperature) of the first heat treatment is divided into two ranges, 700 °C to 800 °C and 800 °C to 832 °C. Differential thermal analysis on tape is used in order to capture and characterise liquid phase formation events. In the temperature range 800 °C to 832 °C of the first heat treatment, the DTA analysis showed two endotherms with onset temperatures 800 °C and 820 °C: both endotherms are seem to be transient reaction routes leading to the formation of Bi-2223. It is thought that a rapid heating rate effectively bypasses the 800 °C transient and promotes the 820 °C reaction route. The nature of the endotherms and the possible reasons for the measured increases in transport current are discussed in the light of SEM and XRD analysis to draw a link between the transient events characterised by DTA and tape transport properties.

2.2. The BSCCO Superconductor

Since the discovery of the first High-Tc superconductor (HTS) by Muller and Bednorz [3] in the La-Sr-Cu-O system, a few new families of HTS have been synthesised with Tc>30 K. The most interesting HTS are the cuprate oxides, the superconducting properties of which depend strongly on the cationic substitutions in the lattice cell and the oxygen content of the oxide. Among the family of cuprate oxides, the most well known is the $YBa_2Cu_3O_7$ [4] as being the very first high temperature superconductor to be discovered with critical temperature above the boiling point of nitrogen, 77 K (Tc ~ 92 K). The high temperature superconductors are type II superconductors. The common feature in the structure of the high Tc superconducting oxides is the perovskite structure. The perovskite structure includes one or more planes of copper atoms with four strongly bonded oxygen atom neighbours at a distance approximately 1.9 Angstroms which are known as the CuO_2 planes. The CuO_2 layers are important because superconductivity takes place in them, i.e. the supercurrent flows among them. The family of the cuprates can be represented by the formula $A'_xX_yA_{n-1}Cu_nO_{2n}$ where A'_xX_y is the interlayer group, which is Bi_2O_2 in the case of BSCCO, n is the number of the CuO_2 layers in the unit cell. A_{n-1} cations exist between CuO_2 layers that are adjacent to each other, most often are Ca or rare earths.

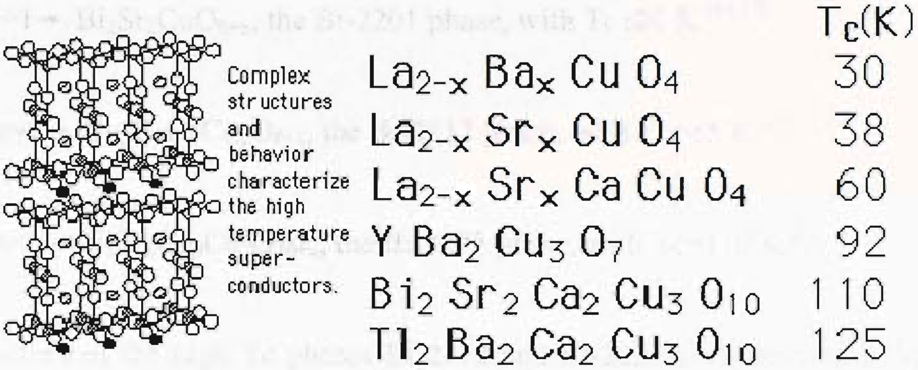

	T_c(K)
$La_{2-x}Ba_xCuO_4$	30
$La_{2-x}Sr_xCuO_4$	38
$La_{2-x}Sr_xCaCuO_4$	60
$YBa_2Cu_3O_7$	92
$Bi_2Sr_2Ca_2Cu_3O_{10}$	110
$Tl_2Ba_2Ca_2Cu_3O_{10}$	125

Figure 2.1. *Values of critical temperatures of some high temperatures superconductors*

There is no oxygen between these adjacent sheets. The CuO_2 sheets are negatively charged because the oxidation number of the Cu is close to the value of 2. The net charge of the interlayer group A'_xX_y is positive. The superconducting effect takes place in the 2-dimensional CuO_2 sheets. The Cu ions in un-doped compounds are anti-ferromagnetically coupled to neighbouring Cu ions and therefore the plane is insulator. The intercalated layers act as charge reservoir that supply charge into the CuO_2 planes.

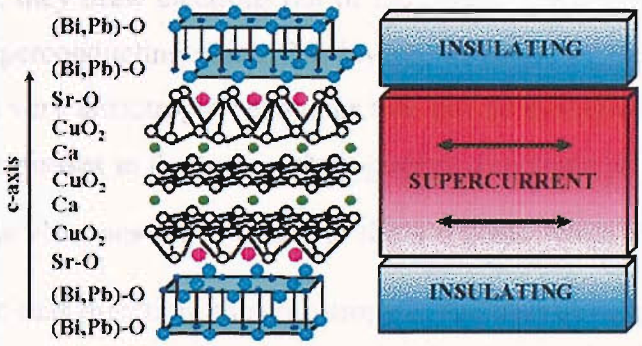

The Supercurrent Is Confined In 2D Blocks

Figure 2.2. *Schematic of the crystal structure and supercurrent flow in HTS materials*

The class of high-Tc superconductors in the Bi-Sr-Ca-Cu-O (BSCCO) system was discovered at December 24 1987, when an oxide of Tc about 105 K was found [5]. The phases of Bi-based family of HTS oxide superconductors are generally formulated by the chemical formula $Bi_2Sr_2Ca_{n-1}Cu_nO_{2n+4+x}$. Three phases encompass this family according to the n value:

- n=1→ $Bi_2Sr_2CuO_{6+x}$, the Bi-2201 phase, with $Tc \leq 20$ K [6], [7].
- n=2→ $Bi_2Sr_2CaCu_2O_{8+x}$, the Bi-2212 phase, with Tc=85 K [5].
- n=3→ $Bi_2Sr_2Ca_2Cu_3O_{10+x}$, the Bi-2223 phase, with Tc=110 K [5].

The structure of the high Tc phases Bi-2212 and Bi-2223 is of perovskite-like $(Sr_{1-x}Ca_x)_{n+1}Cu_nO_{2n+2}$ layers sandwiched between rock-salt-type Bi_2O_2 layers. The lattice constants have the values: $a = 5.39\,\overset{\circ}{A}$, $b = 5.41\,\overset{\circ}{A}$ and $c = 30.8\,\overset{\circ}{A}$ for the *n=2* phase (2212). The *n=3* phase (2223) has $c = 37\,\overset{\circ}{A}$, due to the presence of the additional CuO_2 and Ca layers. In figure 2.4 is a schematic representation of the unit cell structure that can be described as double BiO layers alternating with $Sr_2Ca_2Cu_3O_8$ units which contain three CuO_2 sheets formed by corner sharing CuO_4 units orientated parallel to the *α-b* plane. The copper oxide planes are separated by a single calcium ion; the intercalated calcium plane contains no oxygen and is sometimes known as the mediating layer. The CuO_2 planes are the conduction planes where superconductivity takes place. The intercalated planes of SrO and BiO are the characteristic of HTS oxides "charge reservoir" layers; they draw electrons out of the central CuO_2 and Ca layers, leaving holes to form superconducting pairs. The layered structure of the Bi-2223 crystal is responsible for a very anisotropic behaviour that can be evaluated by the ratio of the effective electron masses in the two crystallographic directions (c-axis and a-b plane): $\left({}^{m_c}\!/_{m_a} = \gamma^2 \right)$. The electrons move easier in the a-b plane while they encounter great difficulty in the c-axis direction; the anisotropy in the bismuth cuprates has the value of $\approx 10^5$ which practically means that the superconductor is two-dimensional. The coherence length in the a-b plane is of the order of 25 Angstroms while in the c-axis direction is about 30 times smaller. Transport current measurements at 77 K on tapes have shown that the magnitude of the c-axis transport current is less than the a-b plane transport current by a factor of 10. Electron tunnelling measurements in the c-axis direction above 80 K have shown evidence that the c-axis current travels by a tunnelling mechanism, jumping from one CuO layer to the next, which is supported by the fact the c-axis lattice constant is much larger than the coherence length.

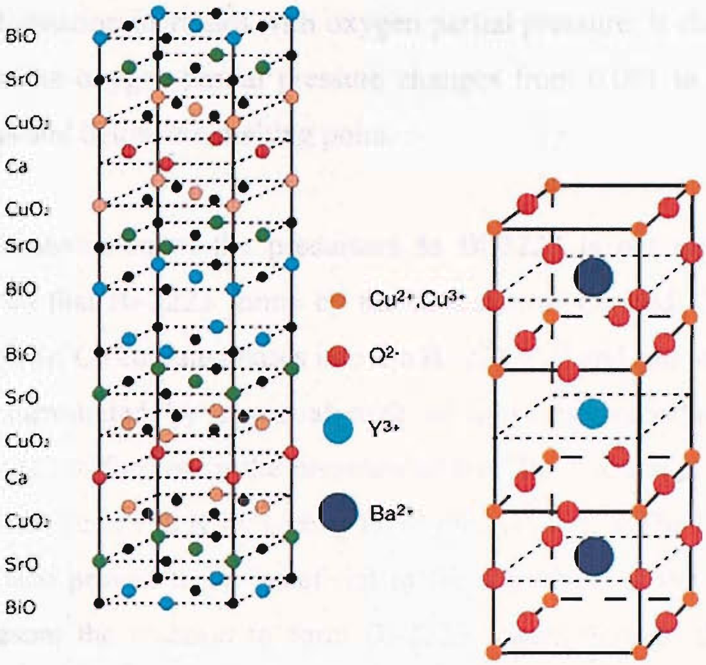

Figure 2.3. *Schematic representation of the Bi-2223 unit cell*

2.3. (Pb,Bi)2223 phase formation

The growth of pure Bi-2223 phase from its precursors is a complicated process and very sensitive to a various of processing parameters. Great part of the general difficulty is assigned to the very narrow temperature range over which the Bi-2223 phase forms. Moreover, sufficient knowledge of the Bi-2223 phase field formation which is essential to obtain high Jc values in tapes requires the field description in multi-dimensional space, but due to the complexity of the description more simplified approximations have to be used in two or three dimensional projections. This is not easy in the case of the powder in tube tapes which is not only the phase equilibria of the Bi-2223 that will determine the current capability, and therefore these approximations usually fail when attempting to map them for the achievement of high Jc. The presence of the silver or silver alloy sheath generates more complications in the phase field. The formation rate of Bi-2223 is a function of both atmosphere and temperature [8]. Bi-2223 is not so stable at low oxygen partial pressures $\sim 10^{-5}$ atm but also it is unstable in pure oxygen. The Bi-2223 forms over a wide range of oxygen partial pressures in contrast to the narrow temperature range of formation; the formation kinetics are faster at low oxygen partial pressures. The melting point of the Bi-2223 increases as the oxygen partial pressure increases [9]. The optimum temperature of formation increases with oxygen partial pressure; it changes from 830 °C to 880 °C as the oxygen partial pressure changes from 0.001 to 0.5 atm. and is above the solidus and below the melting point.

The process of conversion of the precursors to Bi-2223 is not well known. It is generally believed that Bi-2223 forms by the diffusion of Cu and Ca from a liquid phase or from the Sr, Ca cuprate phases into the Bi-2212 [10] and can be visualised as a Bi-2212 grain surrounded by a partial melt of assisting secondary phases. The majority of Bi-2223 is formed in the presence of lead Pb. Takano et al made a pure Bi-2223 phase with Tc at 110 K by adding Pb to the system [11]. The Pb doping of the Bi system has been proved to be beneficial to the formation of the Bi-2223 phase. When Pb is present the reaction to form Bi-2223 passes through the intermediate phase (Bi,Pb)-2212 which is solid solution of the Bi-2212 phase with Pb incorporated. The Pb substitutes partially the Bi atoms; the unit cell remains orthorhombic but the ratio b/a is larger. The Bi-2212 phase undergoes a compositional change correlated to the dissolution of a certain amount of Pb. This dissolution results in a structural modification from tetragonal to an orthorhombic phase. Grivel et al with the use of XRD and EDS measurements characterised qualitatively the phases of quenched tapes. The tape that has reached the 1st endothermic peak was compared to the tape that was quenched at 36 C lower and was found to have the Bi-2212 (200) and (020) XRD peaks split, whilst the Ca_2PbO_4 peak is reduced. These are indications of a reduction in the c-axis of the Bi-2212 cell. The reduction in the c-axis was the confirmation of the presence of Pb in the Bi-2212 cell. Larger portions of Pb doping are formed in a shorter period of time in comparison to the Pb-free phase. It was suggested that the Pb enhances the reaction kinetics between the precursor oxides through the production of the highly reactive $CaPb_2O_4$. The low eutectic reaction between the Ca_2PbO_4, CuO and Bi-2212 phases will provide the liquid during the heat treatment of the Bi-2223. The partial replacement of the Bi with Pb makes small difference in the electronic configuration, and therefore the critical temperature will not change. Substitution of Bi by Pb supports the crystallization of the Bi-2223 phase [12] [13], [14] and in addition the Pb doping shifts the phase stability to lower temperatures (unleaded Bi-2223 phase: 840 °C-890 °C; Pb-doped Bi-2223 phase: 830-880 °C) [15].

There is effect of silver doping to the Bi-2223 phase formation since a few microstructures develop by the influence of the silver. Enhanced melting has been found to occur at the ceramic/silver interface, which means that the silver lowers the melting points of both Bi-2212 and Bi-2223. Studies of the influence of silver on the phase stability of the Bi-2212 and Bi-2223 has yielded that the Ag can lead to a depression of the incongruent melting temperature of the Bi-2212; in addition, the presence of silver can cause reduction in the viscosity of the liquid phase [16]. The formation of the Bi-2223 phase in the silver tape from the Bi-2212 and secondary phases is more rapid and more complete at the silver/ceramic interface in comparison to central regions of the inner core. The degree of Bi-2223 formation decreases with increasing distance from the interface with the silver, as well as the grain size of the Bi-2223 does [17]. The processing parameters heating and cooling rate, sintering temperature, time and atmosphere can influence the degree at which the silver interface affects the Bi-2223. Addition of silver powders to the precursor powders has been found to accelerate the rate of Bi-2223 formation with beneficial effects on the Jc. A 10wt% of appr. 45 μm Ag powder deforms in a filament like form during the drawing and rolling when the tape is formed [18]. This increases the silver/ceramic interface area which is beneficial for the conversion to the Bi-2223 phase, while it increases the textured volume of the tape core and resulted in 20% increase in the Jc. In other work larger silver particles were added of size 80 μm and a higher percentage of the silver to the precursor powders, 30wt% and 50wt%. The silver particles elongate during the mechanical deformation to a tape of 1:8 aspect ratio, thus dividing the ceramic core into thin multi-connected filaments thus ensuring a large percentage of the core in close proximity to the partially aligned silver filaments. Increased density of the samples was observed with a more homogenous distribution of the Bi-2223 which had formed more rapidly in comparison to a control sample without Ag doping.

2.4. Models of formation of Bi-2223 phase from Bi-2212

The proposed models for the growth of the Bi-2223 phase are **intercalation** [15]-[17] and **precipitation** [18], [19]-[21].

The intercalation model supports the idea that the transformation to the Bi-2223 phase is via insertion of additional Ca and Cu-O layers into the structure of the pre-existing Bi-2212 crystals. There has been found evidence to support the validity of this model, which is TEM images [15] that show stacking faults between grains of Bi-2223 and Bi-2212 with a structure of 4435. The faults are attributed as a result of the insertion of the additional Ca and Cu-O. The insertion mechanism is one-dimensional diffusion at an edge dislocation in the Bi-2212 grain. In the work of Wang et al [16] the Bi-2223 and Bi-2212 phase were monitored in order to detect that a decrease of the Bi-2212 phase occurs simultaneously to the formation of Bi-2223 phase. It has been found that the formation of the Bi-2223 occurs in three stages that can be represented as a conversion graph with an S shape. This route of formation supports that the Bi-2212 grains are wetted by a liquid phase which partially dissolves the Bi-2212 grains. The Bi-2223 phase nuclei are formed at the boundaries of the Bi-2212 grains. This is followed by the Bi-2223 growth as a diffusion process in which the Ca, Cu and Pb ions are transported into the Bi-2212. In the work of Luo et al [17], it was attempted to match the conversion rate equation with the phase evolution of the Bi-2223 in Ag tapes. They compared two different calcinations of the precursor powder; in one some Bi-2223 has already formed and in the other no Bi-2223 was present. The formation of the Bi-2223 as a function of time can be represented by an S shape graph. In the early stages there is no conversion, which is the incubation period where the Bi-2223 nucleation sites are forming. After the Bi-2223 starts to form, fast at the beginning but is slowing down at the end. It was found that a two-dimensional controlled growth fits the experimental data more closely, in which an Avrami relationship models the S shape of the conversion curve of the Bi-2223 free precursor sample. In the sample that already contains some Bi-2223 the rate of growth was much accelerated due to the presence of already formed nucleation sites. Also it suggested that at the later stages of the growth, the growth slows down; at this stage, the nucleation and growth mechanism is indistinguishable from the diffusion mechanism. The results suggest that there is an intercalation process occurring; the Bi-2212 acts as a nucleation site with the presence of a liquid phase that accelerates the diffusion process.

The precipitation model supports that Bi-2223 nucleates directly from a liquid phase whilst it does not form from pre-existing Bi-2212 grains. The Bi-2223 phase will nucleate from a partial melt that is produced from the melting of the Bi-2212 phase. Work of Grivel et al [19] underlines that the texturing of the Bi-2212 phase and the just formed Bi-2223 phase are different. This suggests that the Bi-2212 does not act as a nucleation site. It is more likely that these results suggest the Bi-2223 phase nucleates from the melting of the Bi-2212 phase and the growth occurs layer by layer. Using a precursor powder that contains amounts of Ca_2PbO_4 as secondary phase content, the disappearance of the Ca_2PbO_4 during the first our of the heat treatment is evidence that Pb and Ca ions diffuse into the Bi-2212 crystal structure and lower its melting temperature. When the Bi-2212 phase has been melted, the Bi-2223 phase will precipitate from the melt until the moment that the cationic ratio can no longer favour the crystal growth; then intergrowths of Bi-2212 occur in Bi-2223 structure. In the work of Morgan et al [20] it was shown in SEM images that droplets of liquid phase migrate which form the Bi-2223 phase on the Bi-2212 grains. Hu et al [21] in their work underlined that Bi-2223 grows by nucleation and growth in the partial melting of the Bi-2212 and secondary phases.

A variety of observations suggests that Bi-2223 formation occurs under various different sintering conditions, whilst there is difficulty in defining the composition and evolution of the intermediate phases during the heat treatment, the growth mechanism of the Bi-2223 phase is not easy to define. Both of the above models can explain the induction period that occurs prior to the phase conversion and at the same time the existence of Bi-2212 phase intergrowths due to non-complete conversion to Bi-2223. It could be that both of these growth mechanisms may occur at different heat treatment conditions, in the sense that one of them is more kinetically favourable than the other.

2.5. Tape fabrication through the OPIT technique [1]

2.5.1. OPIT review

The future application of the HTS tapes in the high field magnets, energy storage, motors and generators or the electrical power transmission requires the fabrication of long lengths high quality conductor. The Bi-2223 high temperature superconductor can take the form of a composite wire or tape suitable for the above mentioned applications, after undergoing a series of processing techniques that are known altogether as **OPIT**, i.e. **Oxide Powder in Tube** technique. The laboratory OPIT procedure consists of the following steps:

(a) Filling a silver or silver alloy tube with stoichiometric precursor powder of the Bi-2223 phase, which consists mainly of Bi-2212 and other phases such as Ca_2PbO_4 and Ca_2CuO_3.

(b) Cold drawing of the tube in the drawing machine until a thin diameter wire is obtained.

(c) Cold rolling or pressing of the wire on the rolling mill to deform the wire into a tape.

(d) Heat treatment of the composite in flowing gas (a mixture of argon and oxygen in various percentages), in order the unreacted chemical components of the precursor powder to react and form the Bi-2223 superconductor.

Steps (b) and (c) are the mechanical deformation of the composite. The result of the above mechanical processing-heat treatment process is the formation of a superconducting single core tape able to carry high electrical current after being cooled below the critical temperature. Multi-core composite wire and tape can be obtained if a silver tube is filled with several single core unreacted wires produced by steps (a) and (b) in hexagonal and triangular configurations, and then repeat steps (b), (c) and (d) again. The microstructure of the tape superconducting core is granular as all the HTS ceramics, with high textured Bi-2223 grains along the a-b conduction plane parallel to the tape surface. Critical current density values of 30 kA·cm^2 (77 K and self-field) have been achieved with multiple rolling-heat treatment single core tapes [22]. Higher Jc values up to 69 kA·cm^2 (77 K and self field) have been reported for uniaxial pressed tapes produced with three press-heat treatment cycles [23]. In figure (2.5) the OPIT process is shown schematically.

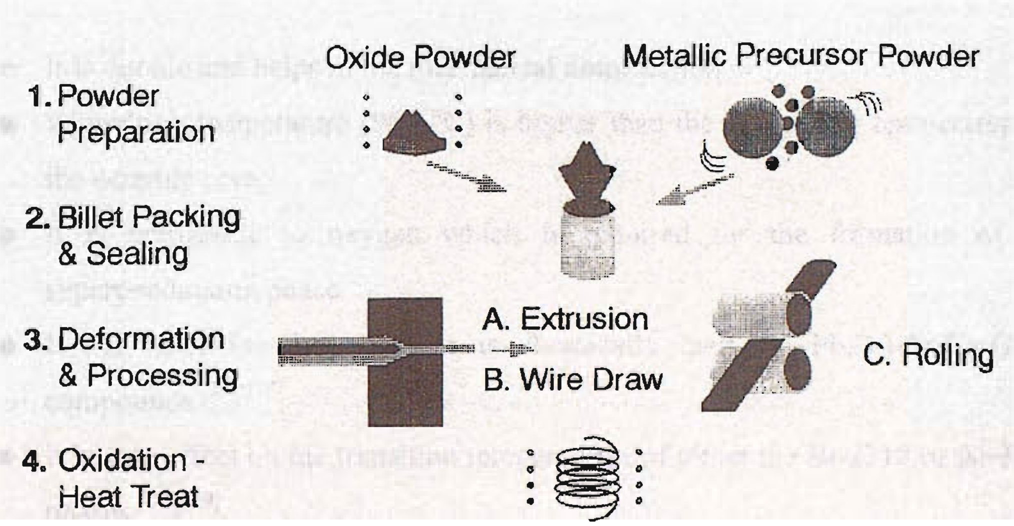

Figure 2.4. *The Oxide-powder-in-tube method for fabrication of composite silver sheathed Bi-2223 tape*

2.5.2. The sheath material

The metal sheath of the composite tape offers the following advantages:

a. It is a protective barrier to the sensitive core to various environmental hazards that the conductor is often exposed (for example moisture and poisonous gasses such as CO_2).

b. It provides mechanical reinforcement to the mechanically weak superconducting core at both room temperature, when is being manipulated in order to be installed in devices, for example in winding of superconducting coils, and at low temperature during operation, where it encounters mechanical stresses and electromagnetic forces in magnets.

c. It provides electrical stability as a parallel electrical current path in the event of quench and also thermal stability.

Copper, steel and nickel are excluded as choices of the sheath as they have been found to affect the (Bi,Pb)-2223 phase formation [24]. Aluminium has been found to deteriorate the properties of YBCO oxides [25]. The pure silver is the most suitable as a sheath material for the following reasons:

- It is ductile and helps in the mechanical deformation
- Its melting temperature (960 °C) is higher than the processing temperature of the ceramic core.
- It is permeable to oxygen which is required for the formation of the superconducting phase.
- It has been found that silver is chemically inert to (Pb,Bi)-Sr-Ca-Cu-O compounds [26], [27].
- It has no effect on the transition temperatures of either the Bi-2212 or Bi-2223 phases [28], [29].
- Evidence has been found that silver enhances the grain alignment of the Bi-2223 grains near the Ag/Bi-2223 interface [30], [31]. Details of the interaction of the silver with the (Bi,Pb)-Sr-Ca-Cu-O compounds can be found in the literature [32]. Morgan et al have presented evidence for a silver-containing eutectic liquid that promotes the solution precipitation of Bi-2223 [33].

In addition, silver has been found to lower the melting temperature of the BSCCO due to dissolution of Ag in the liquid phase [34], which can be thought as an advantage for the Bi-2223 processing as being more stable at lower temperatures.

In the applications the tapes are subjected to mechanical and thermal stresses. The sheath material needs to be of sufficiently high tensile strength and also to be able to retain the property after long term annealing. The pure silver is not suitable for most large electrical power applications since the yield strength (~40MPa) [35] and the strain tolerance (<0.5%) [36] are lower than the required limits. The poor mechanical properties of the silver can be enhanced by alloying the silver with elements such as Mg, Al, Mn and Sb. The mechanical strength and hardness are increased which not only improves the functionality of the composites in applications but also assists the mechanical deformation during the tape manufacturing stages by increasing the green core density which favours the achievement of high critical current densities. AgMg alloys were found to increase the hardness of the sheath which results in higher resistance to sausaging. The AgMg also improves the strain tolerance of the tapes [37].

2.5.3. Packing of the precursor powder

The precursor powder is ground with a pestle and mortar in order to break any agglomerates. A silver tube 14 cm long is supported with a wooden clamp and in one of its ends a seal is applied. The seal is made of silver foil but also it can be made of indium if no annealing at high temperature will be performed. The whole packing procedure takes place inside a plastic bag under oxygen atmosphere. The powder is inserted in the tube by doses of 0.25 gr each and compressed by 1 kilo of weight for 30 seconds each dose. The other end is sealed and holes are drilled on the seals in order to allow permeability to gas; in both ends of the tube, balloons filled with oxygen gas are applied for short time storage of the billet.

2.5.4. Cold mechanical deformation of the composite

The high temperature superconductors are ceramic materials with poor mechanical properties that set obstacles in their formability to wires and tapes. The applications require that these materials must have adequate mechanical strength and good electrical properties. The brittle core of the ceramics can be easily cracked during deformation; a crack means local interruption of the transport current path, while in some cases under strain condition, cracks will propagate thus setting total irreversible barriers to the transport of electrical current. The mechanical deformation which consists of drawing and rolling requires special attention because it will determine to a high degree the electrical transport properties of the tapes through the strong influence that has on the formation of the superconducting core. The drawing and rolling procedures will be discussed briefly:

A. Drawing-wire formation

Drawing is a wire formation technique, a cold deformation process, where an initial tube or rod is forced to pass through a hollow die with a tapered bore; the output diameter is smaller than the input. The output diameter of the die is smaller than the diameter of the wire to be drawn. As a result, the tube diameter is reduced and the wire is elongated by successive passages through dies of decreasing diameters. The limits in the drawing load are set by the tensile strength of the material, which in turn sets a limit in the maximum reduction per passing through a die because increased reductions require increased drawing loads. The deformation force must be less than the tensile strength of the composite Ag/BSCCO wire; reductions of 10% to 20% in the cross sectional area are usually applied.

The cold working induces stresses in the silver sheath and hardens it, i.e. it increases its mean yield strength σ_M. The metal hardening will eventually cause the wire to break if the drawing force increases as it can be seen in relation (2.1), which calculates the drawing force that increases with the yield strength [38], [39], [40].

$$F_{Drawing} = \sigma_M \cdot A_{out} \cdot \ln\left({A_{in}}/{A_{out}} \right) \cdot \left\{ 1 + {\mu}/{\vartheta} \right\} \qquad \textbf{\textit{(2.1)}}$$

The drawing force is proportional to the cross sectional area of the wire before the deformation starts. The induced stresses that cause hardening of the silver can be released by annealing of the wire at temperatures 400 °C to 450 °C at regular intervals between successive steps of the drawing procedure. This will soften the metal and it will be drown more easily against the hard and non-plastically deformed compacted powder core.

The friction restricts the uniform deformation which occurs inhomogenously. Friction acts at the interface between the die and the wire. As a result, lateral stress develops in the wire, which has a maximum value at the interface and falls to a minimum in the centre of the composite. The consequence is that variations in the mechanical properties along the thickness of the wire will occur. The outer layers of the wire will be worked to a higher degree than the inner parts. The frictional force is divided into a radial and an axial component. The axial friction will develop shear force. The deformation state of the ceramic core is distinguished from that of the silver metal because the ceramic is resistive to plastic deformation and the silver is easily plastically deformed due to the shear force. Then the mechanical deformation of the composite becomes more complicated than if it was a single material. This shear force will produce flow of the powder particles in the interior of the wire. The inter-distances between the powder particles will change. At the same time, "plastic" flow of silver occurs on top of the hard core. The shear force acts on the powder through the silver sheath. The powder will stop to flow when the friction between the powder grains becomes equal to the driving force on the powder. At this point the powder packing density reaches a critical value and would not be expected to go to higher values [41]. The prediction that a critical value of packing density exists was observed in a few independent experimental works [42], [43], [44-48]. The radial friction opposes the compression force that exists due to the pressure acted by the die walls, i.e. it resists densification of the wire but more importantly homogenous densification and therefore should be eliminated. A common solution is the use of lubricant soap in order to limit the action of the friction force. The inhomogeneities that appear during the OPIT process at any stage should be eliminated; the mechanical deformation procedure requires careful control otherwise it will cause severe inhomogeneities [41], [49]. As a conclusion, it is estimated based on the rather assumed but experimentally verified model of powder flow that the final density of the wire after drawing does not depend on the initial packing density of the tube.

B. Rolling-Tape formation

In the OPIT process, the rolling is the final step of the mechanical deformation that forms the final round thin wire into a tape after the drawing process. An alternative process to rolling is pressing. The wire is rolled in the rolling mill into steps. Each rolling step gives a certain amount of reduction in the thickness, with also a small amount of elongation and flattening until the desired final tape thickness is obtained. The deformation zone is defined as the area of contact between the rollers and the tape.

It is believed that the rolling increases the degree of alignment of the precursor powders. The model of powder flow suggests that the powder particles at the centre of the tape have higher velocity than the powder at the sheath-core interface. The

BSCCO precursor powder grains have the form of flat flakes and such a velocity profile tends to align the grains with the c-axis perpendicular to the a-b plane [50].

2.5.5. Heat treatments

After the cold rolling process the core of the tape consists of a highly densified powder. The core requires heat-treatment in order the components of the precursor powder to react and convert to (Pb,Bi)-2223 grains; this process forms a solid conductor with a well connected grain structure that will be capable of carrying electrical current below the critical temperature. The required temperatures for heat treatments are in the range 800 °C to 850 °C. The heat treatment takes place in a tube furnace in a flowing gas atmosphere. The furnace is composed of the following components (figure 2.5) :

a. An Al_2O_3 tube, which is the space where the heat treatment of the sample takes place; the tube does not permit the diffusion of gases through its walls.
b. Heating coil around the tube composed by insulated electrical wire.
c. Thermal insulation around the tube in order to prevent thermal radiation losses.
d. Two insulation plugs at the ends of the Al_2O_3 tube in order to protect from radiation losses from the open ends of the tube and also to homogenise the temperature distribution in the tube.
e. Temperature controller

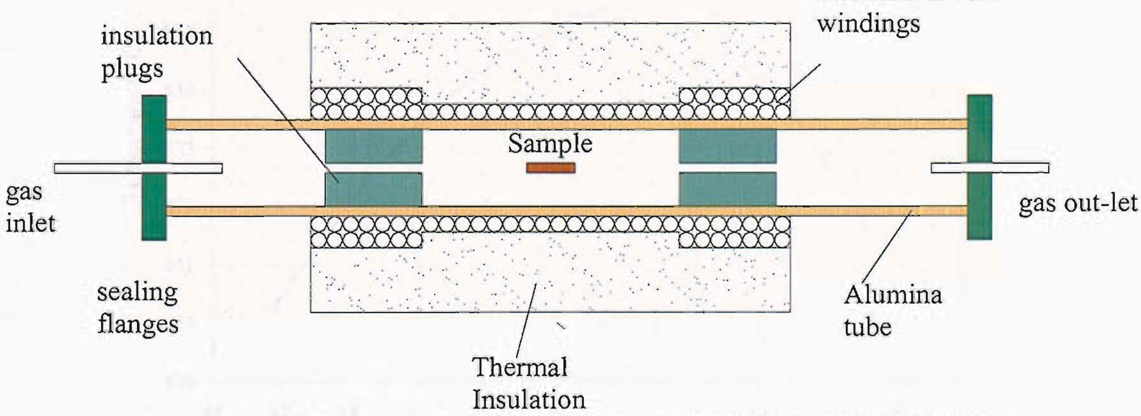

Figure 2.5. *Schematic of a tube furnace used for the heat treatments*

2.5.6. Furnace calibration and testing

The hot zone of the furnace is defined as the region near the centre where the temperature has the best spatial homogeneity and is chosen to be the sample's position (figure 2.6). A long hot zone is preferable in order to allow heat treatment of long length samples or many small samples simultaneously. The acceptable temperature homogeneity in the hot zone of the furnace is ±0.5 °C because the temperature formation window of Bi-2223 is very narrow and the final tape transport properties are very sensitive to furnace temperature variations or disturbances; even two or one degrees of temperature fluctuations have been seen to be detrimental in our experiments. In order to record the temperature distribution along the tube length (i.e. temperature profile), the furnace is set to a level close to the heat treatment temperature with the two insulation plugs at their positions and a type N thermocouple referenced at 0 °C into an ICELL is inserted from the one of the tube and shifted along the length. The furnace is subjected to another important for the experiments test. The thermocouple is placed at the sample's position and the furnace is subjected to high heating rate. It is recorded whether temperature over-shooting occurs over the defined heat treatment temperature level due to high heating rate (figure 2.7). If temperature over-shooting of about 0.5 °C – 1 °C occurs, the furnace is unsuitable for use at high heating rates.

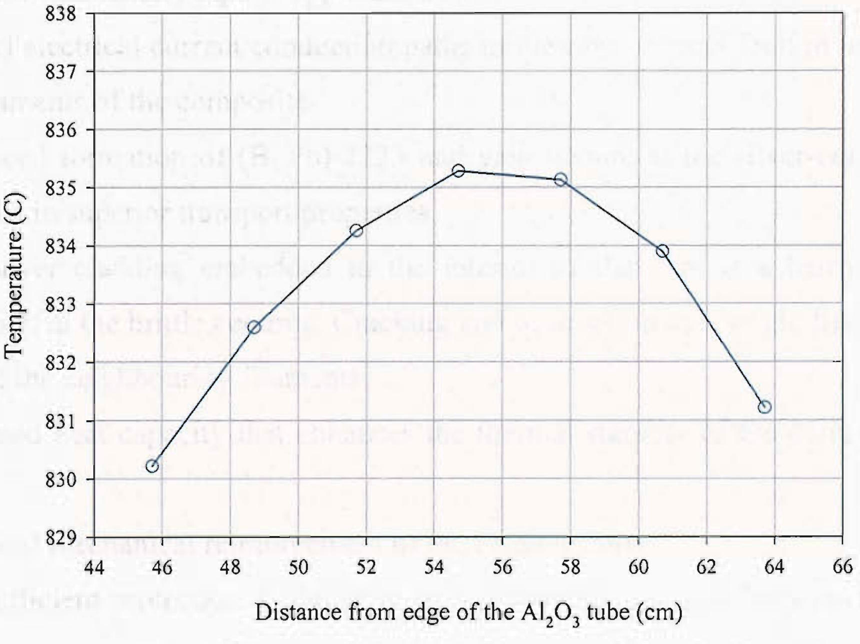

Figure 2.6.*The recorded hot zone of the tube furnace with controller set point 840 °C*

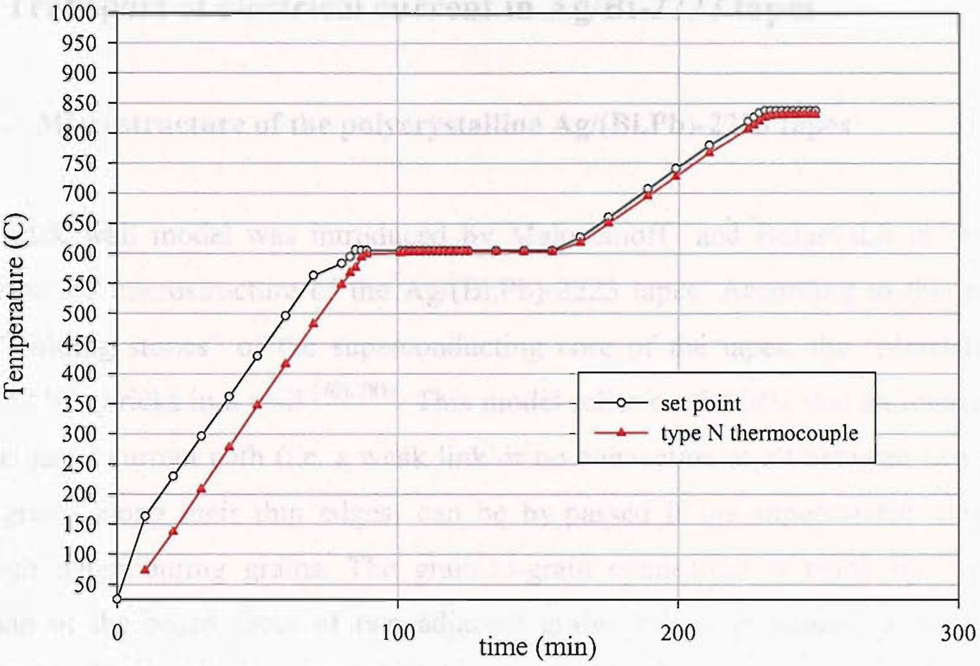

Figure 2.7. *Temperature overshooting test of the furnace with heating rate 800 °C/h*

2.5.7. Production of multi-core tape

After a single core composite wire has been obtained with the drawing process, it is possible to manufacture a multi-core wire by packing a number of mono-core unreacted wires (19, 37, 55, 85 etc) in a silver tube and then draw it. Then it can be formed to a multi-core or multi-filamentary tape by rolling. The advantages when using multi-filamentary tape in applications are:

a. Parallel electrical current conduction paths in the case of local fault in one or more of the filaments of the composite

b. Enhanced formation of (Bi,Pb)-2223 and gain texture at the silver-core interface that results in superior transport properties

c. The silver cladding embedded in the interior of the core is a barrier to crack propagation in the brittle ceramic. Cracking and destruction of a single filament could not affect the neighbouring filaments.

d. Increased heat capacity that enhances the thermal stability of the composite (heat sink)

e. Enhanced mechanical reinforcement of the ceramic core

f. More efficient protection of the delicate superconducting core from environmental hazards

2.6. Transport of electrical current in Ag/Bi-2223 tapes

2.6.1. Microstructure of the polycrystalline Ag/(Bi,Pb)-2223 tapes

The brick wall model was introduced by Malozemoff and Bulaevskii in order to describe the microstructure of the Ag/(Bi,Pb)-2223 tapes. According to this model, the "building stones" of the superconducting core of the tapes, the "platelets" are stacked like bricks in a wall [80], [81]. This model relies on the idea that an interruption of the direct current path (i.e. a weak link or no connection at all between two plate-like grains along their thin edges) can be by-passed if the supercurrent meanders through neighbouring grains. The grain-to-grain connection is made by a partial overlap of the broad faces of two adjacent grains that is in general a twist grain boundary. The microstructure of high current carrying tapes, however, does not resemble a brick wall. Based on the investigations of tapes with critical current densities at 77 K and self field > 15000 kA/cm^2, Hensel et al proposed the railway switch model with a more adequate microstructural foundation for high-current tapes. The fundamental elements of this model are the small-angle-c-axis tilt grain boundaries or railway switches that connect adjacent grains. There is evidence that the grain boundaries are not the limiting factor for the critical current density; that is weak links play only a minor role in high-current tapes (expected at very low fields). Through TEM (Transmission electron microscopy) it was made clear that each platelet is made of a stack of grains. The TEM investigations revealed frequent (001) twist grain boundaries in the (Bi,Pb)-2223 structure. Two adjacent (Bi,Pb)-2223 layers have parallel c-axes, whereas the a and b axes of the tow layers can be more or less twisted around the common c-axis. Several layers of (Bi,Pb)-2223 with relative twist form a grain colony. The twist boundaries will generally reduce the critical current density perpendicular to the a-b planes across the twist boundary (depending on the twist angle. A boundary that is formed by the partial overlap of the broad faces of two adjacent colonies is a twist grain boundary and constitutes the main building block of the brick wall model. Such colony boundaries, however, are only rarely found in high current (Bi,Pb)-2223 tapes. A second type of boundary is the "edge-on c-axis" tilt grain boundary. These boundaries are formed by the touching edges of two neighbouring colonies whose c axes lie in the same plane but are tilted with respect to each other. The third type of boundary is the frequently observed small-angle c-axis tilt grain boundary. In this case, the edge of one colony meets the board face of another colony under a sharp angle (railway switch). The electrical current preferentially flows through selected paths in order to avoid weak-linked regions between adjacent grains ("bad" connections). The railway switch model for current flow in a tape [51], [52] relies on the assumption that small-angle c-axis grain boundaries constitute strong connections and do not represent weak links for the supercurrent with the detrimental effect of a strongly reduced critical current already in very small magnetic fields. Dimos et al [53] and Amrein et al [54] have assessed the transport properties of grain boundaries of $YBa_2Cu_3O_7$ and Bi-2212 bicrystals. The latter were obtained on well defined grain boundaries in thin films that have been deposited on bicrystals with different relative orientation. For both superconductors, grain boundaries were found to reduce Jc by more than an order of magnitude when exceeding miss-orientation angles of about 10°. The above mentioned edge-on c-axis tilt grain boundaries are very similar to the thin film grain boundaries, although in the tapes no substrate leads to possible distortions of the boundary. Small angle c-axis tilt grain boundaries cannot be realised in bicrystal experiments. The contact cross section of a railway switch grows like $1/\sin(\phi)$ with decreasing tilt angle ϕ. It is thus enhanced by a factor of 4 for a 15° boundary angle and by 7 for 8° (relative to the constant transverse cross section of the grains). Thus the reduction of Jc across the boundary is partly compensated by the larger contact surface. Figure 2.8 compares the grain structure of a thin film and a Bi-2223 tape.

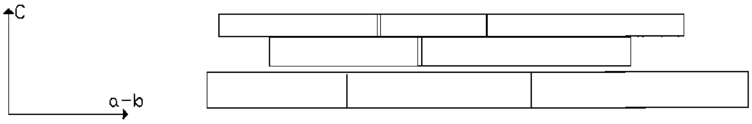

Thin film

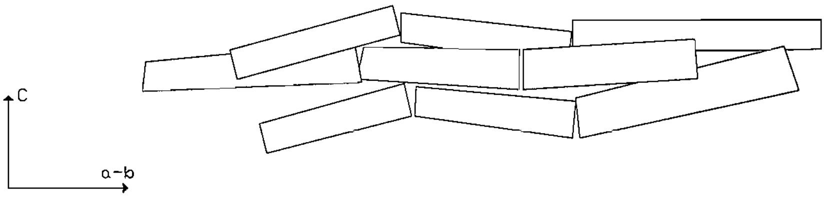

Tape

Figure 2.8. *Schematic representation of the grain structure in a thin film and a tape*

2.6.2. Current limiting factors

At 77 K and self field the maximum critical current density in Ag/(Bi,Pb)2223 tapes is lower than the Jc values of thin films by a factor of 50 to 100. However this comparison is not appropriate because the thin films represent single-crystal layers, where for magnetic field B// the angle between B and the film surface is 0°. Due to the misalignment angle of about 8° - 10° in Ag/(Bi,Pb)2223 tapes, however, the critical current density of the latter has to be compared with that one of thin films, with the same angle between B and the film surface. At this orientation, Jc is almost an order of magnitude lower than for $\theta = 0°$. Another limitation is given by the fact that the density inside the tapes is not 100%, but always below 80-90%. Within the framework of the railway switch model, the following arguments can be considered as the main reasons for the limitation of the critical current values in Ag/(Bi,Pb)2223 tapes:

The low value of the critical current density perpendicular to the tape surface

This low value, deriving from the extreme anisotropy, is the major factor determining an upper limit for the achievable critical current density of the tapes. The low critical current density perpendicular to the CuO_2 planes J_C^c compared to the in-plane critical current density J_C^{ab} does not promote a distribution of the supercurrent in the individual grains, especially in such grains having small aspect ratios. On the level of the single colony, the problem is even aggravated by an increase of the effective anisotropy of the critical current due to twist boundaries and intergrowths. All this leads to an inefficient use of the available cross section for the current transport: not all possible current paths are used.

The average aspect ratio of the grains and colonies

Longer grains and colonies lead to an increase of the current carrying capacity of the tapes and are certainly responsible for the improvements obtained in the last years.

The lack of pinning in the grains inside a tape (in contrast to thin films)

The assumption that the grain boundaries are not the limiting factor in the tapes is supported by the fact that an improvement of the pinning properties of the grains is due to columnar defects that are introduced by heavy ion irradiation [55]. But also to a lower extent by dislocations created by hot deformation [56]. Both treatments lead to an enhancement of the critical current of the tapes in magnetic fields. This finding sharply contradicts a current limiting mechanism by grain boundary weak links in the direct current path.

The degree of texturing

Due to the particular formation and growth process of the (Bi,Pb)2223 phase, starting from the already textured Bi-2212 phase inside the tapes, a certain imperfection in the degree of texturing will always persist when using the OPIT technique. More sophisticated preparation processes will possibly lead to an improvement of the misalignment or tilt angle, which is 6-8° for the best tapes. However, it is not advantageous to go below a certain tilt angle, a too sharp field dependence of Jc rendering the tape is impractical for industrial purposes and therefore a compromise has to be found.

The homogeneity of the superconductor

Due to the particular formation process of the (Bi,Pb)-2223 phase, it is necessary to start with a slightly non-stoichiometric composition. After the reactions, a certain volume fraction inside the oxide layer will thus always be filled by secondary phases. This cannot be lowered below a certain level. An improvement may be obtained by a distribution of these secondary phases, which should be as fine as possible.

The measurement of Ic(B) is used to evaluate the quality of the grain boundaries and the degree of alignment of the grains in the BSCCO core. The high Tc cuprates are highly anisotropic materials and the critical current of the Bi-2223 has been found to have quite different values in the two crystallographic directions a-b plane and c-axis [57]-[60]. The maximum and minimum values of Ic occur when the applied magnetic field is in the parallel and perpendicular direction to the a-b plane of the tape respectively [61]. The ratio $a = {J_c(B // ab)} / {J_c\{B // (c-axis)\}}$ can be used as an indication of the texture of the Bi-2223 grains [61]. In externally applied magnetic fields, the tape critical current at 77 K reduces in general by a factor of three to six in comparison to the Ic value at zero applied field, when a field of 1 Tesla is applied perpendicular to the a-b plane. The fall off of in the Ic values under applied magnetic fields is greater in fields parallel to the c-axis; in the I-V graphs the sample is found to show resistive behaviour in fields above 0.5 Tesla in LN_2. In the c-axis direction, the low value of irreversibility field is attributed to the lack of pinning force along this direction which cannot pin the flux lines. The railway switch model for current flow in the tape [60] predicts that in fields applied parallel to the c-axis direction, the drop-off in the Ic values is due to lack off pining potential. In contrast, the drop-off in the Ic values for fields applied parallel to the a-b plane is attributed to low quality grain boundaries with large misalignment boundary angle, or additionally, perhaps to the presence of weak links and is more sensitive to the grain texture rather than the pinning potential. In order to improve the irreversibility field, columnar defects have been introduced by irradiation of the tapes and enhance the pinning force [62], [63].

2.6.3. Interface between the Ag sheath and oxide core

The interface between the silver sheath and the superconducting core has some effects to the flow of the supercurrent in Ag/(Bi,Pb)-2223 tapes. The silver reduces the melting temperature of the precursors and thus the core microstructure will be different near the interface from that at the centre of the core. There is enhanced grain alignment occurring near the interface during the superconducting core development at the processing stages. Luo et al and Feng et al observed via TEM imaging that the Bi-2223 grains have the tension to orientate with the a-b planes along the interface with the silver. The rolling deformation produces a non-uniform interface between the Ag and the core, which makes the interface wavy, due to periodic variations in the core thickness along the tape; this effect caused by the rolling is called “sausaging”. Sausaging reduces the effective cross sectional area of the core, thus limiting the overall critical current of the tape. Also sausaging may cause grain misalignment. The explanation of this phenomenon was given by Han et al using the “powder flow” model. During the rolling deformation, the pressure of the rolling mil is transmitted to the core through the silver sheath. The flow of the powder in the core will eventually stop when the friction between the grains becomes equal to the driving force that causes the densification and powder flow.

2.7. Review in the material science of the Ag/Bi-2223 tapes

This review of the material science of the tapes is presented here with strong orientation to the role that the liquid phase which occurs due to partial melting of the precursors in the tape plays in the tape microstructure. It is known that the Bi-2223 formation is assisted by the formation of a Pb-rich liquid, hence the focusing of research towards this direction may lead to improvements in the tape performance. The physical microstructural features such as density, porosity and homogeneity are important and depend strongly on the liquid phase kinetics. With low temperatures, little liquid phase forms and consequently the microstructure will not be dense and the transport current will be low. Higher temperatures form more liquid, so rearrangement and densification can occur but secondary phases can grow. Recent studies by E A Young [64], [70] have reached to important conclusions with regard to the effect of the heat treatment temperature and atmosphere on the Bi-2223 formation and tape microstructure. In that work, the tapes have been produced with the same precursors as in this work; therefore any comparison between the two cases is valid. The conclusions are briefly concluded in the following:

For 7.5% partial pressure O_2 in the range 798 °C → 816 °C there is little liquid phase or secondary phase formation. In the range 816 °C → 847 °C there is a larger amount of liquid phase. Grain colonies and grain groups grow. Formation of the secondary phases $Bi_2(Sr_{1.6}Ca_{0.4})CuO_6$, Cu_2O and Cu-free takes place. The $Bi_2(Sr_{1.6}Ca_{0.4})CuO_6$ is known as the Bi-2201 phase and is known to form from liquid phase, when the liquid has reached the proper ionic composition [65]; the peak height of $(00\underline{6})$ is related to the volume of the liquid phase. The observation that there is increasing content of the $Bi_2(Sr_{1.6}C_{0.4})CuO_6$ phase suggests that the volume of the liquid phase is enhanced with the heat treatment temperature, also confirmed by Poulsen et al [66]. The best texturing of the grains occurs at 839 °C in air and 832 °C in atmosphere of partial pressure 7.5% O_2 where there is maximum percentage of the Bi-2201 observed. The higher heat treatment temperatures encourage the growth of large grains and well connected grain groups, whilst the amount of texturing is determined by the volume of the liquid phase which is monitored by the amount of the Bi-2201 phase. Kim et al [67] have seen the existing Bi-2223 to perform as nucleation site for the following growth of the Bi-2223 phase. Grain colonies will be formed by the build-up of Bi-2223 grains onto pre-existing Bi-2223 grains via the liquid phase. The nucleation energy associated with a Bi-2223 template is lower than the Bi-2212 [68]; since the volume of the liquid is increased at higher temperatures then the grain colonies will be formed also at higher temperatures. The nucleation and growth of the Bi-2223 grain colonies is the dominant mode of growth of such structure, since any formation by the intercalation model would have as a requirement the pre-existing Bi-2212 grain colonies which to the best of our knowledge has not been detected up to know in the literature. The Bi-2201 phase forms when pockets of non-stoichiometric liquid appear. Wang et al [69] show that the Bi-2201 reduces the critical current of the tapes by of a factor of 50% to 100%. In the phase composition the percentage of the Bi-2201 showed variations with the heat treatment temperature and therefore the effects on the critical current are expected to vary. It has been observed that the maximum and minimum values of Ic occurs when the amount of Bi-2201 has reached the minimum and maximum percentages respectively. The textured Bi-2201 phase has been observed on top of Bi-2223 grains, which in the context of the railway switch model translates that the Bi-2201 is a barrier to the current path through the c-axis transport and tilt grain boundaries. The effect of the Bi-2201 on the transport properties can be better understood through the observation that the maximum Ic occurs when the Bi-2223 percentage reaches a maximum in the atmosphere of air but not for the atmosphere of 7.5% due to the presence of large amount of Bi-2201 [70]. In the temperature range 798 °C to 820 °C and 7.5% O_2 partial pressure, the structure of the tape is characterised by loosely connected Bi-2223 grains. The critical current Ic level is low and there is little or no secondary phase formation. In the temperature range 820 °C to 847 °C and 7.5% O_2 partial pressure, strongly connected Bi-2223 grains are observed. Grain colonies similar to the railway switch model [60] form. The critical current Ic is high. The microstructure is characterised by a high Bi-2223 (0010) absolute peak intensity and large grain groups, ~ 3 times the Bi-2223 grain size. Also formation of $Bi_2(Sr_{1.6}Ca_{0.4})CuO_6$ – Cu_2O and Cu-free secondary phases takes place. The formation mechanism is likely to be nucleation and growth. In air, in the temperature region 830 °C to 836 °C loosely connected grains are formed that are characterised by low diffraction intensity and there is absence of well connected grain groups. The Ic is low and some Cu_2O and Bi-2212 forms. In air, in the temperature region 839 °C to 846 °C, the microstructure is strongly connected Bi-2223 grains via well connected grain groups as in the railway switch model which favours high values of critical current. Nucleation and growth is the dominant mechanism of formation. Larger grain size than in 7.5% O_2 occurs, formation of large Bi-2212 grains and $Bi_2(Sr_{1.6}Ca_{0.4})CuO_6$ – Cu_2O – Cu free secondary phases. At 852 °C in air is similar to 839 °C – 846 °C but there is large percentage of large Bi-2212 grains. Small secondary phases form, which distribute within the Bi-2223 grains.

As a brief summary and conclusion to the above discussion it can be said that for processing atmospheres of 7.5% partial pressure oxygen, two distinct temperature regions exist with regard to the Bi-2223 formation: (a) 798 °C to 816 °C, characterised by little liquid phase and little secondary phase formation and (b) 816 °C to 847 °C with large amount of liquid, grain colonies and grain groups, formation of the phases Bi-2201, Cu_2O and Cu-free. This suggests that a possibility exists that in the low temperature range the intercalation model of formation dominates; in contrast in the higher temperature range the nucleation and growth mechanism dominates, fact that is supported by the grain colony formation which only occurs by this type of formation mechanism but also the distinct phase stability of the Bi-2201 phase indicates a phase boundary. The above experimental results lead to a "model" for the formation of Bi-2223 well connected grain groups with grain colonies and $Bi_2(Sr_{1.6}Ca_{0.4})CuO_6$ – Cu_2O – Cu-free secondary phases included, since this type of microstructure seems to favour high Ic values in the tapes. Firstly, the precursor powder has to be kept in the same stoichiometry $Bi_{1.8}Pb_{0.3}Sr_{1.9}Ca_{2.1}Cu_{3.1}O_x$ to avoid secondary phase formation by the use of any other powder. Among the secondary phases in the powder must be $(Ca,Sr)_2PbO_4$ and Cu_2O. The ideal heat treatment atmosphere is 7.5% partial pressure O_2 since in higher partial pressures more Bi-2212 forms and there is less liquid phase. The heat treatment temperature lies between 822 °C and 847 °C since below 822 °C little or no Cu_2O, $Bi_2(Sr_{1.6}Ca_{0.4})CuO_6$ or Cu-free phase forms. The mechanisms through which the Bi-2223 grains align are most likely to be the following (figure 2.9):

a. Capillary force attracts two adjacent grains that are wetted by the liquid and therefore aligns them
b. A c-axis textured growth of the Bi-2223 grains on pre-existing Bi-2223 grains

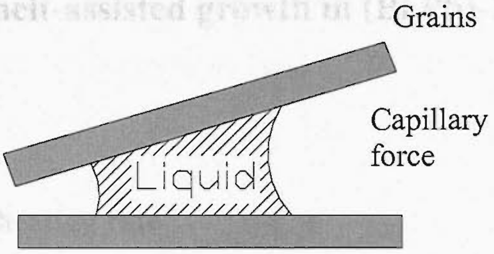

Two adjacent grains wetted by the liquid are attracted by capillary forces

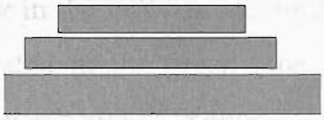

Bi-2223 grains grow on pre-existing Bi-2223 templates through a nucleation and growth mechanism

Figure 2.9. *Schematic representation of possible texturing mechanisms in Ag/Bi-2223 tapes*

The merging of the grain boundaries, solid-solid or solid-liquid-solid will depend on the contact angle and the heat treatment temperature. The model consists of the following steps: The precursor powder is "green" Bi-2212 compact with $(Ca,Sr)_2PbO_4$ and Cu_2O. During the heating, melting of $(Ca,Sr)_2PbO_4$ first and then Cu_2O occurs that forms liquid between 600 °C to 800 °C. The wetting will depend on the heating rate. Next, partial melting of the Bi-2212 phase occurs and then rapid growth of the Bi-2223 from Bi-2212 template at temperature >822 °C and 7.5% partial pressure O_2 atmosphere, whilst porosity occurs. The grains will align by capillary forces with the presence of liquid phase. The volume of liquid phase will depend on the temperature and the partial pressure. Alignment and local densification can happen simultaneously by the action of capillary forces. Bi-2223 grains form through nucleation and growth on Bi-2223 templates and grain colonies are formed. The grain boundaries merge thus forming a current path, but it is possible to form trapped pockets of liquid. At higher temperatures more grain boundaries form with lower grain boundary angles as a result of larger volume of liquid phase. Annealing at low temperatures as 805 °C in 7.5% p.p. O_2 causes the reaction: Cu_2O, $Bi_2(Sr_{1.6}Ca_{0.4})CuO_6$ + Cu-free phase → Bi-2223 + Bi-2212. Cu_2O and Cu-free phase can exist due to the long diffusion distance in the dense and rigid microstructure, thus resulting in Bi-2212 phase formation in the place of Bi-2223. Blocks in the current path can form with the formation of Cu_2O, $Bi_2(Sr_{1.6}Ca_{0.4})CuO_6$ and Cu-free phases from trapped pockets of liquid phase.

2.8. Promotion of melt-assisted growth in (Bi,Pb)-2223 tapes utilizing rapid heating rates

2.8.1. The effect of the heating rate

The heating rate is a parameter in the OPIT processing that can influence the amount of liquid phase that is generated in the green tape during heating upon the heat treatment temperature. Recent work by E A Young [71] has shown that the Ic improves with increasing heating rate in the first heat treatment at a heat treatment temperature of 832 °C whilst for heat treatment temperature below 822 °C there is no improvement of the Ic with the heating rate. The high temperature range is associated with the nucleation and growth of the Bi-2223. The lower temperature range <822 °C is associated with the model of intercalation growth of the Bi-2223, which produces little secondary phases but low Ic. At lower temperatures where there is little liquid phase formation and no formation of $Bi_2(Sr_{1.6}Ca_{0.4})CuO_6$ and Cu_2O, the heating rate is not beneficiary. One of the models for Bi-2223 growth suggests that this phase forms

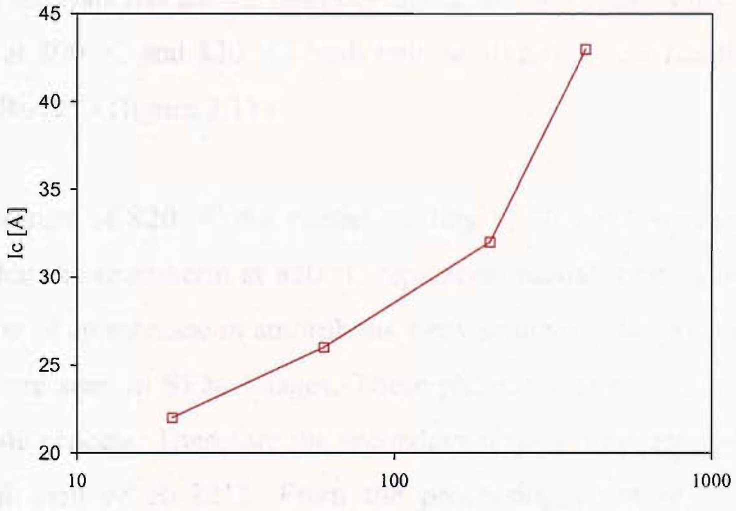

Figure 2.10. *The Ic was found to increase with the 1st heat treatment heating rate* [64]

through a diffusion of Ca and Cu ions into the Bi-2212 phase. The work of Luo et al has shown that the reaction kinetics are different at lower temperatures. In the low temperature range perhaps the intercalation is the dominant formation mechanism, and therefore a low heating rate is beneficial due to the time that is given to the Bi-2212 grains to mature from their precursor state through the formation of the (Bi,Pb)-2212 phase. The enhancement of the transport properties with the increasing heating rate (figure 2.10) was accompanied by a reduction in the amount and size of secondary phases $Bi_2(Sr_{1.6}Ca_{0.4})CuO_6$ and Cu_2O which was thought to be due to an increased volume of liquid phase. Since these secondary phases are linked to the volume of liquid phase and cannot be less at higher volumes of liquid caused by higher heating rate, it seems that they are formed perhaps from trapped pockets of melt thus the high heating rate leads to improved distribution of the liquid phase.

2.8.2. The effect of transients in the tape microstructure

The XRD analysis of tapes heated for prolonged periods show two distinct secondary phase formation regions [70]: between 800 °C and 820 °C and above 820 °C. Above the temperature of 820 °C there is substantial secondary phase formation with the phases Bi-2201 and Bi-211 included, but in the range 800 °C and 820 °C little secondary phase formation was observed without the previously mentioned phases present. DTA analysis has shown direct evidence for two phase transitions with onset temperatures at 800 °C and 820 °C, both representing transient reaction routs for the formation of Bi-2223 (figure 2.11).

At the temperature of 820 °C the partial melting of Bi-2212 appears to occur. The explanation that the endotherm at 820 °C represents partial melting lies in the fact of the observation of an increase in amorphous x-ray scattering, but also Bi-2201 and Bi-211 phases were seen in SEM images. These phases cannot form from the Bi-2212 via a solid state process. Therefore the secondary phases must precipitate from liquid that is partial melt of Bi-2212. From the processing point of view it has been established that there is not secondary phase formation in the first endotherm region 800 °C – 820 °C which together with the observation of the smaller endotherm peak height they present evidence for quite a different reaction pathway to Bi-2223 formation.

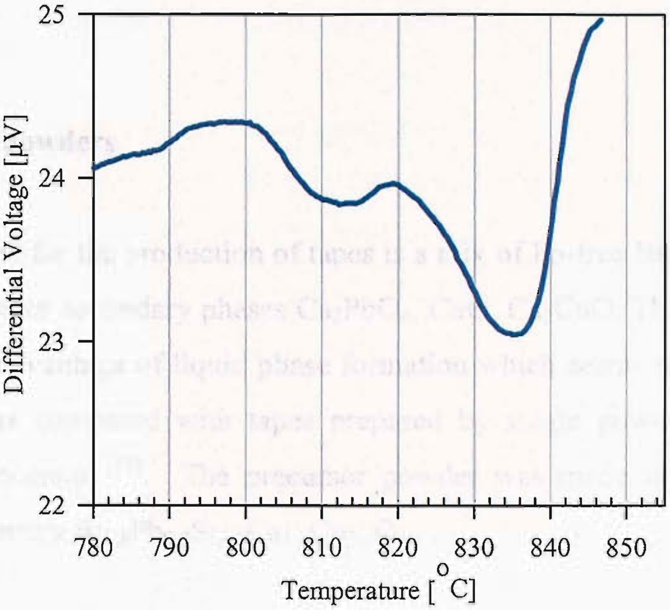

Figure 2.11. *DTA for green tape at 60 °C/h shows two transients in the temperature range 800 °C to 832 °C* [74]

The endotherm shows that there is a transient formation of an intermediate phase and the XRD indicates rapid Bi-2223 formation. The phase formation division at 820 °C also divides the reaction kinetics [74]. This splitting of the temperature region utilised to grow Bi-2223 could perhaps explain why some authors have observed a solid state formation mechanism for the Bi-2223 growth, whilst some others have observed melt-assisted growth [76], [77]-[79]. Therefore a link has been established between the two transients and the long term secondary phase formation.

If there is any way to control the melting then it should mean that better superconductor microstructure will occur, if this concept is linked to the favourable role that the liquid phase plays in the microstructure of the final tape, with a corresponding enhancement of the transport properties. This well established relationship has framed this discussion for the material science of the tapes. As a conclusion, it could be said that for completeness of these results, it is left to investigate whether the observed endotherms are the cause of the increased transport current in the context of melt- assisted growth of Bi-2223. The following experimental work is focusing towards this direction.

Experimental

2.8.3. Precursor powders

The precursor used for the production of tapes is a mix of Pb-free Bi-2212 or (Pb,Bi)-2212 phase and other secondary phases Ca_2PbO_4, CuO, Ca_2CuO. The use of a mix of powders has the advantage of liquid phase formation which seems to result in higher Jc in the tapes as compared with tapes prepared by single powder (fully reacted (Pb,Bi)-2223) precursor [72]. The precursor powder was made in Merck and has nominal stoichiometry $Bi_{1.8}Pb_{0.3}Sr_{1.9}Ca_{2.1}Cu_{3.1}O_x$.

2.8.4. Sample preparation

19-filament pure Ag (tape A) and 37-filament AgMg alloy (tape B) multifilamentary tape was made by the Oxide Powder in Tube (OPIT) process using Merck powder of nominal stoichiometry $Bi_{1.8}Pb_{0.3}Sr_{1.9}Ca_{2.1}Cu_{3.1}O_x$. Samples were processed with two heat treatments in 7.5% O_2 and one intermediate rolling of 10% reduction in tape thickness. Different heating rates between 20 °C/h and 800 °C/h were used in the first heat treatment. The accuracy of the temperature control was tested with a thermocouple at the sample's position prior to the heat treatments. No temperature overshoot was observed for the entire range of heating rates used. The 1st heat treatment time was 10 hours at 832 °C and the cooling rate 60 °C/h. The 2nd heat treatment was at 826 °C for 60 hours, followed by a slow cooling (1 °C/h) down to 800 °C, then a secondary heat treatment for 30 hours and finally cooled at 60 °C/h.

To explore the effect of the 1st heat treatment heating rate over well-defined temperature ranges, the heating rate was varied in the temperature range 800 °C to 832 °C whilst between 700 °C to 800 °C the heating rate was 100 °C/h. For another sample batch the heating rate was varied in the temperature range 700 °C to 800 °C whilst between 800 °C and 832 °C the heating rate was 400 °C/h.

2.8.5. Differential thermal analysis (DTA) measurements

DTA measurements were carried out on green tape with different heating rates (30, 45, 60, 120 °C/h) in a flowing 7.5% p.p. O_2 atmosphere. The measurements were carried out using a Stanton Redcroft DTA/TG thermal analyser (figure 2.12) with a platinum stage. The tapes were bent into a harmonica shape (mass ~ 0.25 gr), laid directly on the sample stage, and a flat silver tape was used for the reference.

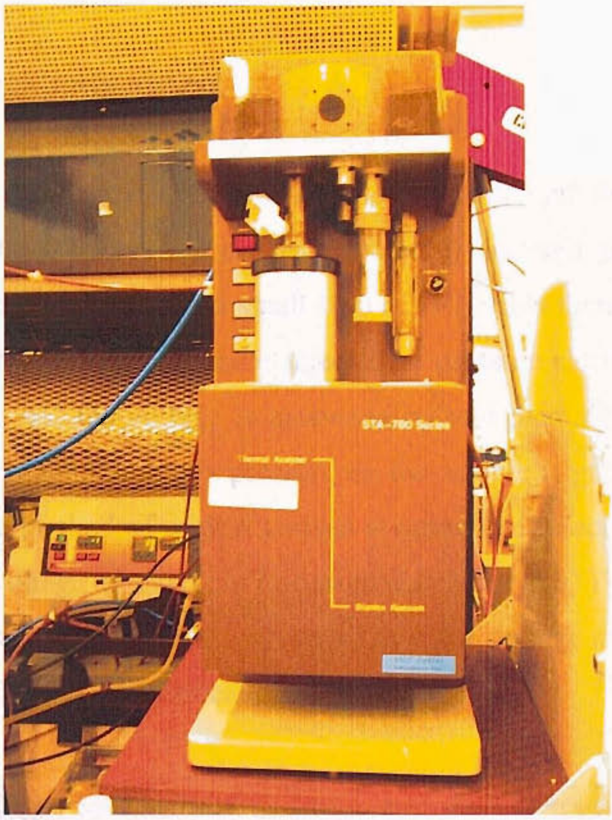

Figure 2.12. *The Stanton Redcroft Differential Thermal Analyzer*

2.8.6. XRD and SEM analysis

The tapes are subjected to X-ray examination in order to identify the chemical phase composition of the superconducting core qualitatively and quantitatively. In order to expose the superconducting core in the X-ray radiation, the silver alloy has to be removed. This is done by placing the sample in a solution of NH_3-H_2O_2 (10 ml distilled water, 30 ml NH_3 and 30 ml H_2O_2). The silver alloy is dissolved and removed completely from the sample in 5-10 minutes. Caution has to be taken when handling the solution because it causes burns to skin and eyes and is harmful if it is inhaled. The procedure of removal of the sheath by this way is called etching. For XRD analysis, tapes were quenched by a rapid DTA furnace cool at ~ 3000 °C/h and then etched. Also transverse cross sections of tape were polished for SEM imaging.

2.8.7. Transport property measurements

The transport properties measurements include:

a) Critical current measurement

The critical current is measured in a tape sample of length 5 cm that is immersed in a liquid nitrogen bath (77 K at atmospheric pressure) and self magnetic field. The sample is glued with GE varnish in a small strip of G-10 (low thermal contraction) for mechanical support. Electrical current is injected by pressure electrical contacts at the ends of the sample and the voltage is measured by two pairs of successive voltage taps that make electrical contact by pressure on the sample (figure 2.13). This is the standard four-probe method of critical current measurement. Each one of the voltage taps measures the voltage of a sample's section of length 1 cm. The critical current is defined by the electric field criterion, where a rise in the voltage at 1 μV/cm is chosen as the voltage threshold for the critical current determination.

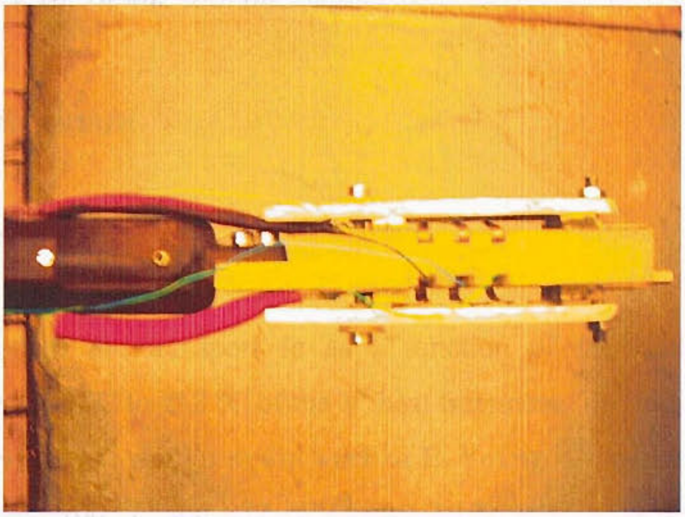

Figure 2.13. *Sample holder for the Ic and Ic(B) measurement*

b) Magnetic field dependence of the critical current

The dependence of the critical current to applied external magnetic field is measured in the rig used for the critical current measurement (figure 2.14). The field is provided by the electro-magnet that gives maximum magnetic field value of 0.5 Tesla. The rig has the facility to rotate the sample around the direction of the tape a-b plane by 360°, which changes the orientation of the applied magnetic field with respect to the direction of the a-b plane and gives the ability to measure the dependence of the Ic with the magnetic field orientated in different angles with respect to the a-b plane.

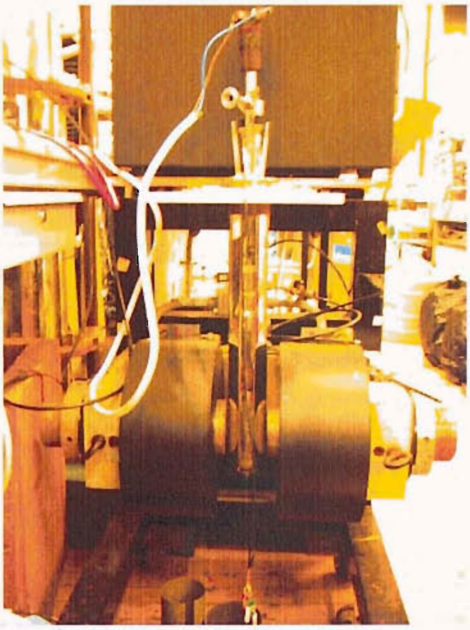

Figure 2.14. *Dewar with the magnet for Ic and Ic(B) measurement*

Results and discussion

2.8.8. Transport current

Figure 2.15 displays the transport Ic as a function of the heating rate in the temperature range 800 °C to 832 °C of the 1st heat treatment. The observed increase in Ic with the heating rate is similar to the work of E. Young [74], where the heating rate was varied between 700 °C and 832 °C (figure 2.17). Also shown in figure 2.16 is how there is little change in Ic when the heating rate is varied between 700 °C and 800 °C. Evidently the temperature range over which the heating rate can be crucial is that at which Bi-2223 forms. This is similar to results in other transient liquid systems such as Fe-Al, where faster heating rates in the vicinity of the melt were shown to improve the density, which would in the case of (Bi,Pb)2223 tapes correspond to increased Jc. In a transient liquid system densification is a result of an increased volume of liquid phase which a slow heating rate can totally suppress. Indeed this is the case for (Bi,Pb)2223 tapes as the lowest Ic results are for low heating rates from 700 °C to 832 °C.

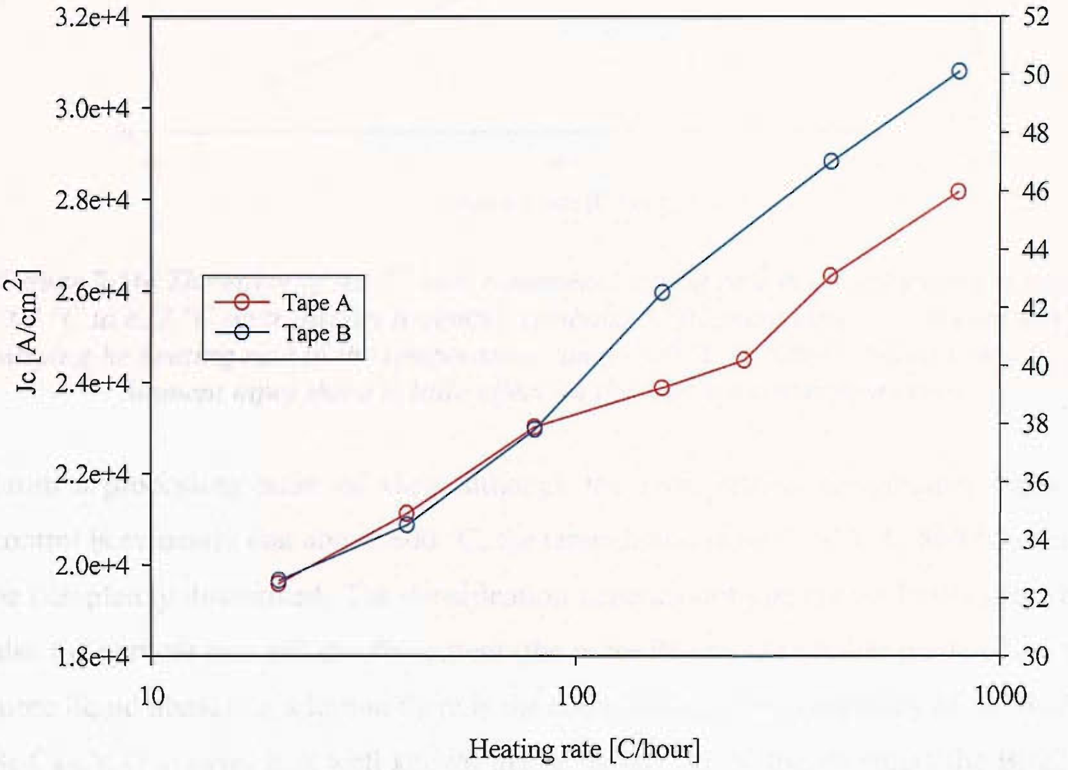

Figure 2.15. *The tape transport properties are improved with high heating rate in the temperature range 800 °C to 832 °C of the 1st heat treatment, almost a 50% increase between 20 °C/h and 800 °C/h*

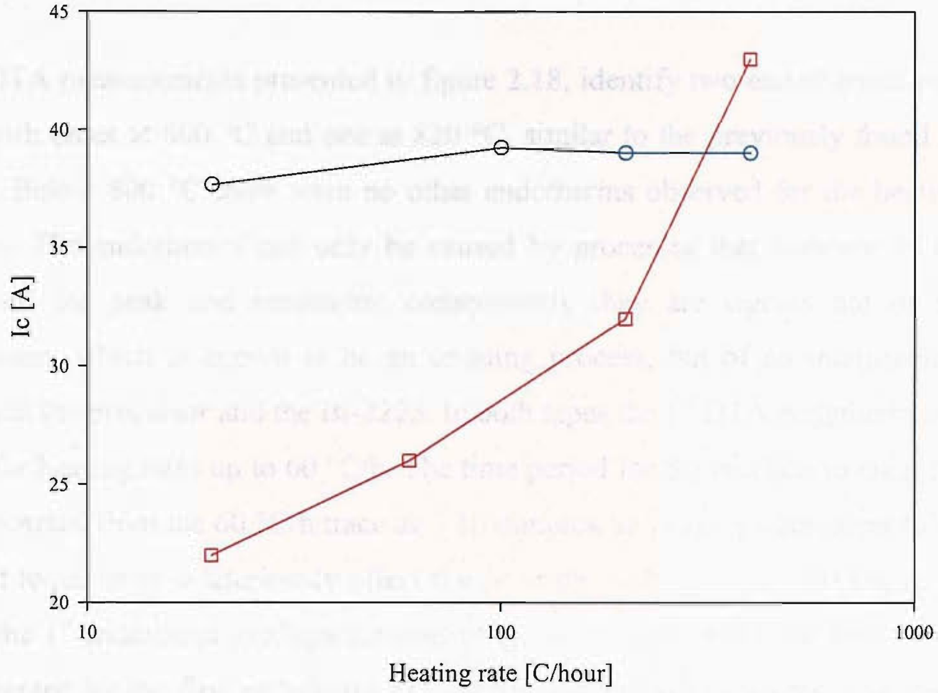

Figure 2.16. *The effect of the 1st heat treatment heating rate in the temperature range 700 °C to 832 °C on transport Ic (empty symbols, 37 filament tape [68]). In contrast by varying he heating rate in the temperature range 700 °C to 800 °C (filled symbols, 19 filament tape) there is little effect on the tape transport properties.*

From a processing point of view although the most critical temperature range to control is evidently that above 800 °C, the temperature range 700 °C to 800 °C cannot be completely discounted. The densification depends not just on the heating rate but also the particle size and the Pb content (the more Pb and the smaller particle size the more liquid phase). In addition there is the complicated phase chemistry of the Bi-Pb-Sr-Ca-Cu-O system. It is well known that at about 780 °C the Pb enters the Bi-2212 precursor phase and that the amount of Pb in the Bi-2212 precursor affects the reaction kinetics and subsequently the tape Jc. The precursor powders used in these studies already contain a large percentage of (Bi,Pb)-2212 and so do not need a period of time at 780 °C to "lead" the Bi-2212 phase, however in other powders with less (Bi,Pb)-2212 this may not be the case and ramping slowly below 800 °C may effect the Jc in a positive sense. However growth of the Bi-2212 grain size on this temperature region may suppress the formation of liquid phase.

2.8.9. Transient reactions in the range 800 °C – 832 °C

The DTA measurements presented in figure 2.18, identify two endothermic reactions, one with onset at 800 °C and one at 820 °C, similar to the previously found in other work. Below 800 °C there were no other endotherms observed for the heating rates shown. The endotherms can only be caused by processes that compete in the time between the peak and minimum; consequently they are signals not of Bi-2223 formation, which is known to be an ongoing process, but of an intermediate state between the precursor and the Bi-2223. In both tapes the 1st DTA endotherm is clearly seen for heating rates up to 60 °C/h. The time period for the reaction to take place can be estimated from the 60 °C/h trace as ~ 10 minutes, so roughly equivalent to the time period required to deleteriously affect the Jc in the heat treatment. At higher heating rates the 1st endotherm overlaps the start of the next endotherm; therefore the reaction represented by the first endotherm has insufficient time to complete. The magnitude of the endotherms increases with the heating rate, as would be expected, but in addition an enhanced 2nd endotherm signal is observed when the 1st endotherm is incomplete, i.e. it seems that by heating fast, the system bypasses the 1st reaction and consequently the 2nd reaction is favoured. This data can be interpreted as an enhancement volume of melt formation with increasing heating rate. The DTA traces are different for the two tapes: for tape B, the first endotherm completes more rapidly, indicating faster reaction kinetics, the onset temperature of the second endotherm is at a lower temperature and the first endotherm magnitude is lower (relative to the second endotherm). The lower endotherm onset temperatures show tape B to be more reactive than tape A, consequently more melt is formed and a larger second endotherm is seen. The greater reactivity is probably due to the larger number filaments which gives a larger area of contact with the Ag inner sheath. The core density and the particle size may also be different depending on the outer sheath material and this would have an effect on the reactivity. During the OPIT mechanical drawing and rolling the stronger alloy outer sheath will result in a denser core, it may also result in a reduced particle size to due shear forces breaking-up the precursor. The higher density may be counteractive to the melt processing as it restricts rearrangement of the particles. However small particles can rearrange more easily, and if the particle size is reduced the increased surface area will increase the precursor reactivity.

The DTA demonstrates that increases in the heating rate enhance the partial melt at 820 °C which is likely to be a direct result of bypassing the transitory reaction at 800 °C. The material analysis through SEM and XRD measurements that follows, aims to understand better the effect of the endotherms on the tape microstructure.

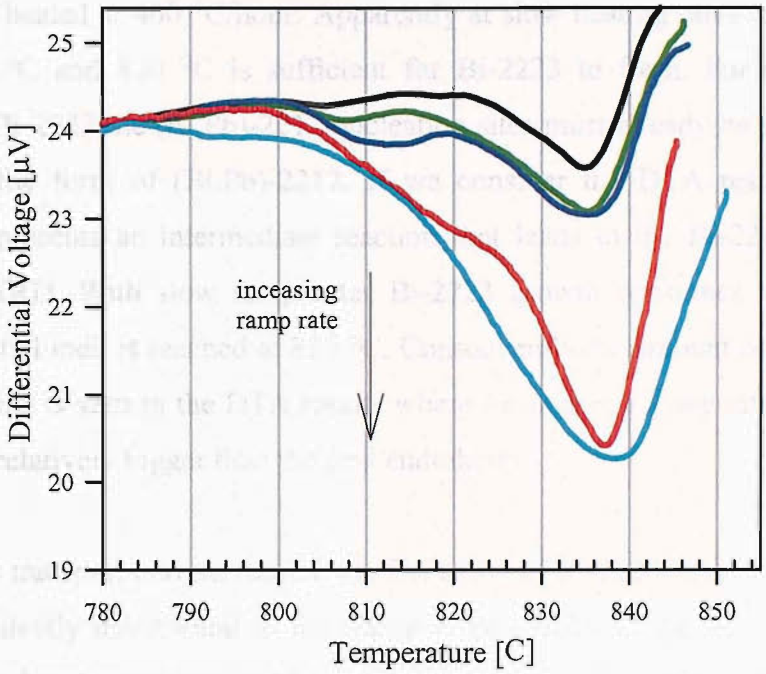

(a) DTA for tape A with heating rates 30, 45, 60, 120, 200 C/h

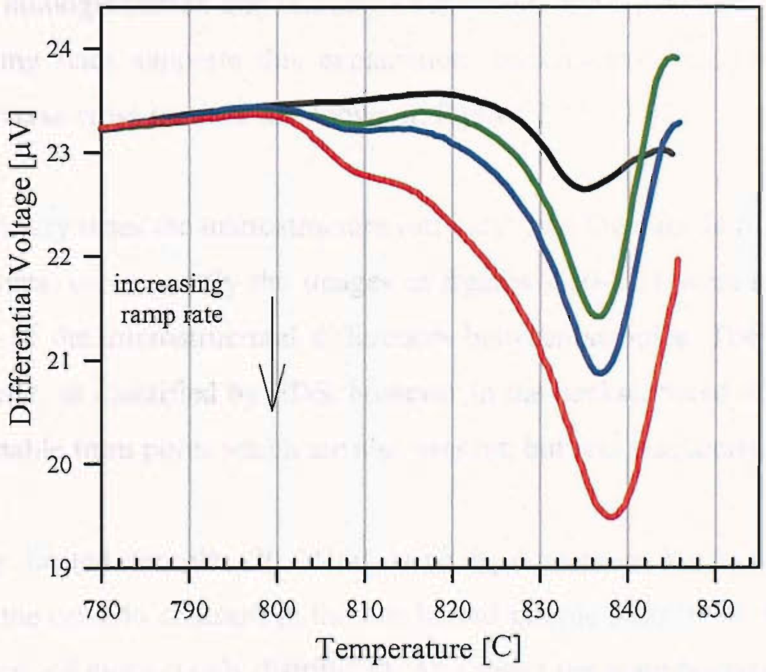

(b) DTA for tape B with heating rates 30, 45, 60, 120 C/h

***Figure 2.18.** Differential thermal analysis curves*

2.8.10. Materials analysis

XRD data on samples heated to 832 °C and then fast cooled are presented in figure 2.19. In the 100 °C/hour sample there is Bi-2223 phase, but there is none discernable in the sample heated at 400 °C/hour. Apparently at slow heating rates the time spent between 800 °C and 820 °C is sufficient for Bi-2223 to form. For such a rapid formation of Bi-2223 the (Bi,Pb)-2212 nucleation sites must already be present in the precursor in the form of (Bi,Pb)-2212. If we consider the DTA results, the first endotherm represents an intermediate reaction that leads to the Bi-2223 formation seen in the XRD. With slow ramp rates Bi-2223 growth consumes the precursor before the partial melt is reached at 820 °C. Consequently the amount of liquid phase is reduced – this is seen in the DTA results where for higher heating rates the second endotherm is relatively bigger than the first endotherm.

In view of the transport current results, the formation of Bi-2223 between 800 °C and 820 °C is evidently detrimental to the transport properties of the tape. This can be explained as a direct consequence of a reduced volume of liquid phase which inhibits ion transport, homogenisation and rearrangement in the melt. The microstructure for the high heating rates supports this explanation: backscattered electron images of polished transverse cross sections are shown in figures 2.20 – 2.21.

In multifilamentary tapes the microstructure can vary from the outside filaments to the internal filaments, consequently the images in figures 2.20-2.21 were selected to be representative of the microstructural differences between samples. The dark patches are mostly Cu_2O, as identified by EDS, however in the backscattered image they are not distinguishable from pores which are also present, but less frequently.

In the slowly heated sample (20 °C/h) large agglomerates are inhomogenously distributed in the core. In contrast, in the fast heated sample (400 °C/h) the secondary phases are finer and more evenly distributed. As a result the grain boundary tilt angles are reduced and there is less impedance to the current path. As a consequence of the reduction in secondary phases it is also likely that there is a larger volume fraction of Bi2223 phase and less residual Bi-2212. The improved microstructure can be explained by a larger volume of liquid phase. In a larger volume of melt, fast diffusion of ingredients to the Bi-2223 growth front ensures homogenisation of the precursor.

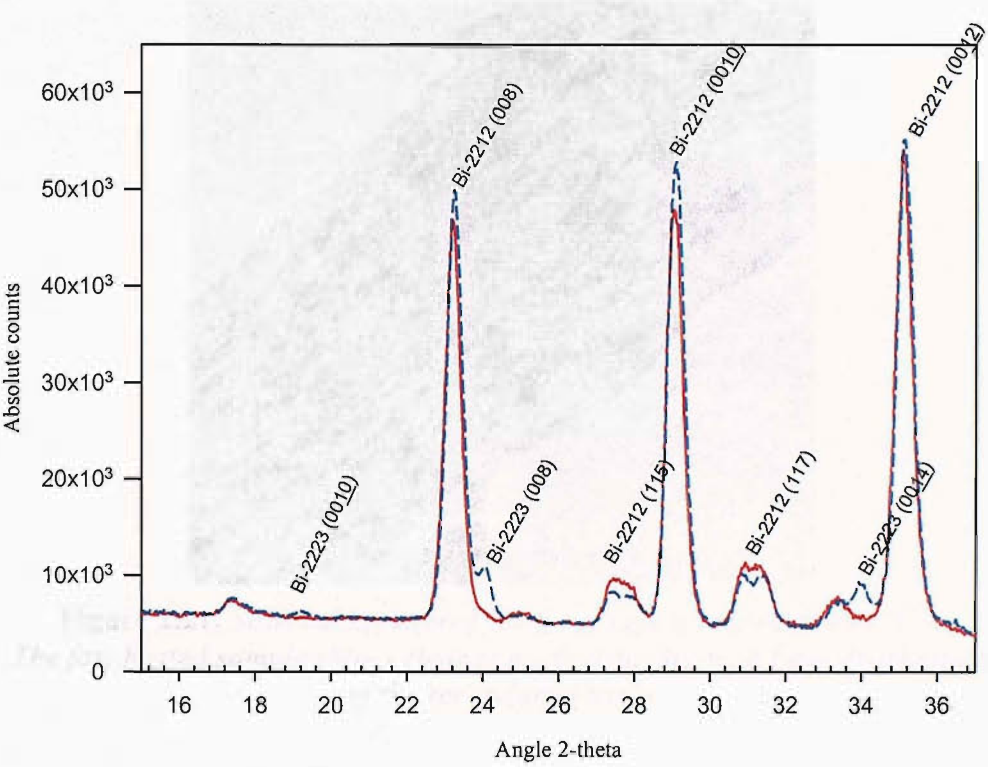

Figure 2.19. *Samples ramped to 832 °C then rapidly cooled show that for slow ramp rates, 100 °C/h, (blue dashed line) Bi-2223 has already formed, but for high heating rates, 400 °C/h, (red continuous line), the formation of Bi-2223 is suppressed.*

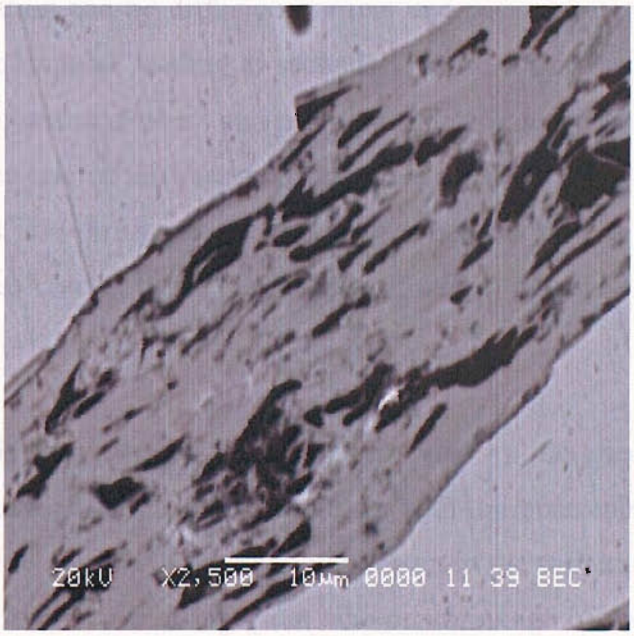

Figure 2.20. *SEM backscattered image of tape A heated at 20 °C/h*

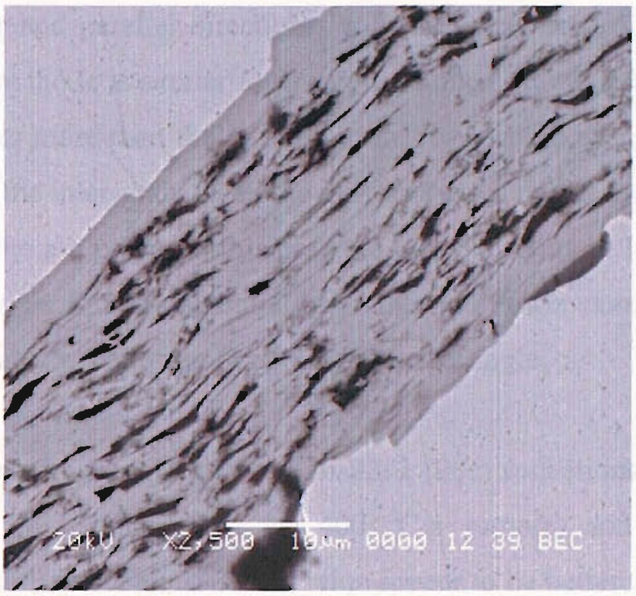

Figure 2.21. *SEM backscattered image of tape A heated at 400 °C/h. The fast heated sample shows cleaner microstructure with finer distribution of the secondary phases*

In the Bi-2223 precursor there is a physical separation of (Bi,Pb)-2212 from the Ca and Cu required for Bi-2223 formation. Without rapid homogenisation secondary phase formation can initiate in Ca and Cu rich regions. Localised formation of Bi-2223 and densification can be diffusion barriers and consequently pockets of liquid phases can become trapped, leading to secondary phase formation. In dry regions of the core there is no rearrangement and pores can remain despite long heat treatment times. The common use of an intermediate rolling stage in the OPIT processing of (Bi,Pb)-2223 tapes is a direct consequence of trapped pockets of liquid phase. The formation of micro-cracks from the rolling provides pathways for the melt to penetrate and react with isolated Bi-2212 phase.

The partial melt is suppressed at low heating rates as the precursor ingredients necessary for the partial melt are consumed. In addition coarsening of the Bi-2212 grains during the slow ramp will have a direct impact in the shrinkage of the compact. The detrimental effect of increasing grain size on shrinkage of the compact is well documented in other systems.

Figure 2.22 shows how the field dependence of the transport Ic is improved for a heating rate of 400 °C/h by about 20% over the 20 °C/h sample. Improvements are in both perpendicular and parallel directions, with the exception of above 400 mT in parallel field, where the Ic is similar for the two samples. At moderate fields the inter-grain Ic deteriorates more than the intra-grain Ic, so it would seem the rapid heating rate had improved the inter-grain Ic. In the railway switch model the weakest links are tilt boundaries in the a-b plane. In this case the improvements in Ic(B) would not be attributed to a stronger pinning potential but rather to a lower number of weak links, which can also be attributed to smaller grain boundary angle.

It is noticeable from figure 2.19 that the Bi-2212 (00c) reflections are larger for the 100 °C/hour sample (compared to the 400 °C/h sample) and the (115), (117) reflections are diminished. The Bi-2212 grains appear to be better textured in the 100 °C/h sample, however in the final tape the Bi-2223 grain alignment is better in the fast heated samples. It is well known that the final Bi-2223 grain alignment is much superior to the Bi-2212 precursor yet there has not been a model proposed for the alignment mechanism. One possible alignment mechanism is the rearrangement of the grains in the partial melt. It should be mentioned that the argument for rearrangement in a melt does not exclude existing models for Bi-2223 growth: for example melt precipitation; or nucleation and growth on the Bi-2212 precursor grain. Rearrangement in a liquid phase explains how the final grain orientation is improved in the fast heated sample. This is a physical process that occurs due to capillary forces drawing the Bi-2223 and Bi-2212 grains together and is aided by solution reprecipitation. Pores in the precursor are removed by penetration of the melt and shrinkage of the compact. The long order alignment may be assisted by the Ag interface and shrinkage, which both mechanically force the grains in the core to flatten and align. Diffusional homogenisation due to the liquid phase reduces the formation of isolated non stoichiometric pockets that lead to secondary phase formation. With smaller and fewer secondary phases there are less physical barriers to the alignment of the Bi-2223 grains.

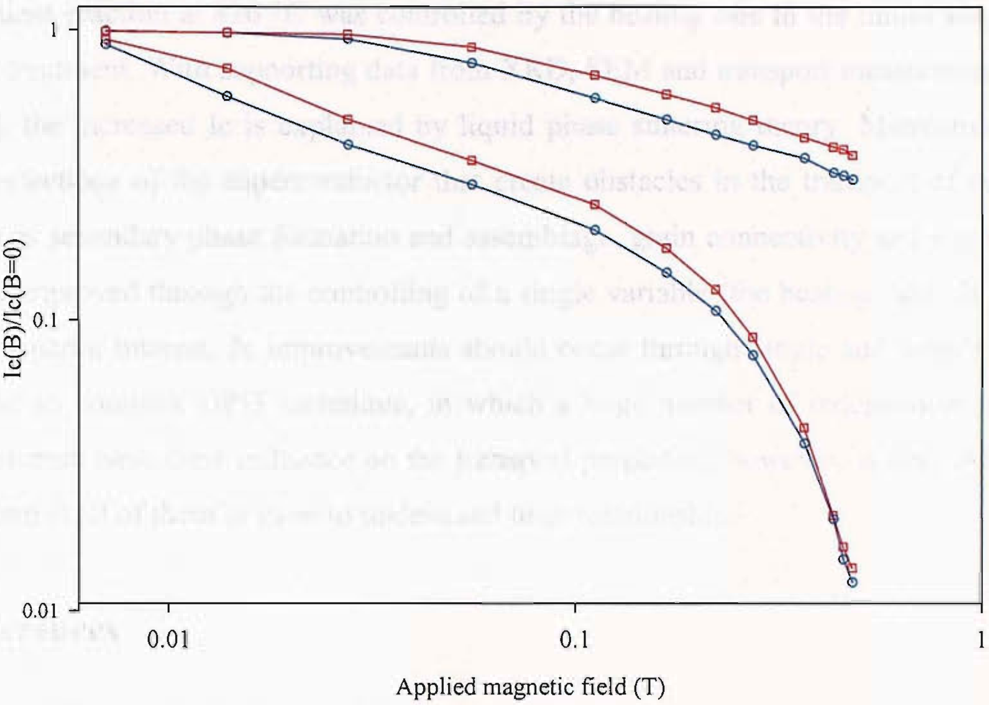

Figure 2.22. *Rapid heating rates in the temperature range 800 °C to 832 °C of the 1st heat treatment improve the magnetic field dependence of the Ic. Square symbols: 20 °C/h, round symbols: 400 °C/h*

2.9. Summary and conclusion

A review in the OPIT processing route for fabrication of Ag/(Bi,Pb)-2223 HTS tapes was presented. The recent developments in the material science of the tapes have yielded that high tape transport properties can only be obtained by improving the OPIT process in order to achieve simultaneously: a) smaller misalignment angles between neighbouring grains, b) high quality grain boundaries and c) a lower amount of voids or reduced porosity. It is commonly accepted that the formation of (Bi,Pb)-2223 inside the Ag sheath involves the presence of a transient liquid, the properties of which play a positive role in the development of a superconductor microstructure able to carry high currents. The question was left open whether new reaction paths can be found involving larger amounts of liquid phase. The work focused towards this direction. High temperature superconducting Ag/(Bi,Pb)-2223 composite tapes were fabricated through the OPIT processing route. Through extensive investigations over a long period of study, two transients in the first moments of Bi-2223 formation were observed by DTA for multifilamentary tape. A correlation between an increased Ic and an enhanced reaction at 820 °C has been observed in Ag/(Bi,Pb)-2223 tapes. The transient reaction at 820 °C was controlled by the heating rate in the initial stages of heat treatment. With supporting data from XRD, SEM and transport measurements in field, the increased Ic is explained by liquid phase sintering theory. Microstructural imperfections of the superconductor that create obstacles in the transport of current such as secondary phase formation and assemblage, grain connectivity and alignment were improved through the controlling of a single variable (the heating rate). In view of industrial interest, Jc improvements should occur through single and simple steps in the so complex OPIT technique, in which a huge number of independent or not parameters have their influence on the transport properties, however, is very difficult to control all of them or even to understand their relationships.

References

[1] Martini L, ***Supercond. Sci. Technol.,*** 1998, 11 231-237

[2] Ballarino A, ***IEEE Trans. Appl. Supercond.***, 2002, 12, 1275-1280

[3] J. G. Bednorz and K. A. Muller, ***Z. Phys. B*** 64, 189 (1986)

[4] M. K. Wu et al, ***Phys. Rev. Lett.*** 58, 908 (1987)

[5] H. Maeda et al, ***Jpn. J. Appl. Phys.*** 27:L209 (1988)

[6] C. Michel et al, ***Z. Phys. B*** 68:421 (1987)

[7] J. Akimitsu et al, ***Jpn. J. Appl. Phys.*** 26:L2080 (1987)

[8] W. Zhy et al, ***Appl. Phys. Letters*** 61 (6), 1992, pg. 717

[9] Y. Idemoto et al, ***Jpn. J. Appl. Phys***. 29, no. 12, (1990), pp. 2729-2731

[10] R. Ramesh et al, ***J. Mat. Res.*** 6 (1991), pg. 278

[11] Takano M. et al, ***Jpn. J. Appl. Phys***. 27, 6 L1041-1043

[12] B. W. Statt et al, Physica C 157 (1988) 251

[13] M. Takano et al, Jpn. J. Appl. Phys. 27 (1988) L1041

[14] M. Mizuno et al, Jpn. J. Appl. Phys. 27 (1988) L1225

[15] P. Strobel et al, Physica C 201 (1992) 27

[16] J.L. MacManus-Driscoll et al, ***J. Am. Ceram. Soc***. 77 (1994) 2305-2313

[1] Z. Yi et al, ***Physica C*** 254 (1995) 193-200

[14] Y. Yamada et al, ***Supercond. Sci. Technol.*** 4 (1991) 165

[15] Bian W. et al, ***Physica C*** 248 (1995) 119-126

[16] Wang M. et al, ***Physica C*** 210 (1993) 423-416

[17] Luo J. et al, ***Appl. Supercond.*** 1 (1993) 101-107

[18] Morgan P. et al, ***Physica C***191 (1992) 179-184

[19] Grivel J et al, ***Supercond. Sci. Tech.*** 9 (1996) 555-564

[20] Morgan P. et al, ***Physica C*** 176 (1991) 279-284

[21] Hu Q. et al, ***Physica C*** 250 (1995) 7-14

[22] G. Grasso et al, ***IEEE Trans. Appl. Supercond.,*** 5, No. 2 (1995)

[23] K. Sato et al, ***IEEE Trans. Magn.*** 27 (1991) 1231

[24] Gao W. et al, ***Physica C,*** 1991, vol. 181, pp. 105-120

[25] Madhavrao R et al, ***Journal of Materials Science***, 1990, vol. 25, pp. 2349-2352

[26] Motowildo L. R. et al, ***Appl. Phys. Lett.*** (1991), vol. 59, no. 6, pp. 736-738

[27] Kohno O. et al, ***Japn. J. Appl. Phys.*** (1987), vol. 26, part 1, no. 10, pp. 1653-1656

[28] S. Jin et al, ***Appl. Phys. Lett.*** 52, 1682 (1988)

[29] R. Flukiger et al, ***IEEE Trans. Magn.*** 27, 1258 (1991)

[30] Y. Yamada et al, ***Supercond. Sci. Technol.*** 4, pg. 165 (1991)

[31] Y. Feng et al, ***Appl. Phys. Lett.*** 62, 1553 (1993)

[32] Y. Feng et al, ***Appl. Phys. Lett.*** 62, 1553 (1993)

[33] P. E. D. Morgan et al, ***Physica C*** 191, 179 (1992)

[34] Morgan P. et al, ***Physica C*** 191 (1992) 179-184

[35] Tasaki K. et al, ***16th ICEC Conference***, Kitakyushu, Japan, 20-24, May 1996

[36] Yamada Y. et al, ***Advances in Superconductivity V***, 1992, ***Proceedings of the 5th ISS '92,*** Kobe, Edited by Bando Y. and Yamauchi H, pp. 717-720

[37] W. Goldacker et al, ***IEEE Trans. Appl. Supercond.*** 5, No. 2 (1995) 1834-1837

[38] D. F. Lee et al, ***Supercond. Sci. Technol.*** 10 (1997) 702-711

[39] Schey J A, ***"Metal Deformation Process, Friction and Lubrication",*** Marcel Dekker Inc, New York, 1970, 23-47

[40] Altan T. et al, ***"Metal forming, fundamentals and applications",*** American Society of Metals, 1083, ISBN 0-87170-167-7

[41] ASM International, ***"Metals Handbook 9th Edition, volume 14 Forming and Forging",*** ASM International Handbook Committee, USA

[42] Z. Han et al, ***Supercond. Sci. Technol.*** 10 (1997) 371-387

[43] Z. Han and T. Freltoft, ***Appl. Supercond.*** No. ¾, (1994), 201

[44] Korzekwa D. A. et al, 1994, ***Appl. Supercond.*** 2 261

[45] Kanna M. et al, 1995, ***IEEE Trans. Appl. Supercond.*** AS-5 1279

[46] Wolf B. et al, 1996, ***Supercond. Sci. Technol.*** 9 589

[47] Wenk H. R. and Phillips D. S. 1992 ***Physica C*** 200 105

[48] Zeimetz B., et al, 1995 ***Physica C*** 250 170

[49] Hu Q. Y., 1996 ***Appl. Supercond.*** 4 17

[50] Z. Han et al, ***Appl. Supercond.*** No ¾ (1994), 201

[51] B. Hensel et al Physica C 205 (1993) 329

[52] B. Hensel et al, Phys. Rev. B. 51 (1995) 15456

[53] Dimos et al, Phys. Rev. B 41 (1990) 4038

[54] T. Amrein et al Phys. Rev. B 51 (1995) 6792

[57] Hong Z. et al, ***Supercond. Sci. Technol.*** 9 (1996) 303-309

[58] Ashworth S. and Glowacki B. ***Physica C*** 226 (1994) 159-164

[59] Sun Y. et al, ***Phys. Rev. B*** 51 (1995) 519-522

[60] Hensel B. et al, ***Phys. Rev. B*** 51 (1995) 15456-15473

[61] Dou S. and Liu H. ***Supercond. Sci. Technol.*** 6 (1993) 297-314

[62] Safar H., ***Appl. Phys. Lett.*** (1995) 67, pg. 130

[63] Hensel B. et al, ***IEEE Trans. Appl. Supercond.*** 7 (2): 2030-2033 Part 2 Jun. 1997

[64] E A Young, ***PhD Thesis***, University of Southampton, 2002

[65] Chen Y L et al, J. Am. Ceram. Soc. 75 [5] 1160-1166 (1992)

[66] Poulsen H. F. et al, Physica C 315 (1999) 254-262

[67] Kim W. et al, Supercond. Sci. Technol. 12, (1999) 97-101]

[68] Grindatto et al, Physica C 298 (1998) 41-48

[69] Wang et al, IEEE Trans. Appl. Supercond. Vol. 7, no. 2, June 1997

[70] E A Young et al, IEEE Trans. Appl. Supercond., vol. 11, no. 1, March 2001, 2979

[71] Young, E.A.; Yang, Y.; Lehmann, M.; Riddle, R.; Beduz, C., 2003 ***IEEE Trans. Appl. Supercond.,*** vol. 13, part III, pp. 2941

[72] Yamada Y. et al, ***Supercond. Sci. Technol.*** (1991), vol. 4, pp. 165-171

[73] J. Tundidor, ***PhD Thesis***, University of Southampton, 2003

[74] E A Young, S. Avgeros and Y. Yang, 2004, ***Supercond. Sci. Technol.*** 17 571-574

[75] Wong-Ng W et al, (1999) ***J. Matter. Res.*** 14 1695-1706

[76] Morgan et al, ***Physica C*** 176 279-284

[77] Grivel et al, ***Supercond. Sci. Technol.*** 9 (1996) 555-564

[78] Bian W et al, ***Physica C*** (1995) 248 118-126

[79] Grindatto D. P. et al, ***Physica C*** (1998) 298 41-48

[80] Bulaevskii L. N. et al, ***Phys. Rev. B*** 1992, vol. 45, no. 5, pp. 2545-2548

[81] Bulaevskii L. N. et al, ***Phys. Rev. B***, 1993, vol. 48, no. 18, pp. 13798-13816

Chapter 3

Design and construction of HTS current leads for superconducting particle accelerator magnets

3.1. Introduction

In particle accelerator systems, the current leads connect the superconducting LTS windings of the magnets to the room temperature power supplies. This is a source of heat leak that will cause significant loss of liquid helium. This heat can be thought of as the summation of two major terms:

a. Conduction heat from room temperature to cryogenic temperatures

$$Q_{cond} = \frac{A}{L} \int_{4.2K}^{300K} k(T)dT \qquad \textbf{\textit{(3.1)}}$$

b. Intrinsic resistive Joule heat generation in the conductor current lead

$$Q_{Joule} = I^2 \times R \qquad \textbf{\textit{(3.2)}}$$

It is proved to be beneficial to use some of the available refrigeration power in order to remove significant amounts of heat from the current leads before entering the cryogenic environment. The current leads for superconducting particle accelerator magnets must be designed to operate according to the two following physical constrains:

a. Minimum refrigeration power requirements for cooling of the conductor.

b. To conduct minimum heat leak to the liquid helium that cools the superconducting magnet system.

These two factors determine the fundamental current lead design strategies and their accomplishment is termed as optimisation of current leads, or quite often the term can be met as thermodynamic optimisation. The engineering design principles for the construction of "economical" current leads are derived from fundamental physical arguments. The theoretical studies have as target to define the optimum in the creation of a current lead that will meet the requirements of a high demand for economic use of sources in large scale applications of superconductivity such as the Large Hadron Collider at CERN. The passing from the theory to the realisation of such device is not a simple procedure. Its practicality is always assessed together with the capability and realism of massive production within the existing machinery as well as the final cost and human factor. The design of the lead varies according to the specification of each application. Important element for the optimisation is the incorporation of superconducting material (HTS and LTS) that will limit the heat generation, which at the level of kilo-amperes of feeding electrical current contributes significantly as a source of heat leak. Obviously, the current lead cannot be entirely made from superconductor, but also conventional metal must be used when it is not possible to apply superconducting material due to temperature limitations at the upper warmer sections (the characterisation *"binary"* justifies the existence of two different types of materials: HTS/LTS and metal). In many cases, the HTS part of the leads is preferred to be made of Ag/Bi-2223 tapes but also many are the other alternative choices. In this section of the thesis, technical aspects in the design and construction of current leads for superconducting particle accelerator magnets are addressed. The two prototypes HTS current leads (of current rating 7.5 kA) for the Inner Triplet Magnets at the Large Hadron Collider (LHC) at CERN have been designed and constructed in the Institute of Cryogenics. This is an example of application of Ag/Bi-2223 tapes for resistanceless carriage of kilo amperes of electrical current. It is a real life application of HTS wire that shows from first hand how effective is the HTS material in gaining energy in electrical systems. The procedure of design and construction is reviewed.

3.2. Classification of current leads according to the cooling scheme

Heat can be removed from the conductor by two major ways, which define two major types of current leads.

- ***Type A***: Heat removal by **conduction**

The conductor is thermally linked to refrigerators at positions along its length between the room temperature and liquid helium end. Heat is then gradually absorbed by thermal conduction from the conductor before it enters the liquid helium. In the design of such type of current lead, the issue that has to be dealt is the optimum positional distribution and temperatures of the intermediate refrigerators, in order to require the minimum refrigeration power and of course to conduct the minimum heat leak to the liquid helium.

- ***Type B***: Heat removal by **convection**

The helium gas that is vaporised due to the heat leak that originates from the current leads themselves is guided to flow past the conductor and therefore it cools it by heat exchange (convective cooling) along the whole length. The design of such current lead is then induced to the design of a heat exchanger.

In both cases superconducting material is beneficial to be incorporated in combination with conventional conductor material and therefore the resistive heat can be totally eliminated. According to their design, the current leads can be divided into the following sub-categories.

A. Helium cooled copper-HTS (binary) current leads

The current leads of this type are self-cooled (type B current leads), i.e. they are cooled by heat exchange with the helium vapour that is generated from the heat that is conducted to the liquid helium. Leads of this type incorporate a copper section that is extended from room temperature to an intermediate temperature T_{int} below the critical temperature of the superconductor. At this point there is the electro-mechanical joint to the HTS section. The HTS section is extended from the temperature T_{int} to the liquid helium temperature 4.2 K. The intermediate temperature T_{int} is maintained by conduction cooling of the junction to a refrigerator system. In some cases, like the LHC 7.5 kA current leads, there is abundant supply of helium gas at 20 K, which is used to maintain the HTS-Cu junction at temperature T_{int} = 50 K. At the bottom of the HTS part there is the electrical joint to the LTS Rutherford type cable, which connects to the bus-bar that feeds the magnet at 1.9 K super-fluid helium. Due to the existence of two types of materials, copper and superconducting, the current leads are termed as binary or hydrid current leads.

B. Conduction cooled binary copper-HTS current leads

These current leads are of type A. The upper section is made of resistive material (copper) which is intercepted at a temperature T_{int} (below the critical temperature of the superconductor) by the refrigeration system. The electrical conduction is continued by the HTS section down to 4.2 K, where there is the joint to the LTS wire which is the final conduction path to the magnet.

C. Conduction cooled resistive current leads

These current leads are of type A. They are used for low electrical current applications where the incorporation of superconducting material does not have significant beneficial effect but rather the simplicity of construction and installation is a prior design goal. The conductor extends from the room temperature to the cryogenic environment of the magnet and is intercepted at intermediate points by refrigerators. The intermediate refrigerators divide the conductor into sections that sometimes have different cross sectional areas and lengths. The lengths usually are determined by the space requirements at the installation sites of the current leads. The minimisation of the heat leak requires dimensional optimisation of the conductor because the conduction heat leak and the heat generation are dependent on the conductor geometrical characteristics according to the following relations:

$$Q_{condution} = \frac{A_{conductor}}{L_{conductor}} \times \int_{T_1}^{T_2} k(T) \cdot dT \qquad (3.3)$$

$$Q_{Joule} = I^2 \times \frac{\rho \times L_{conductor}}{A_{conductor}} \qquad (3.4)$$

The total heat $Q_{total} = \frac{A_{conductor}}{L_{conductor}} \times \int_{T_1}^{T_2} k(T) \cdot dT + I^2 \times \frac{\rho \times L_{conductor}}{A_{conductor}}$ is composed of two terms; the first is $\propto A/L$ and the second is $\propto L/A$. Therefore the function Q_{total} will have a minimum with respect to the aspect ratio $\left(A/L\right)$, which has to be found through numerical simulations. The total refrigeration power consumption that is required to maintain the intermediate heat intercepts has to be minimised by selecting the optimum temperatures and positions of the refrigerators.

Basic design considerations for binary HTS current leads

The current progress in superconducting magnet technology has necessitated the design of special conductors in order to transfer high electrical current from the room temperature power supplies down to the cryogenic support environment of the magnet. The current leads are an important component of the superconducting magnet system. Their design includes a variety of issues in order to obtain an optimised, low heat leak and reliable current lead. These issues can be categorized more or less to three major elements in an HTS current lead: the upper resistive stage, the thermal intercept and the lower superconducting stage. The issue of current lead optimisation has been the subject of study for over than 40 years. Since then, it is well known that the optimum design is defined by the selection of an appropriate aspect ratio for the conductor, and further developments in the area of current lead manufacturing technology yield that a good heat exchanger design is required for vapour cooled designs. Also the heat leak to the cryogen is determined by the choice of the temperatures and operating current. The new generation of current leads incorporates a thermal intercept at the junction between the upper and lower stages, whilst it allows a variety of cooling modes and electrical insulation methods. The issues that have to be dealt in the design of the HTS leads include the material choice, the configuration that will reduce the influence of the magnetic field on the HTS current capacity, the use of a parallel shunt for magnet protection, various heat load measurements, thermal runway (quench), the influence of contact resistance between the HTS and conventional materials or any other joints that may appear and the use of a variable HTS cross sectional area to reduce the heat leak to the cryogenic environment. It has to be pointed out that not only the reduction in the liquid helium boil off should be a prior design goal, but also the minimization of the room temperature refrigeration power that is required to reduce the heat leak to the cold end.

3.3. Theoretical analysis

It is important to discus the underlying principles of the current lead thermo-electric behaviour. These arise from fundamental heat transfer equations, and as M. Wilson has shown, they can lead to an optimisation theory of gas-cooled current leads. In fact, the necessity for the development of mathematical models to describe the current lead behaviour arises from the need to design and construct optimised current leads. The associated factors that determine the thermo-electric performance of the current leads must be assessed via models; the construction of the current lead has to be based on thermoelectric analysis that will lead to designs which strictly meet the requirements of a highly economical superconducting magnet system. Before the adoption of any current lead design, always a model solution comes first to confirm the optimum performance. In the following sections, the basic frame of the associated theory is presented.

3.3.1. Steady state operation

A resistive lead is considered in the form of a copper bar. The conductor is in a stream of cold helium vapour and is cooled by heat exchange. The total power Q_{in} that is flowing into and generated within a differential volume A·Δx of the conductor is given by the relation:

$$Q_{in} = \left[A \cdot k(T) \cdot \frac{dT(x)}{dx} \right]_{x+dx} + \dot{m} \cdot C_p^{copper}(T) \cdot T + \frac{\rho(T) \cdot I^2}{A} \cdot \Delta x$$

The first term represents the heat conduction, the second the heat exchange with the helium gas and the third the Joule heat generation. The total power that is flowing out of the differential volume A·Δz is given by the relation:

$$Q_{out} = \left[A \cdot k(T) \cdot \frac{dT(x)}{dx} \right]_{x} + \dot{m} \cdot C_p^{copper}(T)(T + \Delta T)$$

In the steady state operation, the energy balance condition requires that $Q_{in}=Q_{out}$.

$$\left[A\cdot k(T)\cdot\frac{dT(x)}{dx}\right]_{x+dx}-\left[A\cdot k(T)\cdot\frac{dT(x)}{dx}\right]_{x}-\dot{m}\cdot C_p^{copper}(T)\cdot\Delta T+\frac{\rho(T)\cdot I^2}{A}=0$$

Division by Δx and in the limit that $\Delta x \rightarrow 0$, the differential equation that describes the heat transfer process in the conductor is obtained.

$$\frac{d}{dx}\left\{A\cdot k(T)\cdot\frac{dT(x)}{dx}\right\}-\dot{m}\cdot C_p^{copper}(T)\cdot\frac{dT(x)}{dx}+\frac{\rho(T)\cdot I^2}{A}=0 \tag{3.5}$$

3.3.2. Wiedemann-Franz law

The product of electrical resistivity and thermal conductivity in most of the metal electrical conductors is proportional to the temperature. This proportionality is known as the Wiedemann-Franz law.

$$k(T)\times\rho(T)=L_o\times T \tag{3.6}$$

The constant of proportionality L_o is the Lorenz number. The model of the electronic sea in metals predicts that this constant is a universal number for all metals and has the value:

$$L_o=\left(\frac{\pi\cdot k_B}{\sqrt{3}\cdot e}\right)^2=2.45\times10^{-8}\ {(W\cdot\Omega)}/{K^2}$$

3.3.3. Transient state operation

Transient state during the current lead operation occurs when over heating because of sudden coolant interruption, time varying operating current, quenching etc. The transient can be described by the following relation

$$\frac{\partial}{\partial x}\left[k(T)\frac{\partial T}{\partial x}\right]-\frac{\dot{m}C_P^{vapor}(T)}{A}\cdot\frac{\partial T}{\partial x}+\frac{\rho(T)\cdot I^2}{A^2}=C_P^{copper}\delta(T)\frac{\partial T}{\partial t} \tag{3.7}$$

where

A = conductor cross section

I =current (A)

$k(T)$ = conductor thermal conductivity $\left({}^{W}\!/\!{}_{mK}\right)$

$\rho(T)$ =conductor electrical resistivity $(\Omega \cdot m)$

$C_P^{copper}(T)$ =conductor specific heat $\left[{}^{J}\!/\!{}_{kg} \cdot K\right]$

$\delta(T)$ =conductor density $\left[{}^{kg}\!/\!{}_{m^3}\right]$

$C_P^{vapor}(T)$ =gas/vapor specific heat $\left[{}^{J}\!/\!{}_{kg} \cdot K\right]$

$\dot{m}$ =gas/vapor mass flow rate $\left[{}^{kg}\!/\!{}_{s}\right]$

The mass flow rate is determined by the boiled off of the liquid helium for self-cooled leads

$$\dot{m} = \frac{Q_0}{\lambda_{ev}}$$

where:

λ_{ev} =liquid helium latent heat of vaporization (at atmospheric pressure)

Q_0 =heat leak at the cold end of the current lead in the helium bath given by

$$Q_0(t) = k((T_0)A\frac{\partial T}{\partial x}\bigg|_{(x=0,t)} \tag{3.8}$$

3.3.4. Current lead optimization theory for conventional leads

A resistive vapour cooled current lead operating between room temperature T_2 and liquid helium temperature T_1 can be optimised according to the following theory [1]. The liquid helium is boiled off by the heat leaks with a mass flow rate $\dot{m}$. The heat balance equation in a differential length of the conductor dx and cross sectional area A has already been shown to be:

$$k(T)\cdot A\cdot\frac{dT(x)}{dx}\bigg|_{x+dx} - k(T)\cdot A\cdot\frac{dT(x)}{dx}\bigg|_{x} - H + \frac{I^2\cdot\rho(T)}{A}\cdot dx = 0$$

The third term in the equation expresses the rate of heat transfer from the lead to the gas coolant

$$H = f\cdot\dot{m}\cdot C_P(T)\cdot dT$$

f expresses the efficiency of heat transfer. Firstly it is assumed that at any given point x, the lead and the gas are both at the same temperature and the specific heat at constant pressure C_P is taken as constant. Therefore the above relation is transformed to the following:

$$\frac{d}{dx}\left\{k(T)\cdot A\cdot\frac{dT(x)}{dx}\right\}-f\cdot\dot{m}\cdot C_P(T)\cdot\frac{dT(x)}{dx}+\frac{I^2\cdot\rho(T)}{A}=0 \tag{3.9}$$

Analytical solutions of the above equation can be obtained by introducing new variables.

Transformation of length: $dz=\frac{I\cdot dx}{k(T)\cdot A}$

Heat leak: $w=\dot{m}\cdot C_L$

Ratio of heat capacity to latent heat: $\frac{C_P}{C_L}=u$

Wiedemann-Franz law: $k(T)\times\rho(T)=L_o\times T$

Combination of the above relations transforms the heat balance equation into the following relation:

$$\frac{d^2T(z)}{dz^2}-\frac{f\cdot w\cdot u}{I}\times\frac{dT(z)}{dz}+L_o\cdot T=0$$

The solutions are obtained in the range $4\cdot L_o>\left(f\cdot w\cdot u/I\right)^2$, in which case the solution is:

$$T(z)=e^{az}\left[D\cdot\sin(\beta\cdot z)+E\cdot\cos(\beta\cdot z)\right]$$

$$\text{where } a=\frac{fwu}{2I}$$

$$\beta=\sqrt{(L_0-a^2}$$

and the constants D and E are determined by the boundary conditions. At the top of the lead $z=Z_2$ and $T=T_2$, i.e. room temperature. At the bottom, $z=0$ and $T=T_1$. For simplification it is set $T_1=0$, and the solution is obtained

$$T(z)=T_2\cdot\frac{e^{az}\cdot\sin(\beta z)}{e^{aZ_2}\cdot\sin(\beta Z_2)}$$

At the bottom of the lead the amount of the vaporized liquid helium $\dot{m}C_L$ is equal to the conducted heat

$$\frac{k\cdot A}{I}\cdot\left.\frac{dT}{dx}\right|_{x=0}=\left.\frac{dT}{dz}\right|_{z=0}=\frac{\beta T_2}{e^{aZ_2}\cdot\sin(\beta Z_2)}$$

The optimum lead geometry is obtained with the minimization of the ${w}/{I}$ with respect to Z_2, i.e. $\frac{d\left({w}/{I}\right)}{dZ_2}=0$, which gives

$$a_0 \sin(\beta Z_{20}) + \beta_0 \cos(\beta_0 Z_{20}) = 0$$

This is a relation between optimized quantities. A combination of the above equations gives

$$\beta_0 Z_{20} = \tan(\beta_0 Z_{20}) \ln\left\{\frac{-2\cos(\beta_0 Z_{20})}{fuT_2}\right\}$$

This can be solved graphically or numerically for $\beta_0 Z_{20}$.

$$\cos(\beta_0 Z_{20}) = -\frac{1}{\left(1+\tan^2(\beta_0 Z_{20})\right)^{1/2}} = -\frac{a_0}{L_0^{1/2}}$$

From (2.16) the heat leak at optimum current can be found.

The optimum length of the lead can be obtained as follows:

In order to translate the values of z into physical distance x along the lead, the relation

$$\frac{Ix}{A} = \int k(T(z))dz \qquad \textit{(3.10)}$$

is integrated. The dependence of temperature with z is calculated using the temperature distribution $T(z)$ of the solution

$$T(z) = T_2 \cdot \frac{e^{az}\sin(\beta z)}{e^{aZ_2}\sin(\beta Z_2)}$$

The optimum temperature profile has zero gradient at the top hot end. This arises also from physical principles, i.e. for an optimum current lead there will not be heat entering from the top end, so therefore $Q = -kA\frac{dT}{dx} = 0 \Rightarrow \frac{dT}{dx} = 0$.

Using the temperature distribution, the physical length x may be calculated as a function of z by numerical integration of equation (3.10). The total length of lead X_{20} is found by integration of equation x from $z=0$ to $z=Z_2$ and most of the times is expressed in terms of a *shape factor*

$$S.F = {I_0 X_{20}}/{A}$$

This factor is a universal factor and applies to all optimized leads for a given material independently of the electrical current. Therefore this theory leads to the optimum shape factor SF which can be used to derive the optimum geometrical characteristics of the current lead.

3.3.5. The effect of helium gas cooling on the heat leak of an HTS lead

The differential equation that describes the heat transfer process in the HTS part of a binary current lead is the following:

$$\frac{d}{dx}\left(k\cdot A\cdot\frac{dT(x)}{dx}\right)-\dot{m}\cdot C_P\cdot\frac{dT(x)}{dx}=0$$

The Joule heat generation term is omitted because the lead is in the superconducting state. K is the thermal conductivity of the HTS material and C_P is the heat capacity of helium. For the conditions $T(x=0)=T_0$ and $T(x=L)=T_L$, the following analytic solution can be obtained [2], [3].

$$T(x)=\left(\frac{T_L-T_o}{e^{a_l}-1}\right)\times\left\{\exp\left(a_l\cdot\left(\frac{x}{L}\right)\right)+\frac{e^{a_l}\cdot T_o-T_L}{T_L-T_o}\right\}$$

where $a_l=\dfrac{\dot{m}\cdot C_P\cdot L}{k\cdot A}$

The heat input to the liquid helium is $Q_{in}=\dot{m}\cdot h_l=k\cdot A\cdot\left.\dfrac{dT(x)}{dx}\right|_{x=0}$, where $h_l = 20\ {}^{J}\!/_{gr}$ is the latent heat of vaporization of the liquid helium. The 1st derivative of the solution with respect to x gives:

$$\frac{dT(x)}{dx}=\left(\frac{T_L-T_o}{e^{a_l}-1}\right)\times\frac{a_l}{L}\times\exp\left\{a_l\cdot\frac{x}{L}\right\}$$

$$\left.\frac{dT(x)}{dx}\right|_{x=0}=\left(\frac{T_L-T_o}{e^{a_l}-1}\right)\times\frac{a_l}{L}$$

$$Q_{in}=\dot{m}\cdot h_l=k\cdot A\cdot\left(\frac{T_L-T_o}{e^{a_l}-1}\times\frac{a_l}{L}\right)$$

$$Q_{in}=\frac{\dot{m}\cdot C_P\cdot\Delta T}{\exp\left(\dot{m}\cdot C_P\cdot L/_{k\cdot A}\right)-1}$$

For very small values of helium mass flow rate $\dot{m}\to 0$, the exponential term converges: $\exp\left(\dfrac{\dot{m}\cdot C_P\cdot L}{k\cdot A}\right)\xrightarrow{\dot{m}\to 0}1+\dot{m}\cdot C_P\cdot L/_{k\cdot A}$, and therefore the heat input to the LHe is $Q_{in}=\dfrac{k\cdot A\cdot\Delta T}{L}$. This relation can be obtained straightforward as the heat conduction term without helium gas cooling. For large values of mass flow rate, the heat leak has the value

$$Q_{in} = \frac{\dot{m} \cdot C_P \cdot \Delta T}{\exp\left(\dot{m} \cdot C_P \cdot L \big/ k \cdot A \right)}$$

From this relation when the Q_{in} is equalized to the value $\dot{m} \cdot h_l$ (for self cooled leads) the following is obtained:

$$\frac{C_P \cdot \Delta T}{h_l} = \exp\left\{ \frac{\dot{m} \cdot C_P \cdot L}{k \cdot A} \right\} \rightarrow \frac{\dot{m} \cdot C_P \cdot L}{k \cdot A} = \ln \zeta$$

$$\dot{m} \cdot h_l \cdot \frac{C_P \cdot L}{h_l \cdot k \cdot A} \cdot \frac{\Delta T}{\Delta T} = \ln \zeta$$

$$\therefore \; Q_{in} = Q_o \times \frac{\ln \zeta}{\zeta}$$

where $Q_o = k \cdot A \cdot \frac{\Delta T}{L}$, $\zeta = \frac{C_P \cdot \Delta T}{h_l}$

If an HTS current lead is considered with cross sectional area 92 mm^2 and length 35 cm operating in the temperature range 50 K to 4.2 K, the conduction heat leak without helium vapor cooling, is:

$$Q_o = \frac{A}{L} \times \int_{4.2^o K}^{50^o K} k_{AgAu}(T) \cdot dT = \frac{92 \times 10^{-6}}{0.35} \times 2385 = 0.63 \text{ W}$$

If the helium cooling is considered, then $\zeta = \frac{5.28 \times 46}{20} = 12.144$ and

$$Q_{in}^{\substack{helium \\ cooling}} = Q_o \times \frac{\ln \zeta}{\zeta} = 0.63 \times \frac{\ln(12.144)}{12.144} = 0.13 \text{ W}$$

The heat leak is reduced by $\frac{0.63 - 0.13}{0.63} = 80$ %.

3.4. Main issues in the design and construction of the 7.5 kA current leads

3.4.1. Introduction

In the Large Hadron Collider at CERN a complicated superconducting magnet system exists, which is supported by an extensive cryogenic system of pressurised super-fluid helium below 2 K. The strong focussing at the four collision points is obtained by the low-β quadrupoles of the Inner Triplets that are placed symmetrically at a distance of 23 m on each side of the interaction regions [4]. The Inner Triplet magnet systems provide the final focus of the two proton beams immediately after the four interaction points in the machine. Important components in the magnet system are the Distribution Feed Boxes (DFBX).

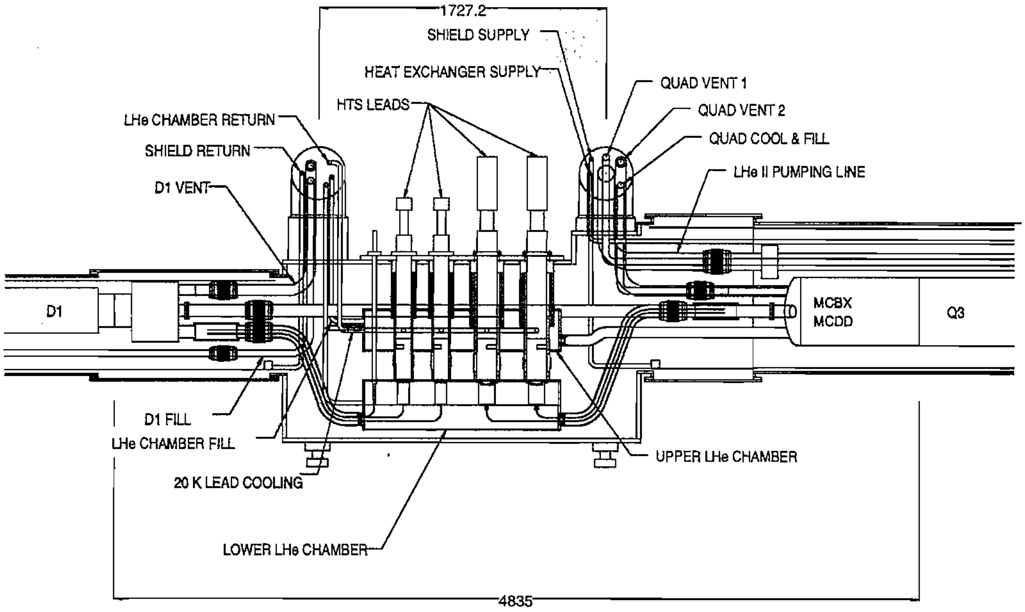

Figure 3.7. *Schematic of the DFBX, where it is indicated the position of the HTS current leads*

The connections for all the cryogenic and electrical services of the Inner Triplets are located in the DFBX's. The DFBX connects the LHC helium cryogenic distribution system with the superconducting magnets. There is cooling at 1.9 K for the magnets and 4.4 K for the DFBX helium tank. The Distribution Feed Boxes are part of the contribution from the US to the CERN Large Hadron Collider. Major components of the DFBX assembly are the HTS binary gas-cooled current leads that are rated for electrical current 7.5 kA. The lower part of the HTS lead is connected to the NbTi cable that is in the 4.5 K helium bath inside the DFBX helium tank. The upper end of the HTS leads and the vapour-cooled leads are cooled by conduction to the helium tank and by the helium gas line at 20 K that comes from the CERN cryogenic QRL system [5]. Forty 7.5 kA current leads were fabricated by Pirelli Ltd. in UK. The two prototypes were designed and fabricated in the Institute of Cryogenics at Southampton University.

3.4.2. General outline

According to the classification of the various types of current leads in the previous section, the 7.5 kA current leads are type-B helium vapour self-cooled binary HTS leads. In the figure below is the schematic of the general outline of the 7.5 kA current lead.

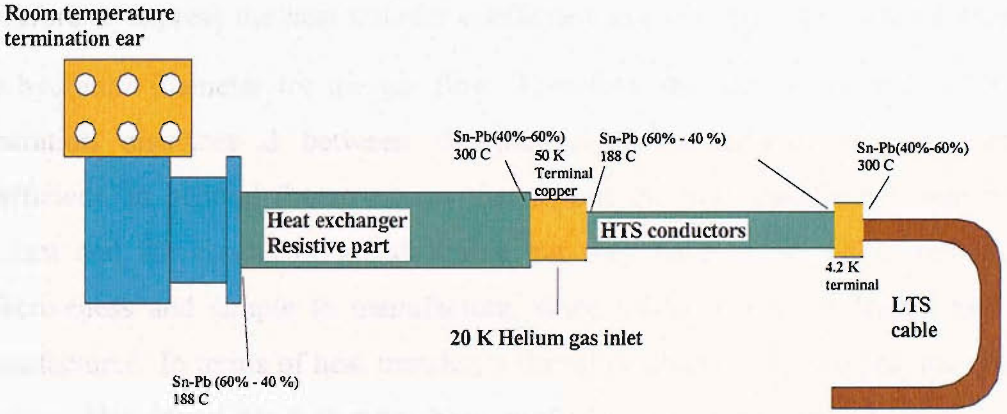

Figure 3.8. *General outline of the 7.5 kA binary HTS current lead*

The upper heat exchanger/electrical conductor section is made of copper that extends from the room temperature termination ear that connects to the power supply cable down to the 50 K terminal copper electromechanical junction to the HTS part. The structure of the heat exchanger has been designed in order to enhance the heat transfer between the conductor and helium gas. This is achieved by maximising the area of conductor in contact with the cold gas for effective convection cooling. In order to achieve this, the conductor is composed of eight copper rectangular plates in a parallel configuration that are separated by small gaps thus narrow channels are formed between two successive plates. This configuration provides larger surface area of conductor for heat transfer with the gas than if a copper bar was used or a hollow copper cylinder. The conductor is cooled by the natural convection mode of heat transfer with the cold helium gas. In the heat exchanger analysis of the conductor, the equations that govern the cooling scheme of the current lead can be written as follows, considering the analysis in the previous section:

$$\frac{d}{dx}\left\{k_{lead}\left(T_{lead}\right)A\frac{dT_{lead}(x)}{dx}\right\}+\frac{\rho\left(T_{lead}\right)\cdot I^{2}}{A}=h(T)\cdot P\cdot\left(T_{lead}-T_{gas}\right)$$

$$\dot{m}\cdot C_{P}^{gas}\left(T_{gas}\right)\cdot\left(\frac{dT_{gas}}{dx}\right)=h\left(T_{lead}\right)\cdot P\cdot\left(T_{lead}-T_{gas}\right)$$

The factor *h(T)* is the convective heat transfer coefficient. The heat transfer coefficient can be expressed in a non-dimensional form by means of the Nusselt number $Nu = {h\cdot d}/{k}$. It is usual to adopt the Dittus-Boetler correlation to describe the turbulent flow of the helium gas within the channels, i.e. $Nu = 0.023\cdot \mathrm{Re}^{0.8}\cdot \mathrm{Pr}^{0.4}$ and therefore to express the heat transfer coefficient as $h = {Nu\cdot k}/{d}$. The factor d expresses the hydraulic diameter for the gas flow. Therefore, the narrow channels with small separation distances d between the parallel plates enhance the heat transfer coefficient. In general the structures that favour the heat transfer between the gas coolant and the conductor are desirable but they have to be within reliable cost effectiveness and simple to manufacture, since tenths of current leads have to be manufactured. In terms of heat transfer, a finned conductor can also provide effective cooling. The finned conductor has been applied in the case of the 13 kA and 600 A HTS current leads that were manufactured after the 7.5 kA current leads. The HTS section also is made like a heat exchanger that extends from the 50 K terminal to the 4.2 K electromechanical junction to the LTS Rutherford type NbTi cable. The HTS elements are eight stainless steel rectangular plates with Ag/Bi-2223 tapes brazed from both sides, also in a parallel configuration, in which the cold helium evaporated gas flows in the narrow channels between the plates. The electromechanical junctions Cu termination ear (at 300 K) – Cu plates, Cu plates – HTS elements and HTS elements – LTS cable are obtained by soldering of the Cu or HTS boards in the grooves of the Cu joint blocks, thus ensuring good electrical conduction. The soldered joints will have unavoidable electrical contact resistance, which has to be kept at low levels (of the order of nΩs) in order to limit the Joule heat generation that will contribute to the heat leak to the cold end. Good electrical joint is ensured with careful soldering/brazing (avoiding dry-joints); a method that has been employed is also the coating of the Cu block junctions with a protective layer of metal in order to avoid the phenomenon of the oxidation of the Cu surface. When the Cu is heated to the high temperature for the soldering process, oxide layer will form on the Cu surface which is detrimental to the electrical joint, thus the protective metal coating is necessary in order to ensure good electrical contact. The upper Cu and HTS heat exchangers are enclosed in G-10 cylinders in order to insulate the helium gas and also to provide electrical insulation. The lead is enclosed in stainless steel vessel. The inner space of the steel vessel that contains the current lead is evacuated in order to eliminate the convective thermal losses from the environment.

3.4.3. Assembly of the resistive part

The resistive part is made of eight parallel copper C 106 rectangular plates. The plates are washed with detergent and dried. The room temperature end of each plate is tined with solder Sn(60%)/Pb(40%) over a length of 15 mm. The 50 K end is tined with solder Sn(15%)/Pb(85%) over a length of 15 mm. The plates are assembled in a parallel configuration that is held in place by M4 copper screws through holes on the plates. The plates are separated by copper spacers, in order to provide narrow channels between the plates for flow of cold helium gas for heat exchange. The assembly is finger-tightened by M4 nuts and the thermometer housing is added on the outer plate.

Figure 3.9. *The resistive part assembled*

Soldering of the resistive assembly to the room temperature termination ear

The grooves on the room temperature termination ear are closed with several turns of PTFE tape. The cartridge heaters are attached on the holes on the base on the grooves. The termination ear is heated to 200 °C-220 °C and the grooves are tined with solder Sn(60%)/Pb(40%) using plumbers flux on the nickel-plated surfaces. The grooves are filled with solder Sn(60%)/Pb(40%). The resistive assembly is lowered down slowly in the grooves using small amount of plumbers flux to ensure good wetting of the surfaces.

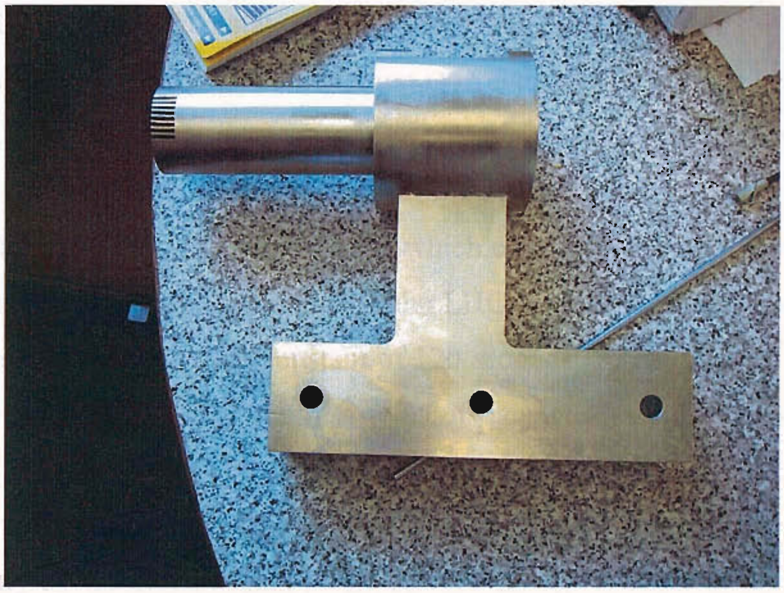

Figure 3.10. *The room temperature termination ear*

3.5. Design and fabrication of the HTS part

3.5.1. Material selection/characterization

The HTS part of the current lead is a highly effective thermal break while maintaining the electrical current conduction from the upper copper part down to the liquid helium temperatures. Various are the choices of HTS material that are used in HTS current leads. Important criterion for the selection of the type of HTS conductor is that it should be of low thermal conductivity, in order to conduct minimum heat to the liquid helium. In the case of the 7.5 kA current leads, Ag/Bi-2223 tape has been used to construct the HTS elements as being a very reliable choice. Most often OPIT tapes are used due to their high critical current densities, the good strain tolerance during the thermal cycling and the feasibility of complex geometries. Due to mechanical weakness of the composite silver sheath/ceramic oxide, the tapes have to be mechanically reinforced by a rigid support, the shunt. The shunt is incorporated in order:

(a) To provide mechanical support to the weak tapes.

(b) To provide thermal stability against localized thermal disturbances (quenches) that could occur in the HTS part. A quench is the accidental transition of a superconductor to the normal state and usually in the current leads case it occurs due to loss of the cooling ability. If the transition is irreversible then it can be catastrophic for the lead. The transition is detected by quench detection systems and then the magnets are unloaded within a certain short time but not rapidly in order to avoid the generation of high voltages in the magnets which cannot be afforded. An example of discharge time is for the dipole circuits in the LHC where the current has been set to decay exponentially with a time constant of 120 seconds [4]. The current lead must be able to withstand the electrical current without damage during the time of magnet discharging. The shunt must be good electrical conductor (metal) in order to provide a parallel electrical current path during quench since the feeding current is too much to be carried only by the metal sheath of the tapes. Also the shunt must be poor thermal conductor in order to keep the heat conduction to the liquid helium at low levels during steady state operation. It is well known that alloying the silver sheath with elements such as gold and Mg reduces its thermal conductivity. For current lead applications, the most frequent choice is AgAu alloys. An apparatus was designed and built in order to assess the thermal conductivity of HTS tapes for current lead applications.

3.5.2. Measurement of the thermal conductivity in an apparatus based on the two stage G-M cryocooler

In the measurement of thermal conductivity the steady state heat flow method is applied (figure 3.11). An electrical heater (constantan wire) is wound at one end of the sample of uniform cross section A; this generates a well-defined heat flow $\dot{Q}$ into the sample flowing towards the colder heat sink. The other end is thermally linked to the 2nd stage of the G-M cryocooler (heat sink).

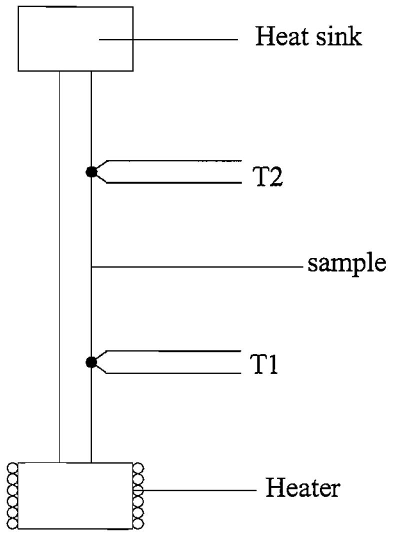

Figure 3.11. *Principle of the steady state heat flow method for thermal conductivity measurements*

The temperature difference $\Delta T = T_1 - T_2$ across the length L of the sample is recorded with the diode sensors. The amount of heat flow $\dot{Q}$ $(= I^2 \times R_{Heater})$ is estimated and the thermal conductivity is then calculated at the temperature $T_1 + \frac{\Delta T}{2}$ from the following relation (Fourier Law of heat conduction in solids).

$$k = \frac{L}{A} \cdot \frac{\dot{Q}}{(T_1 - T_2)}$$

Apparatus for the thermal conductivity measurements

Figure 3.12 shows the design of the rig that has been designed and constructed for the measurements of thermal conductivity. The apparatus is thermally attached to the second stage of the cryocooler by using six bolts with high thermal conductivity type N Apiezon grease. It can be seen the copper thermal link (cold finger), the sample's radiation shield (high conductivity copper with layers of maylar super-insulation), the sample holder (a copper extension on the flange) and the sample. The sample is soldered to the sample holder and supported from the other end by a stainless steel stud with a cotton thread. Since an HTS tape sample is weak, the last action is necessary in order to avoid vibrations of the sample due to the operation of the Cryocooler.

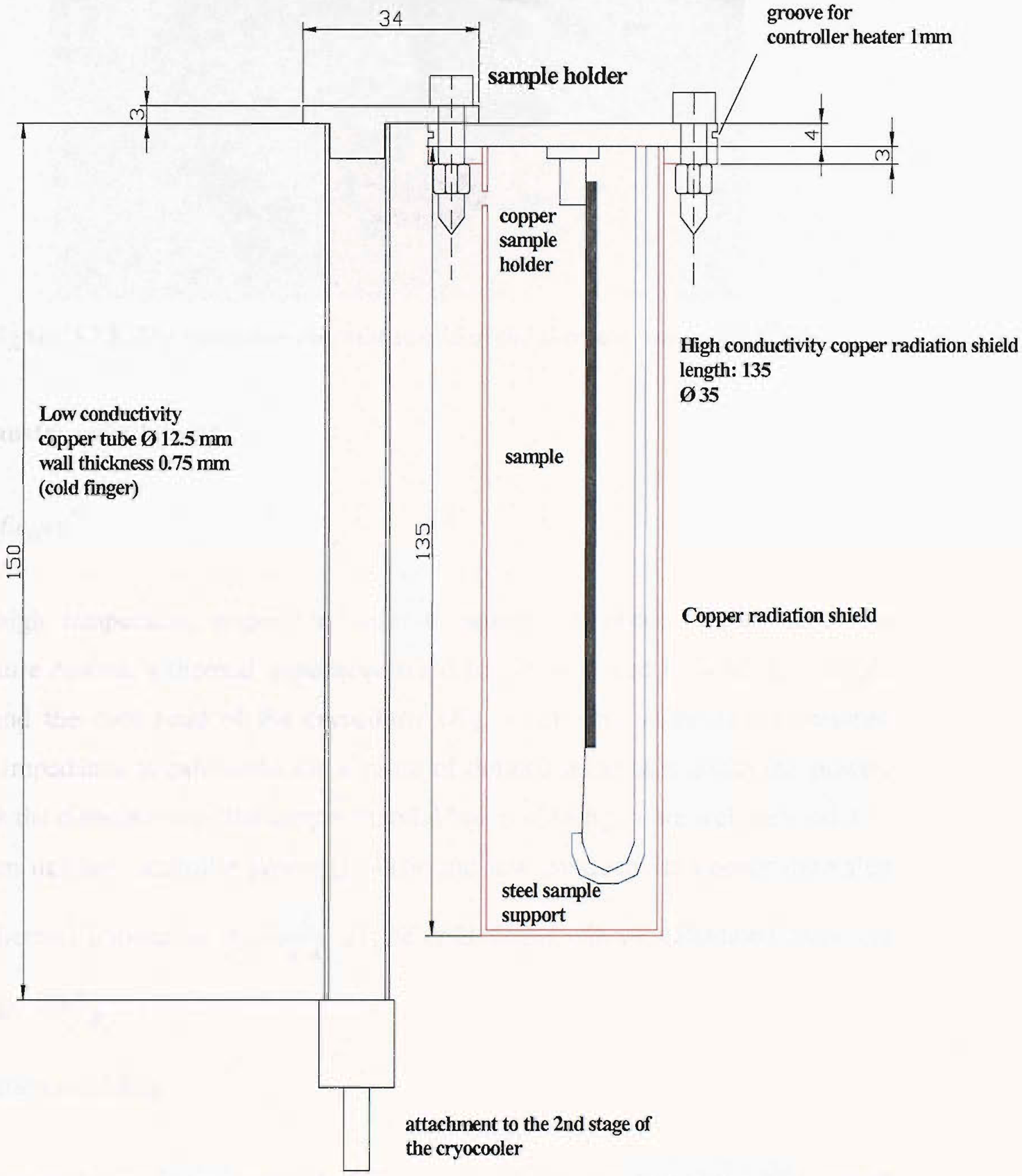

Figure 3.12. *The apparatus for thermal conductivity measurements*

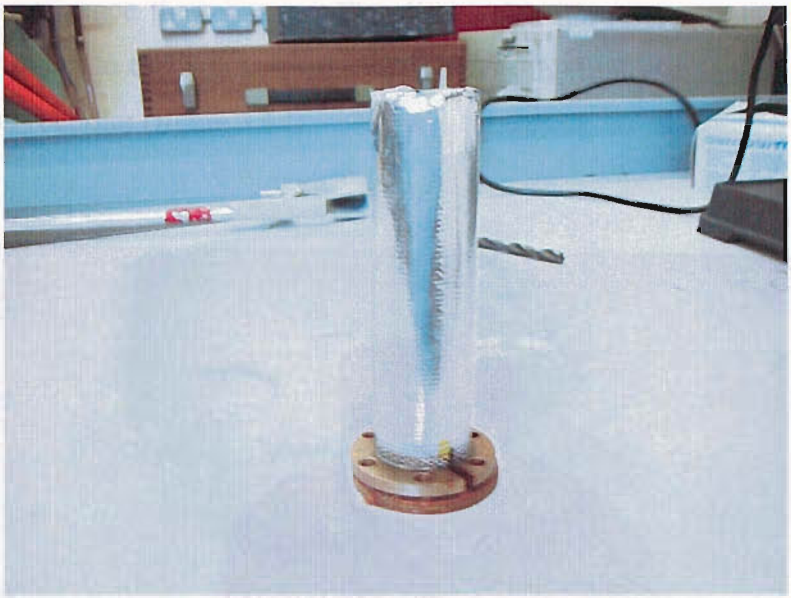

Figure 3.13. *The radiation thermal shield of the thermal conductivity rig*

Heat transfer calculations

A. Cold finger

In the high temperature region, in order to reduce the power requirements for temperature control, a thermal impedance (cold finger) is placed between the sample holder and the cold head of the cryocooler (fig. 3.12). The value of the required thermal impedance is calculated for a value of defined maximum controller power; therefore the dimensions of the copper thermal link (cold finger) are well defined. For maximum defined controller power $Q_C = 15W$ and low conductivity copper the value of the thermal impedance $R_C = \frac{L}{A \cdot K}$ of the cold finger can be calculated from the relation $Q_C = {\Delta T}/{R_C}$.

B. Radiation shielding

A radiation cylindrical copper shield of area $A_S = 10^{-2} m^2$ is attached to the 2nd stage of the cryocooler to enclose the sample; the shield and the sample are therefore at the same temperature.

The Silicon Diode Thermometers are calibrated using a previously Rhodium Iron resistor as a reference thermometer. The diodes and the reference thermometer are thermally attached to the same copper block that is thermally attached to the second stage of the cryocooler (figure 3.14).

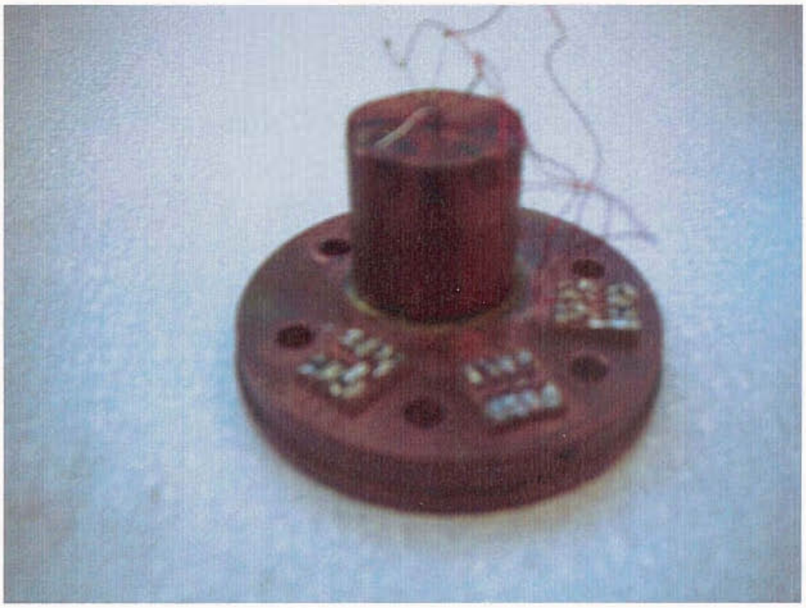

Figure 3.14. *Rig for calibration of the silicon diode thermometers*

The system is cooled down to the lowest temperature possible and then allowed to warm up to room temperature while readings of the thermometers are recorded at regular time intervals. The results are graphs of the diode voltage against the temperature of the reference resistor which is considered as the real temperature. Polynomial regression is used in order to derive the calibration equations $T = f(V)$ that relate the real temperature and the diode voltage. A calibration graph can be seen in figure 3.15.

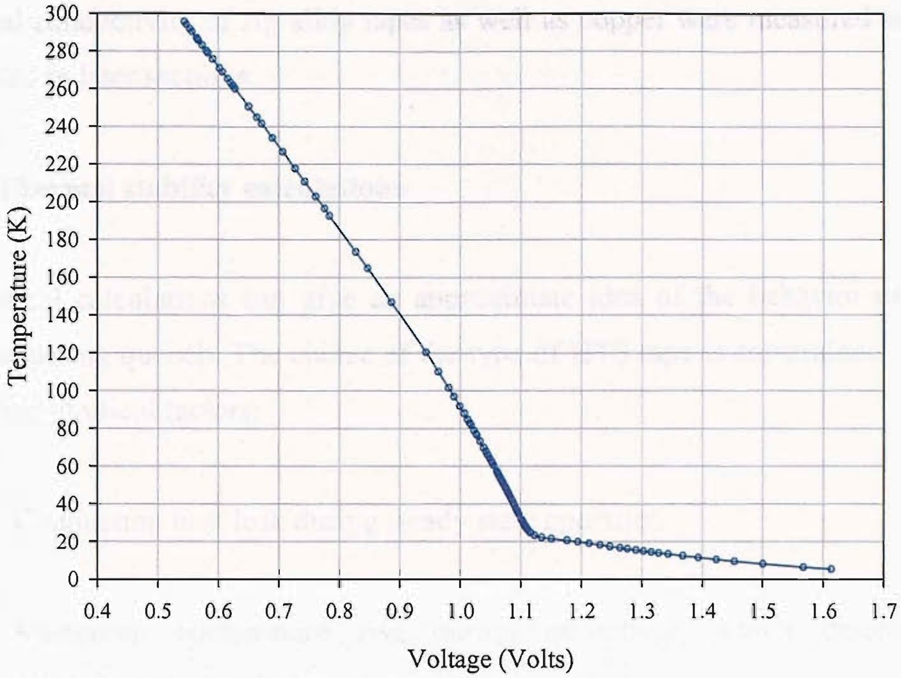

Figure 3.15. *Calibration graph for the silicon diode thermometer*

It can be seen from figure 3.16 that the graph shows two trends. Each trend is individually fitted to a polynomial. The region between 21 K and 25 K is not used because of the kink in the graph.

$$T = f_1(V_{diode}),\ \text{for } 4.2K < T < 21K$$

$$T = f_2(V_{diode}),\ \text{for } 25K < T < 300K$$

Measurement procedure

For differential thermal conductivity measurements a well-defined amount of heat Q has to be applied to the sample heater to cause a temperature difference of $\Delta T \approx 1K$ (the amount of heat is estimated using thermal conductivity for similar materials taken from the literature). The base temperature is controlled for each point with the temperature controller at temperature T_2. After thermal equilibrium has been achieved (T_1=T_2), the sample heater is energised. A new thermal equilibrium is achieved (steady state heat flow) $(T_1' > T_2 \equiv T_1)$ and the constant temperature difference across the sample (ΔT) is recorded.

Thermal conductivity of Ag alloy tapes as well as copper were measured and will be presented in later sections.

3.5.3. Thermal stability calculations

Theoretical calculations can give an approximate idea of the behavior of the HTS element during quench. The choice of the type of HTS tape is constrained by the two following physical factors:

a. Conduction heat leak during steady state operation

b. Maximum temperature rise during quenching, which determines the conduction heat leak during the transient behavior of the quench.

The third factor that has to be considered is the cost of HTS tape, since the use of silver/gold alloy increases the total cost. These factors compete to each other and somehow, the final choice should be a compromise. The two HTS Ag/Bi-2223 tapes that will be compared are:

A. NST tape

Dimensions: width 3.2 mm, thickness 0.2 mm.
Sheath material: Silver-gold alloy (4% gold)
Superconductor filling factor: $f=0.3$ volumetrically
Critical current: 40 Amperes (self field, 77 K)

B. ASC tape

Dimensions: width 4.2 mm, thickness 0.2 mm
Sheath material: Silver-gold alloy (5% gold)
Superconductor filling factor: $f=0.35$ volumetrically
Critical current: 110 Amperes (self field, 77 K)

The use of low current tape such as the NST requires more tapes to carry the total current than if ASC would be used and therefore the total cost of production of 40 current leads will be increased. If ASC tape is used, for stability reasons, additional material has to be incorporated in order to balance the missing amount of silver alloy sheath-stabilizer and carry the electrical current during quench.

(A). If the NST tape is used, the arrangement of tapes in the 7.5 kA current leads can be set as follows:

The nominal current of each tape (the current that is carried by each tape during steady state operation) has to be set to a value lower than 40 A, in order to avoid marginal operation for safety reasons. A configuration of 8 HTS elements (stainless steel boards with soldered tapes) with 26 tapes on each board (13 on each side) gives total number of tapes $N_l = 26 \times 8 = 208$ tapes. The tapes are brazed on a stainless steel board of thickness 1 mm, width 45 mm and length 335 mm. The nominal current is then $I_{Nominal} = {}^{7500}\!/_{208} = 36$ Amperes (<40 A). The maximum temperature rise during quench will be estimated by assuming adiabatic heating of the HTS element for time 10 seconds. The total cross sectional area of silver alloy $A_{NST\text{-}total}$ is estimated as follows:

N_1: number of tapes per board = 26

N_2: number of boards = 8

A_{NST}: cross sectional area of each tape (silver alloy + superconductor) = $3.17 \times 0.2 = 0.634$ mm^2

$$\therefore\ A_{NST-total} = N_1 \times N_2 \times (1-f) \times A_{NST} = 26 \times 8 \times 0.7 \times 0.634 = 92.31 \text{ mm}^2$$

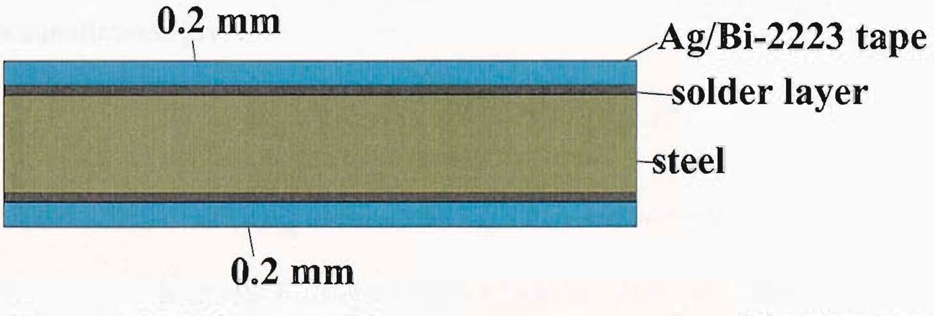

Figure 3.16. *Schematic of the transverse cross section of the composite steel board-Ag/Bi-2223 tape*

During quench, the energy generation is considered to take place in the silver alloy sheath and is absorbed in the composite Ag alloy and steel board. The Bi-2223 ceramic oxide core is excluded as highly resistive material with much lower heat capacity and the contribution of the solder is omitted. The portions of energy absorption in the Ag alloy and steel can be estimated by using the contributions of these two materials in the total cross section of the composite. By proportionality:

Energy generated per area: Ag alloy, 0.2 + 0.2 = 0.4

Energy absorbed per area: Steel and Ag alloy, 1 + 0.4 = 1.4

The ratio $\frac{Energy \quad absorption}{Energy \quad generation} = \frac{1.4}{0.4} = 3.5$ defines the absorption of energy of the composite in the calculations.

The current density when current flows only in the Ag alloy is

$$J = \frac{I}{A_{NSTtotal}} = \frac{7500}{92.3 \times 10^{-6}} = 8.12 \times 10^{7} \, {}^{A}\!/_{m^{2}}$$

The energy generation E_g is defined as:

$$Q_J \times time = \begin{pmatrix} Heat \quad generation \quad per \\ unit \quad volume \end{pmatrix} \times time = J^2 \times \rho_{Ag} \times time = \mathrm{E_g}$$

$$\text{Time} = 10 \text{ seconds}$$

Assuming adiabatic heating of the composite board, the following energy balance equation can be applied:

$$E_g = m \times \int_{T_0}^{T_{\max}} C_P \cdot dT$$

In the above relation T_o is the initial temperature which can be considered as 50 K and T_{max} is the maximum temperature that the composite reaches due to adiabatic heating. Further calculations give:

$$E_g = 3.5 \times m \times \left\{ \int_{50}^{100} C_P \cdot dT + \int_{100}^{T_{\max}} C_P \cdot dT \right\}$$

$$J^2 \times \rho_{Ag} \times time = 3.5 \times \gamma_{Ag} \times \{10 + 4 \times 0.075 \times \Delta T\}$$

$$\left(8.12 \times 10^{7}\right)^2 \times 2 \times 10^{-8} \times 10 = 3.5 \times 9 \times 10^{6} \times (10 + 0.3 \times \Delta T)$$

$$1.318 \times 10^{9} = 3.15 \times 10^{8} + 9.45 \times 10^{6} \times \Delta T$$

$$\rightarrow \Delta T = 106 \text{ K}$$

The maximum temperature will be therefore $T_{max} = 100$ K + 106 K = 206 K.

The conduction heat leak can be estimated according to the following relation:

$$\dot{Q}_{4.2\ K} = \frac{A}{L} \times \int_{4.2K}^{50K} \left\{ f_{steel} \cdot k_{steel}(T) + (1 - f_{steel}) \cdot k_{AgAu}(T) \right\} dT$$

where $f_{steel} = {}^{A_{steel}}\!/_{A}$ is the filling factor of the steel in the total cross sectional area $A = A_{NST\text{-}total} + A_{steel}$ of the composite stainless steel board/AgAu tape. L is the length of the HTS part equal to 350 mm. The above relation can be rearranged as follows:

$$\dot{Q}_{4.2K} = \frac{A_{steel}}{L} \times \int_{4.2K}^{50K} k_{steel}(T) \cdot dT + \frac{A_{NST-total}}{L} \times \int_{4.2\ K}^{50\ K} k_{AgAu}(T) \cdot dT$$

The temperature dependencies of the thermal conductivities of the AgAu (4%) alloy $k_{AgAu}(T)$ and stainless steel ANSI 304 $k_{steel}(T)$ have been measured using the thermal conductivity rig that has been described previously:

AgAu(4%) alloy

$$k_{AgAu}(T) = A_{AgAu} \times T^4 + B_{AgAu} \times T^3 + C_{AgAu} \times T^2 + D_{AgAu} \times T + E_{AgAu}$$

The coefficients are given in the table below:

A_{AgAu}	-1.7465×10^{-6}
B_{AgAu}	4.9848×10^{-4}
C_{AgAu}	-5.4966×10^{-2}
D_{AgAu}	3.5040
E_{AgAu}	-7.4913

Values of the integrated thermal conductivity are given in the following table:

$$Integral(AgAu\quad alloy) = \int_{4.2^{o}K}^{T_i} k_{AgAu}(T) \cdot dT$$

T_i (K)	Integrated k_{AgAu} ($W \cdot m^{-1}$)
40	1614
45	1988
50	2385
55	2804
60	3243

65	3703
70	4181
75	4678
80	5192

<u>ANSI 304 stainless steel</u>

$$k_{steel}(T) = A_{steel} \times T^3 + B_{steel} \times T^2 + C_{steel} \times T + D_{steel}$$

The coefficients are given in the table below:

A_{steel}	-1.8436×10^{-5}
B_{steel}	1.8562×10^{-3}
C_{steel}	7.4769×10^{-2}
D_{steel}	-1.0323×10^{-1}

The values of the integrated thermal conductivity for the stainless steel $Integral\ \ steel = \int_{4.2\ K}^{T_i} k_{steel}(T) \cdot dT$ are given in the following table:

T_i(K)	Integrated k_{steel} ($W \cdot m^{-1} \cdot K^{-1}$)
40	83
45	108
50	136
55	168
60	202
65	239
70	277
75	317
80	359

The conduction heat leak without stainless steel support is:

$$\dot{Q}_{4.2\ K}^{AgAu} = \frac{A_{NST-total}}{L} \times \int_{4.2\ K}^{50K} k_{AgAu}(T) \cdot dT \ = \ \frac{92.31 \times 10^{-6}}{0.35} \times 2385 = 0.63\ \text{W}$$

Hence, the total conduction heat leak of the element which includes AgAu tapes and stainless steel is:

$$\dot{Q}^{total}_{4.2\ K} = \frac{8\times 45\times 10^{-6}}{0.35}\times 136 + 0.63 = 0.77\ \mathrm{W}$$

This total heat leak to the 4.2 K falls well within the specification demanded by CERN.

(B) If the ASC tape is used, the configuration can be set as follows:

Due to the high nominal current of the ASC tape, fewer tapes are needed for the 7.5 kA current leads, consequently a shunt would be needed to compensate for the reduced amount of Ag sheath stabilizer. In order to estimate the amount of shunt required, it is assumed that the shunt will be made of Cu grade C 106.

The total area of silver alloy in the previous case is 92.3 mm^2 but in this case because less amount of silver is used, copper has to be incorporated in order to compensate for the missing amount of silver stabilizer. The amount of copper has to be estimated by taking into account the total conduction heat leak that has to be equal in the two cases according to the circuit model of figure 3.17.

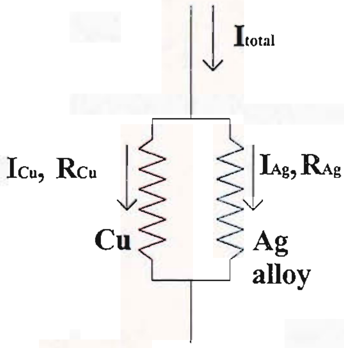

Figure 3.17. *Equivalent electrical circuit*

The cross sectional area of the tape is $A_{ASC} = 4.17\times 0.215 = 0.9$ mm^2. Assuming the total number of tapes to be 80, the total area of silver alloy in this case is:

$$A_{ASC-total} = \left(number\ \ of\ tapes\right)\times(1-f)\times A_{ASC} = 80\times 0.65\times 0.9 = 46.8\ \mathrm{mm}^2$$

The heat conduction occurs through parallel combination of copper and silver alloy thermal resistances. Aiming at a total resistance to be equal to the thermal resistance of the NST tape R^t_{NST} and using R^t_{ASC} and R^t_{Cu} as the thermal resistances of the ASC tape and Cu respectively then it must be:

$$\frac{1}{R^t_{NST}} = \frac{1}{R^t_{ASC}} + \frac{1}{R^t_{Cu}}$$

$$A_{NST-total} \times k_{NST} = A_{ASC} \times k_{ASC} + A_{Cu} \times k_{Cu}$$

$$A_{Cu} = \frac{1}{k_{Cu}} \times \left(A_{NST-total} \times k_{NST} - A_{ASC-total} \times k_{ASC}\right)$$

The thermal conductivities are taken at 25 K.

$K_{Cu}(25\ K) = 160\ W\cdot m^{-1}\cdot K^{-1}$

$K_{NST}(25\ K) = 70\ W\cdot m^{-1}\cdot k^{-1}$

$K_{ASC}(25\ K) = 27\ W\cdot m^{-1}\cdot k^{-1}$

$$\therefore A_{Cu} = 32.5\ mm^2$$

The maximum temperature rise during quench will be estimated with the use of the energy balance equations as follows:

$$E_{generated} = E_{absorbed} \quad \rightarrow$$

$$\left\{ J^2_{Ag} \times \rho_{Ag} \times \frac{A_{Ag}}{A_{Ag} + A_{Cu}} + J^2_{Cu} \times \rho_{Cu} \times \frac{A_{Cu}}{A_{Ag} + A_{Cu}} \right\} \times time = m \times \left\{ \int_{50K}^{100K} C_P \cdot dT + C_P \times \Delta T \right\}$$

The total electrical resistance of the equivalent circuit is

$$R_{total} = \frac{R_{Ag} \times R_{Cu}}{R_{Ag} + R_{Cu}}$$

The current densities of the silver alloy and the copper are estimated based on the equivalent electrical circuit and are:

$$R_{Ag} = \frac{\rho_{Ag}}{A_{Ag}} = 4.84 \times 10^{-4}\, Ohms\ ,\ R_{Cu} = \frac{\rho_{Cu}}{A_{Cu}} = 5.91 \times 10^{-4}\, Ohms\ ,\ R_{total} = 2.66 \times 10^{-4}\, Ohms$$

$$J_{Ag} = \frac{I_{total} \times R_{total}}{A_{Ag} \times R_{Ag}} = 9.973 \times 10^{7}\ A/m^2\ ,\ J_{Cu} = \frac{I_{total} \times R_{total}}{A_{Cu} \times R_{Cu}} = 1.66 \times 10^{8}\ A/m^2$$

It is calculated that the maximum temperature that will occur in 10 seconds is T_{max} = 214 K.

The thermal conductivity of the AgAu(5%) alloy was measured in the laboratory using the previously described rig and is shown in figure 3.18.

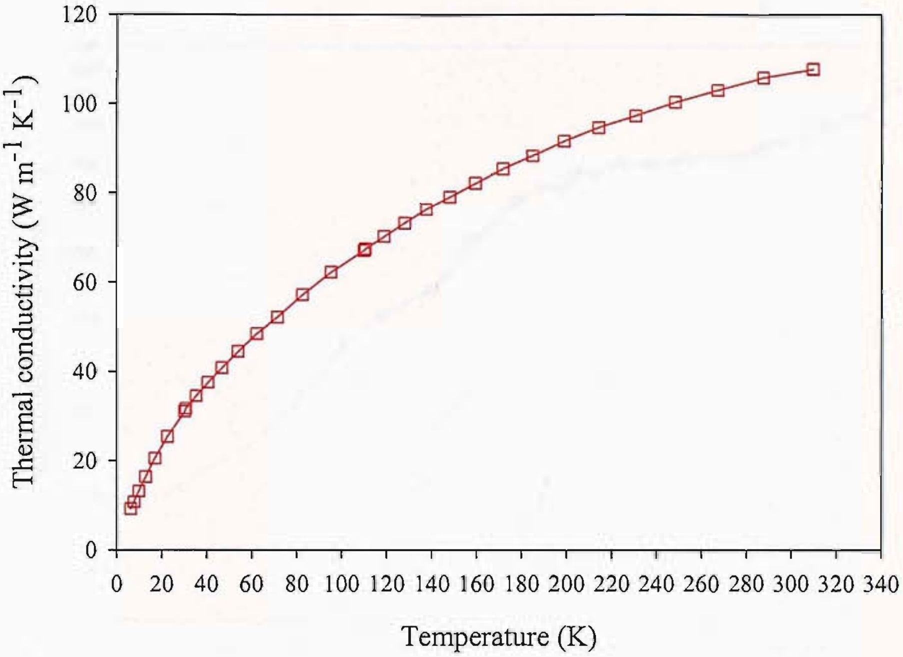

Figure 3.18. *Thermal conductivity of AgAu(5%) alloy*

The above function can be best fitted by the following polynomial:

$$k_{AgAu(5\%)}(T) = A_{AgAu(5\%)} + B_{AgAu(5\%)} \times T + C_{AgAu(5\%)} \times T^2 + D_{AgAu(5\%)} \times T^3 + E_{AgAu(5\%)} \times T^4$$

where the coefficients are tabled below:

$A_{AgAu(5\%)}$	2.8865
$B_{AgAu(5\%)}$	1.1622
$C_{AgAu(5\%)}$	-9.54×10^{-3}
$D_{AgAu(5\%)}$	5.4355×10^{-5}
$E_{AgAu(5\%)}$	-1.5744×10^{-7}

The conduction heat leak through the AgAu(5%) alloy is:

$$\dot{Q}_{4.2^oK}^{AgAu(5\%)} = \frac{A_{ASC}}{L} \times \int_{4.2^oK}^{50^oK} k_{AgAu(5\%)}(T) \cdot dT = \frac{46.8 \times 10^{-6}}{0.35} \times 1253 = 0.167 \text{ W}$$

The thermal conductivity of copper C 106 as measured in the rig is shown in figure 3.19:

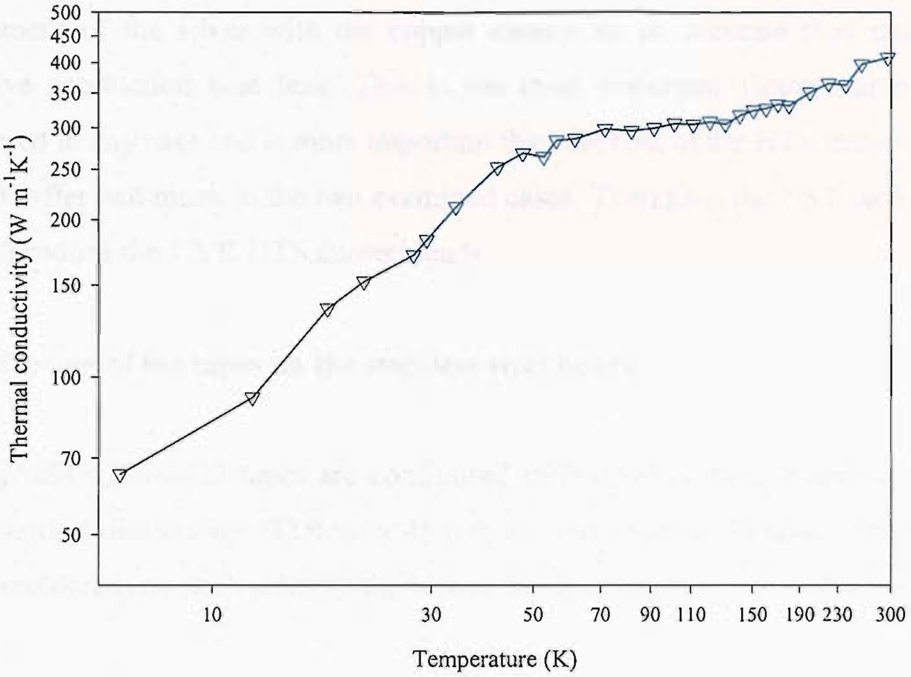

Figure 3.19. *Thermal conductivity of copper grade C 106*

The conduction heat leak through the copper alone is

$$\dot{Q}^{Cu}_{4.2\ K} = \frac{A_{Cu}}{L} \times \int_{4.2K}^{50K} k_{Cu}(T) \cdot dT = \frac{32.5 \times 10^{-6}}{0.35} \times 7000 = 0.65 \text{ W}$$

The conduction through the stainless steel board is:

$$\dot{Q}^{steel}_{4.2\ K} = \frac{A_{steel}}{L} \times \int_{4.2K}^{50\ K} k_{steel}(T) \cdot dT = \frac{8 \times 45 \times 10^{-6}}{0.35} \times 136 = 0.14 \text{ W}$$

Hence, the total conduction heat leak in this case is then

$$\dot{Q}^{total}_{4.2\ K} = 0.167 + 0.65 + 0.14 = 0.96 \text{ W}$$

The calculations have shown that the two cases are close enough to make a very definite decision. Nevertheless, the 1st choice guarantees lower conduction heat leak during steady state operation, as the silver alloy has about two times less thermal conductivity than the copper at this temperature range (4.2 K to 50 K) and the replacement of the silver with the copper cannot be so accurate thus resulting in excessive conduction heat leak. This is the most important factor that has to be considered in any case and is more important than the cost of the HTS material, which will not differ two much in the two examined cases. Therefore, the NST tape has been used to produce the 7.5 K HTS current leads.

3.5.4. Brazing of the tapes on the stainless steel board

The AgAu(4%)/Bi-2223 tapes are configured in 8 stainless steel boards as follows: Each board of dimensions (335mm x 45 mm x 1 mm) carries 26 tapes. The tapes are brazed (soldered) on both sides of the board, 13 on each side, as it is shown in figure 3.20:

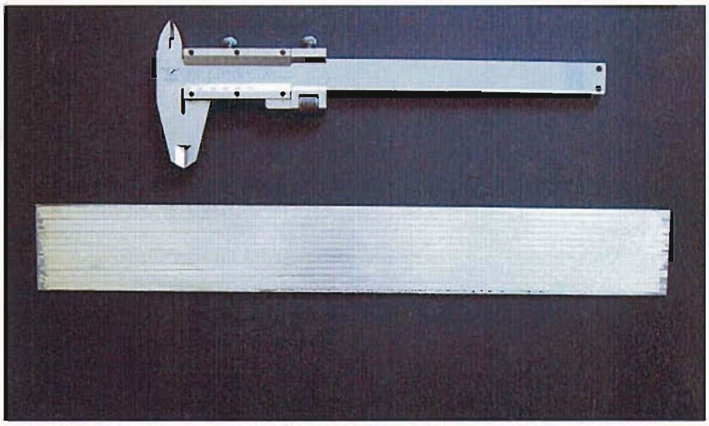

Figure 3.20. *Photo of the stainless steel board with the 13 brazed tapes on each side*

The stainless steel board has a very thin electrolytic deposition of tin solder layer which melts at 232°C. The tapes are cut in length of 35 cm and one side is polished softly with grinding paper and cleaned. Using Indium alloy flux, the tapes are stuck on the board aligned in parallel with their edges almost touching. Their ends were heated with the soldering iron in order to braze them on the steel board and secure its positions. A special "furnace" was made in order to be used for the brazing of the tapes on the boards (figure 3.21). The boards were sandwiched between two aluminum plates that have 8 cartridge heaters (4 on each) inserted in holes from the sides. Two layers of silicon rubber were intervened between the boards and the aluminum. A type T thermocouple was placed between the plates to record the temperature. The plates were bolted with 18 bolts, tight enough to ensure good thermal contact with the tapes and also to press the tapes against the steel boards for effective brazing without air pockets and "dry" joints. With the use of a temperature controller, the plates heated to 250°C for 10 minutes and then cool down.

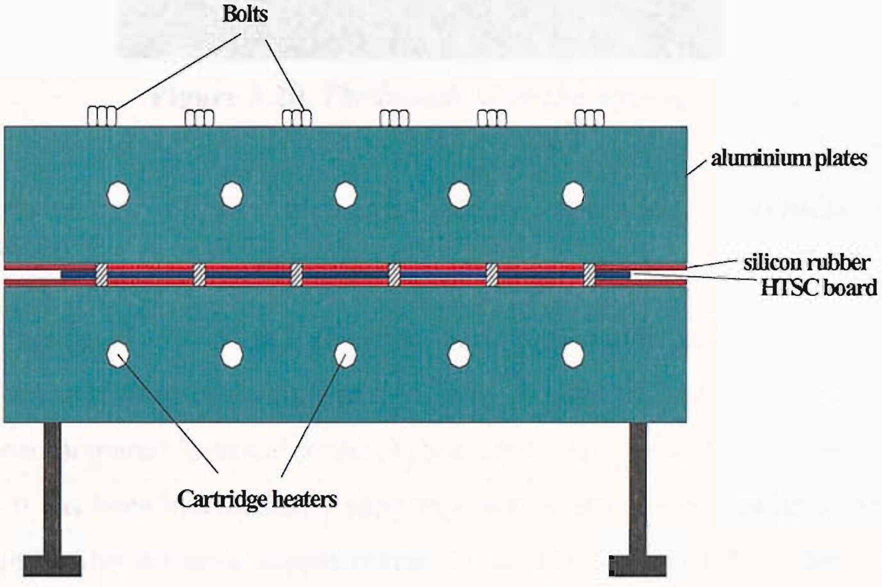

Figure 3.21. *Aluminium plates for brazing the HTSC boards and the temperature controller*

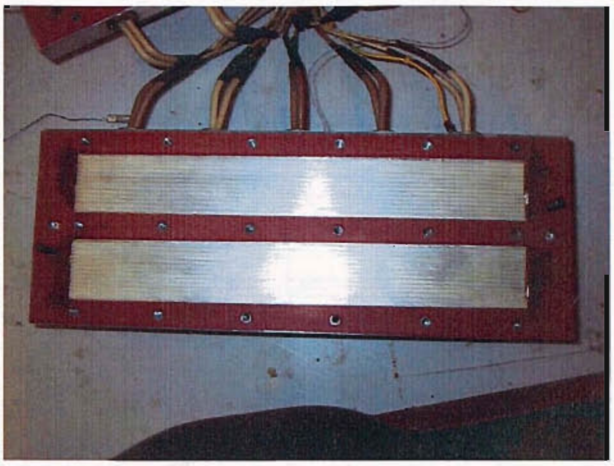

Figure 3.20. *The boards after the brazing*

3.5.5. Performance of the elements during operation – critical current measurements

The performance of the HTSC elements during operation has been assessed by measuring the self field critical current in LN_2. A strip of four tapes (two on each side) has been prepared identical to the HTS boards. Due to the mechanical weakness of the strip it has been mechanically supported with a steel tube in order to withstand the force applied by the thick copper current leads (for current of the order of 200 A) as in figure the figure 3.21.

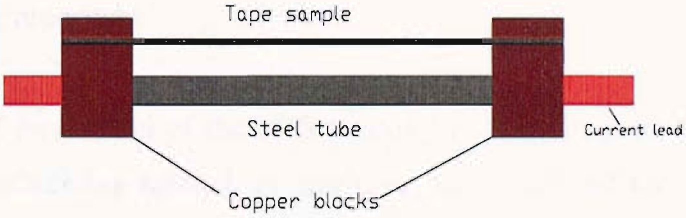

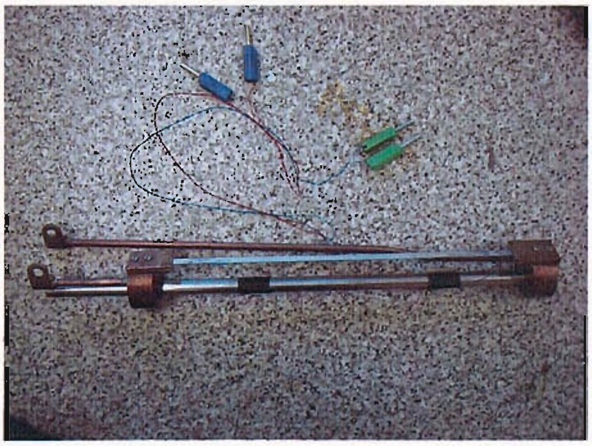

Figure 3.21. *Rig for the HTS element testing*

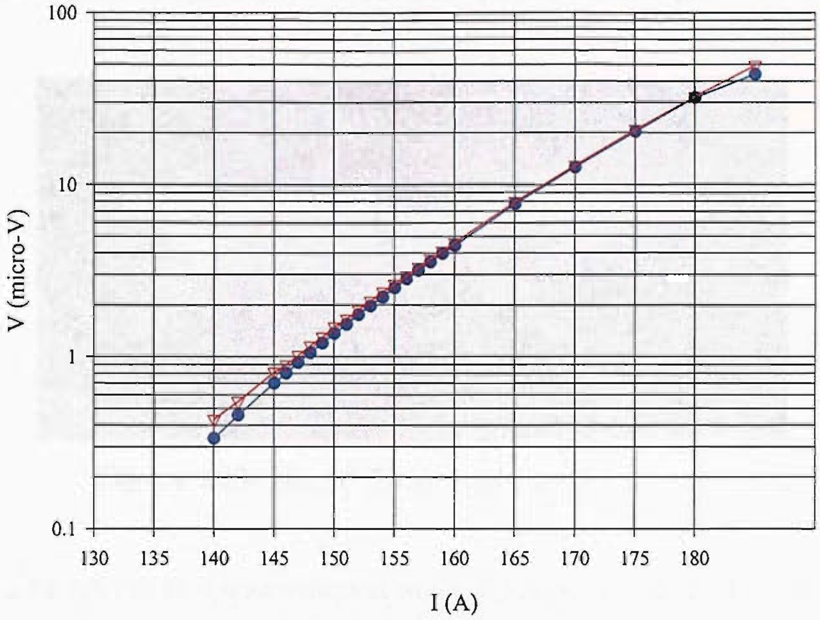

Figure 3.22. *I-V relation of the HTSC elements in self field and* LN_2

The measured critical current with the $1 \mu V/cm$ criterion in figure 3.22 is 148 A (lower than $4 \times 40 = 160A$); is reduced to the self magnetic field influence of the configuration. It is shown that the superconducting properties of the tapes have not been deteriorated during the brazing procedure.

This technique of production of the HTS boards has been innovative in the area of current lead manufacturing technology and successfully applied for the two 7.5 kA prototypes. It was proved to be a fast and efficient procedure thus allowing for its application for a massive production of HTS boards (during the manufacturing of the forty 7.5 kA current leads at Pirelli Cables Ltd) with the minimum of degradation in the delicate AgAu(4%)/Bi-2223 superconducting tapes.

3.5.6. Assembling of the HTS part

For the construction of the HTS assembly we followed a procedure that is described below: The 8 steel/HTS boards are soldered inside the grooves of the two copper blocks/terminals that connect the HTS part to the Cu 50 K terminal (figure 3.23) and the HTS part to the LTS NbTi Rutherford cable (4.2 K terminal).

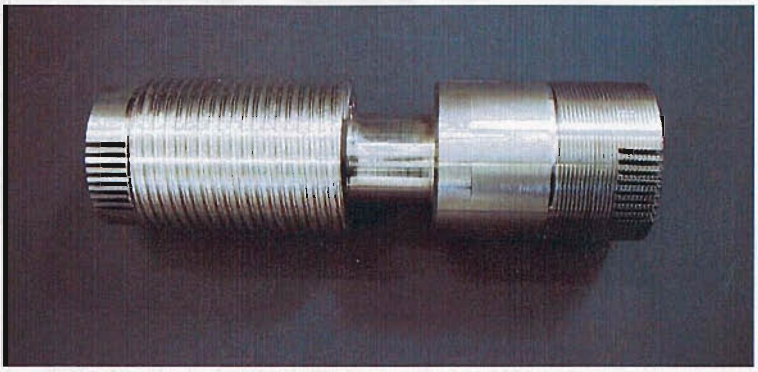

Figure 3.23. *The 50 K terminal Cu-HTS junction*

Firstly, the LTS NbTi cable was soldered in the 4.2 K terminal block with solder alloy Tin/Lead/Copper of high melting point (300 K). The joint HTS/steel boards inside the grooves of the Cu 4.2 K terminal is made by solder alloy tin/lead/silver (2%) of melting point 186°C in order to preserve the soldered contact of the tape on the steel board which melts at 232°C. The HTS part was enclosed within a rectangular box framed by four Tufnol® plates that were glued around the 8 boards with Eco-Bond (figures 3.24, 3.25). The box has the function to guide the cold helium gas to flow along the HTS plates for heat exchange.

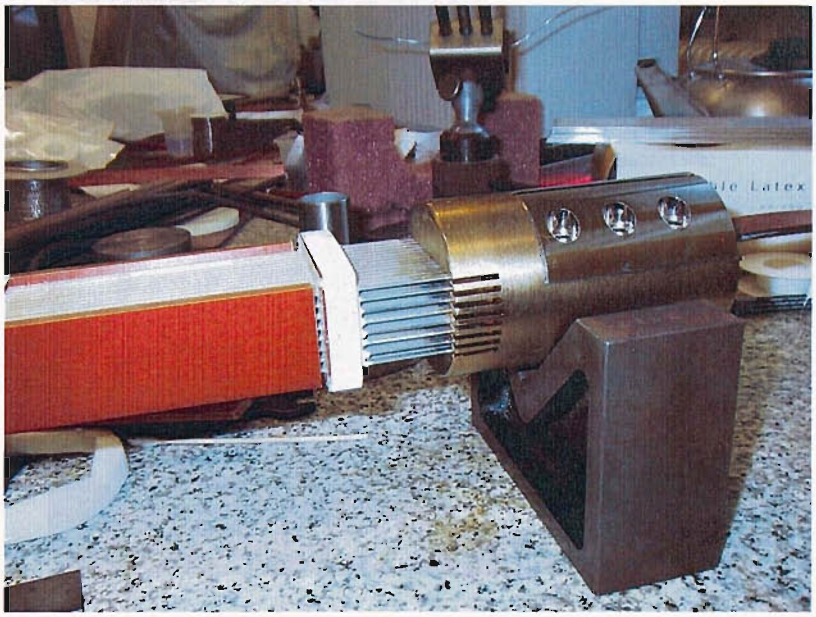

Figure 3.24. *The HTS/steel boards in the grooves of the 4.2 K terminal and the Tufnol® box half made*

Figure 3.25. *The HTS part with the LTS Rutherford cable soldered in the 4.2 K terminal*

The resistive and HTS assembly were joined by soldering the Cu-plates in the grooves of the Cu 50 K terminal (figure 3.26) following a similar procedure as in the soldering of the Cu plates to the room temperature termination ear.

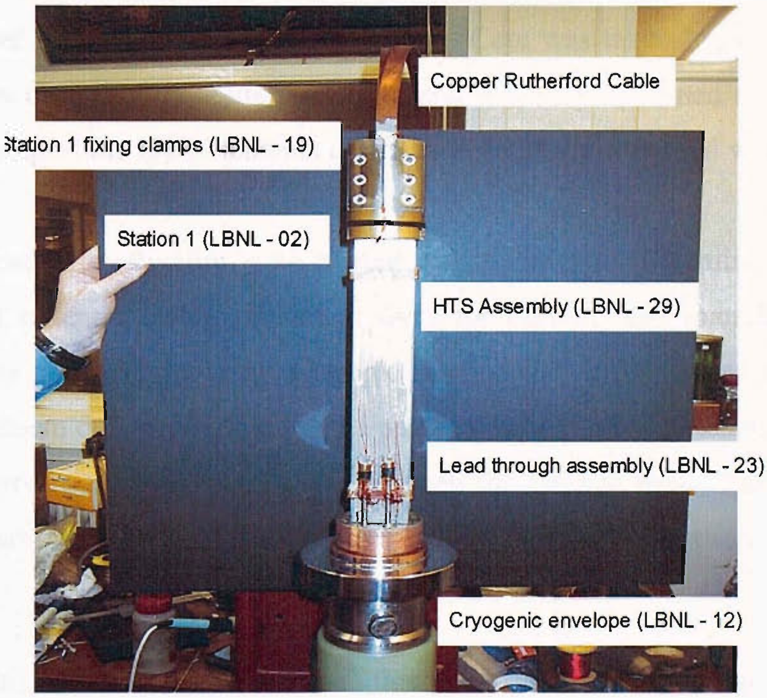

Figure 3.26. *The HTS part soldered in the two copper terminals (50 K and 4.2 K) without the Tufnol® box*

The assembling procedure of the current lead consists of continuously repeated soldering processes. The soldered electromechanical joints provide adequate mechanical strength with excellent current transport properties. It was essential that the joints between the Cu plates and the room termination ear, the Cu plates and the 50 K terminal Cu block, the HTS elements and the 50 K terminal block, the HTS elements and the 4.2 K terminal Cu block and the NbTi cable and the 4.2 K Cu block terminal had a low electrical resistance. The quality of the joint will determine the electrical contact resistance which has to be kept low in order to avoid heat dissipation that will increase the heat leak. The electrical resistance of the joint is determined by the following factors:

- Contact area of the joint
- Thickness of the solder layer between the two interfaces
- Electrical resistivity of the solder used
- Wetting properties of the solder between the two interfaces

The Cu plates are designed to fit into the grooves of the Cu termination ear and 50 K terminal; this is to provide a large area for current transfer. The groove dimensions were designed so that the Cu plate could be inserted easily during assembly but so that the solder layer was not excessively thick. Care was taken to ensure all wetted surfaces were clean before soldering began and that they remained cleaned. Similar for the soldering of the HTS elements to the 50 K and 4.2 K terminal were applied.

An experimental investigation was carried out in order to determine the electrical resistivity of potential solder materials used for current lead manufacturing. The measurements are carried out by a simple method that is known as the four point method. A known d.c. electrical current I passes through a well geometrically defined sample (of cross section A and length between the voltage taps L) and the voltage drop V is measured. The electrical resistivity is obtained by the relation

$$\rho = \frac{V}{I} \cdot \frac{A}{L}$$

The rig for this measurement is shown in figure 3.27. The copper flange is screwed on the 2^{nd} stage of the cryocooler.

Figure 3.27. *Rig for electrical resistivity measurements*

The sample holder is a disk of sapphire which is glued on a cylinder made of copper thin foil as in figure 3.27. The thin copper foil has also cuts along its perimeter in order to increase its flexibility and will allow for differential thermal contraction between the copper and the sapphire without the danger of losing the thermal contact. Sapphire is a good thermal conductor and an electrical insulator so it is very suitable for used as a sample holder. The results are displayed in figure 3.28.

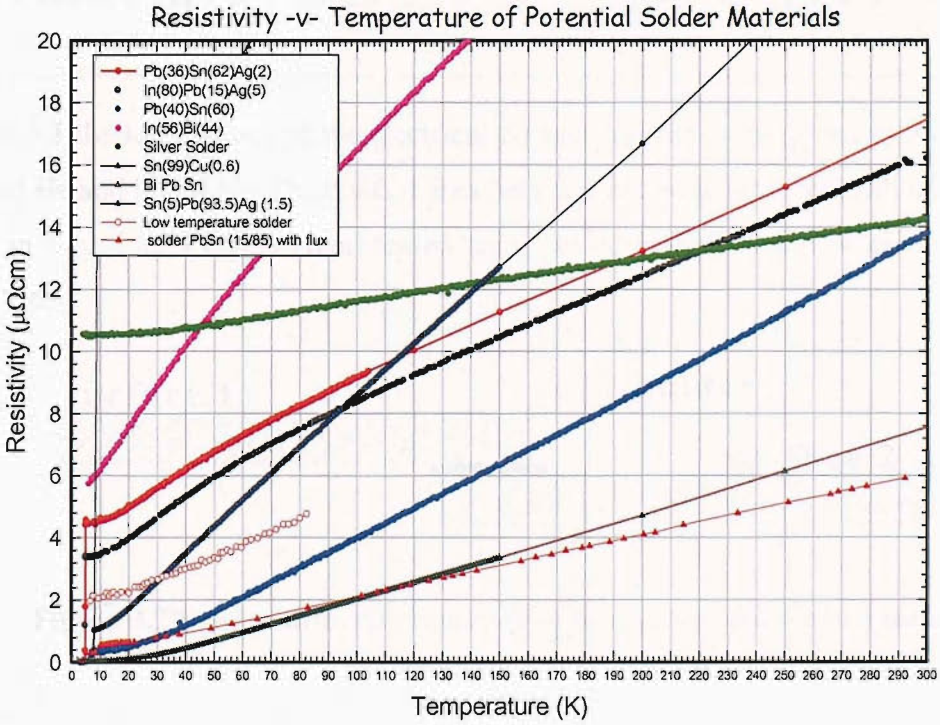

Figure 3.28. *Electrical resistivity of potential solder materials for current lead manufacturing as a function of temperature*

The electrical contact resistance between various interfaces that appear in the current lead was measured in LN_2 and LHe. The interfaces that were examined are:

1. NST tape/Silver solder/NST tape
2. ASC stack of four tapes/silver solder/ASC stack of four tapes
3. Silver coated Cu/silver solder/silver coated Cu
4. Non-magnetic Ni coated Cu/silver solder/non-magnetic Ni coated Cu

The above coatings were performed in order to investigate the effect of the metal coating to the electrical contact resistance and find which coating can reduce its value.

Table 3.1. *Total values of the electrical contact resistance*

contacts	**NST (tape-tape)**	**Stack-stack**	**Ag plated Cu block**	**Ni plated Cu block (non-magnetic)**
LHe	$1.7204\times10^{-8}(\Omega\cdot cm^2)$	$1.379\times10^{-8}(\Omega\cdot cm^2)$	$3.724\times10^{-9}(\Omega\cdot cm^2)$	$7.196\times10^{-8}(\Omega\cdot cm^2)$
LN_2	$3.944\times10^{-8}(\Omega\cdot cm^2)$	$3.2\times10^{-8}(\Omega\cdot cm^2)$	$1.568\times10^{-7}(\Omega\cdot cm^2)$	$2\times10^{-7}(\Omega\cdot cm^{-2})$

In table 3.1 the total values of the electrical contact resistance are given as measured in liquid He and liquid N_2. The contact area between two joint surfaces with a layer of solder in figure 3.29 can be represented using an equivalent electrical circuit as in figure 3.30.

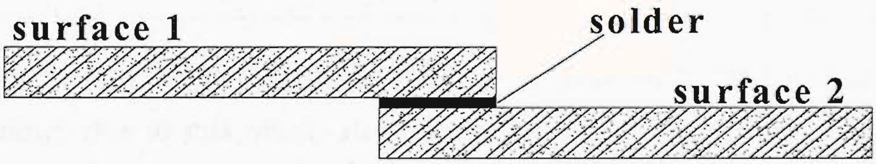

Figure 3.29. *Schematic representation of he contact between two surfaces*

Figure 3.30. *Equivalent electrical circuit of the figure 3.29*

In figure 3.30, R_C is the electrical contact resistance between the surface and the solder layer and R_S is the contribution of the solder to the value of the total electrical resistance. The value of the electrical resistivity of the solder at 4.2 K is about $\rho_s \approx 10.2 n\Omega \cdot cm \approx 10^{-8} \Omega \cdot cm$.

$$R_{total} = 2 \times R_C + R_S$$

From the above equation the value of R_C is extracted. The solder electrical resistance per cm^2 is calculated by the relation $R_S = \rho_S \cdot \frac{\delta}{S}$, where $S = 1cm^2$ and δ is the thickness of the solder layer. In this way the contributions of the two terms in the above equation can be estimated.

Table 3.2. *Calculated contributions ρ_C and ρ_S. A_C is the contact area*

Contacts	**NST (Tape-Tape)**	**ASC Stack - Stack**	**Ag plated Cu block**	**Ni plated Cu block (non-magnetic)**
δ and A_C	$20\mu m$ $0.22cm^2$	$10\mu m$ $0.209cm^2$	$100\mu m$ $0.28cm^2$	$100\mu m$ $0.28cm^2$
LHe ρ_S	$2\times10^{-11}(\Omega\cdot cm^2)$	$1\times10^{-11}(\Omega\cdot cm^2)$	$2.856\times10^{-11}(\Omega\cdot cm^2)$	$2.856\times10^{-11}(\Omega\cdot cm^2)$
ρ_C	$8.592\times10^{-9}(\Omega\cdot cm^2)$	$6.89\times10^{-9}(\Omega\cdot cm^2)$	$1.847\times10^{-9}(\Omega\cdot cm^2)$	$7.837\times10^{-8}(\Omega\cdot cm^2)$
LN$_2$ ρ_S	$2\times10^{-11}(\Omega\cdot cm^2)$	$1\times10^{-11}(\Omega\cdot cm^2)$	$2.856\times10^{-11}(\Omega\cdot cm^2)$	$2.856\times10^{-11}(\Omega\cdot cm^2)$
ρ_C	$1.971\times10^{-8}(\Omega\cdot cm^2)$	$1.5995\times10^{-8}(\Omega\cdot cm^2)$	$7.838\times10^{-8}(\Omega\cdot cm^2)$	$10^{-7}(\Omega\cdot cm^2)$

The silver coating is more effective in reducing the electrical contact resistance than the Ni coating. Due to this result, all the copper parts of the current lead that are involved in soldering were coated with a silver layer.

The cylindrical Cu block (4.2 K terminal) has a spiral like groove on the outer surface for flow of cold helium gas. In order to enhance the flow of the helium gas between the Cu plates of the heat exchanger/conductor, the resistive assembly was wrapped with fibre-glass. GE varnish was mixed with solvent to a ratio 30:70. This mixture was paint onto the surface of the fibre-glass sheet and then allowed to dry. The fibre-glass sheet was then coated with a layer of Stycast 1261, ensuring that the Stycast penetrates into the fibre-glass. The wet fibre-glass was wrapped around the resistive assembly. Also PTFE tape was wrapped tightly along the length of the wrapped with fibre-glass resistive assembly in order to keep the fibre-glass closely wrapped when drying. The intermediate region between the resistive assembly and the termination body was also wrapped with wet fibre-glass. The resistive and HTS assemblies are enclosed in G-10 insulating cylinders as shown in figure 3.31.

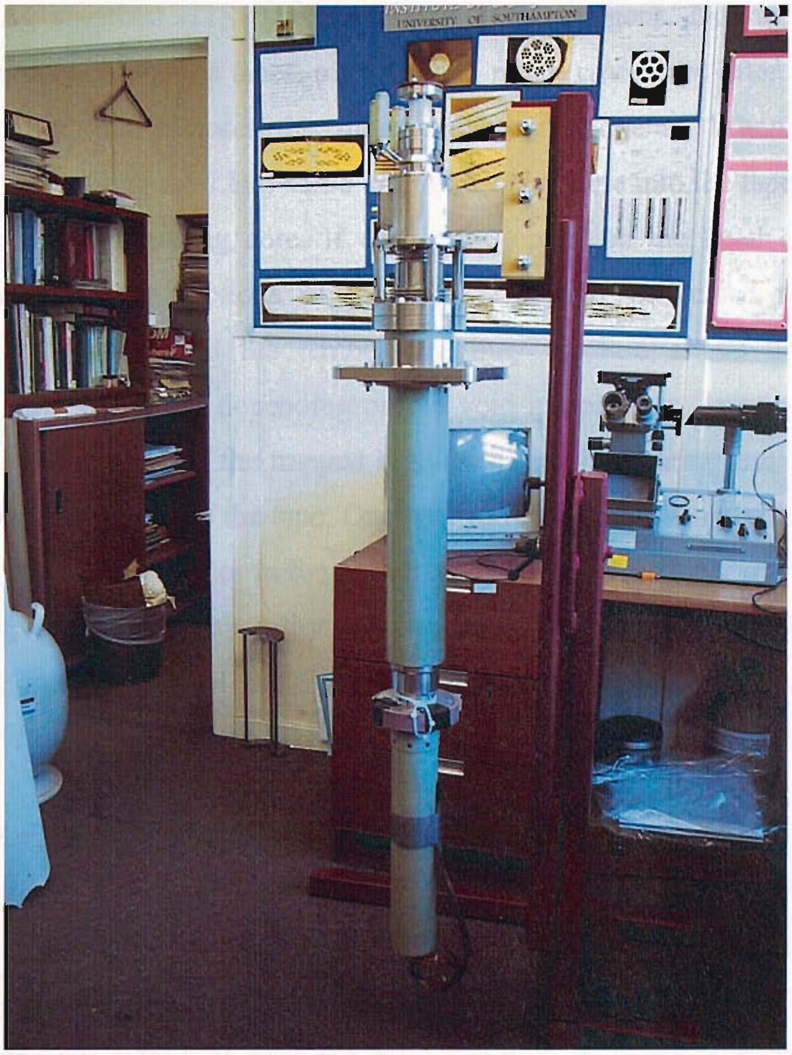

Figure 3.31. *The 7.5 kA current lead ready*

3.6. Bloating test for the HTS elements of the current leads

The good quality of the tapes in the HTS elements of the current leads is of major importance since any deterioration of their superconducting transport properties will result in current flow through the sheath material. Due to resistive heating of the sheath the temperature of the HTS element will rise and the element will eventually burn unless the current is switched off. One possible cause of this deterioration can be the bloating of the tapes. Bloating/bubbling is a well-recognized problem which may arise using Ag sheathed HTS tapes in contact with cryogens. Due to the thermo-mechanical processing of the tapes, pinholes and micro cracks are often produced in the silver matrix that encloses the superconducting filaments. When the tape is immersed in a cryogen (e.g. LHe) some liquid may permeate into the tape through the voids in the superconducting core. If during the operation the level of the liquid cryogen changes, some sections of the tape previously immersed may become exposed to the vapour and the temperature may increase above the saturation temperature. In some cases, depending on the void morphology, large pressures are generated by vaporization of the trapped liquid resulting in bloating and deterioration of the transport properties of the tape. One way to reduce significantly the possibility of bloating is to block pinholes in the sheath using a protective layer of G.E. varnish. In order to investigate the suitability and performance of the coated tapes that were used for the manufacture of the HTS elements of the 7.5 kA current leads, an experimental study has been carried out.

Apparatus for bloating test

Figure 3.32 shows the experimental set-up that was used during this investigation. The mounted sample was moved to positions above and below the LHe level by means of a stainless steel tube operated manually from the room temperature end. A second telescopic tube allowed for the adjustment of the sample according to the LHe level.

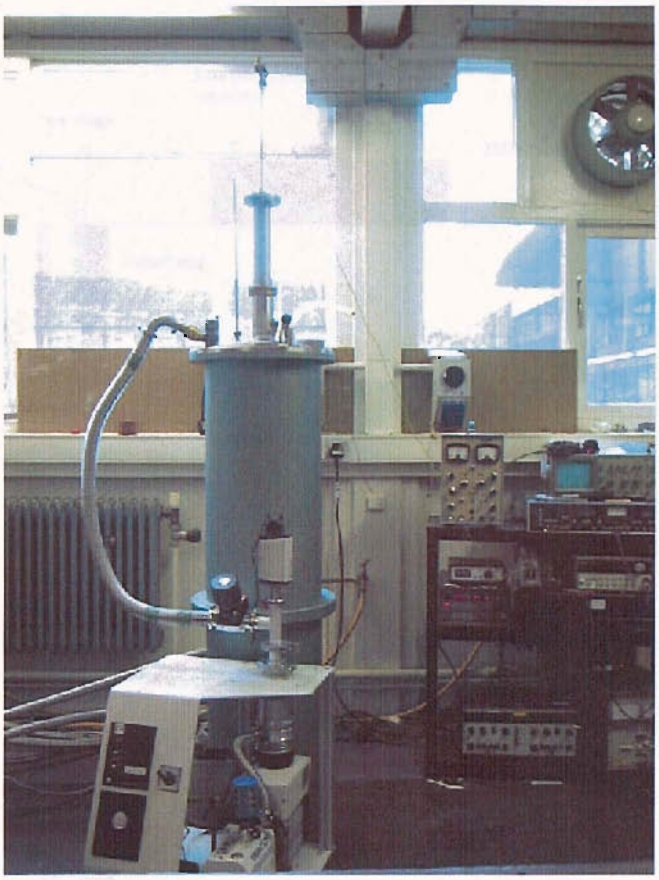

Figure 3.32. *Experimental set-up*

Sample holder and configuration

Figure 3.33 shows the cross sections of the configuration used for the sample mounting. Five pieces of the tape 295 mm long that will be used for the construction of the current lead were brazed onto the outer surface of a stainless steel ring electrodeposited with tin/lead solder using the same method as were proposed for the assembling of the HTS elements of the leads (see above). A 12 mm gap was left between the ends of the tapes. The rings were then mounted onto a Tufnol^{TM} cylinder with a 1 mm gap between rings. The tapes were then connected in series with Copper strips as shown in figure 3.34. Two voltage taps were attached to each tape at a distance of 15 mm away from the current injection points. The assembled tapes are shown in figures 3.35-3.36.

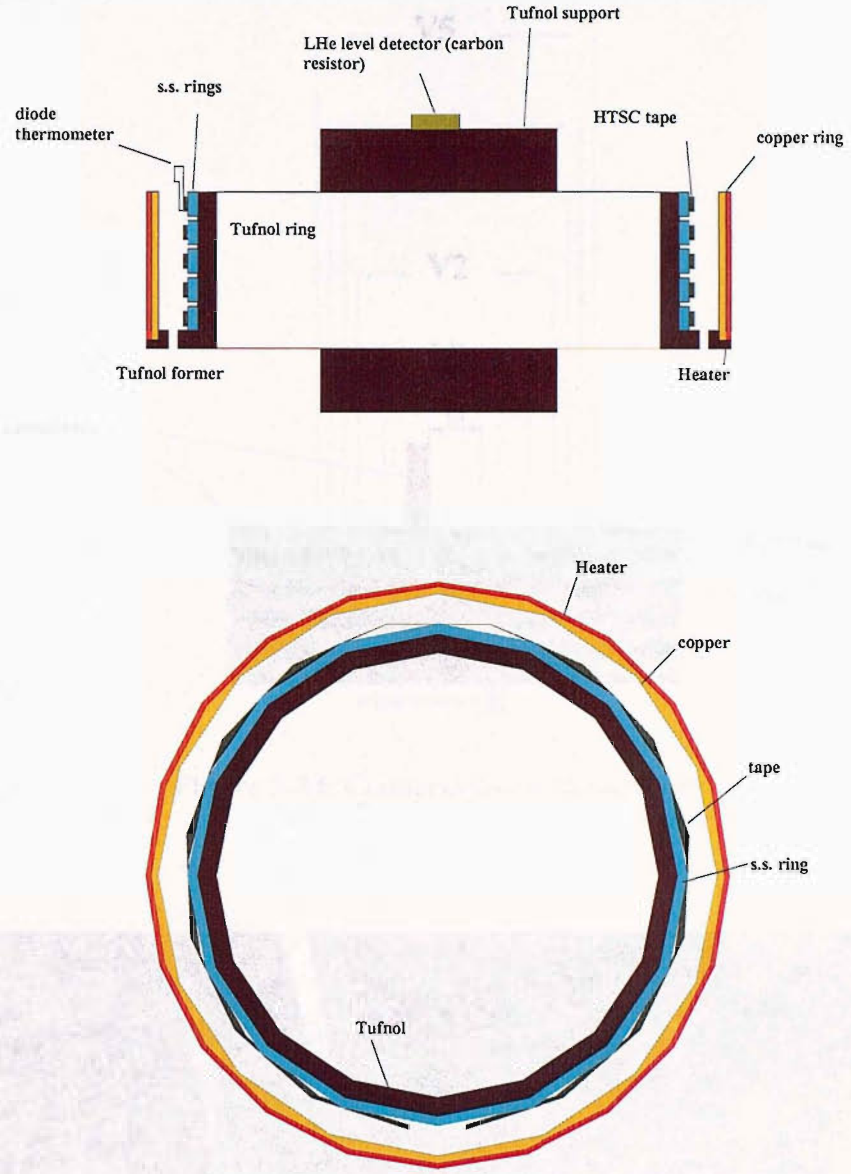

Figure 3.33.*Cross section of the sample holder and samples*

To reduce the effect of magnetic field in the tape electrical properties, current injection into the adjacent tapes was applied from opposite ends (figure 3.34).

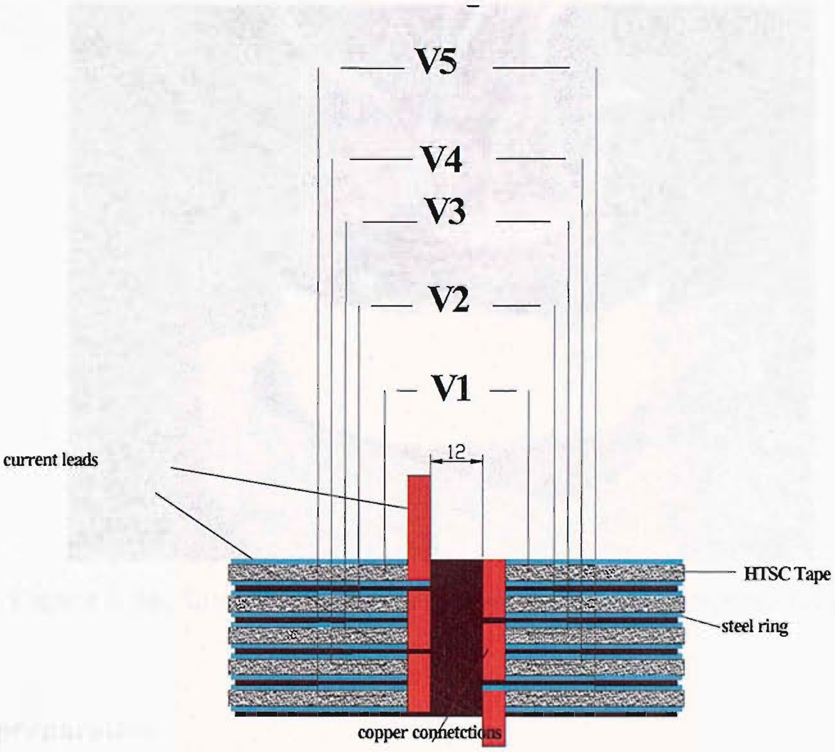

Figure 3.34. *Connections on the samples*

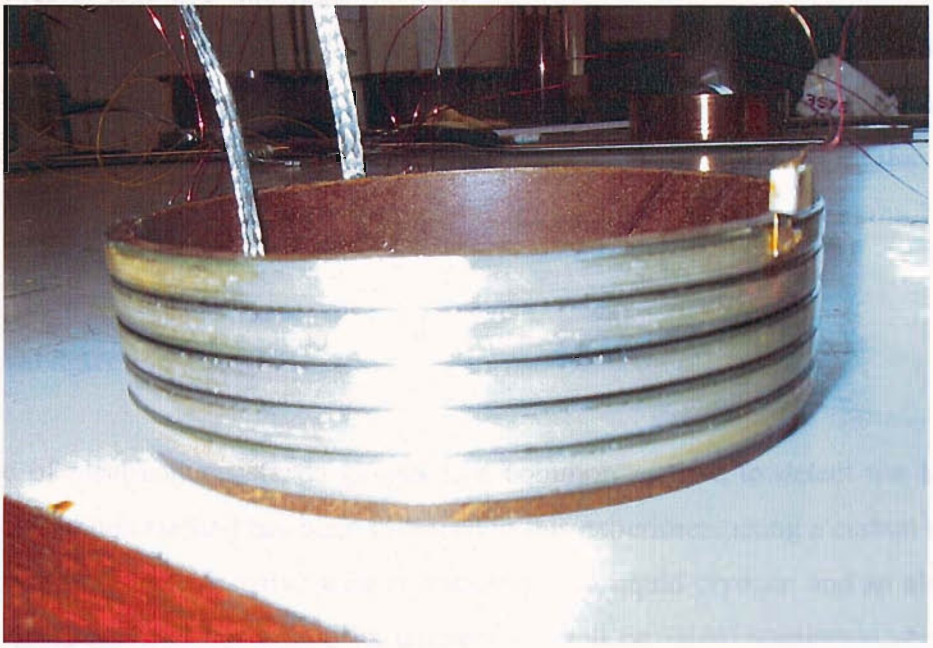

Figure 3.35. *Tape samples on the Tufnol ring. The Silicon Diode thermometer can be seen attached on the top tape (within the silver protecting casing)*

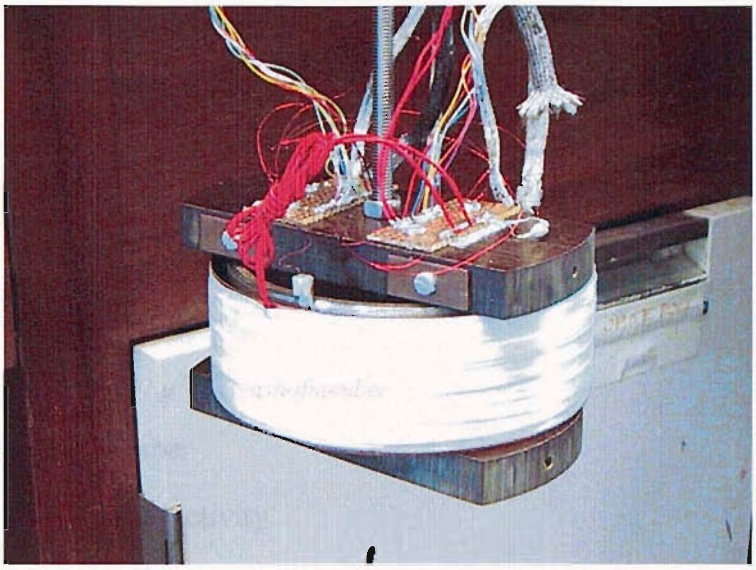

Figure 3.36. *Sample mounted with the heater on the sample holder*

Sample preparation

Five rings were made from a strip of the steel plate that had been electrodeposited with a layer 5 μm of tin solder (melting point 232°C) from both sides of the plate. Five pieces of tape 295 mm long were cut and polished in one side. Then they were rolled around the rings and the two ends were brazed using a soldering iron onto the rings. The rings were heated in a furnace to 250°C for 30 minutes in order to braze the tapes (procedure identical to the manufacturing of the HTS part of the 7.5 kA current leads). After the brazing they were placed equally spaced around the Tufnol® former.

LHe level detection

The use of electrical resistance gauges is a common method to detect the level of cryogens and this method has been followed in this experiment using a carbon resistor as a detector. When a resistive wire is immersed in a liquid cryogen and an electrical current is transmitted through it, its temperature will be raised somewhat above the temperature of the fluid in which the wire is immersed. The convective heat transfer coefficient for a liquid is one or two orders of magnitude greater than that of a vapour so when the wire is exposed to the vapour its temperature will be greater than when the wire is immersed in the liquid. By recording the electrical resistance of the heated wire while it is slowly raised through the liquid, the moment in which the wire passes the liquid-vapour interface can be detected. The free-convection heat transfer is given by the relation

$$h_C = {(2k_t/D)}\Big/{\ln\left(1+\phi N_{Gr}^{-1/4}\right)}$$

where $\phi = 3.70(N_{\mathrm{Pr}} + 0.952)^{1/4} N_{\mathrm{Pr}}^{-1/2}$

$N_{Gr} = g\beta_t \rho^2 D^3 \Delta T / \mu^2 = Grashofnumber$

N_{Pr} =Prandtl number

K_t = thermal conductivity

D = wire diameter

β_t = thermal expansion coefficient

ρ = density

μ = viscosity

ΔT = temperature difference between wire and fluid

Application of values of the variables for nitrogen, i.e. N_2 gas at 1 atm and 77°K, k_t=7.23 $mW/m^{-1}\cdot K^{-1}$ and N_{Pr} = 2.32. For Grashof number of 2.0 and a wire diameter of 0.25 mm, we have

$$h_C = 36\, {W}\!/\!{mK} \text{ (gaseous nitrogen)}$$

$$h_C = 845\, {W}\!/\!{mK} \text{ (liquid nitrogen)}$$

For the same heat-dissipation rate, the difference in temperature between the wire and the surrounding vapour will be approximately $845/36 = 23.5$ times the temperature difference when the wire is immersed in the liquid. This method has been tested experimentally using a sensor made from an Allen-Bradley carbon resistor, for indicating the level of liquid helium. The sensor has been developed so that its signal changes by 100% on passing through the vapour-liquid interface when the heat release in the liquid is W_l=4.9 mW and by 60% when W_l=1.6 mW. The accuracy with which the level is determined is ≤0.2 cm. The position of the carbon resistor on the sample assembly in our experiment is shown in figure 3.33 and approximately the measured electrical resistances of the carbon resistor in and out of the liquid helium as have been measured with the voltmeter are 1.242 kΩ and 1.072 kΩ respectively. To determine the LHe level during the experimental procedure a multi-meter was continuously measuring the electrical resistance of the carbon resistor. The resistor was positioned at the top of the assembly. This made immersion to LHe easy to verify. On removal from LHe the length of the assembly had been added to the distance travelled after the resistor left the LHe.

G.E. varnish impregnation of the tapes in vacuum

The tape assembly was coated with G.E. varnish using the technique of vacuum impregnation. The sample was placed in a glass pot inside a desicator having a copper tube on top with a sliding O-ring seal, for the entrance of the G.E. varnish. A rotary pump was used to pump the desicator. While pumping, a rubber tube immersed in a bottle full of G.E. varnish was applied to the copper tube; the pressure difference caused the liquid G.E. varnish to be transferred through the tube inside the pot in the desicator thus having the sample fully immersed in the liquid G.E. varnish. The advantage of using this procedure was that any possible pinholes on the tape's silver sheath surface were vacuumed thus allowing the liquid G.E. varnish to enter and heal them completely. Any trapped air inside the liquid G.E. varnish in the pot escaped through bubbles while pumping. After finishing the procedure, the sample was taken out of the desicator and was left to dry.

Instrumentation

The instruments used were the following:

1. Power supply for the sample heater
2. A multi-meter for the measurement of the carbon resistor electrical resistance to detect the LHe level.
3. A 10 μA current source for the supply of the sample's silicon diode thermometer.
4. A Keithley digital voltmeter for the recording of the diode voltage.
5. A digital chronometer to measure the sample heating up and cooling down time.

In order to control the rate of temperature increase after removing the sample from the LHe a foil heater of value 57 Ω was thermally attached to the exterior of a thin walled

Copper cylinder close enough to allow heating of the sample as it can be seen in figure 3.33.

Experimental Procedure

After assembling as described in the previous section, the I-V characteristics of each tape were measured in liquid nitrogen. The liquid helium tests were carried out as follows: The sample assembly was immersed in the LHe. After thermal equilibrium has been reached, the assembly was lifted to a level of 150 mm above the LHe level. The heater was then powered to a predetermined level in order to raise the sample temperature to 15 K in approximately 20 seconds. The heater was then switched off and the sample assembly then re-immersed in the LHe for 5min. This cycle was then repeated 30 times. After the final cycle, the I-V characteristics of each tape were measured again in liquid nitrogen. The procedure did not produce any obvious deterioration on the tape as it was confirmed by visual inspection after the I-V measurement. The I-V relations are shown in the figures (3.34-3.38) below in a semi-log scale (V-log, I-linear).

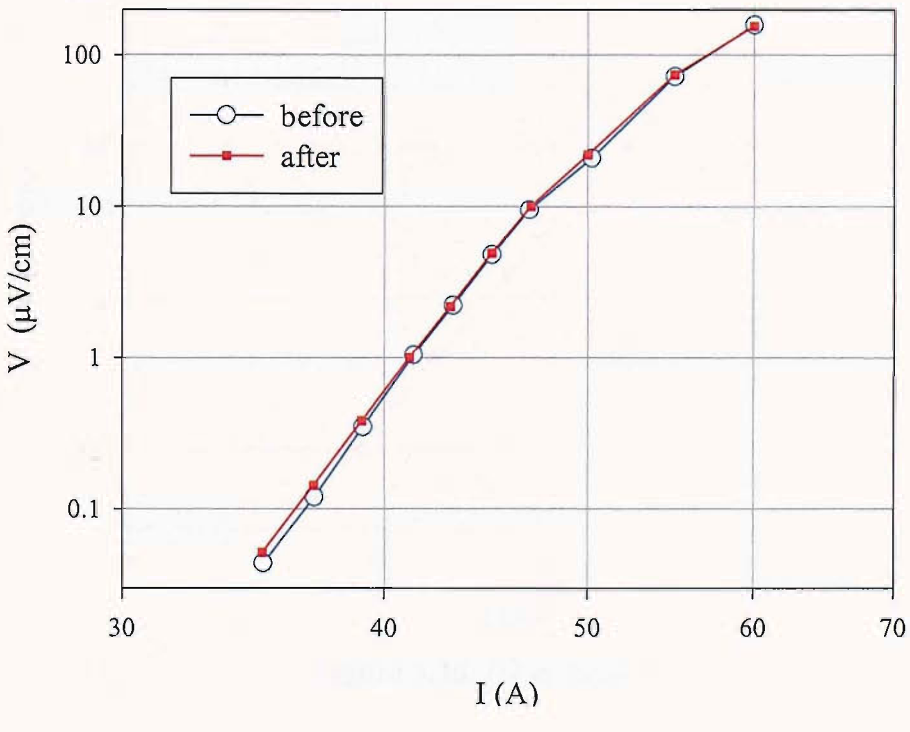

Figure 3.34. *I-V of tape 1*

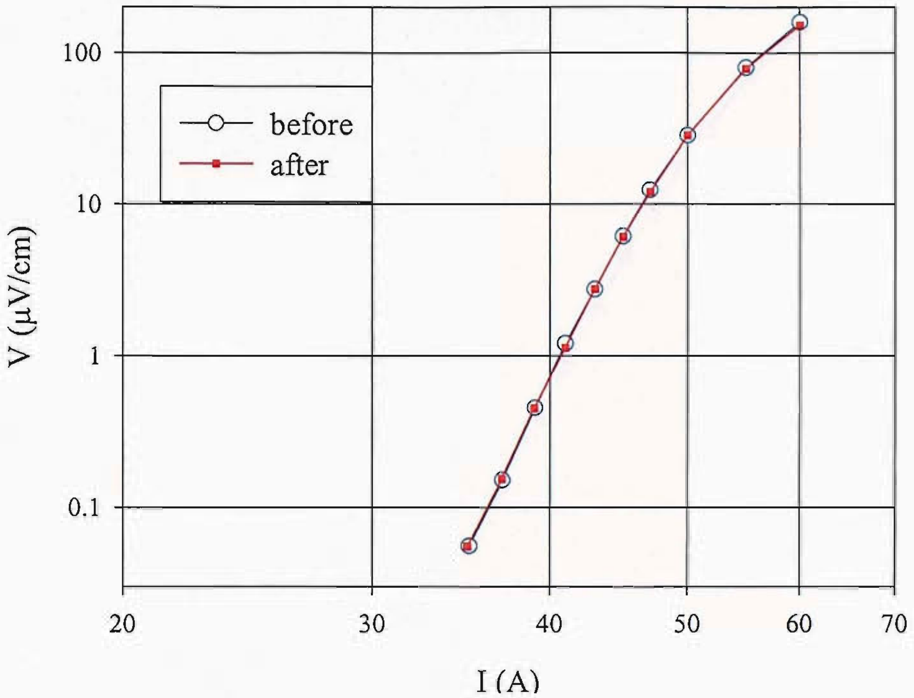

Figure 3.35. *I-V of tape 2*

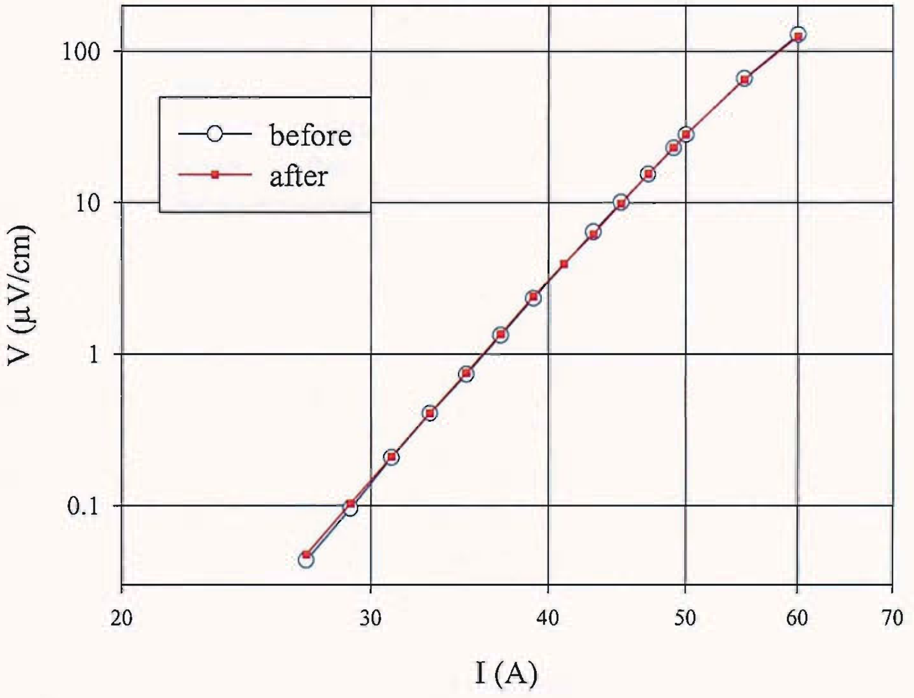

Figure 3.36. *I-V of tape 3*

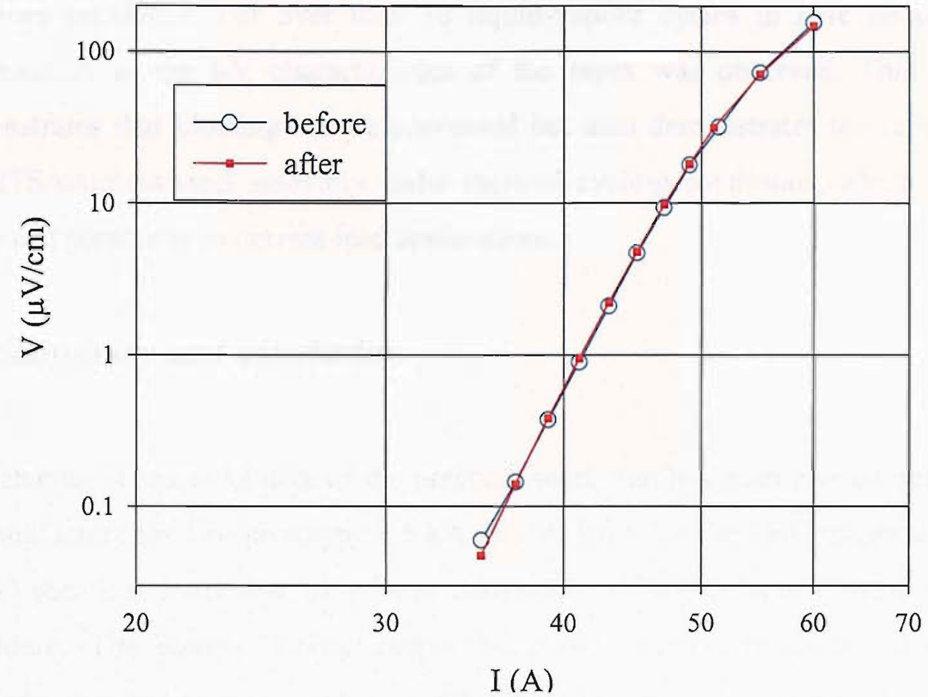

Figure 3.37. *I-V of tape 4*

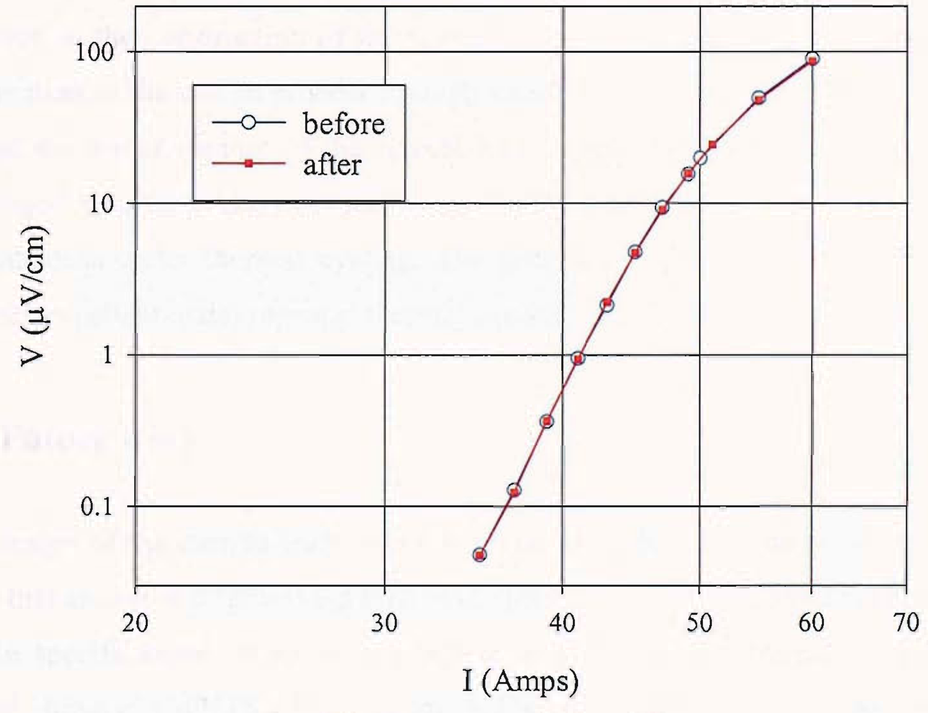

Figure 3.38. *I-V of tape 5*

Conclusively, using vacuum impregnation of G.E. varnish the occurrence of bloating has been prevented. For over than 30 liquid-vapour cycles in LHe no detectable deterioration in the I-V characteristics of the tapes was observed. This not only demonstrates that bloating can be prevented but also demonstrates the reliability of the HTS/stainless steel assembly under thermal cycling conditions, which is a very important parameter in current lead applications.

3.7. Summary and conclusion

This chapter is representative of the practical work that has been carried out in order to manufacture the two prototype 7.5 kA current leads for the LHC magnets and also the 40 identical leads that have been manufactured in the factory using the same procedure. The manual labour cannot be expressed in writing not the various problems that had to be solved during the manufacturing. The technical staff in the factory had to be guided through the manufacturing stages, with emphasis on the fabrication of the HTS elements. A cryogenic station was designed, built and set-up in order to measure the thermal conductivity and electrical resistivity of materials involved in the construction of the current leads. The measurements provide useful information in the design process through selection of the most suitable materials for an optimised performance of the current lead. A test cryostat has been designed and developed in order to carry out routine test of the performance of the HTS part of the current leads under thermal cycling. The tests have shown that the HTS elements perform excellent under repeated thermal cycling.

3.8. Future work

The design of the current leads is not a trivial procedure. Of course there is a basic route that always is followed but then many parameters can be altered in order to meet certain specifications. Work is in progress now for the construction of conduction cooled binary Cu/HTS/LTS current leads that will be used to feed MRI superconducting magnets by the company Magnex Scientific in UK. The resistive part consists of 8 Cu wires of diameters 1.5 mm. The Cu wires are soldered inside holes in the 50 K terminal/thermal anchor block. The HTS part consists of a stainless steel strip of dimension 9.2 mm x 130 mm that has electrolytic deposition of tin solder in order to braze four NST 50 A Ag/Bi-2223 tapes (two on each side). The HTS board is soldered inside a groove to the 50 K terminal from one end and to the 4.2 K terminal Cu block from the other end. Eight NbTi wires are soldered inside holes into the 4.2 K terminal from the opposite side of the HTS board insertion. A stainless steel tube is glued with Eco-Bon around the HTS part for protection. A gold-coated Cu clamp is used to thermal anchor the 50 K terminal which is electrically insulated via a Kapton sheet of thickness 25 μm.

It can be said that in this section of the thesis, the manufacturing stage of HTS current leads has been addressed. Due to time limitation, it was not possible to develop and solve a model. The analysis of the behaviour of the current leads under different conditions of operation is interesting, not only as a useful and necessary tool in the design procedure but as well as an academic exercise. Quite often, the current leads are modelled theoretically and the problem of heat transfer in the current leads is solved. The fundamental mathematical formulation for the analysis of current leads has been presented in the section 3.3 of this chapter and it is the basic frame for modelling of current leads. Through computer calculations is possible to predict the thermoelectric behaviour of current leads. Numerical optimisation techniques are complicated and require extensive study; there is a separate branch of engineering that deals with optimisation based on expertise optimisation methods. A method for solving the heat balance equation based on solution of differential equations with the use of neural network optimisation methods is being developed in MAT-LAB. The steady state analysis has already been solved. Currently, the work is focusing towards the development of codes to deal with transient problems. Also, the option to include all the various factors that constitute a complete current lead as well as different heat exchanger structures is being studied.

References

[1] M. Wilson, ***"Superconducting Magnets"***, Oxford Science Publications, Clarendon Press, Oxford (1983), ISBN 0-19-854810-9

[2] H. Lee et al, ***IEEE Trans. Appl. Supercond.***, vol. 11, no. 1, Mar. 2001, pg. 2539

[3] Hyun-Man Jang et al, ***IEEE Trans. Appl. Supercond.,*** vol. 11, no. 1, March 2001, pg. 2547

[4] N. Siegel, ***Overview of the LHC Magnets Other than the Main Dipoles, Proceedings of EPAC 2000***, Vienna, Austria

[5] M Putti et al, ***Supercond. Sci. Technol.*** 14 (2001) L1-L3

[6] Hyung Sang Park et al, ***IEEE Trans. Appl. Supercond.,*** vol. 11, no. 1, March 2001

[7] H. Fujishiro et al, ***IEEE Trans. Magn.*** Vol. 30, no. 4, July 1994

[8] Putti M. et al, ***Physica C*** 341-8 (2000) pg. 2585

[9] Putti M. et al, ***Proc. ASC 2000***, 17-22 Sept. 2000 (Virginia Beach)

[10] Park H. S. ***Proc. ASC 2000***, 17-22 Sept. 2000 (Virginia Beach)

[11] J. S. Kerby, ***IEEE Trans. Appl. Supercond.***, vol. 13, no. 2, June 2003, pg. 1229

[12] J. P. Zbasnik et al, ***IEEE Trans. Appl. Supercond.***, vol. 13, no.2, June 2003, pg. 1906

[13] A. Ballarino, ***IEEE Trans. Appl. Supercond.***, vol. 9, no. 2, June 1999, pg. 523

[14] R. Wesche, ***"Thermodynamic Optimisation of 70 kA Binary Current Lead",*** LRP 720/02, Feb. 2002

Chapter 4

Conduction cooled current leads for superconducting particle accelerator magnets

4.1. Introduction

One type of current lead for electrical feeding of superconducting particle accelerator magnets is the **conduction cooled**. In some cases, it is used due to its simplicity in construction, installation and operation, in comparison to the vapour-cooled current leads. Superconducting material can be used in this type of current leads at the bottom cold section in combination with copper at the upper warmer sections, but also these leads can be totally **resistive** in applications of low electrical currents where the loss due to heat dissipation is kept at low levels. The system of a conduction cooled current lead requires material and thermodynamic optimisation in order to contribute economically to the feeding of the superconducting magnets of the accelerator system.

In the Large Hadron Collider at CERN in Geneva of Switzerland, the Dipole Corrector magnets are going to be fed electrically by resistive conduction cooled current leads of current ratings 60 A and 120 A [1]. The Institute of Cryogenics has undertaken a project from CERN to examine a few of these current leads in terms of thermal and electrical performance. The results provide important knowledge for the operation of the LHC system with regard to the total thermal loss in the liquid helium. A cryogenic station was designed, constructed and set-up based on a two-stage Gifford MacMahon cryocooler for assessing the thermoelectric performance of the current leads (60 A and 120 A) before their installation in the LHC circuits. The design and construction of the cryogenic station for the testing is presented.

4.2. Analysis of a simple type of resistive current lead

4.2.1. Theoretical prediction of the optimum heat leak per unit current

The simplest type of current lead is a metal bar, usually copper, that operates adiabatically (without heat exchange with a coolant) between the room temperature T_1 and the temperature of the liquid cryogen T_2 that cools the magnet. This connection of the cryogenic environment to the room temperature power supply is responsible for a heat flux flowing from the exterior towards the cold interior. There are two sources of this heat flux: the generated Joule heat in the resistive wire-conductor ($Q_{Joule} = I^2 \times R$) that flows down to the colder sections and the natural heat conduction ($Q_{conduction} = -k \cdot A \cdot {}^{\Delta T}\!/_{\Delta x}$) due to the thermal gradient between T_1 and T_2. The incoming heat flux is a problem because it causes the evaporation of the expensive liquid cryogen and has to be minimised. Usually, this situation is dealt with the use of a long wire with small cross sectional area A of an alloy with low thermal conductivity in order to minimise the heat conduction. However, in applications that require significant electrical current, the dissipation by Joule heating becomes very high in thin and resistive wires as the electrical resistance is inverse proportional to the cross sectional area. The use of thick or short conductors from one hand decreases the electrical resistance, but from the other hand it is not a solution because in this case the contribution of the heat conduction becomes significant. A solution must be found that is a compromise between these two extreme cases, in order to minimise the thermal loss due to the current leads.

In the following analysis, the issue of the optimisation of this simple type of current lead will be dealt with. It will be shown that for a constant cross sectional area A, the optimum heat leak per unit of electrical current depends only on the two end temperatures T_1 and T_2. This statement is valid for current leads that are constructed of materials that obey the Wiedemann-Frantz law in relation (4.2.1).

$$k(T) \cdot \rho(T) = L_0 \cdot T \qquad \textbf{\textit{(4.2.1)}}$$

The differential equation (4.2.2) describes the heat transfer processes in the current lead and contains a heat conduction and a heat generation term. The thermal conductivity k(T) and the electrical resistivity ρ(T) are temperature dependent material properties of the metal conductor. The cross sectional area A is uniform along the whole length L of the current lead.

$$A \cdot \frac{d}{dx}\left\{k(T) \cdot \frac{dT(x)}{dx}\right\} + \frac{I^2 \cdot \rho(T)}{A} \cdot dx = 0 \qquad \textbf{(4.2.2)}$$

The heat conduction q is given by

$$q(T) = -k(T) \cdot A \cdot \frac{dT}{dx} \qquad \textbf{(4.2.3)}$$

hence

$$k(T) = -\frac{q(T)}{A} \cdot \frac{dx}{dT} \qquad \textbf{(4.2.4)}$$

If the Wiedemann-Franz law is considered from (4.2.1), then equation (4.2.2) can be written as follows:

$$\frac{d}{dx} q(T) = -\frac{I^2}{A} \cdot L_o \cdot \frac{T(x)}{k(T)} \qquad \Rightarrow$$

$$-\frac{d}{dx} q(T) = \frac{I^2}{A} \cdot L_o \cdot T(x) \cdot \frac{A}{q(T)} \cdot \frac{dT(x)}{dx} \qquad \textbf{(4.2.5)}$$

Equation (4.2.5) can be integrated with respect to the variable x (the physical length of the conductor).

$$-q(T) \cdot dq = I^2 \cdot L_o \cdot T(x) \cdot dT \qquad \textbf{(4.2.6)}$$

Equation (4.2.6) is integrated between the temperatures T_1 and T_2 and relation (4.2.7) is obtained

$$q_{T_2}^2 = q_{T_1}^2 + I^2 \cdot L_o \cdot \left(T_1^2 - T_2^2\right) \qquad \textbf{(4.2.7)}$$

where

$$q_{T_2} = -k(T_2) \cdot A \cdot \left.\frac{dT(x)}{dx}\right|_{\substack{T=T_2 \\ or \\ x=L}} \quad \textbf{(4.2.8)} \qquad \text{and} \qquad q_{T_1} = -k(T_1) \cdot A \cdot \left.\frac{dT(x)}{dx}\right|_{\substack{T=T_1 \\ or \\ x=0}} \quad \textbf{(4.2.9)}$$

Equation (4.2.7) estimates the heat leak to the liquid cryogen q_{T_2} by definition of equation (4.2.8). If it is required for the current lead to be optimum, i.e. the q_{T_2} is minimum, then it must be $q_{T_1} = 0$. This implies that the heat entering at the top hot end of the current lead should be zero. By principle, for optimum current leads, there should not be any heat entering from the hot end, which translates according to (4.2.3) that the thermal gradient at the top is zero,

$$\left.\frac{dT(x)}{dx}\right|_{T=T_1} = 0 \qquad \textbf{(4.2.10)}$$

The temperature profile of the optimised current lead has zero temperature gradient at the top hot end. In this case, from equation (4.2.7) the optimum heat leak per unit of electrical current can be estimated in relation (4.2.11)

$$\frac{q_{opt}}{I_{opt}} = \sqrt{L_o \cdot \left(T_1^2 - T_2^2\right)} \qquad \textbf{\textit{(4.2.11)}}$$

Relation (4.2.11) shows that for current leads made of material that obeys the Wiedemann-Franz law or any other similar law but with different constant of proportionality than the Lorentz number L_o, the optimum heat leak per unit current depends only on the two end temperatures and not on any geometrical characteristics. The smaller the difference between T_1 and T_2, the smaller the heat leak per unit current. If the two temperatures T_1 and T_2 are constant, then there is only one value of aspect ratio A/L that corresponds to the optimum geometry for a given current. The current lead can be optimised geometrically to give the minimum heat leak at the bottom end by solving equation (4.2.2) for different values of aspect ratio until the minimum q_{T_2} is obtained. This minimum must agree with the value that is defined by relation (4.2.11). The optimisation procedure is then simplified very much with the use of the theoretical prediction of (4.2.11), from which for a given operating electrical current, the minimum heat leak can be calculated straightforward, but the solution of equation (4.2.2), given the result of (4.2.11), will determine the optimum aspect ratio.

In relation (4.2.11), for a given operating current, the heat leak decreases as the temperature difference between the two ends T_1 and T_2 decreases. If a heat sink of an intermediate temperature T_{int} is positioned at some point in thermal contact with the current lead between T_1 and T_2, then only the heat leak of the section between T_{int} and T_2 will contribute to the total thermal loss into the liquid cryogen. The heat leak of the top section between T_1 and T_{int} will be absorbed by the heat sink. There is removal of heat by conduction and not by convection as in the case of vapour cooled current leads; this justifies the definition of this type of current leads as conduction cooled. The current lead has now two sections that are separated by a heat sink of an intermediate temperature and each section has to be optimised separately. The optimisation of the bottom section will determine the total heat leak, but the optimisation of the first section will contribute to the minimisation of the total refrigeration power. Not only is the condition of minimisation of the heat leak to the liquid cryogen that determines the current lead optimisation, but also the condition of the minimum refrigerator power consumption.

Instead of using only one heat sink, a number *n* of intermediate heat sinks can be intervened with thermal contact along the current lead in order to thermally "break" the total temperature range. Each heat sink absorbs an amount of heat that depends on the thermodynamic efficiency. For the ideal case, it is assumed that the heat sink is a Carnot reversible refrigerator. The coefficient of performance (COP) of a Carnot refrigerator is given by relation (4.2.12) [3]

$$a_i = \frac{1}{T_{hot}/T_i - 1} \tag{4.2.12}$$

where T_i is the temperature of the *{i^{th}}* heat sink (from the hot end). If heat flux Q_i enters the *{i^{th}}* heat sink from higher temperature and heat flux Q_{i+1} continues to flow down to the lower temperatures, the refrigeration power W_i at the heat sink *{i}* that is required to absorb the amount of heat $\Delta Q_i = Q_i - Q_{i+1}$ depends on the refrigerator thermodynamic efficiency according to relation (4.2.13).

$$W_i = \frac{\Delta Q_i}{a_i} \tag{4.2.13}$$

The condition of minimisation of the total refrigeration power requires that $\sum_{i=1}^{n} W_i = \min$ in relation (4.2.14).

$$\sum_{i=1}^{n} \left\{ \left(\frac{T_{hot}}{T_i} - 1 \right) \cdot \Delta Q_i \right\} = minimum \tag{4.2.14}$$

For the optimisation of the system, two conditions must be satisfied that have been derived from basic physical principles. The first is given by relation (4.2.14) and the second by relation (4.2.15), that expresses the minimisation of the heat leak at the lowest cold section

$$-k(T) \cdot A \cdot \left. \frac{dT(x)}{dx} \right|_{x=L_{n-1}}^{x=L} = minimum \tag{4.2.15}$$

Usually, for the last condition, the length L_n of the lowest colder section between the liquid cryogen and the last heat sink is defined according to the available space at the installation site of the current lead and therefore only the cross sectional area has to be determined conditionally according to (4.2.15) by solving equation (4.2.2) for this section. For the minimisation of the cooling power, also the rest of the sections have to be optimised independently in order to minimize the quantities ΔQ_i in relation (4.2.14).

4.2.2. An example of dimensional optimization of a resistive current lead

The differential equation (4.2.2) is rearranged:

$$\frac{d}{dx}\cdot\left[A\cdot k(T)\cdot\frac{dT(x)}{dx}\right]+\frac{\rho(T)\cdot I^2}{A}=0$$

$$A\cdot\frac{d}{dx}k(T)\cdot\frac{dT(x)}{dx}+A\cdot k(T)\cdot\frac{d^2T(x)}{dx^2}+\frac{\rho(T)\cdot I^2}{A}=0$$

$$A\cdot\frac{dk(T)}{dT}\cdot\left(\frac{dT}{dx}\right)^2+A\cdot k(T)\cdot\frac{d^2T(x)}{dx^2}+\frac{\rho(T)\cdot I^2}{A}=0$$

$$\frac{d^2T(x)}{dx^2}+\frac{dk(T)/dT}{k(T)}\cdot\left(\frac{dT}{dx}\right)^2+\frac{\rho(T)}{k(T)}\cdot\frac{I^2}{A^2}=0$$

$$\frac{d^2T(x)}{dx^2}+f(T)\cdot\left(\frac{dT}{dx}\right)^2+a\cdot g(T)=0 \qquad \textit{(4.2.16)}$$

where $f(T)=\frac{dk(T)/dT}{k(T)}$, $g(T)=\frac{\rho(T)}{k(T)}$ and $a=\frac{I^2}{A^2}$.

In the simplest case, equation (4.2.16) can be applied to a copper bar operating constantly between temperatures T_1 and T_2 in figure 4.1. The functions k(T)and ρ(T) are determined experimentally can be replaced in equation (4.2.16) for solution with temperature dependent material properties.

The thermal conductivity and electrical resistivity are assumed independent on temperature. This assumption can not be far from the real if the average values of the physical properties in the temperature range T_1 to T_2 are considered. A replacement of $k(T)=\tilde{k}$ and $\rho(T)=\tilde{\rho}$ with the averaged values of thermal conductivity and electrical resistivity over the temperature range of the copper current lead, converts eq. (4.2.16) into a linear second order differential equation.

$$\frac{d^2T(x)}{dx^2}+\frac{\tilde{\rho}\cdot I^2}{\tilde{k}\cdot A^2}=0 \qquad (4.2.17)$$

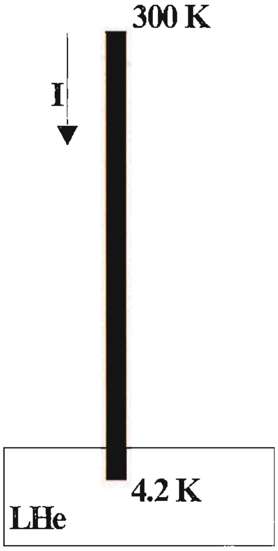

Figure 4.1. *A resistive current lead operating between 300 K and 4.2 K*

A numerical example is: T_1=300 K and T_2=4.2 K. The length is l=1m and the cross sectional area is A=2×10^{-5} m^2. Solutions to the differential equation (4.2.17) are shown in figure (4.2). The problem is solved with boundary conditions the fixed temperatures $T(x)|_{x=0}$ =300 K and $T(x)|_{x=1}$ =4.2 K at the ends of the lead. The average value (4.2 K – 300 K) of the thermal conductivity is $177\left(W/_{m\cdot K}\right)$ and the electrical resistivity 3×10^{-9} Ohm·m, if Phosphorous Deoxidized Copper is used as the conductor material. The above differential equation can be solved through a simple Math-Cad algorithm and in the figure 4.2 the solutions are displayed as temperature distributions along the length of the conductor for different values of operating electrical current.

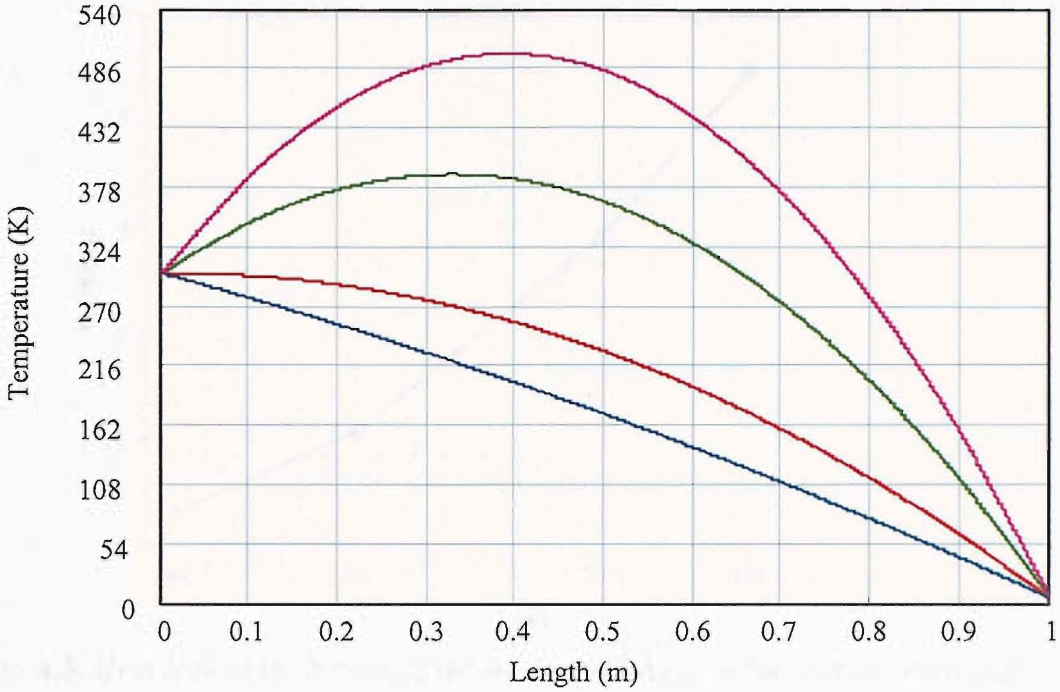

Figure 4.2. *Solution of the heat balance generates the temperature distribution along the copper lead with currents 60 A (blue), 120 A (red), 200 A (green) and 250 A (purple).*

The temperature distribution shows a maximum which shifts at higher temperatures with increasing current. The thermal runaway of the lead will occur when the maximum temperature rises to a level higher than the burn out limit, which depends on the materials used for the components of the current lead.

The heat leak to the bottom end of the lead (at *LHe*) is given by the relation

$$Q_{LHe} = -k \cdot A \cdot \left. \frac{dT(x)}{dx} \right|_{x=1}$$

Figure (4.3) shows the heat leak as a function of current for the above case.

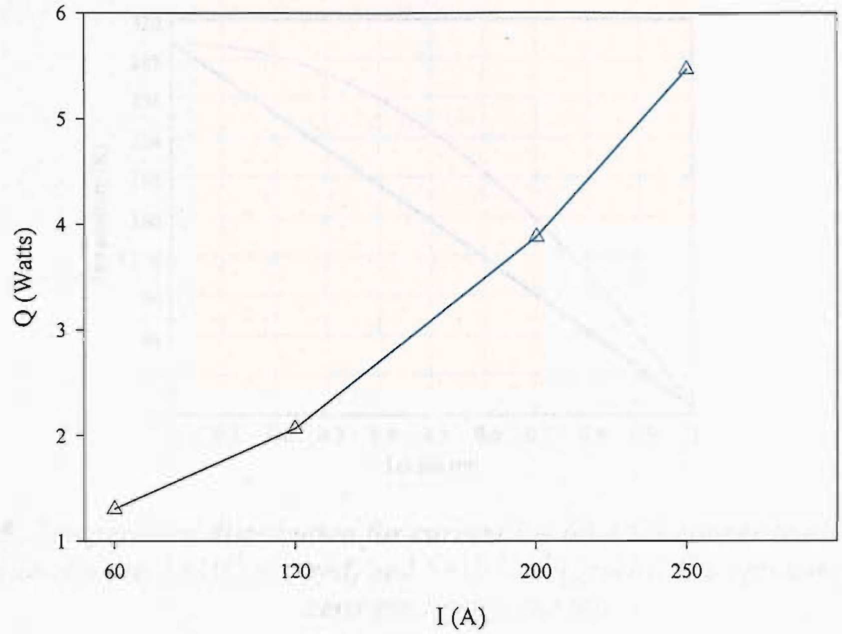

Figure 4.3. *Heat leak at the bottom of the lead (at 4.2 K) as a function of operating current*

The heat leak at the bottom end is an increasing function of operating current, i.e.

$$Q = f(I^2) = Q_{cond} + R \cdot I^2$$

As a simple application the heat balance equation is solved numerically for constant material properties and the heat leak in the LHe is obtained from the above relation and displayed in figure in figure 4.4 as a function of the cross sectional area for a constant length of 1m.

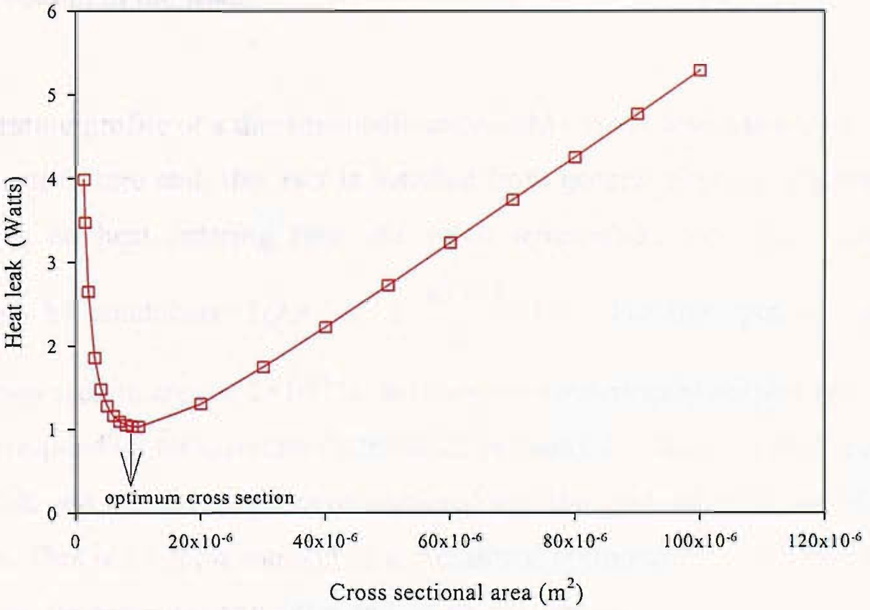

Figure 4.4. *Heat leak at the bottom of the lead as a function of the cross sectional area A of the copper lead*

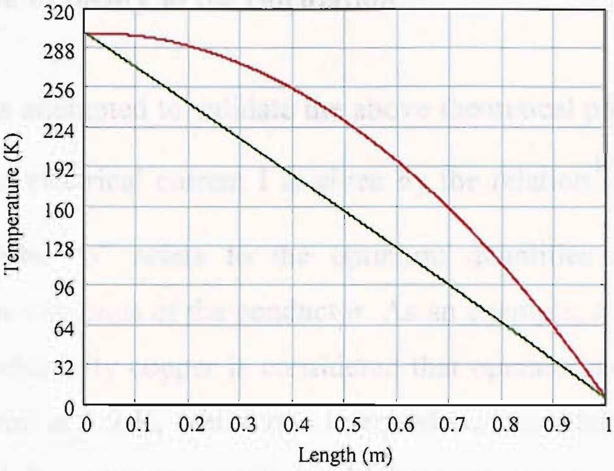

Figure 4.5. *Temperature distribution for current I = 60 A for copper leads of cross sectional areas* 1×10^{-5} m^2 *(red)* and 5×10^{-5} m^2 *(green). The optimum (red) has zero gradient at the top.*

The shape of the graph in figure 4.4 can be explained from the fact that the relation between resistive losses (heat generation) and cross sectional area is $Q_J \propto 1/A$, while for the conducted heat from room temperature is $Q_H \propto A$. Therefore the function of the total heat leak $Q_t = Q_J + Q_H$ will have a minimum with respect to the cross sectional area as in figure 4.4. It can be seen that the optimum cross section for a given length of the current lead is 1×10^{-5} m^2, which corresponds to the minimum heat leak at the bottom of the lead.

The temperature profile of a dimensionally optimized current lead has zero gradient at the room temperature end; this fact is justified from general physical arguments, i.e. that there is no heat entering from the room temperature top end to the lower temperatures by conduction ($\dot{Q} = -K \cdot A \cdot \frac{dT(x)}{dx} = 0$). For the optimum geometry with the cross section area of 1×10^{-5} m^2 that has been determined graphically in figure 4.4 the corresponding temperature distribution in figure 4.5 shows a zero gradient at the top 300 K end. For any other cross sectional area the gradient at the top of the lead is non-zero. This is a simple method of dimensional optimisation of adiabatic current lead based on fundamental principles and graphical methods.

4.2.2. Comparison of theory to the calculation

In this section it is attempted to validate the above theoretical prediction that the heat leak W per unit of electrical current I is given by the relation $W_o / I_o = \left\{ L_o \cdot \left(T_2^2 - T_1^2 \right) \right\}^{1/2}$, where the subscribe "o" refers to the optimum quantities and T_2, T_1 are the temperatures at the two ends of the conductor. As an example, a resistive current lead made of high conductivity copper is considered that operates as follows: Hot end at 300 K and cold end at 1.9 K, whilst one intermediate heat sink at 75 K divides the total length of the lead into two sections: L_1 between 300 K and 75 K with cross sectional area A_1 and L_2 between 75 K and 1.9 K with cross sectional area A_2. In table 1 are the results of a dimensional optimisation of the above system which results in minimum heat load at the 75 K heat sink and the 1.9 K liquid helium. The results have been obtained by solving the differential equation (4.2.2) by setting values for the lengths L_1 and L_2. Under the constraint that the heat leak should be minimum, the optimum cross sectional areas A_1 and A_2 were estimated.

Table 1. *Optimum dimensions*

$L_2^{75\ K\text{-}1.9\ K}$ (m)	$A_2^{optimum}$ (m^2)	$L_1^{300\ K\text{-}75\ K}$ (m)	$A_1^{optimum}$ (m^2)	$(A_2/L_2)_{opt}$	$(A_1/L_1)_{opt}$
0.4	2.12×10^{-6}	1.1	1.77×10^{-5}	5.30×10^{-6}	1.61×10^{-5}
0.6	3.18×10^{-6}	0.9	1.45×10^{-5}	5.31×10^{-6}	1.61×10^{-5}
0.8	4.24×10^{-6}	0.7	1.13×10^{-5}	5.30×10^{-6}	1.61×10^{-5}
1.0	5.30×10^{-6}	0.5	8.06×10^{-6}	5.30×10^{-6}	1.61×10^{-5}

In table 2 are the optimum heat leaks at the two sections of the conductor as they have been estimated: (a) through the solution of equation (4.2.2) and (b) through the theoretical formula

Table 2. *Calculated and theoretical optimum heat leaks*

L_1 (m) / L_2 (m)	$Q_{1.9\ K}^{calculated}$	$Q_{1.9\ K}^{theory}$	$^{+}Q_{75\ K}^{calculated}$	$^{+}Q_{75\ K}^{theory}$
1.1 / 0.4	~ 0.62 W	0.70 W	~ 2.38 W	2.73 W
0.9 / 0.6	~ 0.62 W	0.70 W	~ 2.38 W	2.73 W
0.7 / 0.8	~ 0.62 W	0.70 W	~ 2.38 W	2.73 W
0.5 / 1.0	~ 0.62 W	0.70 W	~ 2.38 W	2.73 W

The above results demonstrate that for dimensionally optimised sections of the conductor, the heat leak depends only on the two boundary temperatures of the corresponding conductor section. The calculated values of the heat leak are close enough to those predicted by the theory that has been developed in the previous section. The most possible reason for the observed deviations between the model calculations and the theoretical values is that the material does not follow exactly the Wiedemann-Franz (WF) law. The fact that the optimum heat leak is found to have always the same value for different lengths through the model calculations indicates that the material follows a similar law to the WF but the constant of proportionality should be assigned with a different value than the Lorentz number L_0, which is used to calculate the values of heat leak from the theory.

4.3. The resistive conduction cooled current leads for the LHC Dipole Corrector Magnets at CERN of current ratings 60 A and 120 A

4.3.1. Introduction

For the feeding of the Dipole Corrector Magnets in CERN, conduction cooled current leads will be used [1]. The current rating of these current leads (60 A and 120 A) is considered low enough such as the use of HTS or LTS material would not produce a significant reduction in the heat leak to the liquid helium. Therefore the lower cost and the simplified design and construction procedure as well as the easier way of installation of the leads have been considered more important factors by the designers at CERN who have decided that these leads shall be totally resistive. Also they shall operate in adiabatic conditions (without helium gas cooling). In order to reduce the heat leak, the conduction cooling method was adopted by thermal linking the conductors at two intermediate points between the room temperature end and the super-fluid helium end. The current leads are an important component in the superconducting magnets system of the Large Hadron Collider and require thermoelectric testing before they will be integrated in the machine for operation. The testing of these leads on behalf of CERN gives the opportunity to study the current leads in the following aspects:

a. The system of the current leads is considered to have been optimised in order to reduce the refrigeration power consumption as well as the heat leak to the liquid helium. This was achieved by the interference of the two heat intercepts at intermediate temperatures and also by adjusting the aspect ratio of the conductors according to the optimising procedure that has been analysed in the previous section. As far as the interest that is concerned here beyond the useful information that the tests will provide to the personnel in CERN is the verification that indeed the system operates optimally or close to the optimum since any theoretical estimation cannot be accurate enough. Therefore the experimentally determined quantities such as the heat leak to the liquid helium and the absorbed refrigeration power at the heat intercepts should be compared to the theoretically obtained values after a model has been constructed and solved that optimises the above current lead assembly.

b. A comprehensive investigation into the performance of various components of the current leads assembly has been carried out. These tests necessitate the design and construction of the test facility which will be present in this chapter. One of the important tests carried out is the thermal contact resistance between the current lead conductor – insulating material-supporting stainless steel outer sheath. In the following sections a brief description of the current lead assembly and the two test facilities will be presented.

c. The design, construction and set-up of the cryogenic station to accommodate the tests of the leads shall give the opportunity to apply the underlying principles of cryogenic design in practice. The building of this cryostat that includes nitrogen, liquid helium and crycooler cooling as well as instrumentation is very interesting both academically and professionally.

4.3.2. Description of the current leads

A detailed description of the system of these current leads can be found in [1]. A brief description is mentioned here: The current leads are resistive wires that are electrically insulated via a Kapton tube. They are intercepted by two intermediate heat sinks at two intermediate temperatures; the warmer station temperature in the range 50 K to 75 K and the colder station in the range 10 K to 20 K. The conductor surrounded by the Kapton tube is enclosed in a thin walled stainless steel tube that welds at the top and bottom end on stainless steel flanges. The current leads are assembled in groups of four wires (figure 4.6), each one rated for 60 A or 120 A. The conductor has variable cross section as it is imposed by an optimum thermal behaviour, but also the cross section is small enough to allow pre-shaping in order to fit in the available space as well as to maintain low thermal conduction in the stand by mode as it is expected that the mode of full current operation will not be so frequent.

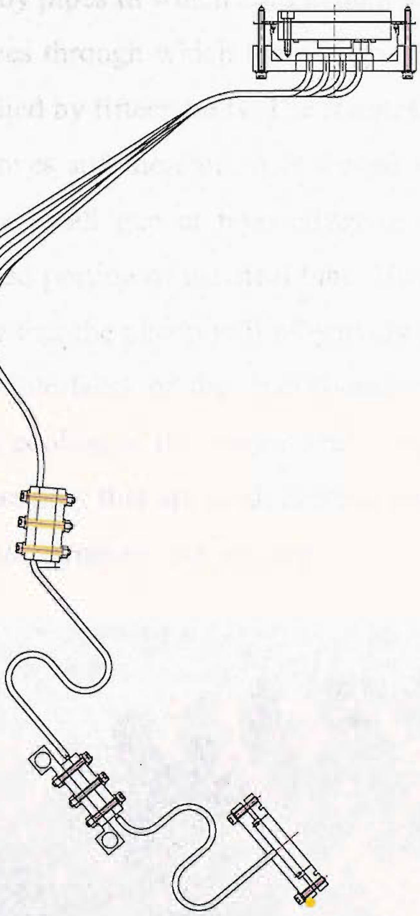

Figure 4.6. *Schematic representation of the assembly of the four 60 A current leads as they are pre-shaped in order to fit the space at the installation site. The two thermal anchoring blocks are seen at two intermediate points along the conductor*

These requirements may complicate the optimisation procedure which at a high degree should be induced to the selection of an appropriate material for the conductor. The designers at CERN have selected a composite brass wire of constant cross section along the hole length with two copper electrolytic depositions of different thicknesses:

900 μm for the upper warm part including the aluminium thermal anchoring block (50 K – 75 K) and 110 μm for the rest of the conductor down to the liquid helium including the copper thermal anchoring block (20 K).

4.3.3. The thermal anchoring metal blocks

The current leads are thermally anchored via pressure contacts using metal clamps. In the real installation place at the LHC, the clamping blocks are thermally connected to heat sinks that are provided by pipes in which cold helium gas passes through [1]. The clamping blocks have grooves through which the current leads pass and clamped in between by the pressure applied by fifteen bolts. The stainless steel tube is "squeezed" by the pressure into the grooves and therefore it is shaped according to the shape of the grooves; there is also a small gap at both edges of the grooves in order to accommodate for the squeezed portion of the steel tube. High enough pressure has to be applied in order to ensure that the clamp will effectively press the current leads in such a way as to bring the interfaces of the steel/Kapton/conductor/clamp in good thermal contact for effective cooling of the current leads. Figures 4.7 and 4.8 display the two different types of clamping that are used; aluminium for the high temperature intercept and copper for the low temperature intercept.

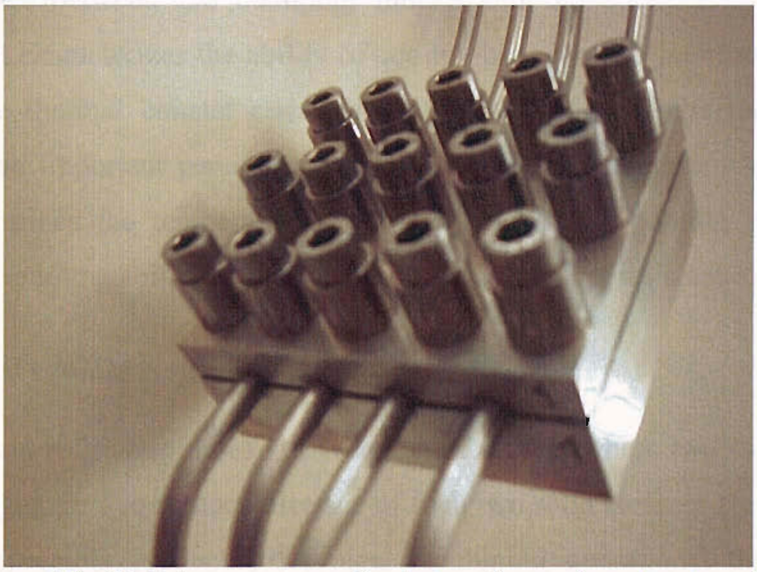

Figure 4.7. *High temperature aluminium thermal anchoring clamp*

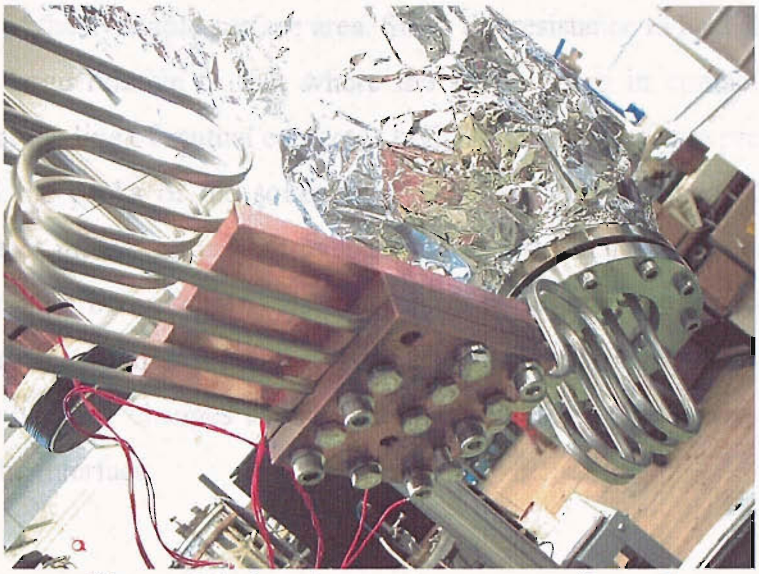

Figure 4.8. *Low temperature copper thermal anchoring copper block*

4.4. The measurement of the thermal contact resistance between the current lead conductor and the thermal anchor metal blocks

4.4.1. Introduction

The effective cooling of the current leads by the clamping blocks is ensured by good thermal contact between the clamping blocks and the conductor. The physical parameter that characterizes the ability of cooling between two interfaces in physical contact is the thermal contact resistance. The knowledge of the thermal contact resistance is an important parameter in the operation of the current lead assembly, since it determines the temperature drop ΔT between the cooling block and the conductor; the cooling ability depends on the thermal contact resistance.

4.4.2. Thermal contact resistance concept

Thermal contact resistance arises in the region of contact where two solid specimens are pressed together. The contact interface of such two solid surfaces consists of peaks and valleys (possible products of typical machining operations) that have been brought together for the purpose of transferring heat from one to the other. Initial contact is made only between the combination of highest peaks, and thus over a rather small portion of the available surface area. Since the resistance to heat flow across the void fluid is large relative to that where the surfaces are in contact, the over-all intersurfaces at the line of mutual contact is high. As the surfaces are pressed together, however, and the peaks of the softer surface material are crushed, the number of points of contact increases, and the over-all thermal resistance is lowered. Thus, the higher the pressure between surfaces, the higher is the intersurface conductance h_c, probably up to the asymptotic value. Heat is transferred from one material to the other, the temperature changes across the contact area, so there must be a thermal resistance at the interface.

An additional temperature drop ΔT will occur due to the imperfect contact at the interface of the two solids when heat Q flows, as described above. By definition the thermal contact resistance is given by:

$$R_C = \frac{\Delta T}{A \cdot Q} \left[K \cdot W^{-1} \right]$$

ΔT is the temperature drop and Q is the heat flow across the interface of the two solids through the area A. The reciprocal of the product of the apparent contact area and this resistance is called **interface conductance** h_C. Clausing and Chao have developed a model for predicting the contact resistance in vacuum between the ends of two circular rods pressed together. A brief description of this model is given below. Using the above equation and the interface conductance we can alternatively define the thermal contact resistance as

$$R_{tc} = \frac{1}{h_c A}$$

It is assumed to be made up of three components: *(1)* the macroscopic constriction resistance R_L, which arises because not all of the area A is in contact due to deviation from perfect flatness of the surfaces, *(2)* the microscopic constriction resistance R_s, which arises because the actual contact area is less than the apparent area due to microscopic protuberances (roughness) on the surface and *(3)* the film resistance R_F which arises due to oxide layers or other impurity layers between the surfaces. The contact resistance is summarized as follows:

$$R_{tc} = R_L + R_S + R_F$$

The macroscopic constriction resistance and the microscopic constriction resistance are related to the conductance by the following relations:

$$R_L = \frac{1}{h_L A}$$

$$R_S = \frac{1}{h_s A}$$

where h_L and h_s are the macroscopic and microscopic constriction conductances. The third component of the thermal contact resistance due to films on the surface, R_F, was found to be negligible for a vacuum environment. If the surface were covered by a hard oxide film, however, this component could be significant. The total conductance may be written in the following form by neglecting the film resistance component:

$$\frac{1}{N_{tc}} = \frac{k_m}{h_{tc} D} = \frac{1}{N_L} + \frac{1}{N_s}$$

4.4.3. The procedure of measurement

Measurements of the temperature dependence (between 10 K and 70 K) of the thermal contact resistance between the clamping blocks and the current leads have been carried out. The Gifford-McMahon two-stage cryocooler was used to provide the required cooling in a test cryogenic station that has been set-up for that purpose. The apparatus is enclosed in a cylindrical stainless steel vessel that provides the vacuum space. All the instrumentation wiring enters the experiment through the bottom flange of the steel vessel, which also holds vacuum tightly the cryocooler. The clamping blocks under investigation are thermally attached on the 2^{nd} stage of the crycooler through a "cold finger" thermal link made of Cu plate of thickness 1 mm. The thermal contacts are improved via the use of Apiezon N grease at the interfaces block/thermal link and thermal link/2^{nd} stage cold head. The measurements were repeated for different applied torques on the 15 bolds that clamp the two parts of the blocks. The effect of the change in the contact pressure between the two blocks on the thermal contact resistance is investigated.

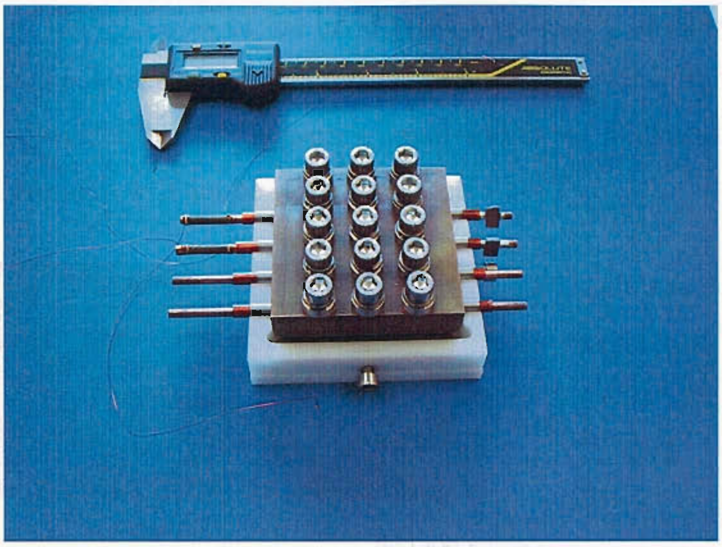

Figure 4.9. *Copper metal thermal anchoring block with the samples*

Due to the differential contraction between the stainless steel bolts and the copper or aluminium blocks, the pressure that is applied by the tightness of the bolts onto the blocks will be lost as the temperature decreases. In order to solve the problem, invar washers on the bolts are used to compensate for this differential thermal contraction. If L_1, α_1 denote the thickness and thermal expansion coefficient of the invar and L_2, α_2 denote the thickness and thermal expansion coefficient of the copper (or aluminium) block, the law of linear thermal expansion as applied to the steel screw and the block gives:

$$L = L_1 + L_2$$

$$\frac{\Delta L_1}{L_1} = a_1$$

$$\frac{\Delta L_2}{L_2} = a_2$$

The total contraction is equal to the contraction of the steel and a simple algebraic manipulation yields:

$$\Delta L_{total} = \Delta L_{steel} = \Delta L_1 + \Delta L_2 \Rightarrow a_{steel} \cdot (L_1 + L_2) = a_1 L_1 + a_2 L_2$$

$$L_{in\,\mathrm{var}} = \left(\frac{a_{steel} - a_{in\,\mathrm{var}}}{a_{copper} - a_{steel}} \right) \cdot L_{steel}$$

The estimation of the thickness of the invar washer necessary to compensate for the differential thermal contraction through this procedure can be done accurately; in fact, the washer was provided by CERN with a small additional thickness, thus ensuring that the applied pressure will not be lost in any case.

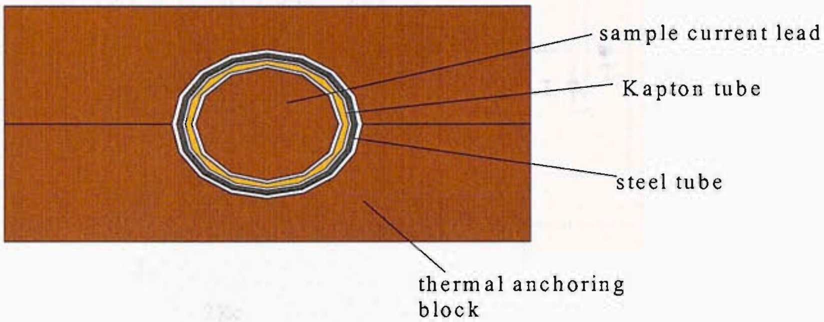

Figure 4.10. *Cross section of the metal thermal anchoring block and the sample*

4.4.4. Experimental set-up

Figure 4.10 above shows a schematic representation of a cross section of the block and the current lead sample; the samples were positioned inside the grooves and clamped between the two parts: A (refrigerated part) and B (clamping part) (fig. 4.11 b). The positions of the lead heaters (H_1 and H_2) and the Silicon Diode thermometers used to measure the temperatures at various positions which are indicated in figure 4.11; T_C is the sensor used for temperature control and H_C is the controller heater. Figure (4.11 b) shows the block mounted on the thermal copper link used for the attachment on the cold head of the Cryocooler. Two adjacent leads were studied in order to assess the influence of dimensional variation of the grooves and sample leads in the reproducibility of the contact resistance. A small copper block has been soldered at one end of the sample to provide a flat and smooth surface for the attachment of the Silicon-Diode Thermometer (using G.E. varnish) for recording the temperature of the lead. The other end has been covered with a layer of G.E. Varnish for electrical insulation and constantan wire (total electrical resistance $20\ \Omega$) has been tightly wound around the lead to provide the sample heat source needed for the thermal contact resistance measurements. The two heaters were connected in series, thus allowing for applying heat to both samples simultaneously and reducing the number of wires; in the case of measurement at high temperatures, the two samples had to be connected separately in order to reduce the amount of heat load

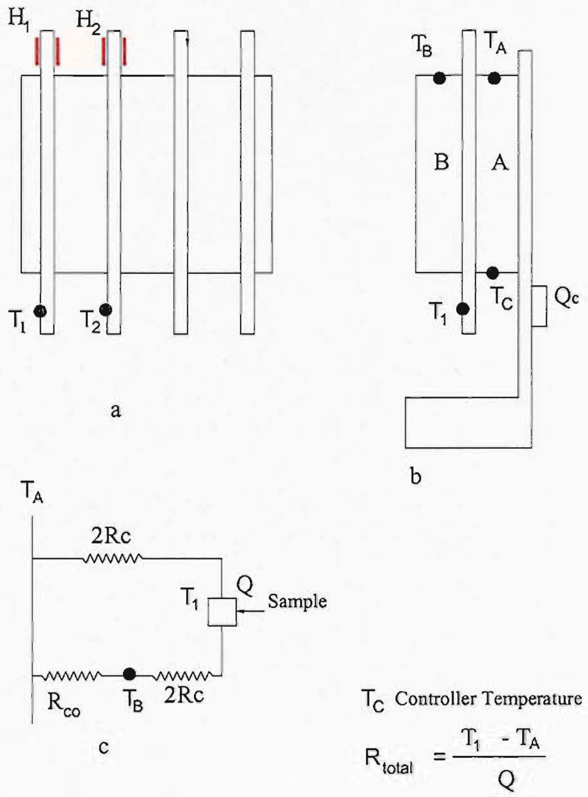

Figure 4.11. *Schematic representation of the sample configuration (block, samples and equivalent electrical circuit)*

(limitations in the cooling power of the GM Cryocooler). Figure 4.11 shows the samples positioned inside the grooves of the metal part and the position of the heaters and thermometers. The equivalent electrical circuit of the thermal network of the system is shown in figure (4.11c). R_C is the contact resistance shown by the sample when T_A=T_B, which is the case when the thermal contact resistance R_{CO} between A and B is much smaller than the sample contact resistance. Allowing for a non-negligible thermal contact resistance R_{CO}, the circuit of figure (4.11c) can be used for the estimation of R_C and R_{CO}. The total thermal contact resistance R_{C_t} is defined as

$$R_{C_t} = \frac{\Delta T}{Q_S}$$

, where $\Delta T = T_1 - T_A$ is the temperature difference between the sample and the part A and Q_S is the power applied to the sample heater. $2R_C$ is the thermal contact resistance corresponding to half of the area in contact with parts A and B. A simple analysis on the circuit of fig. (4.11c) predicts: For ${}^{R_{CO}}\!/_{R_C} \to \infty \Rightarrow R_{C_t} = 2R_C$ and for

${}^{R_{C0}}\!/\!_{R_C} \to 0$ (good thermal contact between part A and B) $\Rightarrow R_{Ct} = R_C$. Figure 4.12 shows the rig open and ready to enclose in the vacuum stainless steel vessel for the measurement.

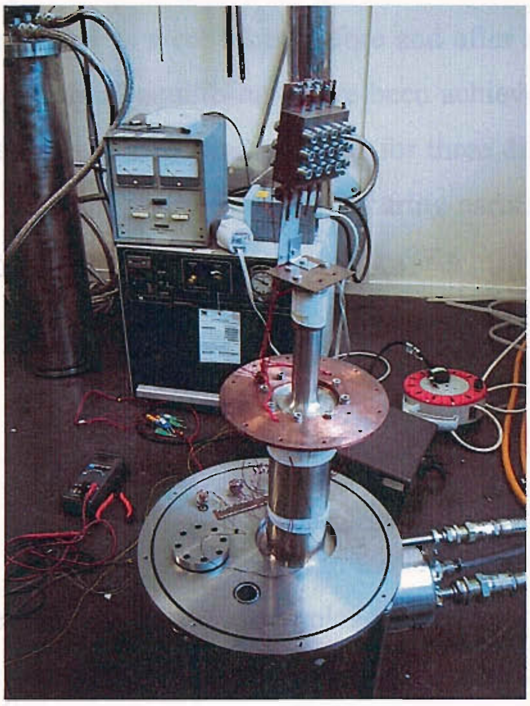

Figure 4.12. *The Cu block mounted on the cryocooler*

Figure 4.13 shows the Cu block mounted on the Cu thermal link.

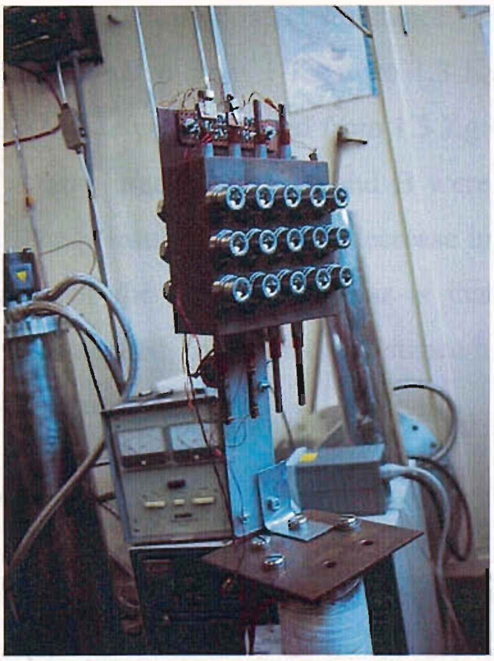

Figure 4.13. *Copper block mounted on the cold head (through the copper thermal link)*

4.4.5. Measurement procedure

The sensor of the temperature controller is attached to part A thus providing a constant reference temperature independent of the heat applied to the sample. The readings of all the thermometers were taken before and after applying an amount of heat to the sample after thermal equilibrium have been achieved in each time. In the case of the copper, the measurement was repeated for three different applied torques (1 Kg·m, 1.3 Kg·m , 1.6 Kg·m) on the 15 bolts securing parts A and B, while for the aluminium sample only two torques (1.3 Kg·m and 1.6 Kg·m) were applied.

4.4.6. Results

A. Copper block

Figure 4.14 shows the measured values of R_{Ct} in the temperature range 10 K to 70 K that has been calculated for the two lead samples and torques of 1 Kg·m, 1.3 Kg·m, 1.6 Kg·m. The total thermal contact resistance for the two samples shows similar behaviour, thus indicating that the clamping force is distributed homogenously between the two parts of the block. An increase in the torque (i.e. contact pressure) will improve the contact between the interfacial surfaces (Copper, Kapton, and stainless steel) and reduce the thermal contact resistance. This decrease in R_{Ct} was larger when the torque was changed from 1 Kg·m to 1.3 Kg·m, compared with the change observed when the torque was increased from 1.3 Kg·m to 1.6 Kg·m. This can be due to the fact that a large area of parts A and B were in contact, and further increase in the torque will only result in a modest decrease in pressure exerted on the leads. Another explanation of the above behaviour is that in the pressure range corresponding to the torques applied, the contact resistance has already been reduced near the lowest asymptotic value achievable.

B. Aluminium block

With the two parts assembled using the positional marks indicated by CERN the interface distance d between the blocks varied by more than 250 μm from hole to hole. When part A was rotated by 180° the variations in d were markedly reduced and it was decided to keep this configuration for the assembly of the samples. It should also be noted that the outer copper layer of the composite current lead is not circular with variations up to 40 μm in diameter. Due to these dimensional variations a torque of 1 Kg·m was not enough to hold all the samples tight between the blocks (one of the copper sample was moving freely inside the s.s. tube). Therefore measurements have only been carried out for torques of 1.3 Kg·m and 1.6 Kg·m as shown in figure 4.15. Figure 4.15 shows that the measured values of R_{Ct} for sample 1 were 100 times larger than for sample 2 at the torque of 1.3 Kg·m. Although this difference was reduced to about 50 fold at a torque of 1.6 Kg·m, it is still unacceptable indicating that local dimensions were not accurate enough to ensure homogenous pressure.

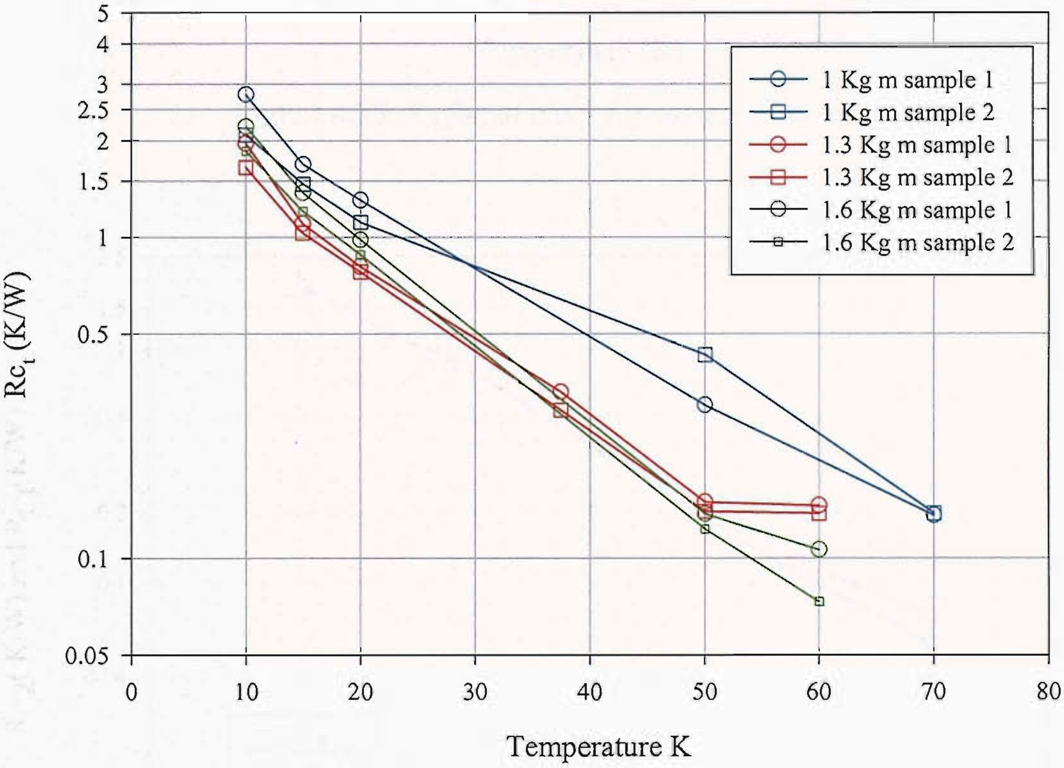

Figure 4.14. *R_{ct} for Cu at torques 1 Kgm, 1.3 Kg m 1.6 Kg m*

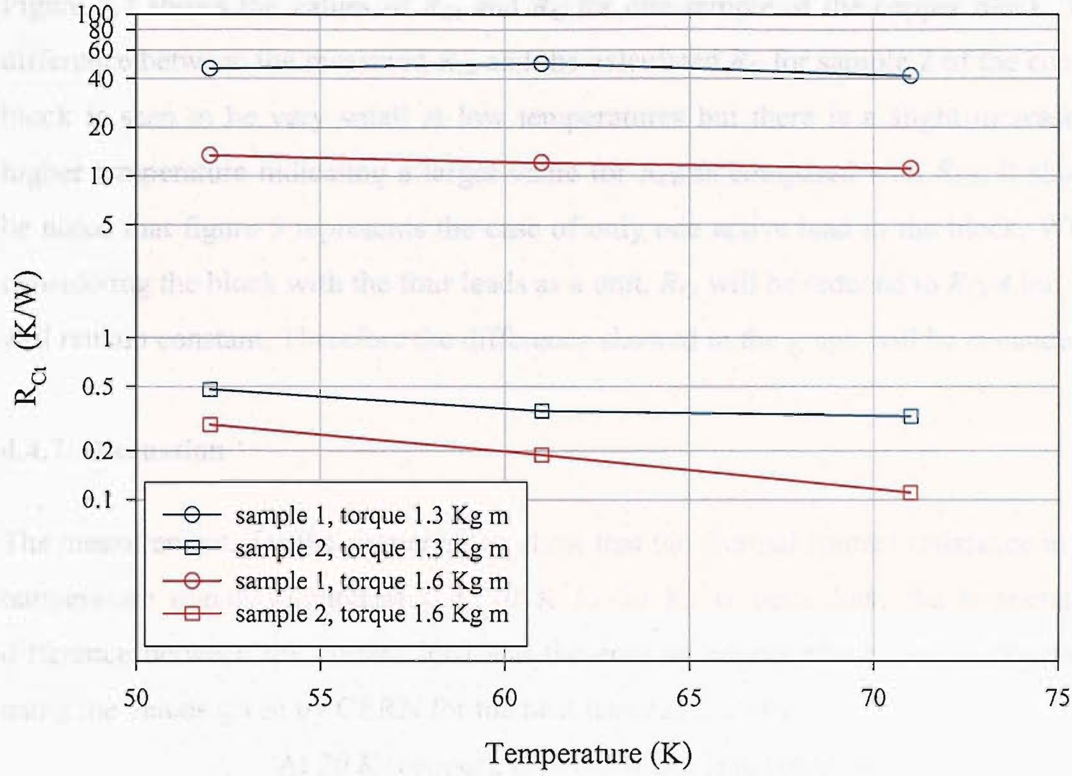

Figure 4.15. *R_{ct} for Al block for samples 1 and 2*

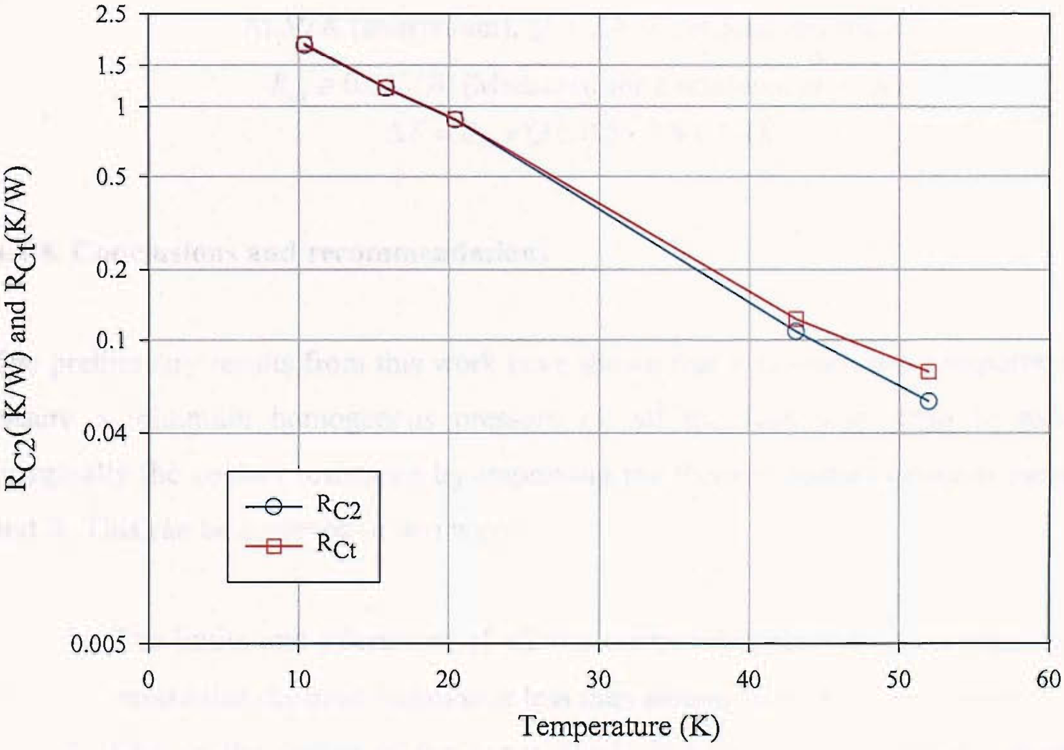

Figure 4.16. *R_{c2} and R_{ct} for Cu block at 1.6 Kg m*

Figure 4.7 shows the values of R_{Ct} and R_C for one sample of the copper block. The difference between the measured R_{Ct} and the calculated R_C for sample 2 of the copper block is seen to be very small at low temperatures but there is a slight increase at higher temperature indicating a larger value for R_{C0} as compared with R_{C2}. It should be noted that figure 5 represents the case of only one active lead in the block. When considering the block with the four leads as a unit, R_{Ct} will be reduced to $R_{Ct}/4$ but R_{C0} will remain constant. Therefore the difference showed in the graph will be enhanced.

4.4.7. Discussion

The measurements for the copper block show that the thermal contact resistance in the temperature region of interest (i.e. 10 K to 20 K) is quite low; the temperature difference between the current lead and the cooling copper block can be estimated using the values given by CERN for the heat leaks as follows:

At $20\ K$ (copper), $Q = 0.3\ W$ per lead (estimated)

$$R_{Ct} \cong 1K/W \text{ (Measured for copper at } 20\ K)$$

$$\Delta T = R_{Ct} \times Q \cong 1 \times 0.3 \cong 0.3K$$

If for the aluminium stage we use the lowest R_{Ct} value measured (sample 2)

At $50\ K$ (aluminium), $Q = 2.8\ W$ per lead (estimated)

$$R_{Ct} \cong 0.5K/W \text{ (Measured for aluminium at } 50\ K)$$

$$\Delta T = R_{Ct} \times Q \cong 0.5 \times 2.8 \cong 1.4K$$

4.4.8. Conclusions and recommendations

The preliminary results from this work have shown that it is much more important to ensure a minimum homogenous pressure on all the four leads than to reduce marginally the contact resistance by improving the thermal contact between parts A and B. This can be achieved in two ways:

1. The limits and tolerances of all the components should be maintained, to ensure that the total variation is less than around 5μm (Very expensive).
2. Change the design of the upper block to allow each lead to be clamped independently as shown in figure 4.8. This will allow the tolerances to be relaxed thus reducing costs. The initial clearances between parts A and B

should be increased to ensure that no contact between them is made when fully compressed. This will result in poor thermal contact between parts A and B and will half the effective area for heat transfer thus doubling the thermal contact resistance. This is acceptable due to the very low values of R_{Ct} *and* it will ensure that all the leads are thermally linked to the base block in a reproducible way.

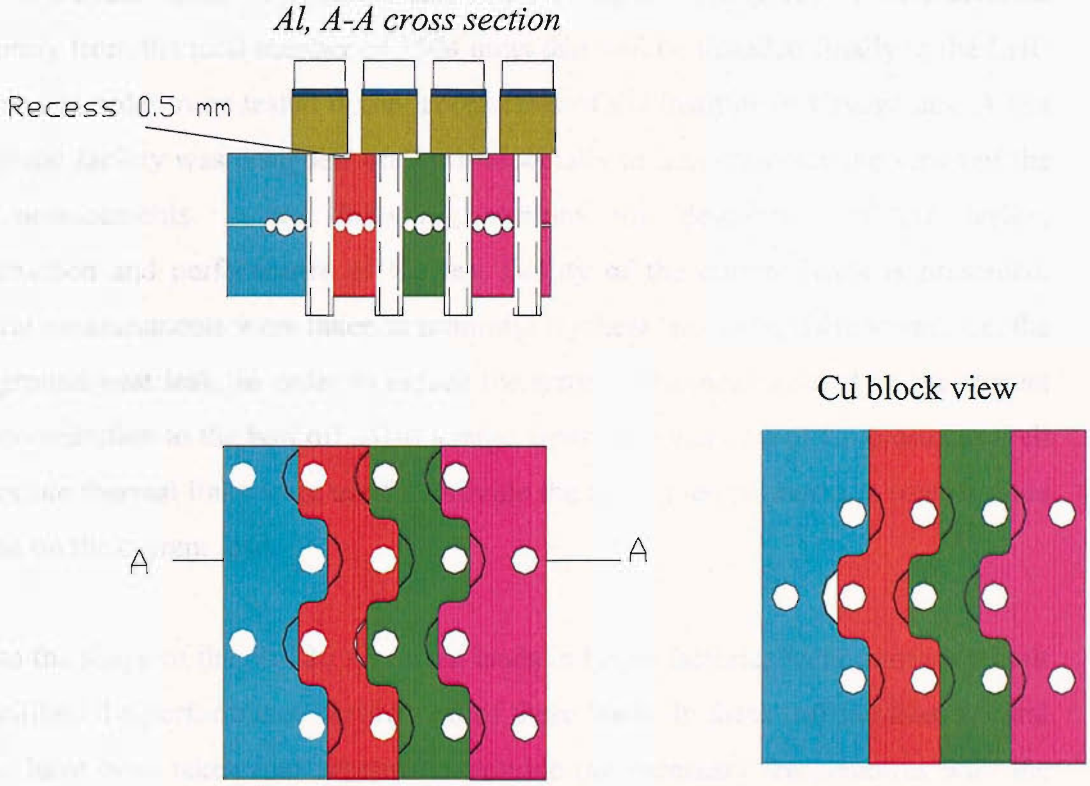

Figure 4.16. *Suggested design for the metal thermal anchoring blocks*

4.5. Design, construction and set-up of the cryostat for the thermoelectric assessment of the 60 A and 120 A conduction cooled current leads

The conduction cooled resistive current leads of current ratings 60 A and 120 A for the LHC Dipole Corrector Magnets have to go through a series of test measurements in order to assess their thermal and electrical behaviour under realistic conditions of operation. The measurements will provide useful information for the operation of the current leads, with emphasis on the heat load into the liquid helium. A batch of 15 leads of current rating 60 A and a batch of 5 of current rating 120 A were selected randomly from the total number of 1504 units that will be installed finally to the LHC machine in order to be tested in the laboratories of the Institute of Cryogenics. A test cryogenic facility was designed and built especially to accommodate the series of the test measurements. In the following sections full description of the design, construction and performance of the test facility of the current leads is presented. Several measurements were taken to minimise the heat leak to the LHe vessel, i.e. the background heat leak, in order to reduce the error in the measurement of the current lead contribution to the boil off. Also a large cross sectional area of Cu blocks as well as flexible thermal links were used to provide the testing temperatures at intermediate station on the current lead.

Due to the shape of the 60/120 A current leads in house facilities were purposely built to facilitate the performance verification of these leads. In these test facilities several issues have been taken into account to provide the necessary temperatures with the fine control at these low temperatures in addition to the low background heat leak from the surrounding.

Two double walled cryostats were designed and constructed for this purpose. The inner cryostat consisted of LHe vessel which is supported and filled with LHe via low thermal conductivity tubes. Due to the shape of the current leads the bottom part of the LHe vessel was shaped as an elbow (figure 4.17) at an angle of approximately 40°. The bottom flange of the LHe vessel was linked to the low temperature flange of the current lead assembly using indium seal. The LHe vessel is housed within a 500 mm OD outer vessel with domed bottom and a flat thick stainless steel flange at the other end. On this flange the appropriate parts and fixtures were attached. The crycooler is positioned and sealed on the top of this flange. The LHe vessel was well wrapped with layers of super-insulation and radiation shield connected to the first stage of the crycooler was positioned at midpoint between the LHe vessel and the cryostat top flange. The LHe vessel was 150 mm OD and 280 mm long capable of holding 4 ½ litres of LHe. Several measures were taken to reduce the background heat in-leak as well as eliminating the effect of LHe level dropping with time on this background heat in-leak. 1mm thick high conductivity Cu sheet was tightly wrapped around the LHe vessel. Although this sheet will cause an increase in the background heat in-leak, it will, however, maintain the background heat in-leak at almost constant value. It was estimated that the heat in-leak due to the filling ports and supporting tubes was about 0.2 Watts which is mainly via heat conduction. Radiation heat in-leak is significantly

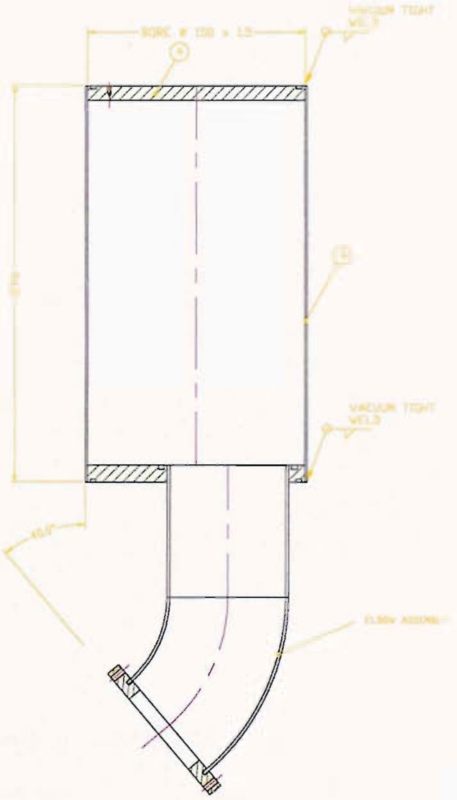

Figure 4.17. *The LHe vessel. The bottom elbow can be seen*

reduced by using the multilayer insulation and vacuum. The Cu sheet around the LHe vessel will help in extending and maintaining the temperature of the LHe vessel at about 4 K, hence achieving a constant radiation heat in-leak. The calibration of this background heat in-leak was measured and will be discussed later. The current leads enter the LHe vessel from the bottom flange of the vessel that seals with indium sealing to the flange of the current lead assembly. Figure 4.18 shows the insert of the assembly of the current leads to the LHe vessel.

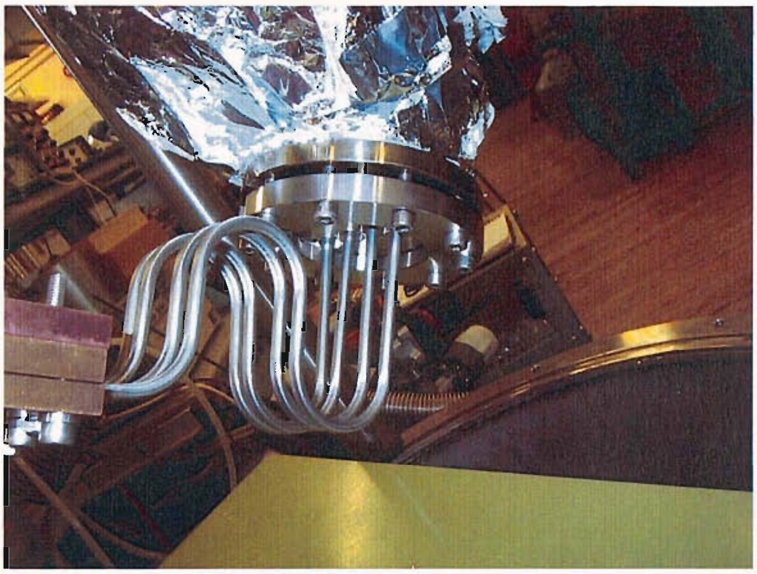

Figure 4.18. *The current lead assembly enters from the bottom flange of the LHe vessel*

The current lead sample is housed within the vacuum space of this cryostat where the top warm end of the lead is attached to the top flange. As mentioned before, the current lead assembly supplied with two intermediate intercepts. The 50 K – 75 K intercept station was made of Al block and thermally linked to the 1st stage of the cryocooler. This link was partly a solid high thermal conductivity Cu block which is carefully linked to the 1st stage of the cryocooler and partly a flexible thermal link. The cross sectional area of this thermal link was carefully chosen in order to satisfy achieving the required operating conditions. Similarly, the 10 K – 20 K intercept station was thermally linked to the 2nd stage of the crycooler. Also this link was carefully dimensioned in order to achieve the required operating conditions. Furthermore, a flux gate was also used through the 1st and 2nd stage link in order to measure the heat flux to this intercept station. Both intercept stations were appropriately instrumented with low temperature sensors and heaters for fine control of the station temperatures. In order to measure the heat flux through this intercept station, the solid part of the link was provided with a heat-flux gate. This gate is simply a 95 mm OD and 3 mm thick Cu tube and 18 mm long which is intervened by brazing in the middle of this solid Cu thermal link as shown in figure 4.19 for the 1st stage flux gate. The 2nd stage flux gate is a constantan rod of dimensions OD 19 mm and length 18.5 mm. The thermal conductivity of these materials is not varied significantly over the temperature range across the gate as it was verified by literature values of material properties. The temperature sensors are attached at both ends of the gate to determine the temperature drop across the gate and by knowing the thermal conductivity the heat flux can be determined. This flux gate was initially calibrated by measuring its thermal conductivity at the operational conditions.

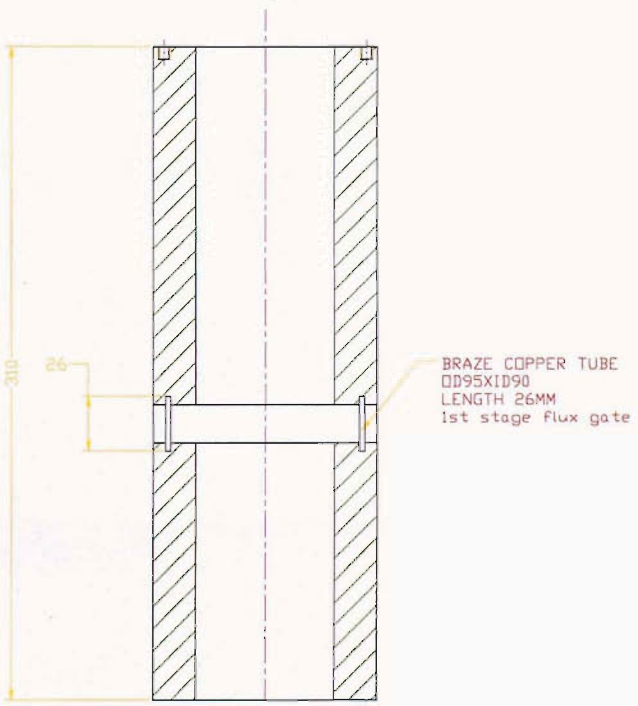

Figure 4.19. *The first stage solid thermal link. The Cu heat flux gate can be seen in the middle*

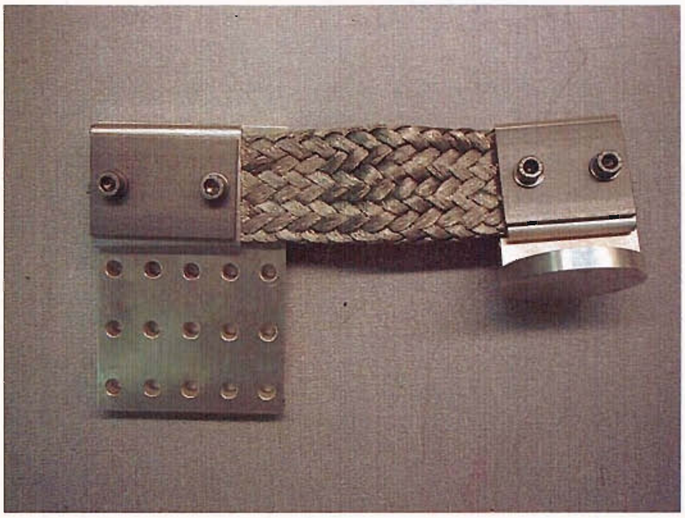

Figure 4.20. *The flexible thermal link of the 2nd stage*

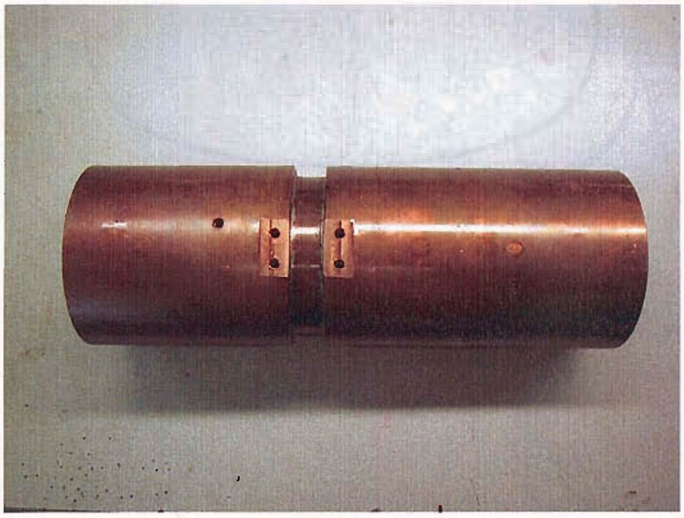

Figure 4.21. *The 1st stage solid thermal link*

The LHe cryostat was placed within a double walled LN_2 dewar (figure 4.22) to provide a 77 K background temperature. In order to eliminate the change in the LN_2 level a thick 1 mm high conductivity Cu sheet was tightly wrapped around the 500 mm outer wall of the cryostat. During the experiment the Cu sheet will maintain the background temperature at about 77 K as always the bottom half of this sheet is maintained below the LN_2 level.

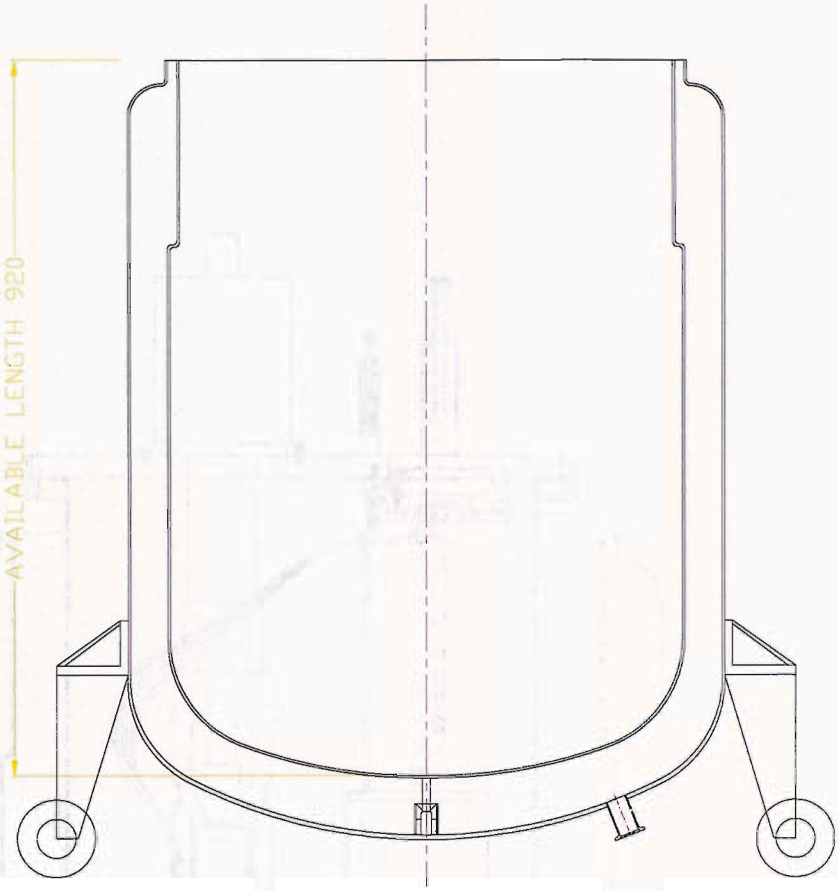

Figure 4.22. *The outer LN_2 dewar*

An overall design of the test facility is presented in figure 4.23 with the current leads included in the interior of the vessel.

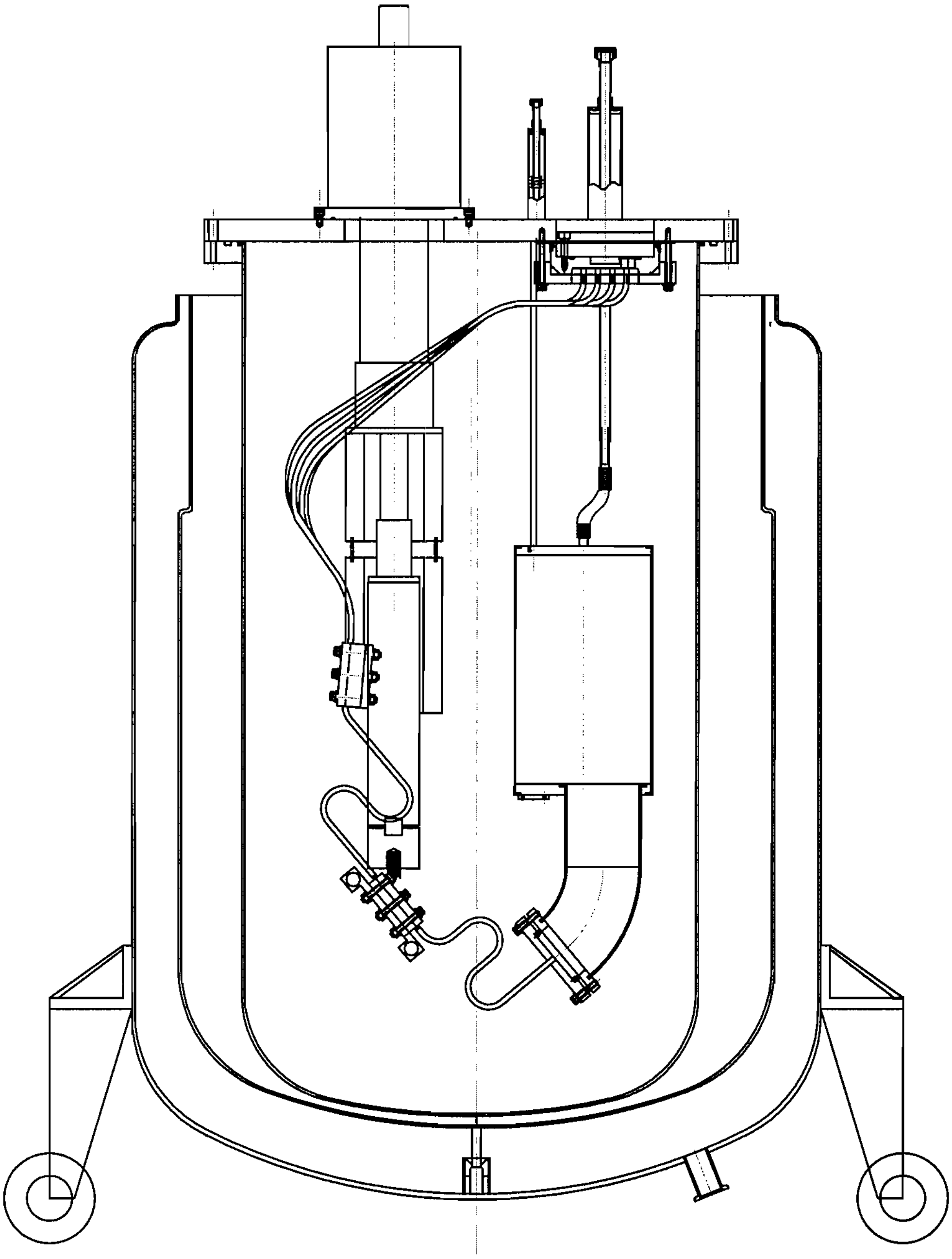

Figure 4.23. *Schematic representation of the cryogenic station*

Measurement of the background loss to the LHe

All the operating conditions were initially achieved, i.e. 77 K background temperature and 1st/2nd crycooler stations maintained at about 50 K and 20 K respectively. The LHe vessel was filled with LHe and the level was monitored using a superconducting level sensor. The boil off was measured using MKS 20 SLM flow meter which was calibrated for the vapour at room temperature. The 1st measurement has unexpectedly shown a relatively high heat in-leak to the LHe vessel which was also varied with the liquid level and time. This phenomenon was mainly attributed to the non-equilibrium condition of the radiation shield of the 1st stage. This was further improved by improving the thermal link to this radiation shield via extra thermal links as shown in figure 4.24. The thermal links are high conductivity Cu strips that are soldered from one end onto a Cu ring that is thermally anchored to the 1st stage of the cryocooler, and soldered from the other end onto the Cu radiation shield.

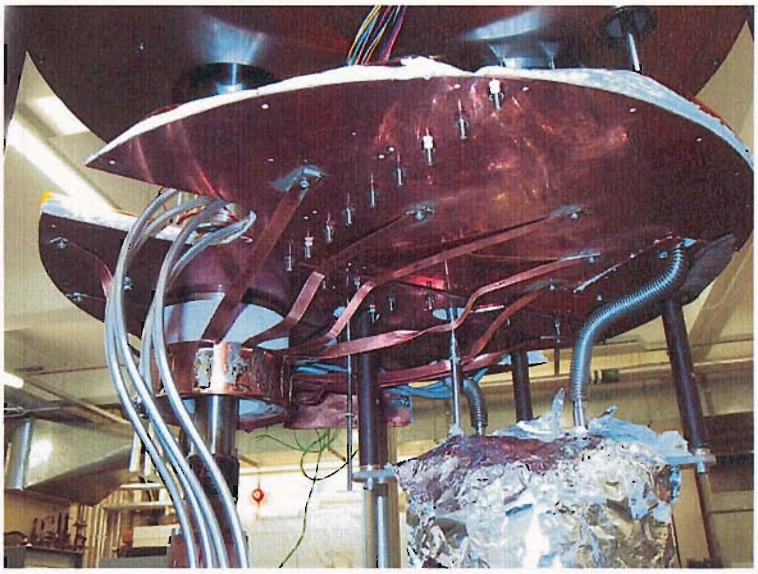

Figure 4.24. *The thermal anchoring of the 1st stage radiation shield was improved via the addition of Cu thermal links*

The second measurement was within the expectation showing a low heat in-leak which stayed almost constant with time. It is estimated that the heat in-leak is about 0.3 Watts. Figures 4.25 and 4.26 show the volume flow rate of the evaporated helium gas at room temperature due to the background heat leak as a function of time and LHe level in the vessel respectively.

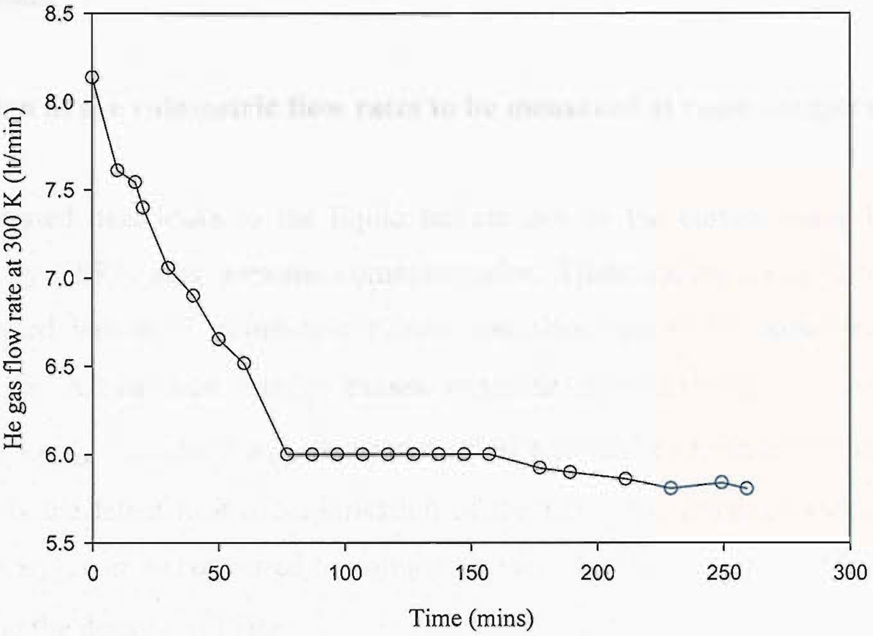

Figure 4.25. *Volume flow rate at 300 K of evaporated helium gas due to the background loss as a function of time*

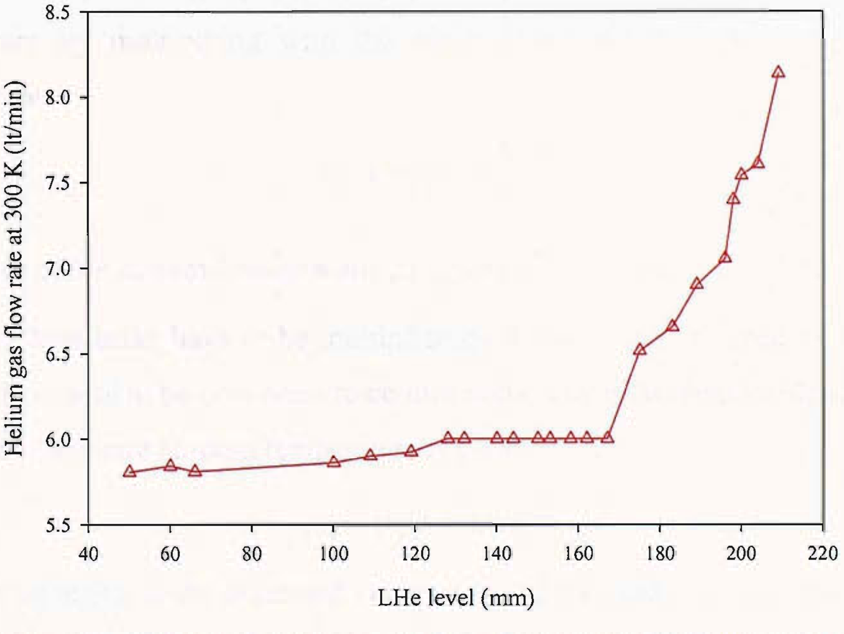

Figure 4.26. *Volume flow rate at 300 K of evaporated helium gas due to the background heat leak as a function of the LHe level in the LHe vessel*

It can be concluded that the performance of this test facility is satisfactory and further improvements will help in achieving better operation and functionality. It is recommended to further monitor the radiation shield temperature in order to be able to achieve reasonable reproducibility during the thermo/electric verification of the current leads.

Estimation of the volumetric flow rates to be measured at room temperature

The estimated heat leaks to the liquid helium due to the current leads have been obtained by CERN after personal communication. These values are used to estimate the expected values of volumetric helium gas flow rate to be measured at room temperature. A heat leak rate $\dot{Q}$ causes vaporization of LHe that is given by the relation $Q = \dot{m}_{4.2K} \cdot \lambda$, where $\dot{m}_{4.2K}$ is the mass flow rate of the vaporised helium and λ = 20 J·gr^{-1} is the latent heat of vaporisation of the LHe. The obtained values of mass flow rate $\dot{m}_{4.2K}$ can be converted to volumetric values of flow rate at 4.2 K if they are divided by the density of LHe.

$$\dot{v}_{4.2K} = {}^{\dot{m}_{4.2K}}\!\big/_{\rho_{LHe}}$$

The volumetric flow rate at 4.2 K can be converted to volumetric flow rate at room temperature by multiplying with the ratio of the densities at 4.2 K and room temperature.

$$\dot{v}_{300K} = \dot{v}_{4.2K} \times \frac{\rho_{4.2K}}{\rho_{300K}}$$

The values of the helium densities are $\rho_{4.2K} = 0.125\ {}^{gr}\!/_{cc}$ and $\rho_{300K} = 1.625 \times 10^{-4}\ {}^{gr}\!/_{cc}$. The given heat leaks have to be multiplied by 4 due to the presence of 4 conductors and the flow rates to be converted to cc/min units. The final relationship that gives the volumetric flow rate at room temperature is then:

$$\dot{v}_{300K} = Q_o^{LHe} \times 18.46\ \left[{}^{lt}\!/_{\min}\right]$$

In the following table the estimated values of heat leaks and flow rates are displayed:

I (A)	Q_{LHe}	$\dot{v}_{300K}\ \left({}^{lt}\!/_{\min}\right)$
0	4 x 0.085	6.277
15	4 x 0.090	6.646
30	4 x 0.110	8.123
60	4 x 0.170	12.554

For the case of the 120 A current leads the above values have to considered as double approximately.

4.6. Summary and conclusions

A low heat leak cryogenic station for thermo-electric assessment of conduction cooled resistive current leads for superconducting accelerator magnets was designed, built and set-up using principles of cryogenic design. The station employs large volume of LN_2 to provide radiation shield at 77 K, cryocooler cooling of the two heat-intercepts of the current leads and a low-heat leak stainless steel liquid helium vessel to keep the end of the leads at 4.2 K. The station has shown satisfactory performance during testing. It has shown that it is possible to achieve the required temperatures at the two heat intercept points with the current leads through Cu thermal links at the two stages of the crycooler. The liquid helium boil-off due to the background heat leaks to the LHe vessel was measured to be at the satisfactory level of 0.3 Watts. A cryogenic test facility was designed, built and set-up in order to measure the thermal contact resistance between the thermal anchoring clamps and the current leads. The thermal contact resistance was measured to be reasonably low. The differences between the measured values and the theoretical predictions were assigned to the morphology of the contact interfaces due to imperfect machining. A modification in the design of the metal blocks has been proposed in order to improve the physical contact between the leads and the thermal anchoring blocks, thus avoiding the consequences of any possible machining imperfections and consequently to improve the thermal contact and hence to increase the effectiveness of the cooling of the current leads.

4.7. Future work

For my future work in this project, the aim is to carry out experimental thermo-electric assessment of the conduction cooled leads 60 A and 120 A using the dedicated set-up that has been previously described. The current leads will be subjected in various tests in order to determine the following parameters:

1. Measurement of the heat leak to the liquid helium at the nominal current of operation and the two stations held at 50 K and 20 K.
2. Measurement of the heat load that is absorbed in the two heat sinks in order to maintain the two heat intercepts at temperatures 50 K (aluminium) and 20 K (copper) at the nominal operation current.
3. Measurements of voltage drops and voltage-time characteristics at various operational currents and heat intercept temperatures.

References

[1] Amalia Ballarino, "*Current Leads for the LHC Magnet System*", IEEE Trans. Appl. Supercond., vol. 12, No. 1, March 2002, pp. 1275-1280

[2] W. Mercouroff, *"Minimization of thermal losses due to electrical connections in cryostats"*, Cryogenics 1963, p. 171

[3] Yunus A. Cengel, *"Introduction to thermodynamics and heat transfer"*, McGraw-Hill, 1997, pg. 217, ISBN 0-07-011498-6

Chapter 5

Quench propagation in composite HTS elements of current leads

5.1. Introduction

Since the discovery of the high Tc oxide superconductors [1], many technological applications in the field of electrical power engineering have been developed based on HTS material. The various applications such as transmission cables and wires, transformers, generators, motors and magnets employ HTS wire that has yet to demonstrate superior mechanical and electrical properties in order to be able to commercialize more of these applications at liquid nitrogen environments. The most frequent choice for the HTS wire is the composite Ag/Bi-2223 that guarantees the best performance among all the existing HTS conductors at 77 K. Although at experimentation and demonstration level the HTS wire has been utilised and already has passed into the stage of wide application, the use of HTS in large scale particle accelerator magnets is yet far from realization, due to low critical current density at 77 K, poor performance under applied magnetic fields and insufficient mechanical strength, which is so important in the magnet environment where the conductor is subjected to bending strain and electromagnetic force [2]. In magnet construction, the LTS technology is by far the most preferred design. The NbTi superconductor is used to build the large particle accelerator, MRI and research magnets until the status of the HTS technology will be advanced to the specifications set by the underlying principles of magnet design. Even the use of superfluid helium as a coolant offers the advantage to fully benefit from the superconducting properties of the LTS conductors. The incorporation of superconducting material in the magnet feeding current leads also meets great functionality and is highly necessitated by the need to reduce the heat leak to the already over-loaded liquid helium and also the refrigeration power. However, the application of HTS material in the current leads that power the magnets cannot be discounted, since fewer restrictions exist in comparison to the application in magnets. The importance and benefits for the economical operation of the magnet system that arise by the application of HTS material in the current leads are obvious, since the electro-mechanical joint of the metal conductor to the HTS part is possible to be held at high temperatures as 50 K, as in the current leads that feed the superconducting magnets at the Large Hadron Collider at CERN. Savings up to 30% in refrigeration power and reduction of the heat leak to the LHe by 10 times in comparison to conventional leads are estimated [3] in the LHC, which is a representative example of a massive application of HTS leads. The recent developments in the field of HTS current lead manufacturing technology yield that a good current lead design should deal with three main issues: the upper resistive stage, the thermal intercept and the lower superconducting stage. In more detail, some technical factors that have to be addressed in the design of the HTS leads include the material choice, the configuration that will reduce the influence of the magnetic field on the HTS current capacity, the use of a parallel conductive shunt for thermoelectric stability, the influence of the contact resistance between the HTS and conventional materials or any other joints that may appear and the quench of the HTS part (or thermal runway) that may occur due to the loss of the cooling ability of the conductor. The HTS section of the current lead is a highly effective thermal break while maintaining the electrical current conduction from the upper copper part down to the liquid helium temperatures. The most popular HTS conductor for current lead applications is the Ag/Bi-2223 tape due to the high critical current density, the good strain tolerance during the thermal cycling and the feasibility of complex geometries. The use of several tapes in the HTS part reduces the nominal current of each individual tape; therefore in the case of partial damage, a parallel current path is provided to ensure resistanceless current flow. A mechanical reinforcement to the weak composite tapes is provided by the additional shunt, which also provides a parallel current path in case of quench, and moreover improves the thermal stability by adding heat capacity to the composite. The shunt should be a good electrical/poor thermal conductor with high heat capacity at low temperatures and high mechanical strength. Stainless steel is widely used [4] in the form of tubes or plates, since it combines all the above mentioned properties. The geometry of the HTS part is determined by the shape of the shunt and should be such as to minimise the influence of the self magnetic field on the superconducting properties of the tapes but to ensure a good heat exchange with the cold helium gas in vapour cooled leads. The tapes need to be in electrical/ thermal contact with the stainless steel shunt in order to take advantage of its thermoelectric properties in case of over current and over heating conditions. To ensure therefore a good mechanical support, good thermal and electrical contact, a technique that is used is the brazing of the tapes onto the stainless steel tube or plate [4].

Due to quenching, the temperature of the composite will increase without bound unless the quench is detected on time and the current is switched off. In general, quench is not easy to predict and identify. Continuous monitoring of the temperature and voltage may detect the margin of an incoming thermal disturbance of the steady state temperature profile and trigger an immediate action to prevent further expansion. The knowledge of the behaviour of the HTS part under quench conditions is of major importance in order to control this undesirable event, which not only can damage the current leads but also can produce excessive boil-off of LHe and therefore the appropriate protection schemes have to be designed. In this study, a cryostat based on a two stage Gifford Mc McMahon cryocooler was designed, built and set-up in order to simulate the quench propagation of the HTS part of current leads consisting of Ag/Bi-2223 tapes and stainless steel shunt under adiabatic conditions. The quench was caused by increasing the current to the minimum required value in order to initiate the thermal runway, namely the quench current Iq.

5.2. Theory of quench propagation in superconductors

5.2.1. Introduction

The three critical physical quantities of a superconductor H_c, T_c and J_c define the critical surface in the H-T-J geometrical space as it was mentioned in chapter 1. Three unique values of (H,T,J) define a point in the H-T-J geometrical space that characterizes the state of the superconducting wire. If the point lies in the space below the critical surface, the superconductor is stably operating in the superconducting state. In applications, it is not rare that the characteristic (H-T-J) point shifts above the critical surface due to the influence of external factors (disturbances). The Joule heating in the superconductor will cause the temperature to rise and unless stabilised in some way the normal zone temperature will increase without bound. In superconducting magnets, the operational temperature is not totally controllable because the energy that is stored in the magnet as magnetic and mechanical energy can be converted to heat and disturb the thermal equilibrium in the windings and cause quenching. The quench can be described as a transient thermal process with fast increases of the temperature with time. In a magnet winding that is cooled by liquid helium or in a composite superconducting wire, the quench transient can be represented by the following relation, which expresses the thermal equilibrium in terms of power densities:

$$\dot{E} = \dot{Q}_{cond} + \dot{Q}_{Joule} + \dot{Q}_{gen} + \dot{Q}_{cool} \tag{5.1}$$

The first term, $\dot{E}$, expresses the rate of change in the internal energy of the conductor:

$$\dot{E} = C_{cond}(T) \times \frac{\partial T}{\partial t} \tag{5.2}$$

where C_{cond} is the conductor heat capacity. The second term, $\dot{Q}_{cond}$, expresses the heat that is conducted along the conductor:

$$\dot{Q}_{cond} = \vec{\nabla} \cdot \{k_{cond}(T) \cdot \vec{\nabla} T\} \tag{5.3}$$

where k_{cond} is the thermal conductivity of the conductor. The third term, $\dot{Q}_{Joule}$, expresses the joule heat generation due to the transition to the normal state

$$\dot{Q}_{Joule} = \rho_{cond} \times J^2 \tag{5.4}$$

where ρ_{cond} is the electrical resistivity of the conductor and J is the current density that flows through the conductor. The fourth term, $\dot{Q}_{gen}$, is the internal heat generation due to the external factors that have disturbed the thermal equilibrium in the conductor and caused the quench; usually it is of magnetic or mechanical origin. The last term $\dot{Q}_{cool}$ expresses the cooling of the conductor by the liquid helium or in the case of current leads by the cold helium vapour; it is absent in the case of adiabatic conditions. If the transition to the normal state is irreversible, which practically means that the cooling is insufficient to recover the superconductor from the quench, the local heating will expand in longer conductor length; the quench will propagate through the conductor. The minimum propagating zone (MPZ) is a characteristic length l_C which determines if the initial local heating in a short conductor length will propagate or shrink.

5.2.2. The circuit model

In order to treat the problem of cryo-stability in a composite superconductor, for example a tape, the composite superconductor is represented by an equivalent electrical circuit as in the figure 5.1:

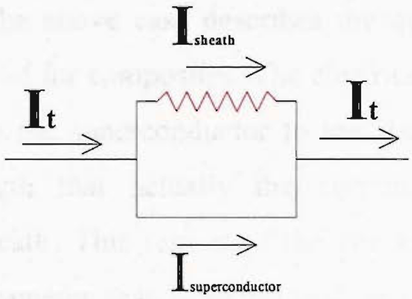

Figure 5.1. *Equivalent electrical circuit of a composite superconductor*

I_t is the total electrical current, I_{sheath} is the electrical current that passes through the sheath of the composite and I_{SC} is the current that passes through the superconductor. I_C is the critical current of the superconductor and R_{SC} is the electrical resistance of the superconductor. In the context of the circuit model, expressions for the heat generation in the composite conductor will be derived. Two cases exist depending on the value of the electrical current I_t in relation to the critical current of the superconductor.

a. $I_t < I_c$

In this case, the superconductor is in the superconducting state and the voltage across the conductor V=0 and therefore the heat dissipation $Q_j = 0$.

b. $I_t \geq I_c$

Because the electrical resistance of the normal state of the superconductor is much bigger than the resistance of the sheath, the excess current above the value of I_c will pass through the sheath, i.e. $I_{sheath} = I_t - I_C$. The voltage that is developed in the conductor is:

$$V = R_{sheath} \times I_{sheath} = R_{sheath} \times (I_t - I_C) = R_{sc} \times I_C$$

$$R_{sc} = R_{sheath} \times \left(\frac{I_t}{I_C} - 1 \right)$$

The heat dissipation is $Q_J = V \times I_t = R_{sheath} \times I_t \times (I_t - I_C)$ ***(5.5)***

In reality, the transition to the normal state is not as sharp as it is supposed in the above treatment. Perhaps the above case describes the quench in a non-composite superconductor; it is not valid for composites. The electrical current of the conductor cannot jump abruptly from the superconductor to the sheath during a quench, but there exists a small length that actually the current is shared between the superconductor and the sheath. This region of the conductor is termed as current sharing region. A new parameter that is introduced in the analysis is the current sharing temperature T_{CS}. As long as the conductor temperature is below the T_{cs}, the conductor will be fully superconducting and hence there will not be any heat generation. At T_{cs}, the total current I_t is equal to the critical current that corresponds to the current sharing temperature T_{cs}, $I_c(T_{cs})$. Above T_{cs}, the superconductor will carry current equal to $I_c(T)$ which is less than I_t and decreases with temperature. The excess current I_t-$I_c(T)$ flows through the sheath material. As the temperature increases above the T_{cs}, the current that flows through the superconductor $I_{sc}(T)$ decreases and the sheath current $I_{sheath}(T)$ increases until the conductor is heated to the critical temperature, where all the electrical current will be flowing through the sheath.

5.2.3. Calculation of the heat generation in the composite superconductor

The heat generation G(T) in the case of a composite superconductor can be calculated by taking into account that current sharing occurs between the superconductor and the metal sheath. The heat generation can be thought as the product of the transport current density with the generated electric field.

$$G(T) = J \times E = \frac{I_t}{A} \times \frac{dV(T)}{dx} \qquad \textbf{(5.6)}$$

The voltage that is generated across a differential length of the conductor is temperature dependent:

$$dV(T) = I_{sheath}(T) \times R_{sheath}(T) = I_{sheath}(T) \times \frac{\rho_{sheath}(T)dx}{A_{sheath}}$$

The temperature dependence of the heat generation is then given by the following relation:

$$G(T) = \rho_{sheath}(T) \times \left(\frac{I_t}{A}\right) \times \left(\frac{I_{sheath}(T)}{A_{sheath}}\right) \qquad (5.7)$$

In relation (5.8), the critical current is approximated by a linear function of the temperature:

$$I_C(T) = -\frac{I_c(T=0)}{T_C} \times T + I_C(T=0) \qquad (5.8)$$

In relation (5.7) the heat generation depends on the portion of electrical current that passes through the metal sheath I_{sheath} which is determined by the temperature:

$$I_{sheath}(T) = \begin{cases} 0, & for \quad T \leq T_{cs} \\ I_t \times \dfrac{T - T_{cs}}{T_C - T_{cs}}, & for \quad T_{cs} \leq T \leq T_C \\ I_t, & for \quad T \geq T_C \end{cases} \qquad (5.9)$$

The heat generation in the composite superconductor has three temperature regimes in relation (5.10).

$$G(T) = \begin{cases} 0, & for \quad T \leq T_{cs} \\ \dfrac{\rho_{sheath}(T) \times J^2}{f} \times \dfrac{T - T_{cs}}{T_C - T_{cs}}, & for \quad T_{cs} \leq T \leq T_C \\ \dfrac{\rho_{sheath}(T) \times J^2}{f}, & for \quad T \geq T_C \end{cases} \qquad (5.10)$$

where f is the superconductor volumetric filling factor of the composite tape. Above the critical temperature the heat generation is totally dominated by the resistive heating of the metal sheath where 100% of the electrical current flows through the metal sheath.

5.2.4. Propagation of the normal zone in the longitudinal direction

The propagation of the normal zone in the longitudinal direction x in a composite superconductor can be studied with the use of the equation (5.1). The problem is treated assuming adiabatic conditions, which means that there is no cooling of the conductor by any coolant, either a liquid cryogen or cold vapour. While some part of the conductor has passed into the normal state and the rest of the conductor sustains the property of superconductivity along the length, there should be a boundary between the two states, normal and superconducting, that travels in the x direction with a constant velocity of propagation, U_l. Schematically the phenomenon is illustrated in the figure below.

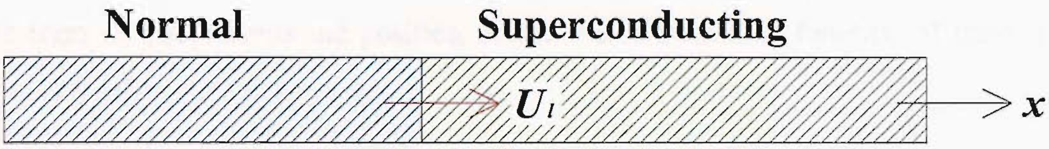

Figure 5.2. *Schematic of the longitudinal propagation of the boundary normal/superconducting with a constant velocity U_l*

The quench propagation velocity is the velocity that the normal zone grows in size or the velocity that the normal/superconducting boundary propagates further in the superconducting region of the conductor. Equation (5.1) is applied in the two regions, normal and superconducting, in one dimensional form:

Normal region

In the x-direction under adiabatic conditions, relation (5.1) takes the form of relation (5.11) where the cooling term has been omitted.

$$C_n \cdot \frac{\partial T_n(x)}{\partial t} = \frac{\partial}{\partial x}\left\{k_n \cdot \frac{\partial T_n(x)}{\partial x}\right\} + \rho_n \cdot J^2 \qquad (5.11)$$

The subscribe n refers to the normal state of the conductor; C_n is the heat capacity, k_n the thermal conductivity and ρ_n the electrical resistivity.

Superconducting region

In the superconducting region, the one dimensional form of relation (5.1) has the following form after the omission of the Joule heating term:

$$C_S \cdot \frac{\partial T_s(x)}{\partial t} = \frac{\partial}{\partial x} \cdot \left\{k_s \cdot \frac{\partial T_s(x)}{\partial x}\right\} \qquad (5.12)$$

The subscribe s that subscribes the physical properties heat capacity C and thermal conductivity refers to the superconducting state of the conductor.

Change of variables

It is considered that the normal-superconducting boundary moves with a constant propagation velocity U_l in the x direction. The new variable y is introduced as

$$y = x - U_l \cdot t \qquad \textbf{(5.13)}$$

The term $U_l \cdot t$ represents the position of the warm front as a function of time. The equations are transformed as follows:

$$C_n \cdot \frac{\partial T_n}{\partial t} = \frac{\partial}{\partial y} \cdot \left\{ k_n \cdot \frac{\partial T_n}{\partial y} \right\} + \rho_n \cdot J^2 \qquad \textbf{(5.14)}$$

$$C_s \cdot \frac{\partial T_s}{\partial t} = \frac{\partial}{\partial y} \cdot \left\{ k_s \cdot \frac{\partial T_s}{\partial y} \right\} \qquad \textbf{(5.15)}$$

The time dependence of the temperature can be transformed as follows:

$$\frac{\partial T}{\partial t} = \frac{\partial T}{\partial y} \cdot \frac{\partial y}{\partial t} = -U_l \cdot \frac{\partial T}{\partial y} \qquad \textbf{(5.16)}$$

The velocity U_l has been introduced in the equations of stability which they can take the following form:

$$-C_n \cdot U_l \cdot \frac{dT_n}{dy} = \frac{d}{dy} \cdot \left\{ k_n \cdot \frac{dT_n}{dy} \right\} + \rho_n \cdot J^2 \qquad \textbf{(5.17)}$$

$$-C_s \cdot U_l \cdot \frac{dT_s}{dy} = \frac{d}{dy} \cdot \left\{ k_s \cdot \frac{dT_s}{dy} \right\} \qquad \textbf{(5.18)}$$

The energy balance equations for the two regions, normal and superconducting take the final form:

Normal region:

$$\frac{d}{dy} \cdot \left\{ k_n \cdot \frac{dT_n}{dy} \right\} + C_n \cdot U_l \cdot \frac{dT_n}{dy} + \rho_n \cdot J^2 = 0 \qquad \textbf{(5.19)}$$

Superconducting region:

$$\frac{d}{dy} \cdot \left\{ k_s \cdot \frac{dT_s}{dy} \right\} + C_s \cdot U_l \cdot \frac{dT_s}{dy} = 0 \qquad \textbf{(5.20)}$$

The boundary conditions will help to extract an expression for the normal zone propagation velocity U_l from the equations (5.19) and (5.20) assuming temperature independent material properties. The position $y = 0$ defines the boundary of the normal to the superconducting region. Close to this point, the temperature of the normal zone should be minimum, as it approaches the superconducting region where the temperature is low enough to sustain superconductivity. Therefore it should be

$$\left. \frac{d^2 T_n}{dz^2} \right|_{y=0} = 0$$

Close to the boundary $y = 0$, the normal and superconducting regions are described by the following equations:

Normal:
$$C_n \cdot U_l \cdot \frac{dT_n}{dy} + \rho_n \cdot J^2 = 0 \qquad \textit{(5.21)}$$

Superconducting:
$$k_s \cdot \frac{d^2 T_s}{dy^2} + C_s \cdot U_l \cdot \frac{dT_s}{dy} = 0 \qquad \textit{(5.22)}$$

The solution of the last equation, which is a linear second order differential equation has the following form:

$$T_s(y) = A \cdot \exp\left\{- C_s \cdot U_l \big/ k_s \cdot y\right\} + T_{cool} \qquad \textit{(5.23)}$$

T_{cool} is the temperature of the superconductor in the region far enough from the boundary that is practically not affected by the appearance of the normal zone. The temperature of the superconductor at the boundary will be equal to its critical temperature T_C if the transition is assumed rapid. Therefore the solution has the following form:

$$T_s(y) = (T_c - T_{cool}) \cdot \exp\left\{- C_s \cdot U_l \big/ k_s \cdot y\right\} + T_{cool} \qquad \textit{(5.24)}$$

At the boundary $y = 0$ the flow of heat must be continuous which defines an important boundary condition:

$$k_n \cdot \left.\frac{dT_n}{dy}\right|_{y=0} = k_s \cdot \left.\frac{dT_s}{dy}\right|_{y=0} \qquad \textit{(5.25)}$$

The combination of equations (5.23), (5.24) and (5.25) gives:

$$-\frac{k_n \cdot \rho_n \cdot J^2}{C_n \cdot U_l} = -C_s \cdot U_l \cdot (T_C - T_{cool}) \qquad \textit{(5.26)}$$

From this equation the expression of the longitudinal normal zone propagation under adiabatic conditions can be derived:

$$U_l = J \cdot \sqrt{\frac{\rho_n \cdot k_n}{C_n \cdot C_s \cdot (T_C - T_{cool})}} \qquad \textit{(5.27)}$$

Direct important conclusions from expression (5.27) are that the normal zone propagation is proportional to the current density and inverse proportional to the heat capacity. Relation (5.28) is the expression for the quench propagation velocity if the temperature dependence of the physical properties is considered [2].

$$U_l = J \times \left\{ \frac{1}{\rho(T_t)\cdot k_n(T_t)} \times \left(C_n(T_t) - \frac{1}{k_n(T_t)} \times \left.\frac{dk_n}{dT}\right|_{T=T_t} \times \int_{T_{cool}}^{T_t} C_s(T)\cdot dT \right) \times \int_{T_{cool}}^{T_t} C_s(T)\cdot dT \right\}^{-1/2} \tag{5.28}$$

5.3. The cryogenic station for measuring the quench propagation

5.3.1. Outer vacuum vessel-housing of the experiment

All the experiments at cryogenic temperatures, especially when using cryocoolers are required to be carried out in vacuum environments. The vacuum is necessary in order to reach low temperatures because the convective thermal losses would make impossible to cool down due to limitations in the refrigeration power of the machine. Also vapour would condense on the cold parts of the experiment thus making undesirable complications. The vacuum space in the rig is provided by an in-house fabricated stainless steel cylindrical vessel of dimensions: Height 100 mm, inner diameter 305 mm and wall thickness 2 mm. At the top, a stainless steel flange of thickness 12.7 mm (1/2 of an inch) seals with O-ring. At the bottom, a stainless steel flange of the same dimensions seals with O-ring but also has the following additional features: (a) Insert hole for the cryocooler (the O-ring is on the cryocooler flange), (b) Insert flange for the electrical current leads with electrically insulated ceramic seals (lead-throughs), (c) Three welded steel tubes that hold three 10-pin vacuum sealed electrical connectors for the electrical wiring of the voltage and temperature sensors, (d) One pumping port for pumping the inner space.

5.3.2. Cooling system

The cooling in the experiment is provided by the two-stage Gifford McMahon refrigerator supplied by Leybold Cryogenics [4]. This machine is capable of producing the temperature of 4.2 K at its second stage with refrigeration power capacity of 0.5 Watts applied thermal load [4]. High purity helium gas (99.99) is used in the cryocooler system. It is possible that the helium gas will lose its high purity after long time use. The impurities condense in the cold parts of the regenerator during operation and create blocks in the passage of the cold helium gas, which results in reduction of the refrigeration power of the machine. After a use of nearly two years in the experiments, it was noticed that the machine was not able to reach the temperature of 4.2 K which is specified by the manufacturer; also oscillation in the temperature of the second stage was observed. These are signs that perhaps impurities had entered the helium gas of the system. In order to purify the gas, the following procedure was followed: The cryocooler was cooled down to the lowest temperature and then isolated from the compressor by unbolting the hermetically sealed helium gas inlet and outlet valves. All the impurities have been condensed on the cold regenerator. The cryocooler warmed to room temperature; the impurities were vaporised. At room temperature, the cryocooler was connected to a pump and pumped; all the impurities were removed. The procedure was repeated three times. The crycooler returned back to the normal operation and reached temperature 3.5 K at the second stage without oscillation.

5.3.3. Radiation shielding

Significant thermal loss in cryogenic systems is the radiation loss. Radiation is the energy emitted by matter in the form of electromagnetic waves and is a result of changes in the electronic configurations of atoms and molecules. This mode of heat transfer does not require the presence of an intermediate medium in order to be transmitted. In the field of heat transfer, the term is better described as thermal radiation and is the form of radiation that is emitted by bodies because of their temperature (above the absolute zero). The radiation loss obeys the Stefan-Boltzmann law; when a body is at absolute temperature Ts, the rate of radiation emission is given by the relation:

$$\dot{Q}_{radiation} = \varepsilon \times \sigma \times A \times T_s^4$$

where $\sigma = 5.67 \times 10^{-8}\ W/(m^2 \cdot K^4)$ is the Stefan-Boltzmann constant and A is the surface area [1]. The term ϵ is the emissivity, which has the maximum value of 1 for a blackbody (idealized case). For real surfaces has values $0<\epsilon<1$. The net rate of radiation heat transfer between two surfaces which are held at temperatures T_1 and T_2 is given by the following relation

$$\dot{Q}_{radiation} = \varepsilon \times \sigma \times A \times \left(T_1^4 - T_2^4\right)$$

In the case of this experimental rig, the radiation loss will cause additional heat load on the cryocooler which cannot be afforded due to limitations in the refrigeration power and therefore the achievement of sufficiently low temperatures will be impossible. The protection against thermal radiation losses in cryogenic systems is provided by radiation_shields. The thermal radiation shield that has been made in this rig is a closed cylinder made of copper sheet of thickness 1 mm, height 627 mm and outer diameter 158 mm. It is enclosed at the top by copper and is attached to the first stage of the cryocooler by a ring flange that bolts on a copper flange of diameter 178 mm bolted on first stage flange of the cryocooler. Sixteen M4 bolts hold tight the two flanges together, while Apiezon N grease is spread at the interface of the two flanges in order to improve the thermal contact. The outer surface of the shield is covered by layers of super-insulation. The super-insulation (or multi-layer insulation) provides reflectivity to the incoming radiation from the room temperature warm outer steel vessel. Super-insulation is made of alternating layers of highly reflecting aluminium foil and a low thermal conductivity spacer made of nylon net that prevents physical contact between the alternating aluminium layers. The super-insulation has very low thermal conductivity because all the modes of heat transfer are almost eliminated. Radiation is minimised by using many layers of reflecting surfaces (aluminium paper). The heat conduction is eliminated by intervening the thermal insulating nylon net spacer between the aluminium layers. The convective heat transfer is reduced by lowering the gas pressure to values as low as 10^{-5} bars. The apparent thermal conductivity of super-insulations of this kind can be estimated from the following relation [1]:

$$K_t = \left(N/\Delta x\right)^{-1} \cdot \left[h_C + \sigma \cdot e \cdot \left(T_h^2 + T_C^2\right) \cdot \left(T_h + T_C\right)/(2-e)\right]$$

h_c is the conductance of the spacer, σ is the Stefan-Boltzmann constant, e is the effective emissivity of the shield material and T_h, T_c are the boundary temperatures of the super-insulation. The first term of the product represents the density of the layers of insulation. Increased number of layers increases the apparent thermal conductivity. If the density of layers is two high, the solid conductivity increases much more than the first term of the product. Therefore there is an optimum layer density that the super-insulation shows the minimum apparent thermal conductivity, which is 3.3 times less than the one which corresponds to about ±100 layers/cm density [1].

The effectiveness of the super-insulation can be assessed through the following calculation: If super-insulation was not present, the rate of radiation thermal loss from the 1^{st} stage copper shield (cooled at 40 K) due to radiation heat exchange with the warm stainless steel vessel (300 K) would be:

$$\dot{Q} = \varepsilon \times \sigma \times A \times \left(300^4 - 40^4\right) = 5.67 \times 10^{-8} \times 0.3 \times 81 \times 10^8 = 137 \text{ Watts}$$

where it was assumed emissivity equal to 1 and the copper area is 0.3 m^2. This value of heat loss cannot be afforded by the cryocooler due to limitation in its refrigeration power and the necessity of the super-insulation is obvious.

5.3.4. Sample holder

The sample holder (figure 5.3) consists of the following parts:

Two thermal anchoring cylindrical copper blocks. These blocks form the basic frame of the sample holder. The "bottom" block is machined as one body and is bolted on the copper cold head of the second stage. The tape samples are soldered (figure 5.4) inside two grooves of depth 8 mm and width 15 mm. One tape is the sample under investigation.

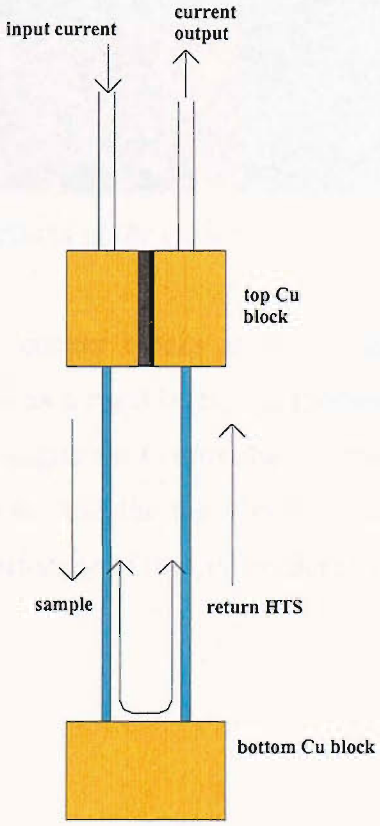

Figure 5.3. *Sample holder and electrical current loop indicated by arrows*

The other tape is not examined and it only serves as the output or return current conductor of the circuit. The top block is machined as two identical halves that are joined by electrical insulating layers of fibre-glass cloths impregnated in Epoxy Eco-Bond 104. Each half is connected to a current lead of the power supply. Therefore an electrical current loop has been made as shown in the figure above; the electrical insulation of the bottom block to the cryocooler head is not necessary.

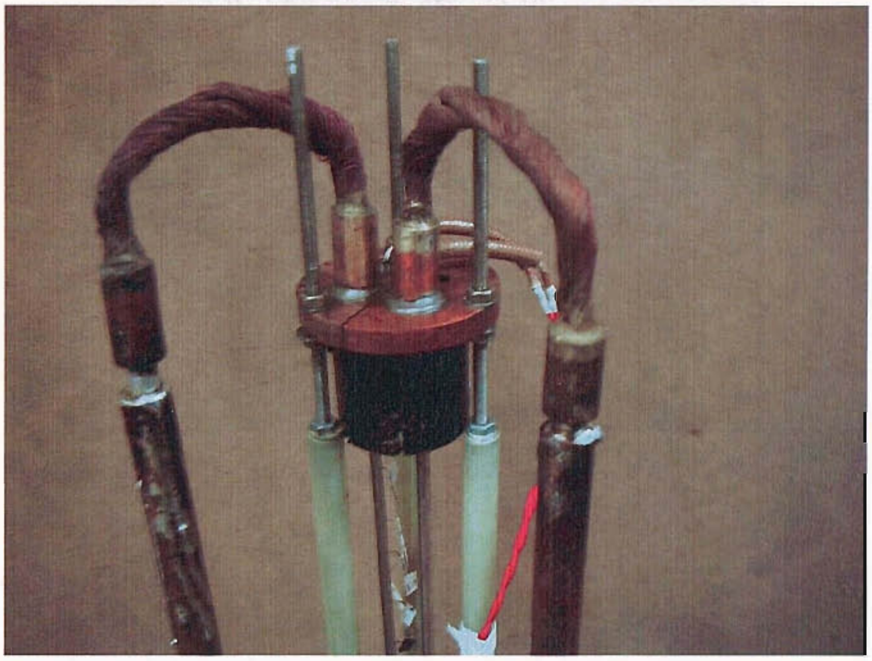

Figure 5.4. *The connections of the current leads to the top copper block*

Three G-10 rods hold the two copper blocks apart at a distance of 250 mm (the sample length) perfectly aligned as a rigid body and provide the mechanical support to the weak tape samples. The alignment is important so the grooves of the opposite blocks face each other in parallel and the tapes don't twist. The sample holder is bolted on the flange of the second stage of the cryocooler (figure 5.5).

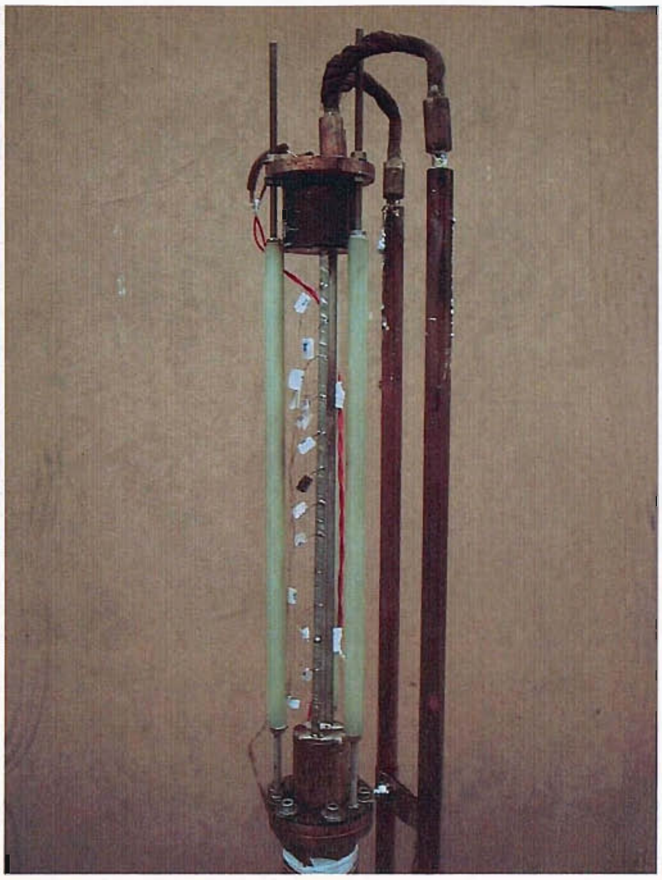

Figure 5.5. *The sample holder mounted on the cryocooler*

5.3.5. The current leads

The feeding of electrical current is achieved through a pair of copper conduction cooled current leads of diameter 12 mm. The current leads enter the vacuum space through two electrically insulting ceramic seals (lead-throughs) that are welded on the insert flange which bolts and seals with O-ring at the bottom external big flange of the system. The current leads enter the space inside the radiation shield from the bottom of the 1st stage copper flange and are thermally anchored using specially made copper clamps. The current leads end at the top copper block and are soldered one on each of the two halves. The current leads have a dual function: Firstly to feed with electrical current the sample and secondly to thermally link the top copper block to the first stage of the crycooler. Therefore it is possible to hold the top end of the sample to temperatures 45 K and above. Crucial for the experiment is the thermal anchoring of the current leads. Through thermal anchoring to the 1st stage of the crycooler, the current leads will be cooled by conduction; also the top copper block will be cooled by conduction via the current leads.

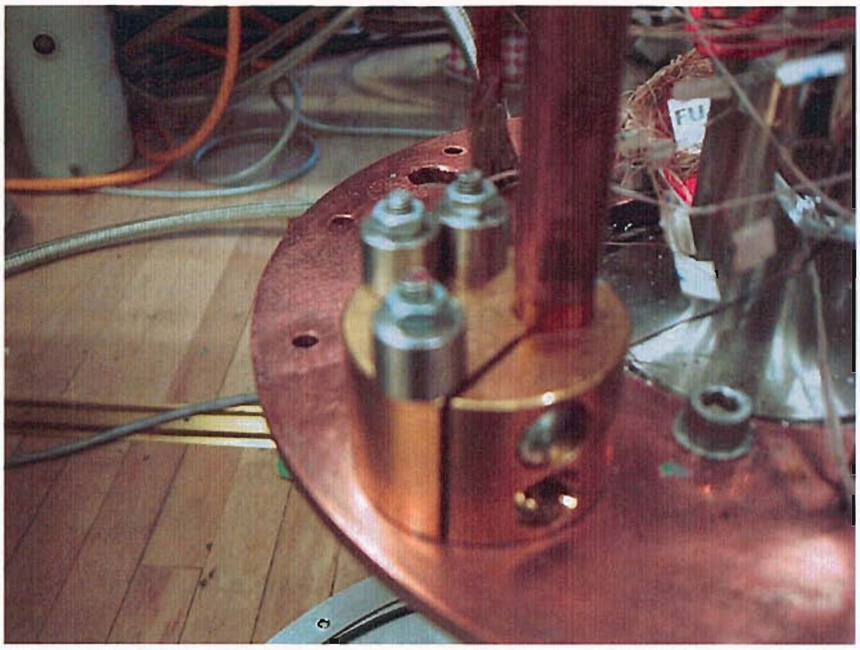

Figure 5.6. *Thermal anchoring clamp of the current leads on the 1st stage copper flange. The Invar washers can be seen*

The current lead is clamped by pressure contact to the copper clamp as shown in figure (5.6). Two M4 screws tighten the clamp around the lead and a layer of Kapton MT of thickness 25 μm (polyimide film) electrically insulates the conductor from the clamp. The clamp has a coating of gold in order to protect the copper from oxidation. The oxide layer that forms on the copper surface is detrimental to the thermal contact. The clamp is tightly bolted on the 1st stage flange in the interior of the thermal shield space. The contact between the clamp and the flange will get weak when the system cools down because of differential contraction between the copper and the steel bolt. As a result poor thermal contact will occur. In order to compensate for the differential contraction, invar alloy washers were fabricated from an invar bar and used to tighten the bolts of the thermal clamp to the copper flange as it can be seen in the figure.

It has to be pointed out that the section of these current leads above the first stage thermal anchor is not necessary to be optimised. There is only one thermal link of the leads to the 2nd stage of the crycooler is via the tape samples, which are very weak thermal links (purposely used in current lead applications) and therefore negligible heat leak will be loaded onto the 2nd stage which has to operate at its lowest possible temperature achievable. The only concern is that a temperature of about 50 K can be achieved at the top Cu block.

5.3.6. Thermometry

In this experiment, two types of temperature sensors are used. Type T differential thermocouples were monitoring the temperature changes along the sample and Silicon Diodes were used as temperature sensors for the copper blocks and also temperature control.

A. *Type T differential thermocouples*

The type T thermocouple is made of copper and copper-nickel (constantan) wires. The electrical insulation of each of the wires at a small sector at the end is peeled off, and then it is tinned with solder. The two wires are twisted together and then are soldered in order to obtain a copper/constantan junction. One junction is soldered on the sample and one is thermally attached to the reference block. Tests were performed in order to ensure that the electrical current that passes through the sample does not affect the junction if they are electrically connected and therefore, since soldering ensures good thermal contact, it is preferred for attachment of the thermocouple. The reference block is a copper block with drilled holes. The reference junction is covered with solid glue Eco-Bon to ensure electrical insulation and is placed inside a hole in the reference block which is filled with Epoxy Stycast in order to obtain a rigid thermal contact. The reference block is bolted on the 1st stage flange, which is estimated to stabilize at constant temperature of 40 K during the experiment (this is confirmed by a silicon diode sensor that is also attached on the same block). The output of the differential thermocouple is two copper wires that are connected to a DVM. When the temperature of the sample junction changes, a thermal EMF ΔV is generated and recorded. The relation of absolute EMF (microvolts) and absolute temperature (C) is given in figure 5.7. The graph in figure 5.7 is produced from calibration data based on the "Guide to thermocouple and resistance thermometry, Issue 6.0"

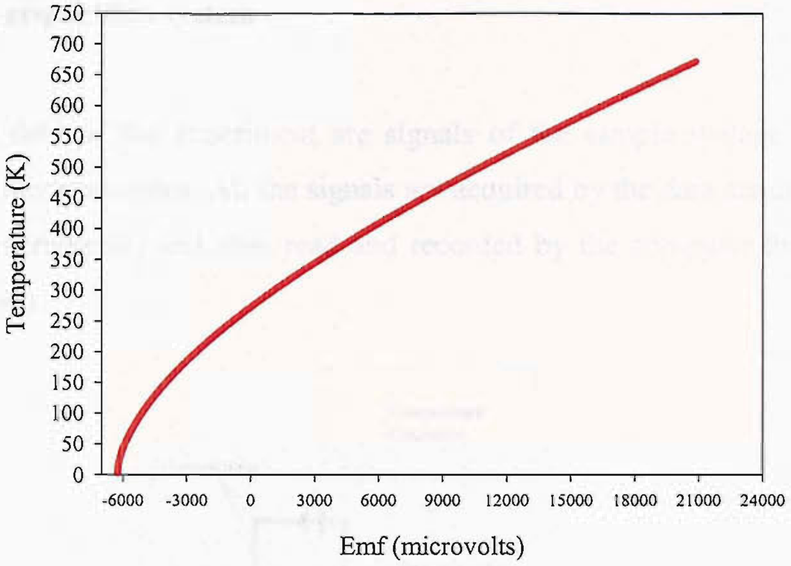

Figure 5.7. *Relation between Emf and temperature in type T thermocouple*

The relation that best describes the above function of *T=f(emf)* is the following

$$T(K) = 276.093 + 0.0246 \times Emf(\mu V) - 1.08638e^{-6} \times \{Emf(\mu V)\}^2$$

Using the above relation, the recorded ΔV's are converted to temperature differences between the reference temperature 40 K and each one of the differential thermocouple junctions temperatures distributed along the length of the sample T_i, ΔT_i. Therefore the absolute temperatures T_i are calculated as $T_i = 40\text{ K} + \Delta T_i$, and the temperature distribution along the tape sample can be obtained.

5.3.7. Temperature control

The top copper block of the sample holder has to be kept at constant temperatures above 45 K for the experiment. An Oxford Instruments PID temperature controller was used for the experiment. The bottom copper block has to be kept to the lowest temperature achievable on the 2nd stage, which is expected to be about 6 K and therefore it doesn't require temperature control. The controller temperature sensor is a silicon diode and the controller heater is a cartridge heater inside a hole on the top copper block in the sample's half.

5.3.8. Data acquisition system

The output data of the experiment are signals of the sample voltage taps and the differential thermocouples. All the signals are acquired by the data acquisition system (National Instruments) and then read and recorded by the computer through a LabView program.

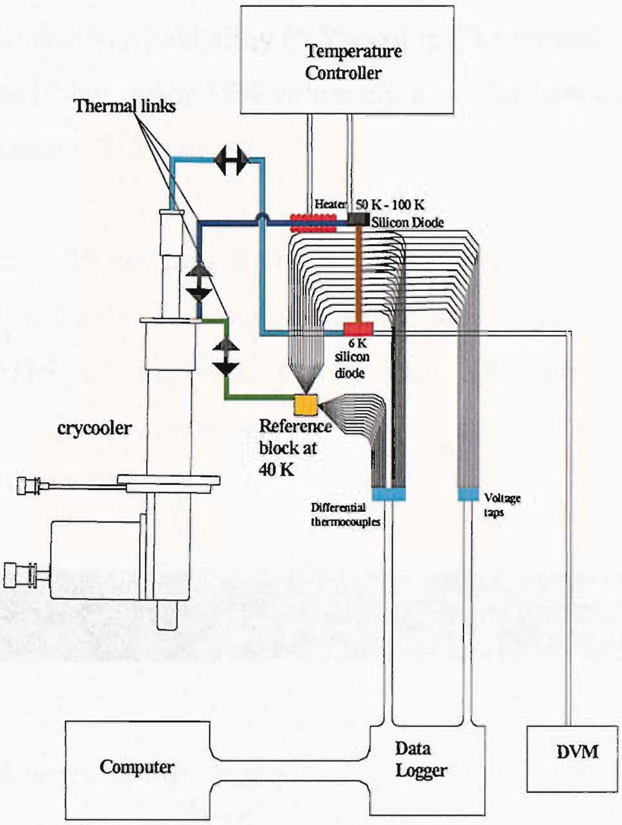

Figure 5.8. *Block diagram of the quench measurement system*

Figure 5.8 displays the block diagram of the quench measurement system.

5.4. Experimental

5.4.1. Sample preparation

The samples under investigation are two types of composite Bi-2223 tape:

a. NST tape 37 filaments

The sheath material is silver gold alloy (4% gold). The critical current is 40 A (self field, 77 K). Tape dimensions: width 3.2 mm, thickness 0.2 mm.

b. ASC tape 55 filaments

The sheath material is silver-gold alloy (5.3% gold). The critical current is 110 A (self field, 77 K) and the filling factor 35% volumetrically. The tape dimensions are: width 4.17 mm and thickness 0.215 mm.

The sample length is 25 cm plus 3 cm for the grooves of the sample holder. The sample has been soldered on a stainless steel strip (figure 5.9) to simulate the conditions of the HTS elements in the current leads. The tape has been attached with Indium alloy flux on the steel strip and then heated up to 250 C inside the aluminium plates for 10 min (chapter 3).

Figure 5.9. *Schematic of the longitudinal cross section of the HTS tape sample soldered on the steel strip*

In order to simulate accurately the quench propagation, the total amount of steel that is used in the real case was also used to the case of a single tape. This is done by using the ratios of cross sectional areas of tape and steel in order to determine the dimensions of the required steel strip for a single tape as below:

$$\frac{A_{total}^{steel}}{A_{stripe}^{strip}} = \frac{A_{total}^{HTS}}{A_{\sin gle}^{HTS}}$$

According to information given by CERN, the support of the tapes is a stainless steel cylinder of outer diameter 75.7 mm and inner diameter 72.1 mm. The cross-sectional area is $A_{total}^{steel} = \frac{\pi}{4} \times \left(D_{outer}^2 - D_{inner}^2\right)$=417.9 mm^2. The HTS tapes are arranged as stacks of 8 tapes soldered to each other on their flat surfaces. Thirty six of these stacks are soldered circularly around the steel cylinder and carry the total electrical current which has the maximum value of 13000 Amperes. The cross sectional area of a single tape is $A^{HTS}_{\sin gle} = 4.17 \times 0.215$ =0.89 mm^2. The total cross sectional area of the tapes is $A^{HTS}_{total} = 4.17 \times 0.215 \times 8 \times 36$ =258.2 mm^2. The cross sectional area of steel that has to be used for a single tape is $A^{steel}_{stripe} = \frac{A^{steel}_{total}}{A^{HTS}_{total}} \times A^{HTS}_{\sin gle}$ =1.44 mm^2. A strip of 4.5 mm width and 0.3 mm thickness was used.

The return/output HTS conductor will not be examined. In order to eliminate the possibility that this conductor will quench which is not desirable because it will affect the experimental conditions, it was “reinforced” by using four NST tapes (brazed two on each side of a steel strip) thus giving a critical current of about 145 A at 77 K and self field. This value is well above the maximum operating current in the experiment and no possibility exists that this will quench at any temperature.

5.4.2. Assembling of the rig

The two copper blocks are joined tightly by the three G-10 rods at a fixed distance apart of 25 cm (the sample’s length) to form a rigid sample holder. The tape sample and current output tape are soldered with solder Pb(40%)-Sn(60%) of melting point 186 C in the grooves of the copper blocks by cartridge heaters that are inserted from the bottom of each block into the drilled holes for that purpose. Also a type K thermocouple was used to monitor the temperature during the soldering process and ensuring that the temperature will not exceed the value of 200 K, otherwise there is danger to unsolder the tapes from the steel substrates. The sample holder is attached on the second stage of the cold head by 6 M5 bolts and invar washers to compensate for the differential contraction, while Apiezon-N grease was spread at the interface of the bottom copper block and the 2nd stage flange to improve the thermal contact.

Thirteen type T thermocouple junctions were soldered on the sample on the steel substrate side at its edge, starting from the top copper block at intervals separated by a distance of 1.5 cm. Also on the same side at the same levels of the thermocouples on the opposite edge of the strip, thirteen voltage taps were soldered. Silicon diode temperature sensors are attached on the top copper block on the sample’s half as the temperature controller temperature sensor and on the thermocouple reference block that is attached on the crycooler first stage flange. The current leads are soldered on the two halves of the top copper block. The electrical wiring (voltage, temperature sensors) is tested to ensure that operates without implications. The thermal radiation shield is added and the system is closed with the steel vacuum vessel. Figure 5.10 displays a schematic representation of the cryostat for the measurement with the all the components assembled.

5.4.3. Procedure of measurement

The system is evacuated to pressure ~10^{-5} bars using a rotary/diffusion pump; usually it is left overnight in pumping action at room temperature. The cryocooler is switched on and the system is left to cool down and thermally stabilise to its lowest temperature achievable. The cold parts of the rig act as cryo-pumps and cause the inner pressure to fall to ~10^{-7} bars. The bottom block on the 2nd stage reaches its lowest temperature of 6 K within 3-4 hours, while the top block needs more time up to 6 hours to reach the lowest temperature of 45 K. The thermal resistance of the current lead that thermally links the block to the 1st stage causes the delay in the cooling down process. The temperature controller stabilises the temperature of the sample's half at the top copper block at the required level for each experimental run. Once the set temperature has been reached at the top copper block, the system is allowed to reach thermal equilibrium. In the established thermal equilibrium, the top copper block and hence the top end of the sample is at a temperature of above 50 K and the bottom copper block and hence the bottom end of the sample is at temperature 6 K. The next step is to identify the value of "quench" current I_q. This is the value of current which will

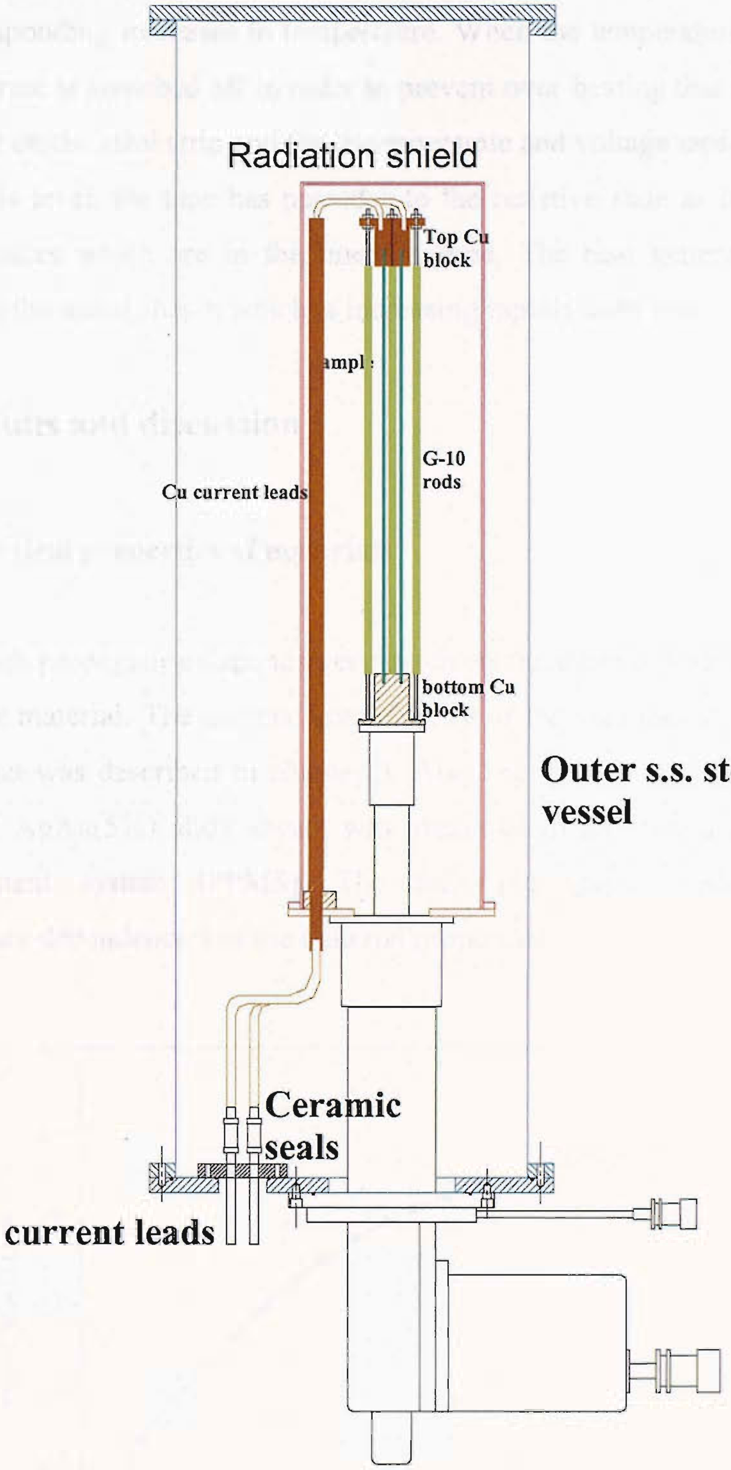

Figure 5.10. *Schematic representation of the cryogenic station for the quench measurement*

initiate the quench propagation in the tape at this temperature level. The current is increased while the voltage signals are carefully being watched on the computer. A slight increase in the voltage level of the first few traces is an indication that quench has initiated. At later stages the voltage levels are increasing. Moreover, more voltage taps are energised; an indication that quench is propagating, which is accompanied by the corresponding increases in temperature. When the temperature reaches about 300 K the current is switched off in order to prevent over-heating that eventually will melt the solder on the steel strip and the thermocouple and voltage taps connections (at 232 C). At this level, the tape has passed into the resistive state as it can be seen in the voltage traces which are in the linear regime. The heat generation is pure ohmic heating in the metal sheath which is increasing rapidly with time.

5.5. Results and discussion

5.5.1. Physical properties of materials

The quench propagation depends very much on the thermo-physical properties of the conductor material. The thermal conductivity of the stainless steel was measured in the rig that was described in chapter 3. Also the specific heat of stainless steel and tape with AgAu(5%) alloy sheath was measured in the in-house Physical Property Measurement system (PPMS). The following graphs display the measured temperature dependencies of the material properties.

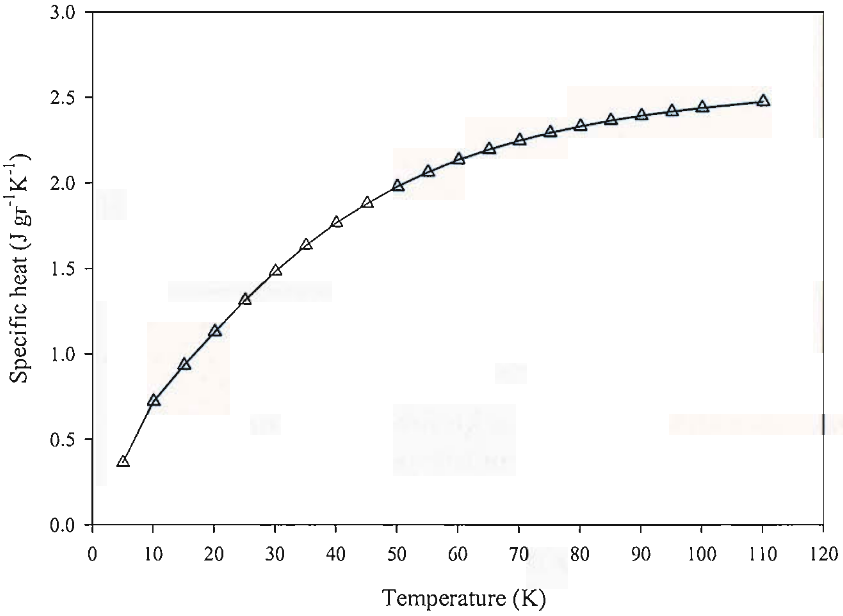

Figure 5.11. *Stainless steel specific heat as a function of temperature*

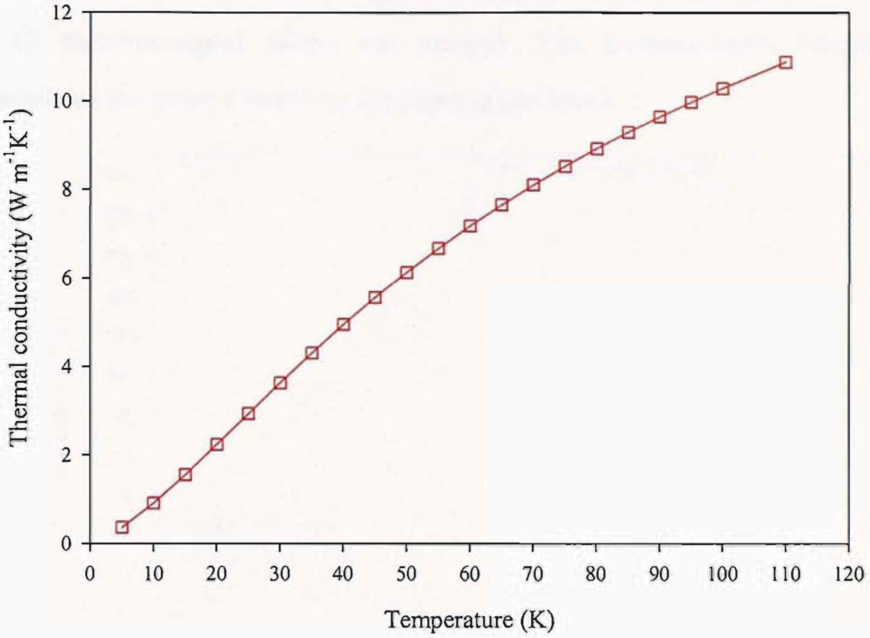

Figure 5.12. *Thermal conductivity of stainless steel as a function of temperature*

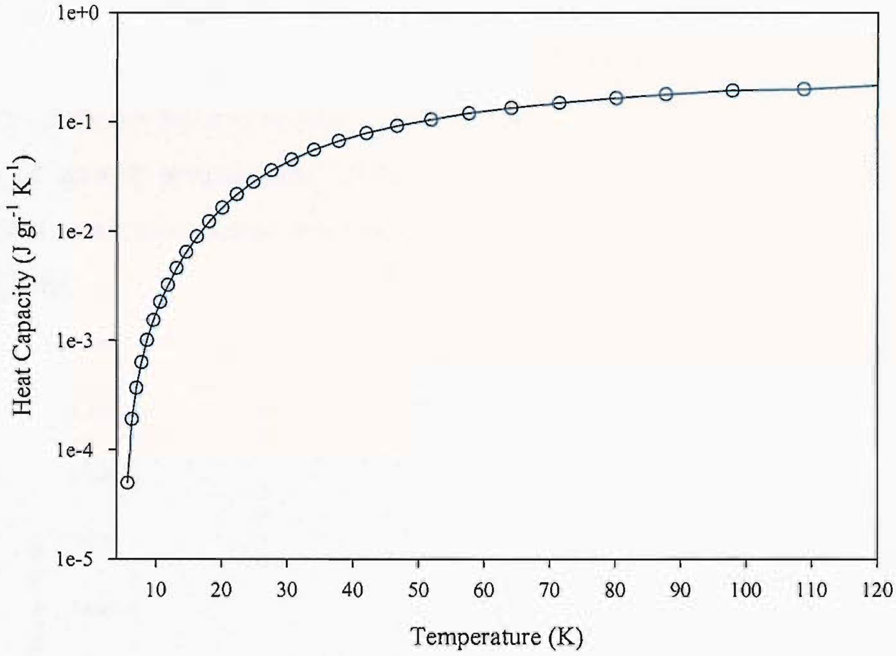

Figure 5.13. *Specific heat of tape with AgAu(5%) alloy sheath as a function of temperature*

5.5.1. Quench propagation in the NST tape with steel substrate

The first experimental run was performed in the NST tape with the steel substrate, the temperature of the top copper block was held at the fixed temperature of 85 K. The quench current is $I_q = 39.4$ A. In figure 5.11 is the time evolution of the temperature in the 13 thermocouples along the sample. The thermocouple labelled as "T_1" corresponds to the point closest to the top copper block.

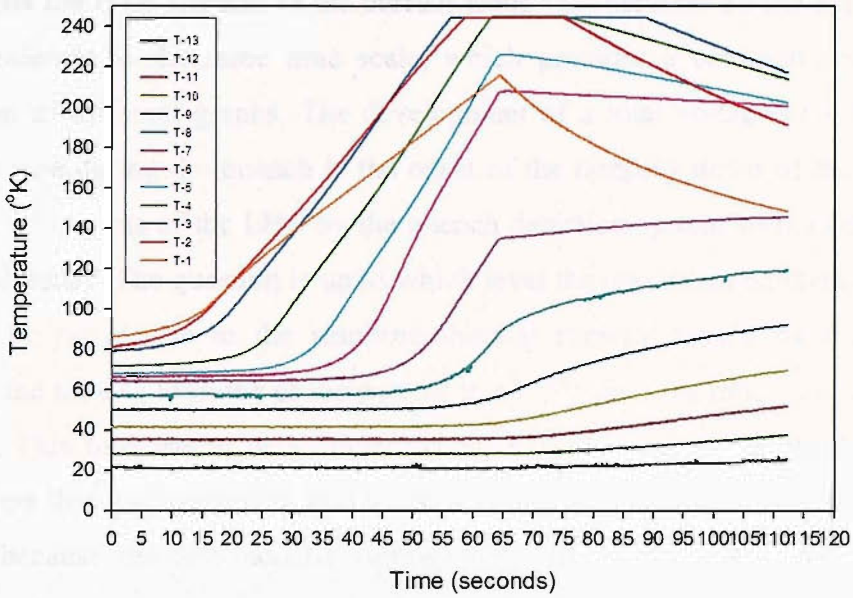

Figure 5.11. *Time evolution of the temperature*

Figure 5.12 shows the time evolution of the voltage along the tape during the transient process of quench propagation. Within the time that the power supply was kept on, the normal zone has reached only up to the 7th voltage tap or to a conductor section of about 12 cm.

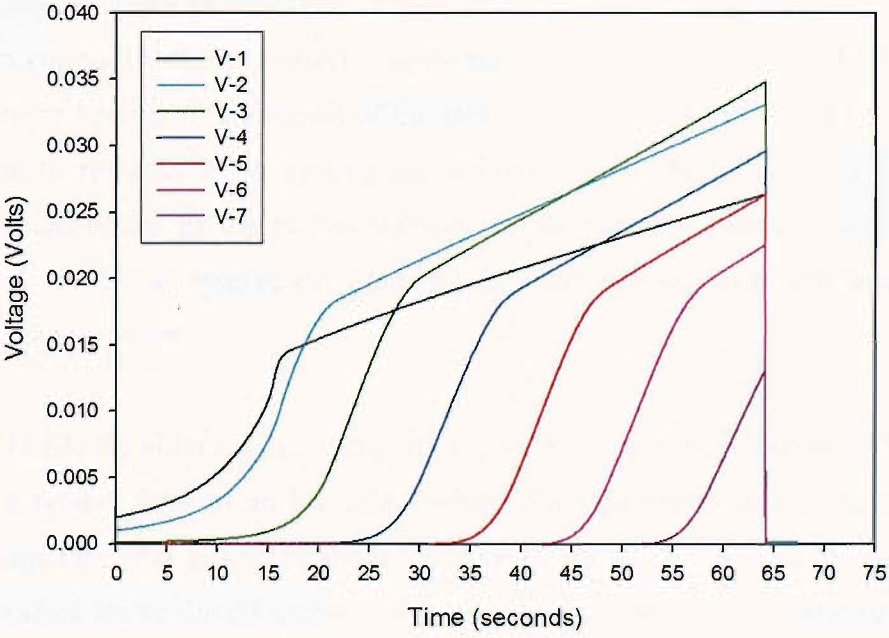

Figure 5.12. *Time evolution of the voltage*

In all the graphs, the origin in the time axis is set as the time at which a predefined voltage threshold is reached. This criterion is set according to the requirements for safe quench detection in the circuits of the LHC at CERN, which is a total voltage of 3 mV across the HTS element of the current leads [6]. Therefore all the experimental runs are referred to the same time scale, which provides a common criterion for comparison of different graphs. The development of a total voltage of value 3 mV across the tape during the quench is the onset of the ramping down of the electrical current in the circuits of the LHC by the quench detection system with a certain time constant of decay. The question is up to which level the maximum temperature of the tape will be raised due to the resulting thermal runway caused by the quench. Therefore the time t_{rd} after the occurrence of the 3 mV until the ramp is completed is important. This time has to be sufficient short in order to avoid overheating of the HTS element that will eventually lead to its damage. In contrast, very short time is not desirable because the self-induced voltage that will be developed in the magnet ($\propto -{}^{dI}\!/_{dt}$) will be large and cannot be afforded. The propagation of the quench can be seen clearly in figure (5.11), where the time evolution of the temperature in the 13 thermocouples across the sample is displayed. The thermocouples are "energised" successively after a time interval of about 7 seconds.

The temperature increase is more rapid in the tape section located 3-4 cm from the top copper block, as it can be seen in the slopes of the temperatures curves. The influence of the top copper block (heat sink) is apparent in the first two traces. The heat sink causes slower heating in the region of the tape closest to it, whilst in the region after the second thermocouple the heating rate becomes higher and identical in the next three thermocouples. In the further sections of the tape, the normal zone has not propagated yet due to insufficient time and gradually the slopes of the temperature curves become smaller.

In figure (5.12) the voltage rise is proportional to the temperature increase. The curve V(t) has a typical form of an I-V relationship of a superconducting composite. For each voltage tap, after a time of about 15 seconds, the temperature of the composite has been raised above the critical temperature and therefore the composite has passed in the resistive state; the voltage increase is dominated by the linear increase of the metal resistance with temperature. In the first tape section, where the presence of the heat sink (top copper block) slows down the heating process, the slope of the linear part of the voltage trace is smaller than the slopes of the sections 2, 3 etc. The voltage traces after section 3 have the same slope in the resistive part as the influence of the heat sink is negligible.

The value of quench current is different for each temperature of the top Cu block. Different experimental runs were carried out at various temperatures of the top Cu block. The relationship of the measured quench current with the temperature is shown in figure 5.13. The quench current decreases with increasing temperature. This observed behaviour can be explained in the context of the analysis in paragraph 5.2.3. With increasing temperature, the portion of electrical current that passes through the metal sheath is increasing (relation 5.9) thus causing increased heat generation in the composite (relation 5.10). The enhanced heat generation in the metal sheath is causing the quench to occur and propagate like a cascade effect along the current lead.

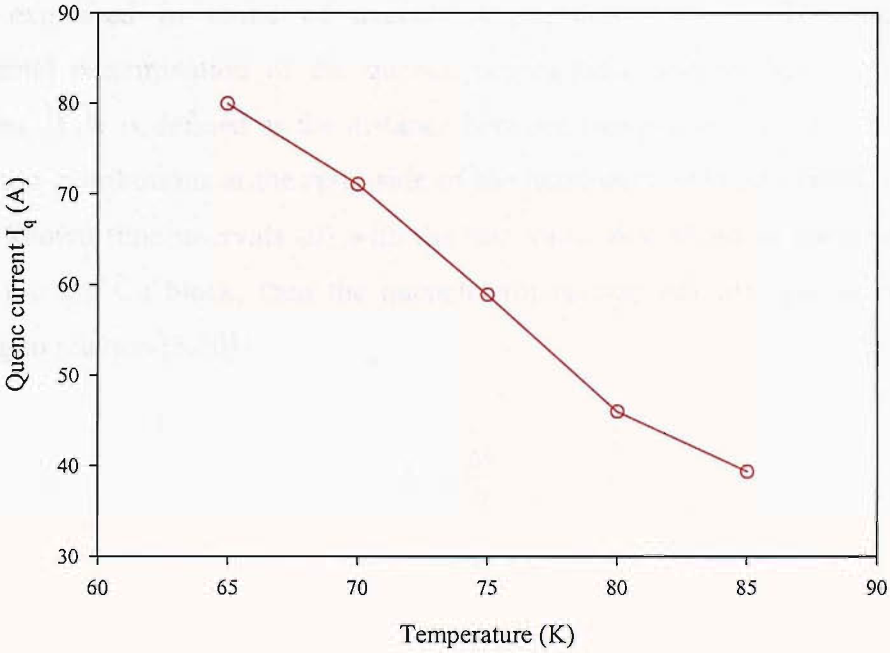

Figure 5.13. *The quench current I_q as a function of the temperature of the top Cu block*

5.5.2. Quench propagation as a function of temperature

The temperature distribution along the length of the current lead x at different time steps is plotted in figures (5.14-5.19) which correspond to different runs with various set temperatures of the top Cu block and consequently different quench currents as shown in figure 5.13. The initial temperature profile at $t = 0$ corresponds to the steady state temperature profile along the current lead, in which the quench process has not yet started. At the next stages, the quench starts to develop thus resulting in heating of the current lead and disturbance of the steady state profile. As the time passes, the maximum temperature shifts to higher levels with the hottest "spot" localised in the region between 3 cm to 5 cm from the top Cu block. The temperature at $x = 0$ remains constant at the fixed value as set by the temperature controller. The "normal zone" is defined as the region of the conductor that is at temperatures above the temperature level of the top Cu block, since at this temperature the quench initiates. The variation in the temperature profiles at different time steps indicates the rate of expansion of the normal zone which grows in size with time. The rate of expansion of the normal zone can be expressed in terms of quench propagation velocity. The method of experimental determination of the quench propagation velocity lies in the above definitions. If Δx is defined as the distance between two successive intercepts of the temperature distributions at the right side of the maximum of the distribution (which occur in known time intervals Δt) with the horizontal line drawn at the temperature level of the top Cu block, then the quench propagation velocity can be estimated according to relation (5.30).

$$U_l = \frac{\Delta x}{\Delta t} \qquad \textit{(5.30)}$$

1. Top block at 85 K, Iq = 39.36 A

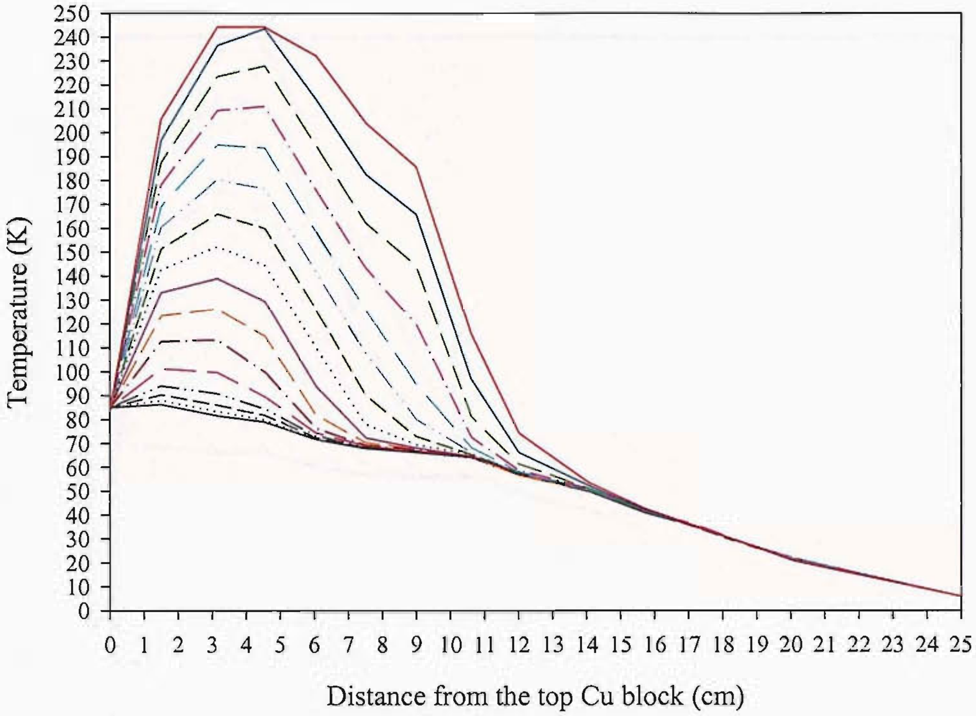

Figure 5.14. *Temperature distributions along the lead at different time steps. Top block at 85 K, Iq = 39.36 A*

2. Top block at 80 K, Iq=46 A

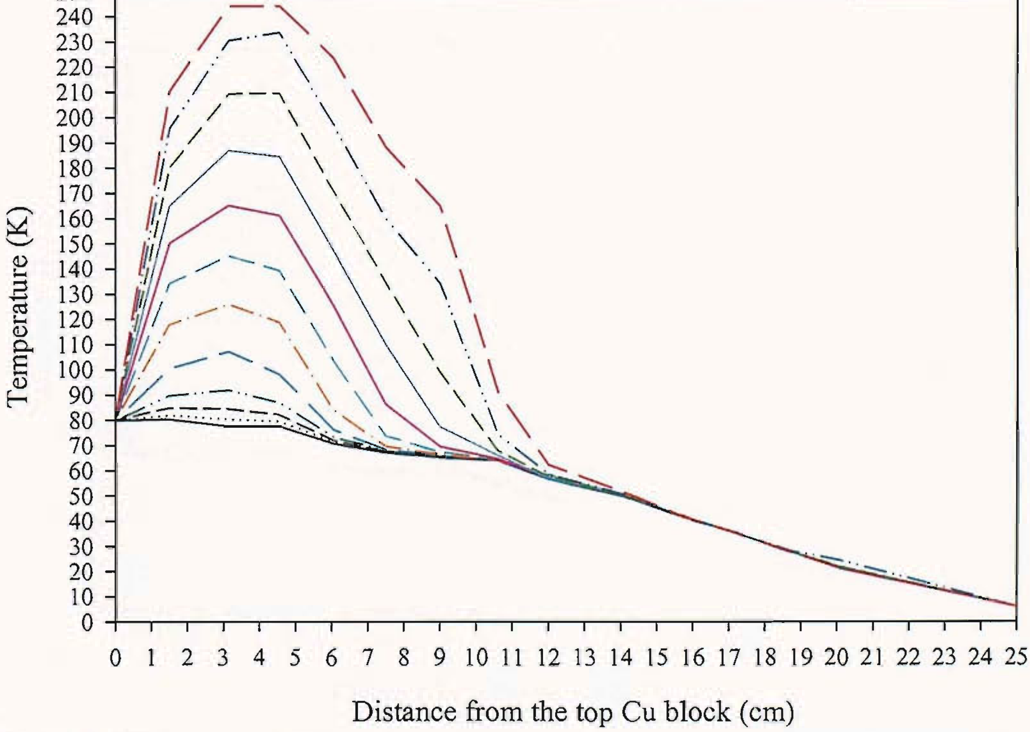

Figure 5.15. *Temperature distributions along the lead at different time steps. Top block at 80 K, Iq=46 A*

3. Top block at 75 K, Iq=58.9 A

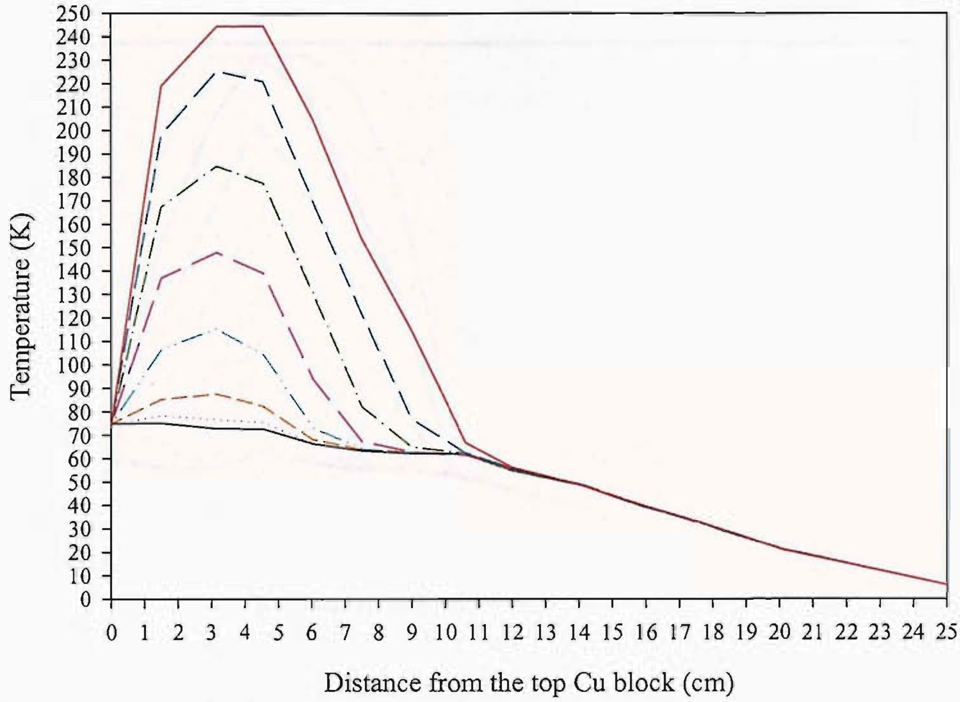

Figure 5.16. *Temperature distributions along the lead at different time steps. Top block at 75 K, Iq=58.9 A*

4. Top block at 70 K, Iq=71.11 A

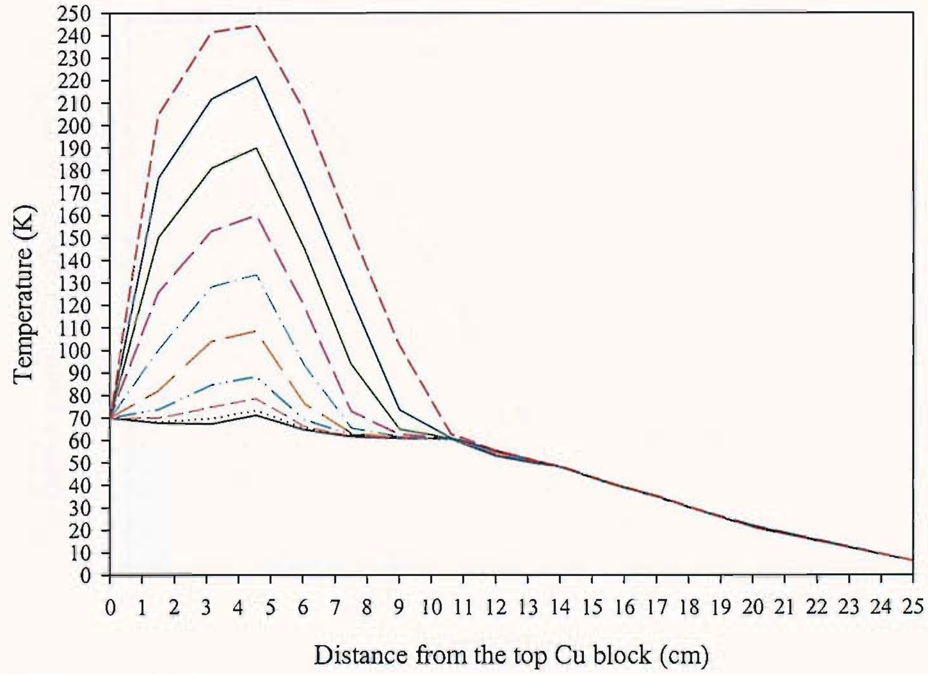

Figure 5.17. *Temperature distributions along the lead at different time steps. Top block at 70 K, Iq=71.11 A*

5. Top block at 65 K, Iq=80 A

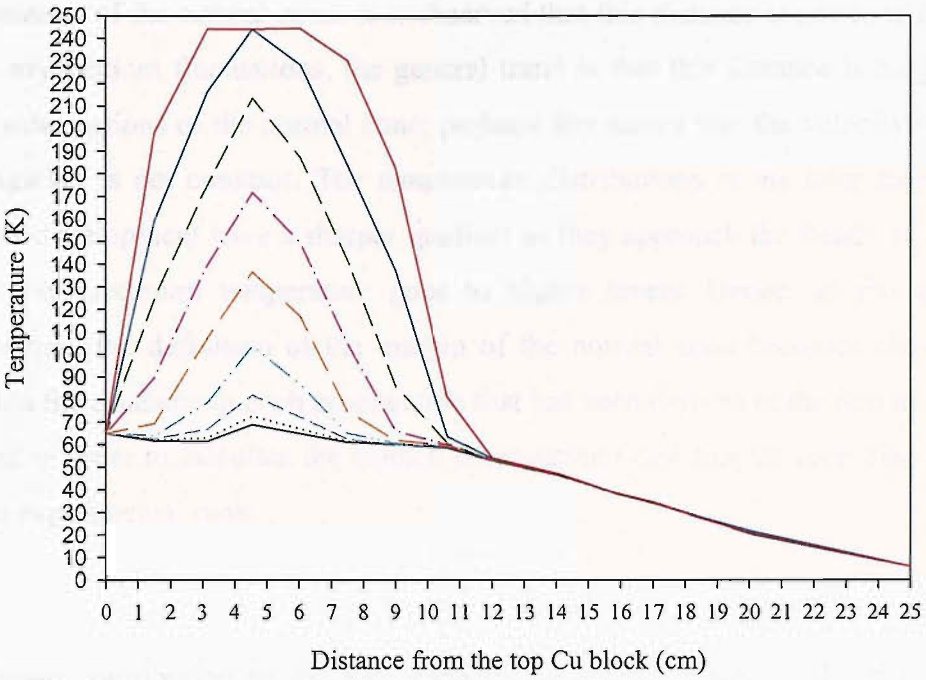

Figure 5.18. *Temperature distributions along the lead at different time steps. Top block at 65 K, Iq=80 A*

Figure 5.19 displays the measured quench propagation velocities as a function of temperature of the top Cu block.

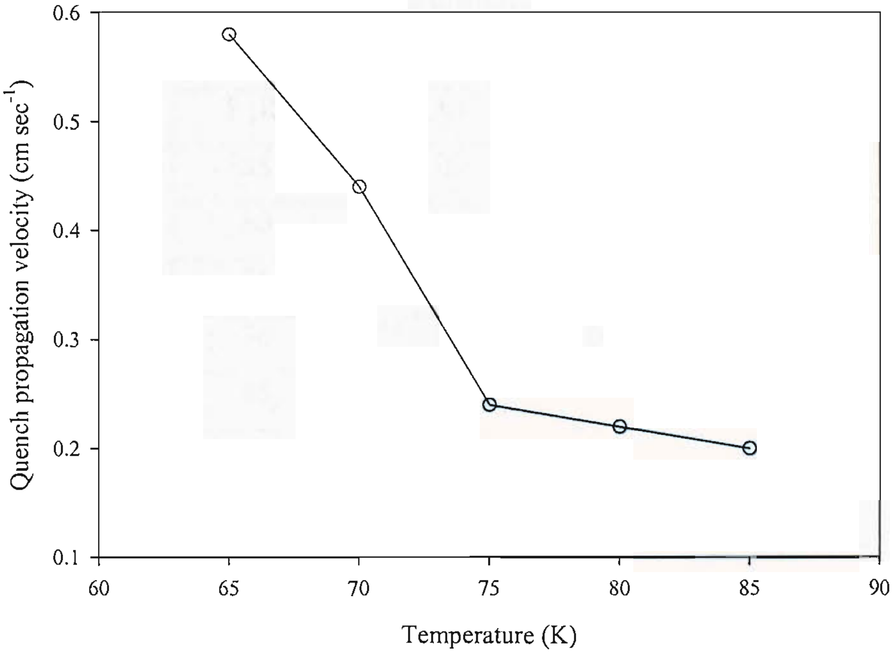

Figure 5.19. *Measured quench propagation velocities as a function of the temperature of the top Cu block*

It has to be mentioned that the quench propagation velocities were obtained by averaging the values of Δx in the section of the tape on the right side of the maximum temperature of the normal zone. It is observed that this distance is not constant. Apart from any random fluctuations, the general trend is that this distance is bigger in the right side sections of the normal zone; perhaps this means that the velocity of quench propagation is not constant. The temperature distributions at the later stages of the quench development have a sharper gradient as they approach the steady state profile since the maximum temperature goes to higher levels. Hence, as the quench is developing, the definition of the margin of the normal zone becomes clearer. The formula for adiabatic quench propagation that has been derived in the previous section is used in order to calculate the quench propagation velocities for each case in all the above experimental runs:

$$U_l = J \cdot \sqrt{\frac{\rho_n \cdot k_n}{C_n \cdot C_s \cdot (T_C - T_{cool})}}$$

The main contribution to the heat capacity of the composite is the steel. All the material properties data are taken from the measured temperature dependencies that have been shown previously. The critical temperature Tc=110 K and as far as the value of T_{cool} is concerned, is the value of temperature that corresponds to the "front" of the propagation wave according to the above graphs. In the table below the values of the quench propagation velocities are displayed:

T (K)	Iq (A)	U (cm/sec)
85	39.36	0.47
80	46	0.55
75	58.9	0.77
70	71.11	0.9
65	80	1.0

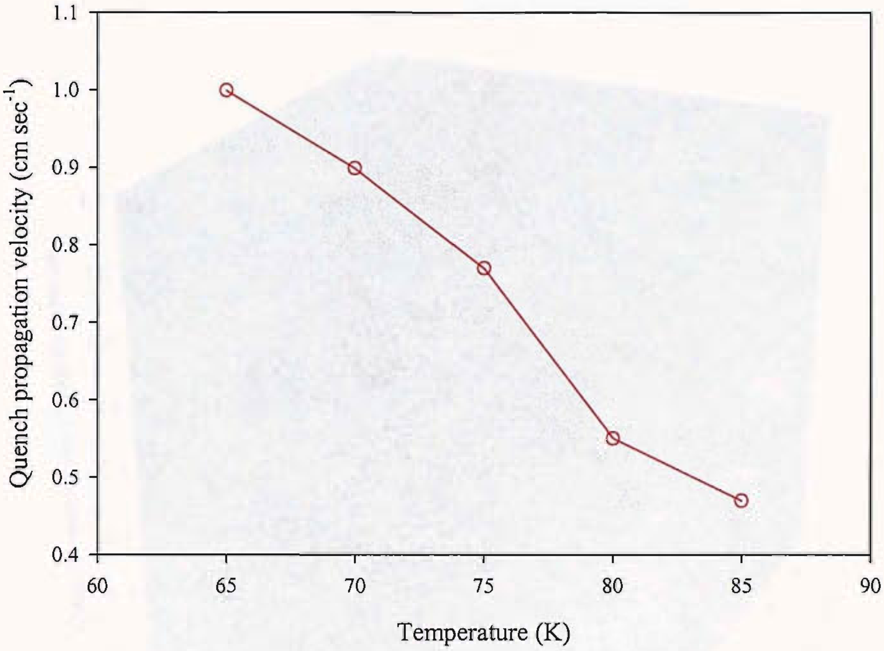

Figure 5.20. *Calculated quench propagation velocity as a function of the temperature of the top Cu block*

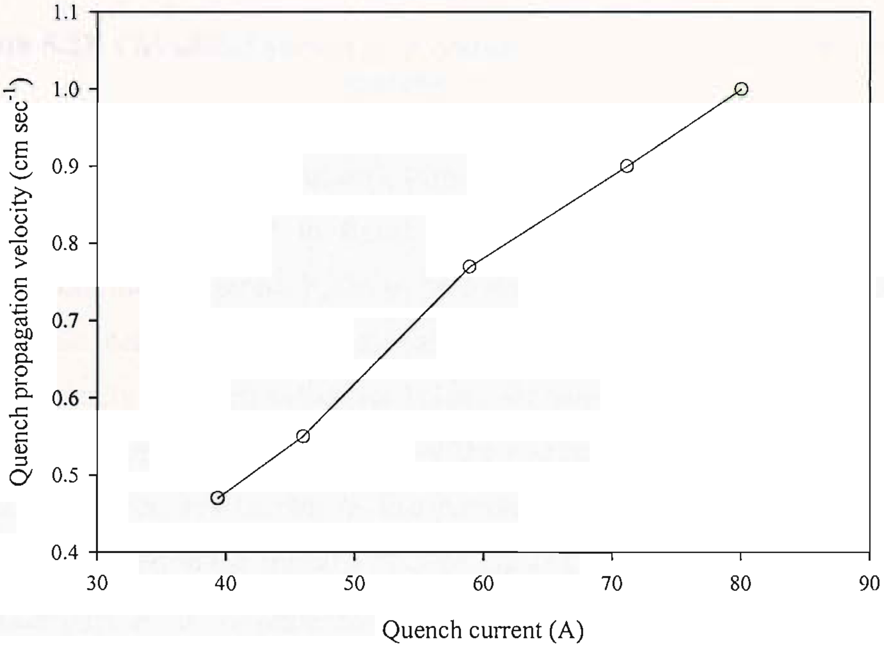

Figure 5.21. *Quench propagation velocity as a function of quench current*

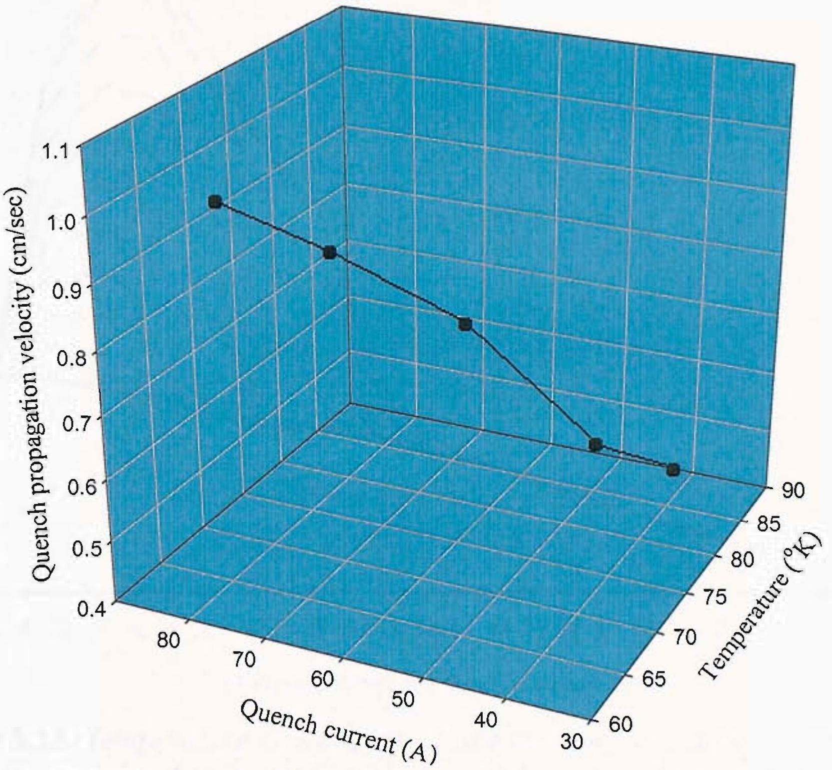

Figure 5.22. *Calculated quench propagation velocity as a function of temperature and quench current*

The relationship between the quench propagation velocity and the temperature of the top Cu block is displayed in figure 5.21. The theoretically obtained values are different from the measured. It has to be pointed out that errors may be attributed to the non clear definition of the material properties as a function of the temperature. The theoretically obtained values are rough estimates of the normal zone propagation velocity; the temperature dependence of the material properties has to be taken into account. Moreover, any current re-distribution in the composite may alter the current density that is used in the formula or even the Joule heating, which can be expressed as a power term $P = J^2 \times \rho$ under the square root in the formula.

5.5.3. Quench propagation as a function of current at constant temperature

An experimental run was carried out under the following conditions: The temperature of the top copper block was held at 85 K while the electrical current was varied at different ratings above the value of the quench current which was found to be I_q=44.5 A at this temperature.

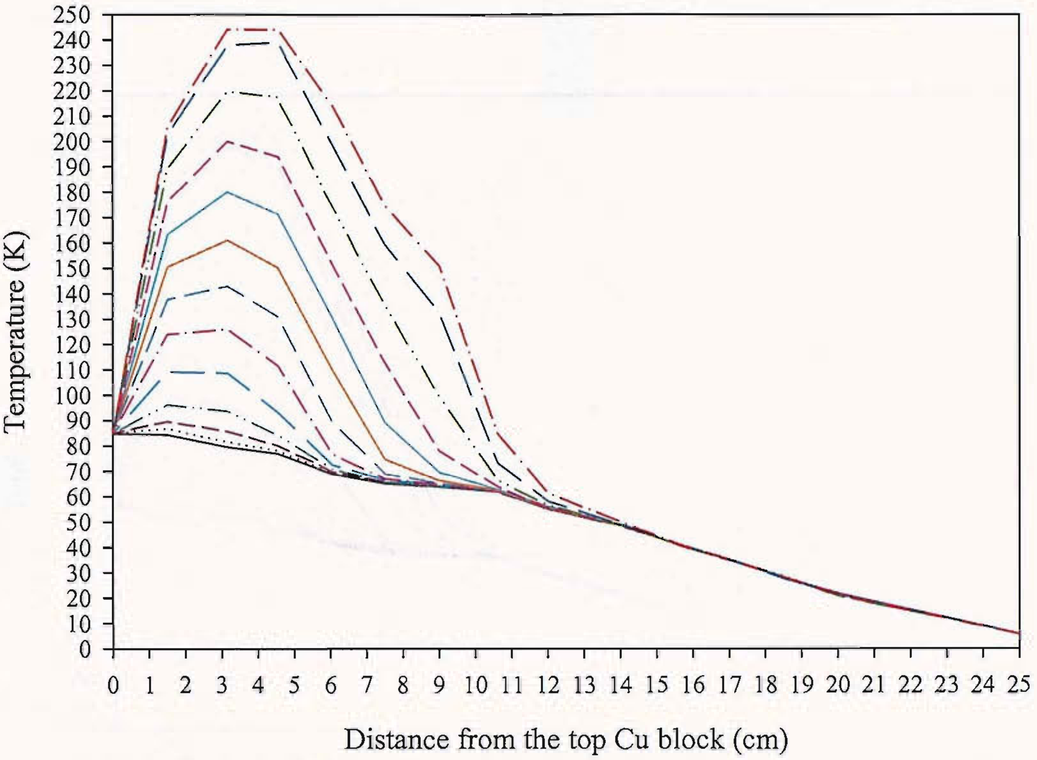

Figure 5.13. *Temperature distributions along the sample at different time steps increasing every 4 seconds. Top block at 85 K, I=44.5 A (quench current).*

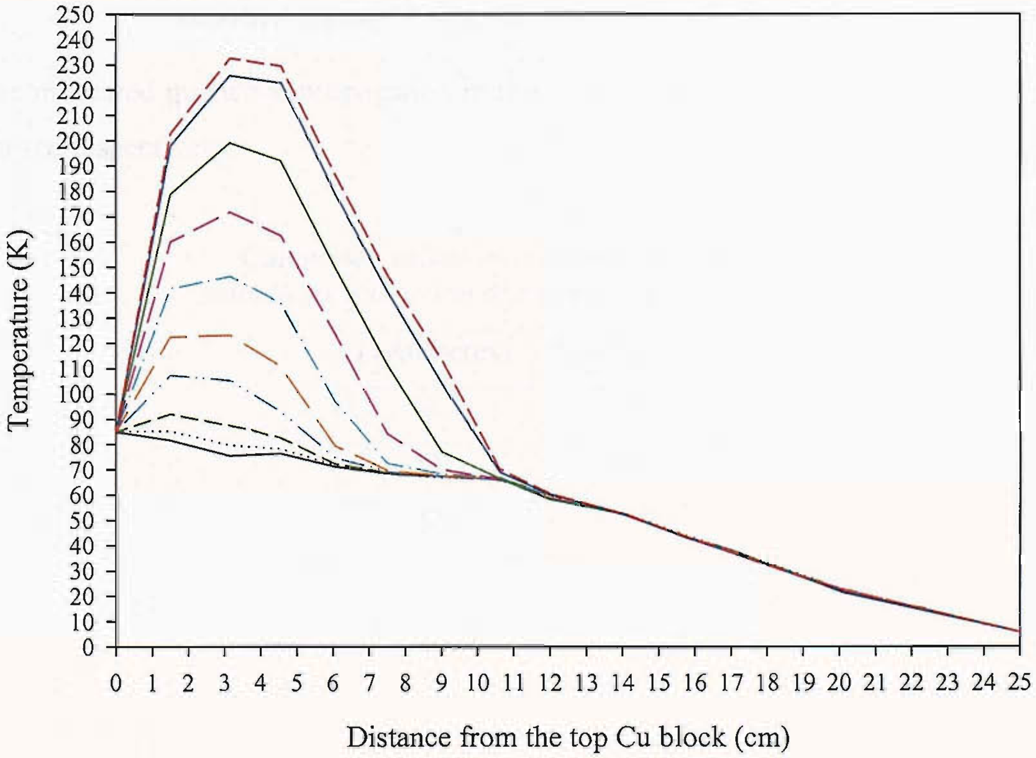

Figure 5.14. *Temperature distributions along the sample at different time steps increasing every 4 seconds. Top block at 85 K, I=50 A*

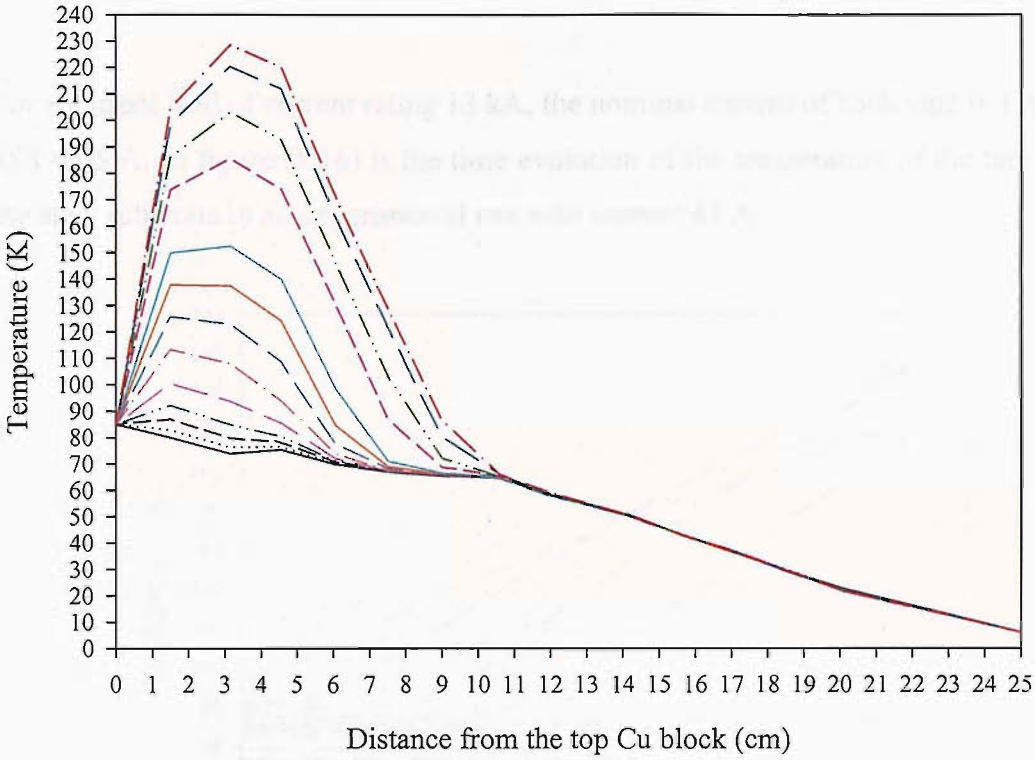

Figure 5.15. *Temperature distributions along the sample at different time steps increasing every 2 seconds. Top block at 85 K, I=55 A*

The measured quenched propagation in this case are 0.25 cm/sec, 0.3 cm/sec and 0.6 cm/sec respectively.

Calculated values of the quench propagation velocity as a function of current (top block at 85 K)

I (Amperes)	U (cm/sec)
44.5	0.6
50	0.7
55	0.82

5.5.4. Quench propagation in the ASC tape under nominal conditions of operation

For a current lead of current rating 13 kA, the nominal current of each tape is 13000 ÷ 288 = 45 A. In figure (5.16) is the time evolution of the temperature of the tape with the steel substrate in an experimental run with current 45 A.

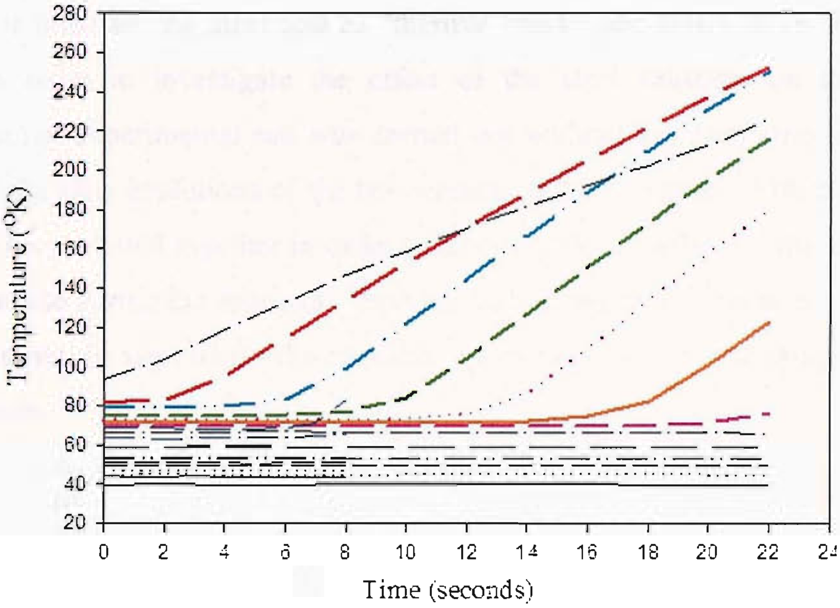

Figure 5.16. *Time evolution of temperature during quench*

It was found that when the top Cu block is 98 K the quench current is 45 A. The practical interest of this relationship lies as follows: If for some reason the cooling ability at the top section of the HTS part in the current lead is lost, the temperature has to raise from the initial value of 50 K up to 98 K in order the thermal runway to begin. The highest temperature in the tape (250 K) is reached in 22 seconds.

5.5.5. The effect of the steel back-up on the quench propagation characteristics

The brazing of the HTS part onto the stainless steel shunt ensures good thermal contact between the Ag/Bi-2223 tape and the shunt and also efficient mechanical reinforcement. With regard to the thermo-electric behaviour of the composite during the thermal runway caused by the quenching of the superconductor, the thermal contact is a very important parameter. The good thermal contact will allow the generated Joule heat that is produced due to the transition to the normal state during the transient to be absorbed by the shunt as well as the silver sheath. The heat capacity of the composite is greatly enhanced, if it is considered that the heat capacity of the stainless steel is about 22 times larger than the silver alloy (see figures 5.11 and 5.13). Due to the larger heat capacity therefore a prolonged time is available before the critical temperature of the superconductor is reached in the case of loss of coolant in the upper section of the HTS heat exchanger of the current lead. Even when the quenching is initiated, the steel acts as "thermal break" and slows down the heating process. In order to investigate the effect of the steel substrate on the quench propagation, an experimental run was carried out without the steel strip present. In figure 5.17 the time evolutions of the temperature in the two cases, with and without steel, have been plotted together in order to demonstrate the effect of the steel to the temperature rise during the transient. The blue dashed and dotted traces correspond to the case without the steel whilst the colourful traces correspond to the sample with the steel substrate.

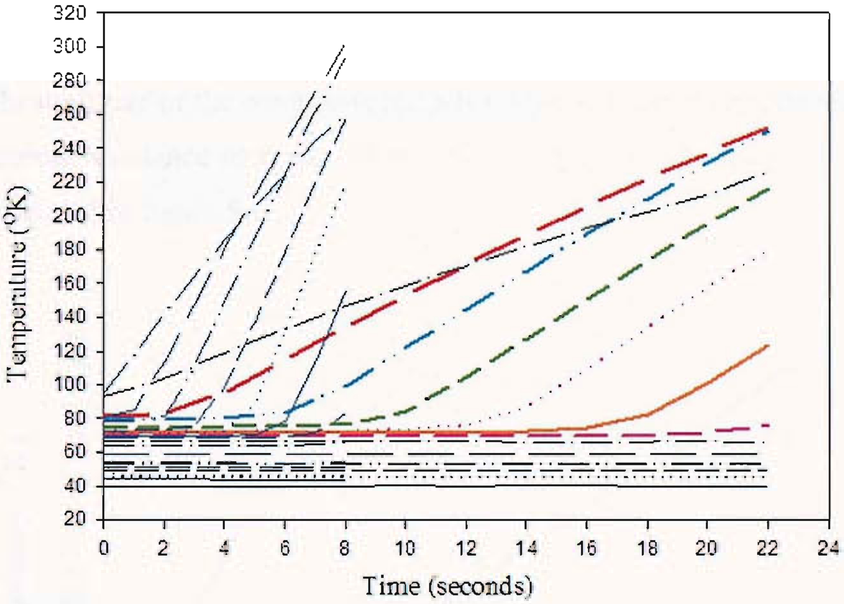

Figure 5.17. *The effect of steel on the temperature rise*

The effect of the steel in reducing the heating rate of the composite is clearly seen in figure 5.17. The bigger slopes of the curves in the case without the steel substrate indicate the faster heating of this tape in comparison to the tape with the substrate. The maximum temperature (300 K) in the case without the substrate is achieved in 7 seconds, whilst in the case with the substrate is achieved in 22 seconds and is lower by 50 K.

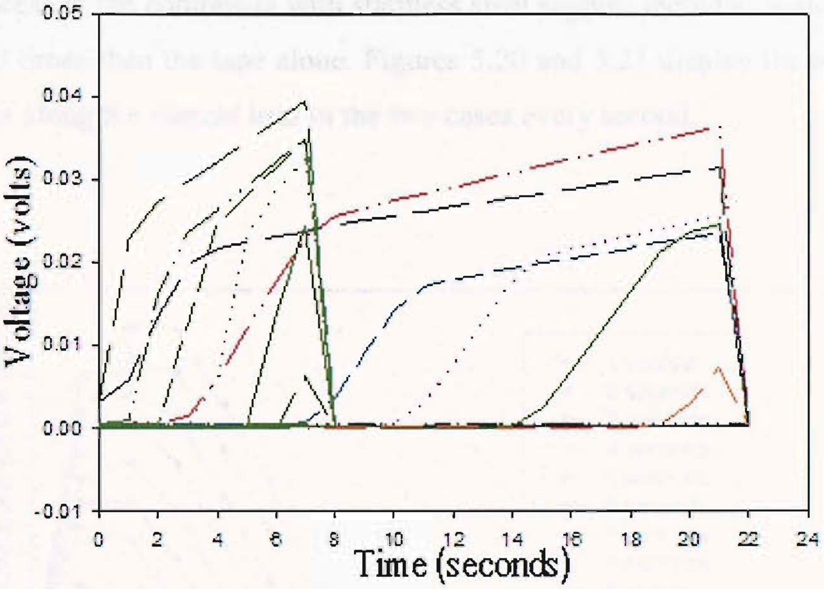

Figure 5.18. *The effect of steel on the voltage rise. Without steel-green dashed lines, with steel-colourful lines*

The lower heating rate of the composite reflects on the voltage development, since the rate of electrical resistance increase is lower in the case with the stainless steel. This effect is illustrated in figure 5.18.

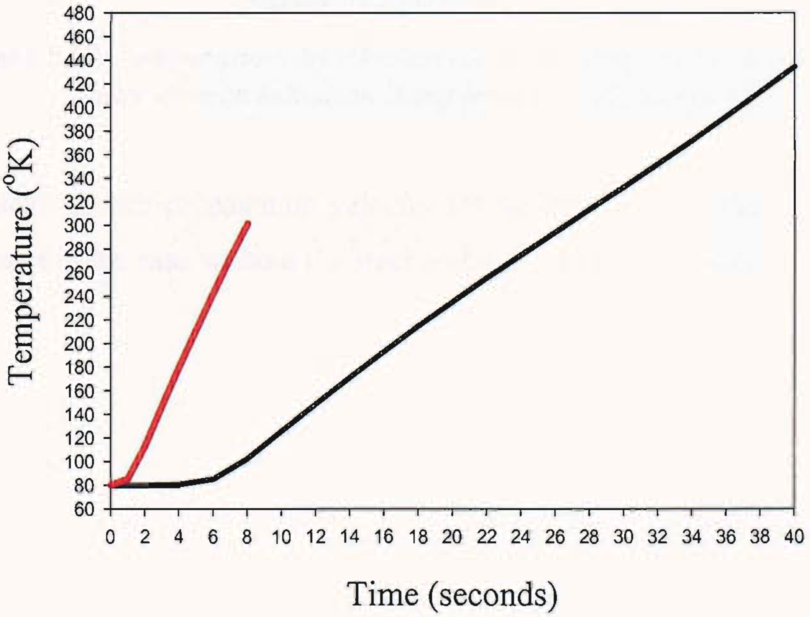

Figure 5.19. *The temperature evolution of the hottest spot in the normal zone (red without steel, black with steel)*

The time evolution of the temperature of the hottest spot is shown in figure 5.19 for the two cases, with and without the stainless steel back-up. The heating rate is 30 C/sec in the case without steel, whilst in the case with steel is 8 C/sec. Therefore, the heating process in the composite with stainless steel support included is slowed down by almost 3 times than the tape alone. Figures 5.20 and 5.21 display the temperature distributions along the current lead in the two cases every second.

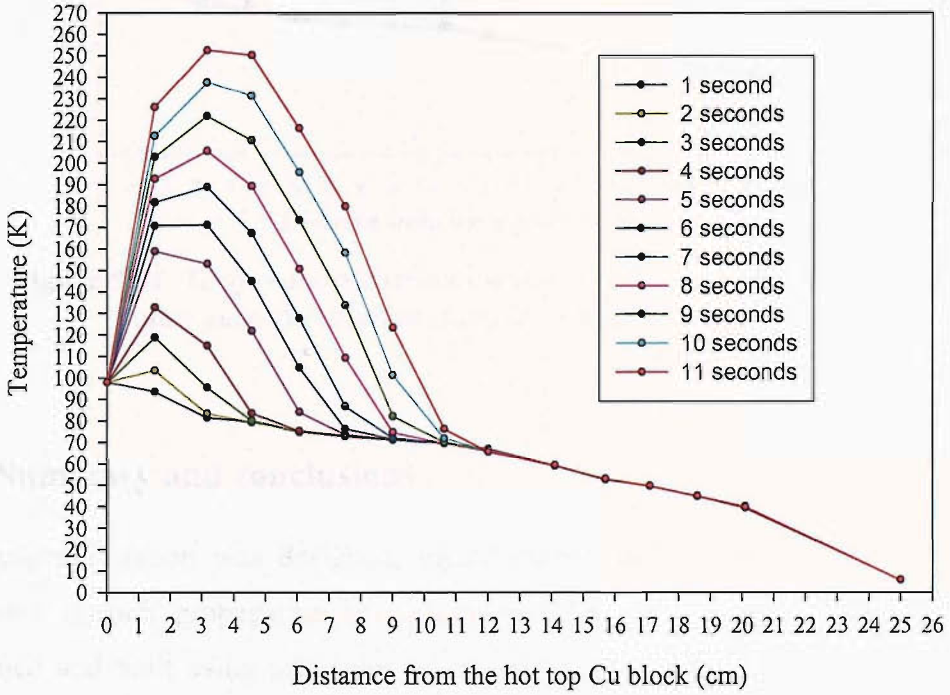

Figure 5.20. *Temperature distribution along the sample at different times after quench initiation (sample with steel substrate)*

The measured quench propagation velocity for the case without the steel is about 1 cm/sec, whilst in the case without the steel is about 1.5 to 1.6 cm/sec.

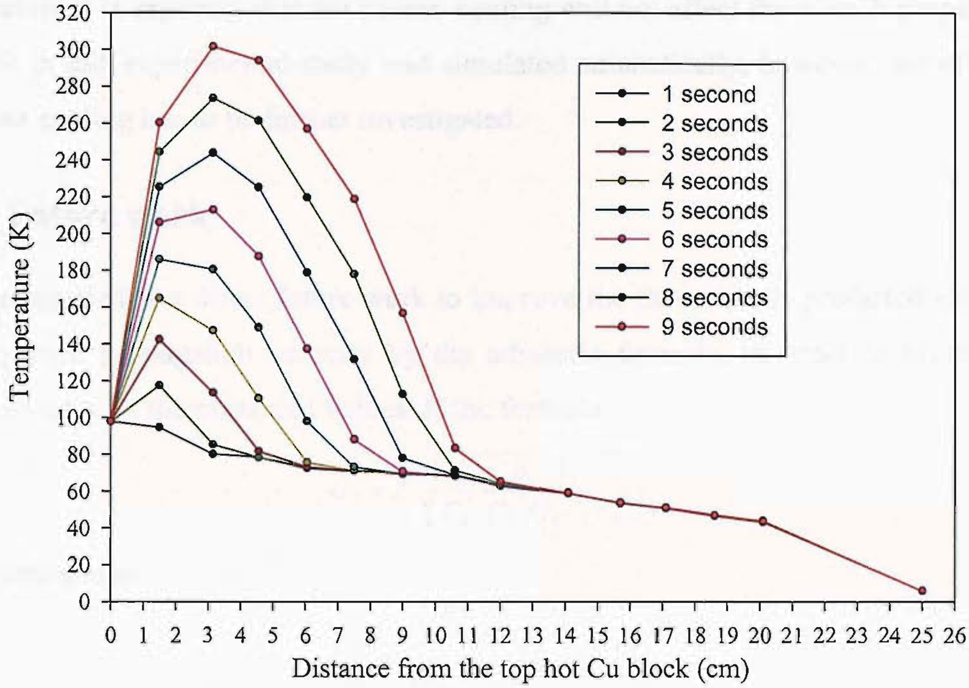

Figure 5.21. *Temperature distribution along the sample at different times after quench initiation (sample without steel substrate)*

5.6. Summary and conclusions

A cryogenic station was designed, manufactured and set-up in order to simulate adiabatic quench propagation in composite HTS current leads. The station was designed and built using principles of cryogenic design. During the experiment the station operated according to the design specifications; all the components have shown very good functionality. It has to be mentioned that the only weak point during the operation was the thermal linking of the current leads onto the first stage, which was proved not to be efficient enough in order to achieve sufficiently low temperature at the top Cu block. The problem was totally solved by reinforcing the thermal contact through an additional pair of Cu thermal links of the current leads to the first stage. The samples under investigation were made according to similar procedures to the manufacturing of the HTS elements of the 7.5 kA and 13 kA current leads for the LHC. The transient process of quench propagation of the composite HTS elements was successfully reproduced in the cryogenic station, thus giving useful results such as temperature and voltage-time characteristics. During the experiment, the quench did not propagate down to the bottom of the current lead. In the real case of operation this means that the boil-off of liquid helium will not increase during quenching.

Therefore it is expected that the helium cooling will not affect the quench propagation which in this experimental study was simulated adiabatically, however, the effect of helium cooling has to be further investigated.

5.7. Future work

It is suggested as a direct future work to improve the theoretically predicted values of the quench propagation velocity by the adiabatic formula, in order to bring close agreement with the measured values. If the formula

$$U_l = J \cdot \sqrt{\frac{\rho_n \cdot k_n}{C_n \cdot C_s \cdot (T_C - T_{cool})}}$$

is rearranged as

$$U_l = \sqrt{\frac{J^2 \cdot \rho_n \cdot k_n}{C_n \cdot C_s \cdot (T_C - T_{cool})}}$$

then the term

$$P = J^2 \times \rho_n$$

expresses the Joule heating in the composite which can be replaced by the value of

$$P = \int_{\substack{normal \\ zone}} \{V(x) \cdot I\} \cdot dx\,,$$

where the measured voltage profile along the current lead is integrated over the length of the normal zone. Therefore the Joule heat generation can be estimated directly from the experimental data thus eliminating the influence of the material properties. Further future work will include:

A. Experimental

The future wok has been planned in order to measure the quench propagation in current leads that are helium vapour cooled in order to simulate more accurate the quench propagation in these current leads. In view of prospect application of MgB_2 conductors for magnet development, the quench propagation in composite MgB_2 tapes will be also measured in order to provide useful and novel information with regard to the thermal stability of composite MgB_2 tapes.

B. Theoretical

Work is in progress now to investigate theoretically the quench propagation in composite HTS conductors. Finite element modelling has been employed using the commercial finite element package ANSYS in order to model the quench propagation in the composite current leads in the following cases:

1. Adiabatic quench propagation
2. Helium cooled quench propagation in the current leads

Both cases will be treated using a 2-dimensional model, in which the thermo-physical properties of the composite are considered to include the volumetrically averaged thermo-physical properties of the components of the composite.

$$C_{composite}^{eff} = \sum_{i=1}^{N} f_i \cdot C_i$$

The superconducting characteristics of the model will be considered in the heat generation term, which shall include the following:

a. Power law accounting for current sharing to the stabilizing matrix
b. Temperature dependent n-values and matrix resistivity
c. Ic values will be included as they have been obtained from experimental determination.

The finite element model will be built based on the following mathematical formulation for the heat generation term:

Input variables

Operational current I_{op}
Critical current $I_c(T)$
n-value, n
Matrix resistivity $\rho_m(T)$
Volumetric heat generation, $G(T, I_{op})$
Operational current density J_{op}

Equation for the operational current I_{op}

$$I_{op} = \left(\frac{E}{E_C}\right)^{1/n(T)} \cdot I_C(T) + \frac{E}{\rho_m(T)} \cdot A_m$$

The above equation is solved in order to find E (electric field in the superconductor) over the temperature range of interest. The values of E that are found are inserted into the following equation that calculates the heat generation:

Calculation of heat generation:

$$G(T, I_{op}) = J_{op} \times E$$

The work shall include the following tasks:

a. Estimation of the thermo-physical properties
b. Calculation of the heat generation term
c. Development of the model in the ANSYS package including the thermo-physical properties and the heat generation term
d. Solution of the model
e. Comparison of the model results with the experimental results that have obtained in the experimental section of this chapter.

The model will be extended in order to consider 3-dimensional modelling of the composite tapes, in which the thermo-physical properties of the components of the composite will be considered independently.

References

[1] Yunus A. Cengel, ***Introduction to thermodynamics and heat transfer***, McGraw-Hill, 1997, ISBN 0-07-0114, pg. 87

[2] Zhao Z.P. and Iwasa Y., ***Cryogenics*** (1991) 31 pg. 817

[3] Randall F. Barron, ***"Cryogenic Systems"***, Monographs on Cryogenics 3, 2nd Edition, Oxford University Press 1985, pg. 398

[4] Leybold Cryogenics, 8 Sagamore Park Road, Hudson, NH 03051, ***"Coolpower Coldhead Operating Manual, Coolpower - Model 4.2 GM"***

[5] A. Ballarino et al, EUCAS 2003, Sorrento, Italy

[6] A. Ballarino, personal communication